UNIVERSITÉ DU LUXEMBOURG

PhD-FSTC-2020-08
The Faculty of Science, Technology and Medicine

Dissertation

Presented on 13/03/2020 in Esch-sur-Alzette
to obtain the degree of

DOCTEUR DE L'UNIVERSITÉ DU LUXEMBOURG EN SCIENCES DE L'INGÉNIEUR

by
MAGLIULO Marco Eduardo Paolo
born on 08/07/1992 in Thionville, France

Non-localized contact between beams with circular and elliptical cross-sections

Doctoral Committee:

Chair:	Prof. BORDAS Stéphane
Jury:	Prof. KONYUKHOV Alexander
	Prof. POPP Alexander
	Prof. ZILIAN Andreas
	Dr.ir. BEEX Lars
	Dr. LENGIEWICZ Jakub
	Dr. HALE Jack

Acknowledgements

Firstly, I would like to express my sincere gratitude to my supervisors Dr. Beex and Prof. Zilian for the continuous support of my research, for their patience, motivation, extensive experience and knowledge. The scientific papers this thesis is based on would not have been possible without their help and guidance.

Besides my supervisors, I would like to thank Jakub Lengiewicz for having me shown the software AceGen without which I could not have experimented as many contact formulation as I did. I am also deeply thankful for the countless discussions we had and for the time you dedicated to me despite having a heavy research agenda on your own. I am also grateful to Jack Hale for his tips and pieces of advice, and also for his stirring vision of Science in general.

A special thanks to Pr. Bordas for having introduced Dr. Lengiewicz to me, and also for your dynamism, attention, endless energy and positivism in any circumstances.

I thank my fellow lab-mates for the stimulating exchanges we had. I am also thankful to my colleagues from the XDEM team, Xavier Besseron, and Alban Rousset that helped me countless times with their suggestions and experience when I got into a jam with my code.

Last but not least, I would like to thank my friends and family.

Table of contents

Symbols

$\mathbf{E}_i$	Basis vector of the global frame
$\mathbf{e}_i$	Basis vector of the local frame, current configuration
$\mathbf{x}_c$	Centroid point, current configuration
$\mathbf{x}_{0c}$	Centroid point, undeformed configuration
$\mathbf{u}$	Displacement of the centroid line
$\mathbf{x}_0$	Location of a point on the surface of the beam, undeformed configuration
$\mathbf{x}$	Location of a point on the surface of the beam, deformed configuration
$\mathbf{v}_0$	Vector connecting centroid point $\mathbf{x}_{0c}$ to surface point $\mathbf{x}_0$
$\mathbf{v}$	Vector connecting centroid point $\mathbf{x}_c$ to surface point $\mathbf{x}$
$\mathcal{B}^i$	Body i
$\partial\mathcal{B}^i$	Surface of body i
$\underline{h}^{\mathcal{B}^i}$	Column of surface parameters of body $\mathcal{B}^i$
$h^{\mathtt{I}k}$	Component k of $\underline{h}^{Bi}$
$\partial\mathcal{B}^i$	Surface of body $\mathcal{B}^i$
$\mathbf{g}$	Gap vector
$\mathbf{\Lambda}$	Rotation tensor
$\mathbf{n}^i$	Normal vector to the surface of body $\mathcal{B}^i$

$\boldsymbol{\tau}_k^{\partial\mathcal{B}^i}$	Tangent vector k (covariant) to the surface of body $\mathcal{B}^i$
$\underline{q}$	Column of local (unknown) variables
$\underline{\bar{q}}$	Column of local variables, solution of the local problem
$\bar{\mathbf{x}}^{\partial\mathcal{B}^i}$	Surface point on $\mathcal{B}^{\mathtt{I}}$'s surface at the solution of the local problem
$\underline{\bar{h}}^{\mathtt{I}}$	Surface parameters of body $\mathcal{B}^{\mathtt{I}}$ at the solution of the local problem
$\underline{f}$	Local residual
$\underline{\underline{H}}$	Stiffness matrix of the local problem
$\mathcal{C}$	A slave beam's cross section
$\partial\mathcal{C}$	Perimeter of a slave beam's cross section
$\underline{p}^{\mathcal{B}^i}$	Trial function body $\mathcal{B}^i$
$\delta\underline{p}^{\mathcal{B}^i}$	Test function for $\mathcal{B}^i$
$\underline{p}^{\mathtt{IJ}}$	Infinite-dimensional trial function of all bodies
$\delta\underline{p}^{\mathtt{IJ}}$	Infinite-dimensional test function for all bodies
$\underline{p}^h$	Finite-dimensional trial function of all bodies
$\delta\underline{p}^h$	Finite-dimensional test function for all bodies
$\underline{\hat{p}}$	Array of nodal trial function
$\delta\underline{\hat{p}}$	Array of nodal test function
Π_c	Contact potential
$\underline{r}_c$	Contact force vector
$\underline{\underline{K}}_c$	Contact stiffness matrix
g_N	Normal gap
$\Delta\mathbf{g}_T$	increment of tangential sliding between two increments projected on the contact plane $\mathcal{T}$
$\mathbf{g}_T$	the tangential gap vector
$\mathbf{g}_{Tel}$	elastic (accumulated) part of $\mathbf{g}_T$
$\Delta\mathbf{g}_{Tsl}$	increment in plastic sliding
t_N	Current normal traction vector

T_N	Nominal normal traction vector
$\mathbf{T}_T$	Nominal tangent traction vector
$\underline{r}_g$	Global residual vector
$\underline{\underline{K}}_g$	Global stiffness matrix
$\underline{f}_{ext}$	External force vector
$\tilde{\mathbf{X}}_c^k$	control point k of the smoothed centroid line, reference configuration
$\underline{\tilde{\mathbf{X}}}_c$	Column of control points, reference configuration
$\underline{\tilde{\mathbf{u}}}_c$	Column of control points for displacements
$\underline{\tilde{\boldsymbol{\theta}}}$	Column of control points for rotations
$\tilde{\mathbf{X}}_c$	Location of a point on the smoothed centroid line, reference configuration
$\tilde{\mathbf{u}}_c$	Interpolated displacement of the smoothed centroid line
$\tilde{\boldsymbol{\theta}}$	Interpolated rotation vector along the smoothed centroid line
$\underline{B}$	Column of Berstein's polynomials
$\tilde{\mathbf{e}}_k$	k^{th} vector of the local basis attached to the smoothed centroid line $\tilde{\mathbf{X}}_c$
$\tilde{\mathbf{v}}_0$	Vector in the (fictitious) cross-section attached to $\tilde{\mathbf{X}}_c$, undeformed configuration
$\tilde{\mathbf{v}}$	Vector in the (fictitious) cross-section attached to $\tilde{\mathbf{X}}_c$, current configuration
$\tilde{\mathbf{x}}^{\mathcal{B}^i}$	Point on the surface of the smoothed geometry of body $\mathcal{B}^i$
η_i	i^{th} parameter of the smoothed geometry
$\boldsymbol{\eta}$	Vector of parameters of the smoothed geometry
$\hat{\mathbf{u}}_k^{\mathcal{B}^i}$	Displacement of node k belonging to body $\mathcal{B}^i$
$\hat{\mathbf{x}}_{0k}^{\mathcal{B}^i}$	Location of node k in the undeformed configuration belonging to body $\mathcal{B}^i$
$\hat{\boldsymbol{\theta}}_k^{\mathcal{B}^i}$	Rotation vector of node k belonging to body $\mathcal{B}^i$.

Abstract

Numerous materials and structures are aggregates of slender bodies. We can, for example, refer to struts in metal foams, yarns in textiles, fibers in muscles or steel wires in wire ropes. To predict the mechanical performance of these materials and structures, it is important to understand how the mechanical load is distributed between the different bodies. If one can predict which slender body is the most likely to fail, changes in the design could be made to enhance its performance. As the aggregates of slender bodies are highly complex, simulations are required to numerically compute their mechanical behaviour. The most widely employed computational framework is the Finite Element Method in which each slender body is modeled as a series of beam elements. On top of an accurate mechanical representation of the individual slender bodies, the contact between the slender bodies must often be accurately modeled. In the past couple of decades, contact between beam elements has received wide-spread attention. However, the focus was mainly directed towards beams with circular cross-sections, whereas elliptical cross-sections are also relevant for numerous applications. Only two works have considered contact between beams with elliptical cross-sections, but they are limited to point-wise contact, which restricts their applicability. In this Ph.D. thesis, different frameworks for beams with elliptical cross-sections are proposed in case a point-wise contact treatment is insufficient. The thesis also reports a framework for contact scenarios where a beam is embedded inside another beam, which is in contrast to conventional contact frameworks for beams in which penetrating beams are actively repelled from each other. Finally, two of the three contact frameworks are enhanced with frictional sliding, where friction not only occurs due to sliding in the beams' longitudinal directions but also in the transversal directions.

CHAPTER I

Introduction

Numerous materials are aggregates of slender bodies. Examples such as metal foams, wire ropes, dry-woven fabrics, paper materials, muscles, electronic textiles and bones all have socio-economical importance, see Fig. 1.1. Their common denominator is that they function as load-carrying materials and that the mechanical failure of a single component can endanger the entire structure and the structure's surrounding. For instance, steel wire-ropes used in off-shore applications are assemblies of steel wires that interact with each other due to mechanical contact. These costly high-performance products carry heavy loads whilst exposed to severe chemical conditions (salt, oil, and oxidation). Consequently, their lifespan is short. Understanding the causes of the ropes' mechanical degradation and failure enables to adjust rope designs in order to reduce maintenance efforts and increase lifespan. This reduces costs and time, yielding more competitive products. Physical experiments can be conducted to assess the mechanical behavior and reliability of such structures, but they are time-consuming, require experimental facilities and sometimes necessitate the interruption of the production line (continuous or batch). Furthermore, only a few designs can be tested, whereas the number of design parameters is enormous. Hence, designs that are only based on physical experiments are sub-optimal. On top of this, physical experiments do not necessarily reveal much insight into the mechanical state of a structure. Virtual experiments based on computational models, however, are fast and reveal substantially more insight into the occurring mechanics. Consequently,

Figure 1.1: Different materials and applications as conglomerates of slender bodies. From left to right: SEM image of a dry-woven fabric; open-foam cell aluminum; a wire-rope; model of a muscle.

they result in better designs, obtained in substantially less time. In order to replace physical experiments with virtual ones, the simulations must accurately predict the important mechanics. The computational model must thus be accurate, but also robust and preferably fast.

1.1 Computational models for slender body mechanics

The computational models used in virtual experiments often rely on the Finite Element Method (FEM), in which the model, which is formulated in terms of partial differential equations (PDE), is transformed into a system of algebraic equations [96, 87]. In the FEM, each body is spatially subdivided into finite subdomains called finite elements in which fields of relevant physical quantities are interpolated from their nodal values. Different types of finite elements exist, and they differ notably by the type of kinematic variables interpolated, their geometry, type of interpolation and type of integration. Typically, tetrahedral or hexahedral elements are used to discretize three-dimensional structures. However, in order to capture the behaviour of slender bodies, a significant number of finite elements are required through slender direction (see Fig. 1.2). This renders simulations substantially slow.

Beam theories have been developed to capture the physics of slender bodies, and dedicated finite elements have been designed to discretise those theories. The mechanical behavior of each slender body is then represented as a series of beam finite elements. Beams are characterized by cross-sections whose centers of gravity

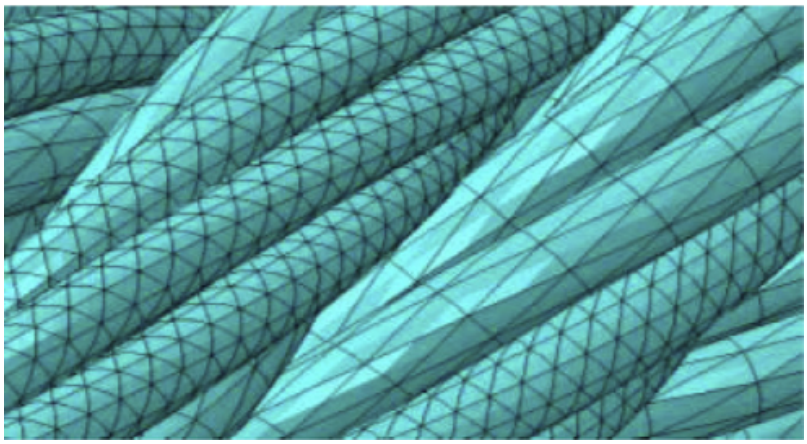

Figure 1.2: Numerous bulk elements used to model slender bodies [10].

form the centroid-line, see Section 2.2. Different beam theories are available in the literature [77, 78, 79, 31, 16, 56, 29, 71] and in this thesis the Simo-Reissner beam theory is employed. This theory allows for finite three-dimensional rotations and provides objective strain measures [77, 78]. Similar to many beam theories, the Simo-Reissner theory considers the cross-sections to be rigid (i.e. they cannot deform). This implies that deformation is only possible due to the cross-sections' relative displacements and rotations.

1.2 Modeling mechanical contact between slender bodies with beams.

Besides the modeling of the individual slender bodies, the modeling of the mechanical contact between the bodies is essential in order to achieve accurate computational models. Several frameworks to treat contact between beams were developed in the past. However, most of them are restricted to beams with circular cross-sections and to contact interactions occurring on a narrow part of the beams' surfaces. Narrow contact zones indeed occur for sparse networks such as presented in Fig. 1.3, but for dense assemblies (first, third and fourth image in Fig. 1.1) the contact zone can span the entire length of the slender bodies. Furthermore, numerous slender bodies

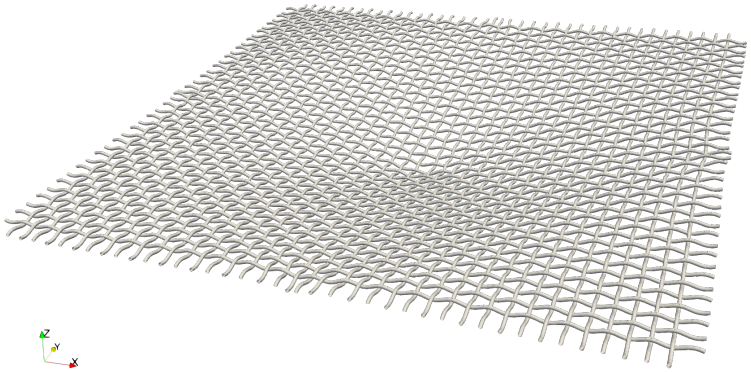

Figure 1.3: A network of yarns in contact.

do not possess circular cross-sections. We can think for instance about yarns [20] or steel wires in wire ropes. The cross-sections' shape in these cases is closer to an ellipse or hyper-ellipse than to a circle. The cross-sectional shape not only influences the bending and torsional resistance of each body independently, but it also governs the mechanical contact between the bodies.

1.3 Aim

Accurate and robust beam-to-beam contact frameworks are clearly crucial to formulate proper computational models. These frameworks exist for beams with circular cross-sections exposed to narrow contact zones [89, 95, 62], for beams with circular cross-sections exposed to large contact zones [59, 62] and for beams with elliptical cross-sections exposed to narrow contact zones [24, 25]. However, no framework is able to handle contact between beams with elliptical cross-section exposed to large contact zones. The aim of this thesis is therefore to propose such a contact framework. Since circles are one instance of ellipses, the contact frameworks proposed in this thesis can be applied to beams with circular as well as elliptical cross-sections.

1.4 Outline

Chapter II presents a framework to treat non-localized contact between beam finite elements with elliptical or circular cross-sections. The first novelty is the introduction of a smooth surface approximation of the beams' surfaces because the surface of the discretized beams are discontinuous. Indeed, the undeformed centroid line of a series of the finite element employed is C^0-continuous. As cross-sections are normal to the centroid-line in the undeformed configuration, gaps and overlaps are present in the discretized beams' surface. This smooth surface approximation is used throughout the other Chapters of this thesis.

The contact framework of Chapter II considers numerous material points on the surface of one of the two beams candidate for contact. The framework computes for each point how deep it penetrates another beam. If a point is found to be penetrating, a contact force is applied between the point and its projection on the other beam's surface. This contact force repels the two bodies. This scheme is only applicable to the penalty method and permits to treat large contact zones. This scheme constitutes, to best of the author's knowledge, the first attempt to treat non-localized contact between beams with cross-sections different from circles.

Chapter III, presents a substantially faster beam-to-beam contact framework than the one presented in Chapter III. The framework of Chapter III does not consider material points with fixed material coordinates on one of the beams' surface. Instead, it considers entire cross-sections at once. This implies that for each selected cross-section, only one measure of penetration is computed and one contact interaction is used to repel the cross-section from the other beam's surface in case of penetration.

Chapter IV, presents the first "beam-inside-beam" contact scheme (to the best of the author's knowledge). Instead of repelling two beams from each other, the contact framework ensures that two beams remain embedded inside each other. This framework is amongst others applicable to describe the response of a slender medical instrument inside an artery. Similar to the framework of Chapter III, the framework considers entire cross-sections at once. The difference is that instead of the amount of penetration, the amount of 'exclusion' is computed.

As friction must often be incorporated to obtain accurate computational models, Chapter V extends the frameworks of Chapters III and IV to frictional contact. Coulomb's law is employed to this end. In contrast to most existing frictional contact frameworks for beams, the framework of Chapter V not only incorporates frictional sliding in the beams' axial direction but also in the circumferential direction.

Finally, conclusions and the potential of the proposed contact frameworks are presented in Chapter 5.5. Also, recommendations for future developments of the presented frameworks are discussed.

CHAPTER II

Contact between shear-deformable beams with elliptical cross-sections[1]

2.1 Introduction

Paper materials (wood fibres [5, 55, 82, 46, 44]), fabrics (yarns [6, 8, 9, 69, 65]), and metal foams (struts [34, 33, 81, 68, 3]) are examples of materials with slender components in their micro-structure. Micro- mechanical models of such materials often represent each slender constituent as a beam, which yields a string of beam finite elements when discretized [4] (or springs [7, 66]). In most cases, contact between the slender constituents is essential to be incorporated. Almost all contact frameworks have however focused on beams with circular cross-sections. To the best of the authors' knowledge, only three frameworks are demonstrated to work for beams with non-circular cross-sections ([24, 25] and [37]), but they are limited by the fact that contact can only occur in a point-wise manner.

In many applications however, the slender constituents do not come with circular cross-sections and contact does not occur at a single point. This contribution therefore aims to partially fill this gap by proposing an algorithm that treats contact between shear-deformable beams with elliptical cross-sections. The scheme is tai-

[1]Reproduced from: Magliulo, M., Zilian, A., and Beex, L.A.A., Contact between shear-deformable beams with elliptical cross-sections. Acta Mechanica (2019). doi:10.1007/s00707-019-02520-w.

lored for contact to occur at an area on the beams' surfaces, instead of only at a pair of surface points. Consequently, it is more widely applicable and can for instance be applied to the cases of Fig. 2.1, which cannot be treated by point-wise contact schemes.

The proposed contact scheme seeds many quadrature points on the surface of beams and determines which ones penetrate the surrounding beams. To do so, a measure of penetration is established for point, which is used in a penalty potential that is incorporated in the potential energy of the system in order to repel penetrating beams in case of penetration.

The scheme is applied to beam elements with two nodes based on the geometrically exact beam (GEB) theory. As the surfaces of strings of such beam elements are only C^0-continuous, and may even be C^{-1}-continuous, the contact scheme works on a smooth (approximated) surface. The smooth surface is obtained by smoothing the strings' centroid-lines using Bézier curves. The kinematic variables (i.e. the displacements and rotations) are also re-interpolated. The capabilities of the contact scheme are demonstrated for several numerical test cases. These include the twisting of wire ropes. We show that cross-sectional shapes may have a critical influence on the deformations. The introduced contact framework remains to converge even when the structures in contact undergo large sliding displacements and/or large rotations and/or large deformations. We also demonstrate that large sliding displacements of the contacting surfaces can occur without the chattering phenomenon [92] thanks to the artificially smoothed surface.

In the next section, we briefly discuss the kinematics of the GEB theory. Section 2.3 discusses the contact framework, still in the space-continuous setting. In Section 2.4, we discretise beams with beam finite-elements with two nodes. We amongst others discuss why the surface of connected beam elements is C^0-continuous at best for this type of beam. The smooth approximations of the discretized beams' surfaces is discussed next and the proposed contact framework is adapted to them. Section 2.5 presents initial numerical results. The contribution closes with some conclusions and an outlook.

(a) Two parallel beams. (b) Two beams folded around each other.

Figure 2.1: Some examples in which the shortest distance between two surfaces is not uniquely or poorly defined, thus preventing the application of a point-wise contact force.

2.2 Kinematics

The Simo-Reissner Geometrically Exact Beam (GEB) theory ([77, 78, 79, 31, 29, 72, 58]) of shear-deformable beams with rigid cross-sections is used in this contribution. A beam is then characterized by centroid-line $\mathbf{x}_c(h^1) : [0, L_0] \to \mathbb{R}^3$ constituted from the center of gravity of its sections, and by the orientations of the cross-sections (see Fig. 2.2). h^1 is the arc-length parameter of the centroid-line of the beam in the reference configuration and L_0 its reference length. Rigid cross-sections are not necessarily orthogonal to $\mathbf{x}_c$ in the current (deformed) configuration if shear deformation is present. A field of rotation tensor $\mathbf{\Lambda}(h^1) : [0, L_0] \to SO(3)$ is used to orientate the cross-sections in the current configuration.

Material points on the beam's centroid-line

The centroid-line in the current configuration, $\mathbf{x}_c(h^1)$, is related to the centroid-line in the reference configuration, $\mathbf{x}_{0c}(h^1)$, by:

$$\mathbf{x}_c(h^1) = \mathbf{x}_{0c}(h^1) + \mathbf{u}(h^1), \tag{2.1}$$

where $\mathbf{u}(h^1) : [0, L_0] \to \mathbb{R}^3$ denotes the displacement field of the centroid-line.

Material points in the rest of the beam

To locate material points on the beam's centroid-line (in the reference and deformed configurations), only h^1 is needed. To locate the remaining material points however, we need to consider cross-sections, which are parametrised by two parameters denoted k^2 and k^3.

The location vector pointing towards a material point with local coordinates $\underline{h} = [h^1, k^2, k^3]$ that is not located on the centroid-line can be expressed in the reference configuration as follows:

$$\mathbf{x}_0(\underline{h}) = \mathbf{x}_{0c}(h^1) + \mathbf{v}_0(\underline{h}), \tag{2.2}$$

and in the deformed configuration as:

$$\mathbf{x}(\underline{h}) = \mathbf{x}_c(h^1) + \mathbf{v}(\underline{h}), \tag{2.3}$$

where $\mathbf{v}_0$ and $\mathbf{v}$ point from the centroid-line to the material point and both lie in the cross-sectional plane associated with h^1. $\mathbf{v}_0$ works in the reference configuration and $\mathbf{v}$ in the deformed configuration. These two vectors can be written as follows:

$$\mathbf{v}_0(\underline{h}) = k_2\mathbf{e}_{02}(h^1) + k_3\mathbf{e}_{03}(h^1), \tag{2.4}$$

$$\mathbf{v}(\underline{h}) = \mathbf{\Lambda}(h^1)(k_2\mathbf{e}_{02}(h^1) + k_3\mathbf{e}_{03}(h^1)), \tag{2.5}$$

where $\mathbf{e}_{02}(h^1)$ and $\mathbf{e}_{03}(h^1)$ form an orthonormal basis with $\mathbf{e}_{01}(h^1)$ (see Fig. 2.2). In Eq. (2.5), $\mathbf{\Lambda} \in SO(3)$ where $SO(3)$ is the rotation group denotes the rotation tensor rotating the cross-section attached to $\mathbf{x}_{0c}$ in the reference configuration.

In the reference configuration the (unit) normal vector to the cross-section attached to $\mathbf{x}_{0c}$, $\mathbf{e}_{01}$, verifies:

$$\mathbf{e}_{01} = \frac{\partial \mathbf{x}_{0c}}{\partial h^1}, \tag{2.6}$$

because no shear deformation is present. As mentioned above however, the normal to the cross-section in the current configuration is not necessarily aligned with the

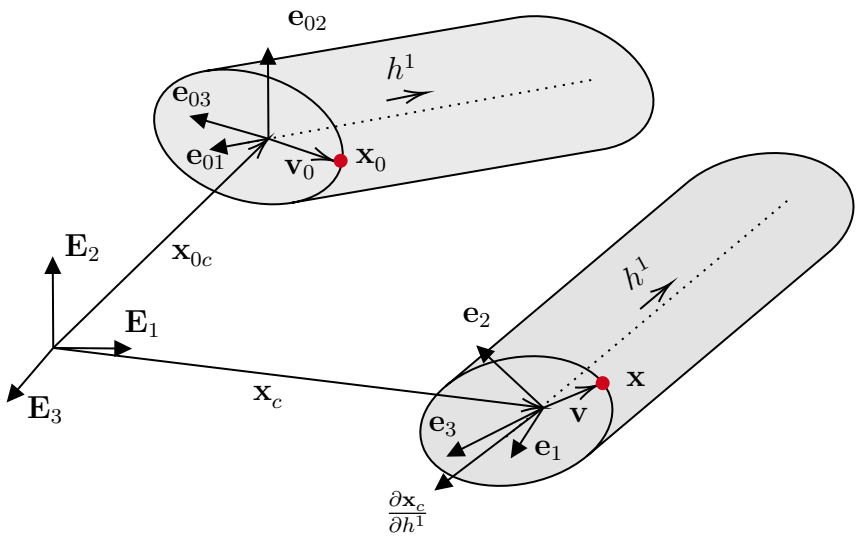

Figure 2.2: A surface point $\mathbf{x}_0$ in the reference configuration (red circle) obtained by adding location vector $\mathbf{x}_{0c}$ and a vector $\mathbf{v}_0$ in the plane $(\mathbf{e}_{02}, \mathbf{e}_{03})$ of the cross-section attached to $\mathbf{x}_{0c}$. The same material point is represented in the deformed configuration. The global basis $\{\mathbf{E}_1, \mathbf{E}_2, \mathbf{E}_3\}$ as well as the local basis $\{\mathbf{e}_{01}, \mathbf{e}_{02}, \mathbf{e}_{03}\}$ attached to the $\mathbf{x}_{0c}$ in the reference configuration and the local basis $\{\mathbf{e}_1, \mathbf{e}_2, \mathbf{e}_3\}$ attached to the same point in the deformed configuration are also presented. These three basis are orthonormal.

tangent direction to the centroid-line, which means that:

$$\mathbf{\Lambda}\mathbf{e}_{01} \neq \frac{\partial \mathbf{x}_c}{\partial h^1}. \tag{2.7}$$

2.3 Contact framework

In the following, we focus on a system with two bodies, $\mathcal{B}^{\mathtt{I}}$ and $\mathcal{B}^{\mathtt{J}}$. The contact framework is based on the integration of a surface-specific contact potential over the surface of one of the beams. To this end, contact points are seeded on the surface of $\mathcal{B}^{\mathtt{I}}$. We check for each of these surface points if it penetrates $\mathcal{B}^{\mathtt{J}}$. If a surface point

is indeed penetrated, a contribution to a contact potential is added. The suggested scheme is thus a type of master-slave approach [85] which asymmetrically treats contact, in contrast to [24, 25, 94, 95]. $\mathcal{B}^{\mathrm{I}}$ is called the slave and $\mathcal{B}^{\mathrm{J}}$ the master.
The surface of both beams is explicitly taken into account. This is different from the approaches in [37, 21, 84] in which the centroid-lines are used to formulate contact due to the limitation of circular cross-sections. A penalty approach is adopted here to regularize unilateral contact conditions. It allows some interpenetration between the bodies, which can be interpreted as the deformation of the rigid cross-sections in case of contact. The latter cannot deform due to the constraint of underfomable cross-sections of the underlying beam theory, therefore, the penalty formulation introduces the additional (cross-section) compliance on the top of the standard beam model.

2.3.1 Projection

In this subsection, we discuss for a single surface point how we determine if it penetrates another beam. We start with the definition of a fixed surface point. We denote its surface coordinates by $\underline{h}^{\mathrm{I}}$ which remain constant. In a deformed configuration, the location of this point is expressed in the global coordinate system by $\mathbf{x}^{\mathrm{I}} = \mathbf{x}^{\mathrm{I}}(\underline{h}^{\mathrm{I}})$. Similarly as for the slave body $\mathcal{B}^{\mathrm{I}}$, we denote the location of a material point on the surface of the master beam $\mathcal{B}^{\mathrm{J}}$ by $\underline{h}^{\mathrm{J}}$ in terms of the local coordinates of the beam and by $\mathbf{x}^{\mathrm{J}} = \mathbf{x}^{\mathrm{J}}(\underline{h}^{\mathrm{J}})$ in the global basis.
It is important to note however that if elliptical cross-sections are used, only two independent variables are required to locate a material point on a beam's surface ([24]). We therefore write $\underline{h}^{\mathrm{I}} = \underline{h}^{\mathrm{I}}(h^{\mathrm{I}1}, h^{\mathrm{I}2}(k_2^{\mathrm{I}}, k_3^{\mathrm{I}}))$ and $\underline{h}^{\mathrm{J}} = \underline{h}^{\mathrm{J}}(h^{\mathrm{J}1}, h^{\mathrm{J}2}(k_2^{\mathrm{J}}, k_3^{\mathrm{J}}))$ where $\underline{h}$ denotes the column with these two independent variables. One of them is $h^1 \in [0, L]$, while the second one is $h^2 \in [0, 2\pi]$ such that k_2 and k_3 in Eqs. (2.4) and (2.5) are given by:

$$k_2 = a\ cos(h^2) \tag{2.8}$$

and

$$k_3 = b\ sin(h^2) \tag{2.9}$$

respectively, where a and b denote the dimensions of the elliptical cross-section in its two principal directions.

We define the projection based on Fig. 2.3 and state that vector $\mathbf{x}^{\mathrm{I}} - \mathbf{x}^{\mathrm{J}}$, must point in the same direction as the vector $\mathbf{x}^{\mathrm{J}} - \mathbf{x}_c^{\mathrm{J}}$. This is verified when the following residual is zero:

$$\underline{f}(\underline{h}^{\mathrm{J}}, g) = \mathbf{x}^{\mathrm{I}} - g\frac{\mathbf{x}^{\mathrm{J}} - \mathbf{x}_c^{\mathrm{J}}}{\|\mathbf{x}^{\mathrm{J}} - \mathbf{x}_c^{\mathrm{J}}\|} - \mathbf{x}^{\mathrm{J}}, \tag{2.10}$$

where g is an independent variable, which is negative in case of penetration and positive otherwise. We denote by $\bar{g}$ the value of g at the solution of Eq. (2.10), that will be used as a measure of penetration in the following. In Eq. (2.10) we used the vector $\frac{\mathbf{x}^{\mathrm{J}}-\mathbf{x}_c^{\mathrm{J}}}{\|\mathbf{x}^{\mathrm{J}}-\mathbf{x}_c^{\mathrm{J}}\|}$ as an approximation of the normal to the master body $\mathbf{n}^{\mathrm{J}}$ at surface point $\mathbf{x}^{\mathrm{J}}$. This choice is justified by the fact that $\mathbf{n}^{\mathrm{J}}$ changes abruptly in the regions of high curvatures of the surface. This can cause convergence problems at the global level because of the direction of the contact forces may change significantly from one (global) iteration to the next. We thus want to find column $\bar{\underline{q}} = [\bar{\underline{h}}^{\mathrm{J}}, g]^T$ for which $\underline{f}(\bar{\underline{q}}) = \underline{0}$. Here and in the following, a bar over a quantity indicates that this quantity is evaluated at the solution of Eq. (2.10).

We solve $\underline{f}(\bar{\underline{q}}) = \underline{0}$ this by linearising $\underline{f}$ in Eq. (2.10) and applying Newton's method, which we write as follows:

$$\underline{f}(\underline{q}^e) + \underline{\underline{H}}(\underline{q}^e)\,\Delta\underline{q} = \underline{0}, \tag{2.11}$$

where $\underline{q}^e$ denotes the previous estimate of $\bar{\underline{q}}$ and $\Delta\underline{q}$ denotes its update. Row of vectors $\underline{\underline{H}}$ is given by:

$$\underline{\underline{H}}(\underline{q}^e) = \left.\frac{\partial \underline{f}}{\partial(\underline{q})}\right|_{\underline{q}=\underline{q}^e}. \tag{2.12}$$

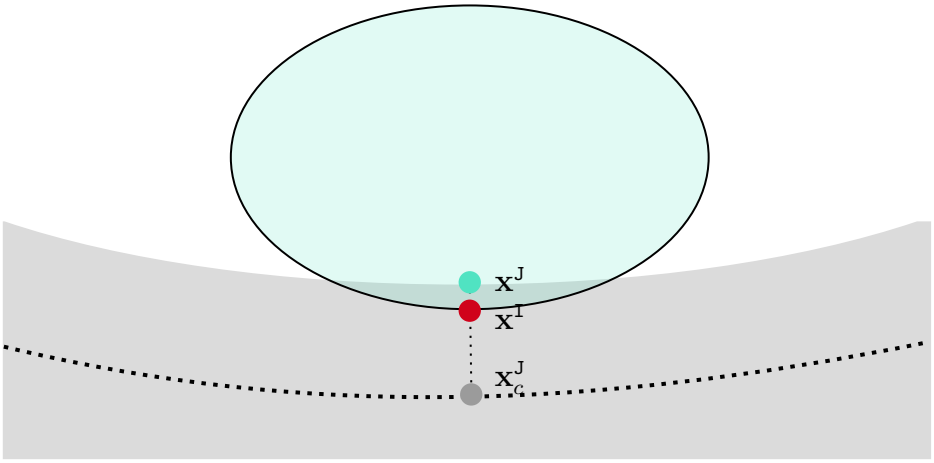

Figure 2.3: Penetrated slave surface point $\mathbf{x}^{\mathrm{I}}$ (in red). The slave cross-section on which $\mathbf{x}^{\mathrm{I}}$ lies is presented in translucent blue. The centroid-line of the master beam (grey) is presented by a thick dashed line. The master surface point at the solution of the projection problem is presented in blue. In this particular configuration, the vectors $\mathbf{x}^{\mathrm{J}} - \mathbf{x}^{\mathrm{J}}_c$ and $\mathbf{x}^{\mathrm{J}} - \mathbf{x}^{\mathrm{I}}$ are colinear and Eq. (2.10) is verfied if $g_N = -\left\|\mathbf{x}^{\mathrm{I}} - \mathbf{x}^{\mathrm{J}}\right\|$ at the solution of the local problem.

2.3.2 Contact potential

The measure of penetration between of surface point $\mathbf{x}^{\mathrm{I}}$ in body $\mathcal{B}^{\mathrm{J}}$ is given by:

$$g_N = (\bar{\mathbf{x}}^{\mathrm{J}} - \mathbf{x}^{\mathrm{I}}) \cdot \bar{\mathbf{n}}^{\mathrm{I}}. \tag{2.13}$$

As mentioned before, we use a penalty potential to limit penetration of surface point $\mathbf{x}^{\mathrm{I}}$ in body $\mathcal{B}^{\mathrm{J}}$. We use the following penalty potential to do so:

$$\Pi_{pen}(\underline{p}^{\mathrm{I}}, \underline{p}^{\mathrm{J}}, \underline{\bar{q}}(\underline{p}^{\mathrm{I}}, \underline{p}^{\mathrm{J}})) = \begin{cases} \frac{\epsilon_N}{2}\left((g_N)^2 - T g_N + \frac{T^2}{3}\right) & \text{if} \quad g_N < T \\ \frac{\epsilon_N}{6T}(g_N)^3 & \text{if} \quad T \leqslant g_N < 0\,, \\ 0 & \text{if} \quad g_N \geqslant 0 \end{cases} \tag{2.14}$$

where ϵ_N denotes the user-selected penalty stiffness and $\underline{p}^i$ denotes the fields of kinematic variables of the i^{th} beam that are involved in the contact. In Eq. (2.14),

T denotes a numerical parameter used to switch between a cubic and a quadratic penalty potential. The cubic potential is effective to regularize contact for surface points with small contact forces, as their contact status (penetrated or detached) may easily change from one global iteration to the next [21] and which may cause convergence issues (at the global level). Note also that the transition between the quadratic and cubic part of the potential is smooth, and so is the transition of its derivative.

2.3.3 Integration of the contact potential over the slave surface.

As contact interactions arise over a finite area, the total contact potential is obtained from the following integral on the slave side:

$$\Pi_c(\underline{p}^{\mathtt{I}}, \underline{p}^{\mathtt{J}}, \bar{\underline{q}}(\underline{p}^{\mathtt{I}}, \underline{p}^{\mathtt{J}})) = \int_{\partial\mathcal{S}^{\mathtt{I}}} \Pi_{pen}\, dS^{\mathtt{I}}, \tag{2.15}$$

where $\partial\mathcal{S}^{\mathtt{I}}$ denotes the slave surface and $\bar{\underline{q}}$ denotes the entire projection of the slave surface on the master surface according to Eq. (2.10) [45, 40]. $dS^{\mathtt{I}}$ denotes an infinitesimal part of the surface $\partial\mathcal{S}^{\mathtt{I}}$ in the current configuration.

To numerically evaluate the integral in Eq. (2.15), numerous slave (quadrature) points are seeded on the surface of the slave body. For each one of them (that is detected as being close enough to the master surface), the projection problem in Section 2.3.1 is solved. If a surface point on the slave surface penetrates the master body, the associated contribution is added to the total contact potential:

$$\Pi_c(\underline{p}^{\mathtt{I}}, \underline{p}^{\mathtt{J}}, \bar{\underline{q}}(\underline{p}^{\mathtt{I}}, \underline{p}^{\mathtt{J}})) = \sum_{k=1}^{n} w_k \Pi_{pen/k} \left\| \mathbf{n}^{\mathtt{I}}(\underline{h}_k^{\mathtt{I}}) \right\|, \tag{2.16}$$

where w_k denotes the weight factor and:

$$\mathbf{n}^{\mathtt{I}}(\underline{h}_k^{\mathtt{I}}) = \frac{\partial \mathbf{x}^{\mathtt{I}}}{\partial h^{\mathtt{I}1}} \times \frac{\partial \mathbf{x}^{\mathtt{I}}}{\partial h^{\mathtt{I}2}}, \tag{2.17}$$

the non-unit normal vector to the surface (which serves as a deformation-dependent

weight to the quadrature point). $\Pi_{pen/k}$ denotes the contact potential of the k^{th} slave surface point with local coordinates $\underline{h}_k^{\mathtt{I}}$ and is given by Eq. (2.14).

2.3.4 Contact potential's contribution to the weak form

Now that the contact potential between $\mathcal{B}^{\mathtt{I}}$ and $\mathcal{B}^{\mathtt{J}}$ is constructed, its contribution to the weak form needs to be derived. To do so, we consider the variation of Eq. (2.16) with respect to the kinematic variables of both bodies in contact:

$$\delta\Pi_c(\underline{p}^{\mathtt{I}}, \underline{p}^{\mathtt{J}}, \underline{\bar{q}}(\underline{p}^{\mathtt{I}}, \underline{p}^{\mathtt{J}})) = \sum_{k=1}^{n} w_k \delta \left(\Pi_{pen/k} \left\| \mathbf{n}^{\mathtt{I}}(\underline{h}_k^{\mathtt{I}}) \right\| \right). \tag{2.18}$$

The variation of the contact potential for a single quadrature point (from now we omit subscript k) can be expressed as follows:

$$\delta \left(\Pi_{pen} \left\| \mathbf{n}^{\mathtt{I}}(\underline{h}^{\mathtt{I}}) \right\| \right) = \left\| \mathbf{n}^{\mathtt{I}}(\underline{h}^{\mathtt{I}}) \right\| \delta\Pi_c + \Pi_{pen} \delta \left\| \mathbf{n}^{\mathtt{I}}(\underline{h}^{\mathtt{I}}) \right\|. \tag{2.19}$$

Now we will work out the two parts of this variation. For the ease of the notation, we collect all kinematic variables in $\underline{p}^{\mathtt{IJ}}$. Π_{pen} depends explicitly on $\underline{p}^{\mathtt{IJ}}$, as well as on $\underline{q}$ (itself depending implicitly on $\underline{p}^{\mathtt{IJ}}$ *i.e.* $\underline{q}(\underline{p}^{\mathtt{IJ}})$). Its variation can thus be expressed as:

$$\delta\Pi_{pen} = \frac{\partial \Pi_{pen}}{\partial \underline{p}^{\mathtt{IJ}}} \cdot \delta \underline{p}^{\mathtt{IJ}} + \frac{\partial \Pi_{pen}}{\partial \underline{q}} \cdot \delta \underline{q}. \tag{2.20}$$

As the primary variables of the problem are the kinematic variables stored in $\underline{p}^{\mathtt{IJ}}$ however, the variation must ultimately be expressed in terms of $\delta\underline{p}^{\mathtt{IJ}}$. To establish the relationship between $\delta\underline{q}$ and $\delta\underline{p}^{\mathtt{IJ}}$, we state that the local residual in Eq. (2.10) must remain valid for an infinitesimal change of $\underline{p}^{\mathtt{IJ}}$. We express this as follows:

$$\delta \underline{f}(\underline{\bar{q}}) = \left. \frac{\partial \underline{f}}{\partial \underline{p}^{\mathtt{IJ}}} \right|_{\underline{q}=\underline{\bar{q}}} \delta \underline{p}^{\mathtt{IJ}} + \left. \frac{\partial \underline{f}}{\partial \underline{q}} \right|_{\underline{q}=\underline{\bar{q}}} \delta \underline{\bar{q}} = \underline{0}. \tag{2.21}$$

We can recognize matrix $\underline{\underline{H}}$ of Eq. (2.11) in this expression as:

$$\underline{\underline{H}}(\bar{\underline{q}}) = \left.\frac{\partial \underline{f}}{\partial \underline{q}}\right|_{\underline{q}=\bar{\underline{q}}}, \tag{2.22}$$

with the only difference that $\underline{\underline{H}}$ in Eq. (2.11) is evaluated at an estimate of $\underline{q}$ (i.e. at $\underline{q}^e$) and here it is evaluated at $\bar{\underline{q}}$. Based on Eq. (2.21), we can now write:

$$\delta\bar{\underline{q}} = \left(-\underline{\underline{H}}(\bar{\underline{q}})^{-1} \left.\frac{\partial \underline{f}}{\partial \underline{p}^{\mathtt{IJ}}}\right|_{\underline{q}=\bar{\underline{q}}}\right) \delta\underline{p}^{\mathtt{IJ}} = \underline{\underline{A}}\,\delta\underline{p}^{\mathtt{IJ}}, \tag{2.23}$$

such that Eq. (2.20) can be written as:

$$\begin{aligned}
\delta\Pi_c &= \left(\frac{\partial \Pi_{pen}}{\partial \underline{p}^{\mathtt{IJ}}}\right) \cdot \delta\underline{p}^{\mathtt{IJ}} + \left(\frac{\partial \Pi_{pen}}{\partial \underline{q}}\right) \cdot \underline{\underline{A}}\,\delta\underline{p}^{\mathtt{IJ}} \\
&= \delta\underline{p}^{\mathtt{IJ}} \cdot \left(\frac{\partial \Pi_{pen}}{\partial \underline{p}^{\mathtt{IJ}}} + \underline{\underline{A}} \cdot \frac{\partial \Pi_{pen}}{\partial \underline{q}}\right) \\
&= \delta\underline{p}^{\mathtt{IJ}} \cdot \underline{r}_c.
\end{aligned} \tag{2.24}$$

The issue with this expression is that $\frac{\partial \Pi_{pen}}{\partial \underline{p}^{\mathtt{IJ}}}$ is significantly elaborated to derive and hence, its derivation is prone to mistakes. We therefore do not derive $\underline{r}_c$ analytically but we employ the automatic differentiation technique. With the formalism introduced in [47], we equivalently obtain $\underline{r}_c$ as follows:

$$\underline{r}_c = \left.\frac{\hat{\partial} \Pi_{pen}}{\hat{\partial} \underline{p}^{\mathtt{IJ}}}\right|_{\frac{\hat{\partial}(\bar{\underline{q}})}{\hat{\partial}\underline{p}^{\mathtt{IJ}}} = \underline{\underline{A}}}, \tag{2.25}$$

where $\frac{\hat{\partial}}{\hat{\partial}\underline{w}}$ denotes differentiation with respect to variables $\underline{w}$ performed by the Automatic Differentiation (AD) algorithm [47, 41].

2.3.4.1 $\delta \left\|\mathbf{n}^{\mathtt{I}}(\underline{h}^{\mathtt{I}})\right\|$

Now that we have treated variation $\delta\Pi_c$ in Eq. (2.19), we continue with variation $\delta \left\|\mathbf{n}^{\mathtt{I}}(\underline{h}^{\mathtt{I}})\right\|$ in Eq. (2.19). As $\mathbf{n}^{\mathtt{I}}$ corresponds to the normal vector of a (fixed) slave surface point, it does not depend on $\underline{q}$, so its variation simply reads:

$$
\begin{aligned}
\delta \left\| \mathbf{n}^{\mathtt{I}} \right\| &= \delta \mathbf{n}^{\mathtt{I}} \frac{\mathbf{n}^{\mathtt{I}}}{\left\| \mathbf{n}^{\mathtt{I}} \right\|} \\
&= \left(\frac{\partial \mathbf{n}^{\mathtt{I}}}{\partial \underline{p}^{\mathtt{IJ}}} \right)^{T} \delta \underline{p}^{\mathtt{IJ}} \frac{\mathbf{n}^{\mathtt{I}}}{\left\| \mathbf{n}^{\mathtt{I}} \right\|} \\
&= \delta \underline{p}^{\mathtt{IJ}} \cdot \frac{\partial \mathbf{n}^{\mathtt{I}}}{\partial \underline{p}^{\mathtt{IJ}}} \frac{\mathbf{n}^{\mathtt{I}}}{\left\| \mathbf{n}^{\mathtt{I}} \right\|} \\
&= \delta \underline{p}^{\mathtt{IJ}} \cdot \underline{d}. \qquad (2.26)
\end{aligned}
$$

In order to compute the consistent tangent matrix of the contact scheme, we again use the automatic differentiation technique (see [47, 48, 42, 41]) which yields:

$$
\underline{\underline{K}} = \left. \frac{\hat{\partial} \underline{r}_c}{\hat{\partial} \underline{p}^{\mathtt{IJ}}} \right|_{\frac{\hat{\partial}(q)}{\partial \underline{p}^{\mathtt{IJ}}} = \underline{\underline{A}}} . \qquad (2.27)
$$

2.4 Spatial discretization with the Finite Element Method and smoothing of the surface

2.4.1 Finite Element Discretization

Each beam is now discretized as a string of successive beam finite elements. Each beam element employed in this contribution uses two nodes. Each node comes with a reference location vector, a displacement vector and three rotations. The displacements and rotations form the six kinematic variables of each node. The elements thus use a linear interpolation of (i) $\mathbf{x}_{0c}$, the original location vector of the centroid-line, (ii) $\mathbf{u}_c$, the displacement vector of the centroid-line, and (iii) $\boldsymbol{\theta}$, the rotation vector. It is important to mention that, consistent with the beam kinematics in the space continuous setting introduced in Section 2.2, the cross-section does not deform (although its orientation relative to the centroid-line can change). It must also be noted that the linear interpolation of the rotation vectors employed here renders the finite-element model strain-variant (see [31] for a discussion). This is in

contrast with the strains employed in the space-continuous geometrically exact beam theory (see [77, 78]) that are not affected by rigid translations and rotations.

In the following, we explain how the kinematics introduced in Section 2.2 are interpolated for a single beam element of length $L_{0_{el}}$ in the reference configuration. The reference location of each material point of this beam element is defined by a vector in the local coordinate system attached to the beam centroid-line by $h_1\mathbf{e}_{01} + k_2\mathbf{e}_{02} + k_3\mathbf{e}_{03}$ (where $h^1 \in [0, L_{0_{el}}]$), as well as by a vector in the global coordinate system, $\mathbf{x}_0 = \sum_{i=1}^{3} X_i\mathbf{E}_i$.

The interpolation of the reference location of the beam element's centroid-line can be expressed as follows:

$$\mathbf{x}_{0c}(h^1) = \underline{N}(h^1) \cdot \underline{\mathbf{x}_0}, \tag{2.28}$$

where $\underline{\mathbf{x}_0}$ denotes the column with the reference location vectors of the beam element's nodes and $\underline{N}$ denotes the column with associated basis functions. The displacement field of the beam element's centroid-line can be expressed as follows:

$$\mathbf{u}_c(h^1) = \underline{N}(h^1) \cdot \underline{\mathbf{u}}, \tag{2.29}$$

where $\underline{\mathbf{u}}$ denotes the column with the displacement vectors of the beam element's nodes. Together, the centroid-line in the deformed configuration follows:

$$\mathbf{x}_c(h^1) = \underline{N}(h^1) \cdot \left(\underline{\mathbf{x}_0} + \underline{\mathbf{u}}\right). \tag{2.30}$$

To locate material points that are not placed on the beam element's centroid-line, the orientation of the local basis attached to the cross-sections are needed (see Eq. (2.4) and (2.5)). To this end, interpolation of the field of rotation tensors $\mathbf{\Lambda}$ is required. As $SO(3)$ is a nonlinear manifold, $\mathbf{\Lambda}(h^1)$ cannot be interpolated directly, but is obtained here by applying Rodrigues' formula (see [72]) to the interpolated rotation vector:

$$\boldsymbol{\theta}(h^1) = \underline{N}(h^1) \cdot \underline{\boldsymbol{\theta}} \tag{2.31}$$

as follows:

$$\mathbf{\Lambda}(h^1) = \mathbf{I} + sin\left(\|\boldsymbol{\theta}\|\right)\mathbf{S}(\boldsymbol{\theta}) + \left(1 - cos\left(\|\boldsymbol{\theta}\|\right)\right)\mathbf{S}(\boldsymbol{\theta})\mathbf{S}(\boldsymbol{\theta}), \tag{2.32}$$

where $\mathbf{I}$ denotes the unit tensor, $\|\bullet\|$ denotes the L_2-norm and $\underline{\boldsymbol{\theta}}$ denotes the column with the nodal rotation vectors. $\mathbf{\Lambda}$ denotes the (unique) rotation tensor corresponding to a rotation around the axis $\frac{\boldsymbol{\theta}}{\|\boldsymbol{\theta}\|}$ by an angle of $\|\boldsymbol{\theta}\|$. $\mathbf{S}$ is skew-symmetric and its matrix form can be furthermore expressed as:

$$\underline{\underline{S}}(\boldsymbol{\theta}(h^1)) = \begin{bmatrix} 0 & -\theta_3(h^1) & \theta_2(h^1) \\ \theta_3(h^1) & 0 & -\theta_1(h^1) \\ -\theta_2(h^1) & \theta_1(h^1) & 0 \end{bmatrix}. \tag{2.33}$$

Eq. (2.3) is used to locate points that are not on the beam element's centroid-line employing the interpolations of $\mathbf{x}_c$ and $\mathbf{\Lambda}$ in Eqs. (2.30) and (2.32), respectively.

2.4.2 Smoothing of the surface

For the type of beam element that we use, local base vector $\mathbf{e}_{01}$ always points in the direction of the beam axis in the initial configuration:

$$\mathbf{e}_{01}(h^1) = \frac{\frac{\partial \underline{N}}{\partial h^1} \cdot \underline{\mathbf{x}_0}}{\left\| \frac{\partial \underline{N}}{\partial h^1} \cdot \underline{\mathbf{x}_0} \right\|}. \tag{2.34}$$

Thus, if a string of successive beam elements is not straight in the reference configuration, its centroid-line is C^0-continuous (see Fig. 2.4). The vector fields of local basis vectors $\mathbf{e}_{01}, \mathbf{e}_{02}, \mathbf{e}_{03}$ are then C^{-1}-continuous. This causes a discontinuity in the orientation of the cross-sections at nodes shared by two successive elements, meaning that the surface of the string of beams is discontinuous. Contact is then obviously hard to formulate.

To avoid this issue, we introduce a smooth surface, to which contact constraints are applied. This smooth surface also has the advantage that the C^0- or C^{-1}-continuity of the string's surface is replaced by a C^1-continuous surface, which we

believe improves the convergence properties of the framework (although we do not compare this in the results Section).

In this subsection, the construction of this smooth surface is discussed. It is important to mention that contact is considered for this smooth approximation, instead of the string's actual surface, but that the beam formulation itself remains unchanged. The smoothing approach could thus be applied to other types of beam formulation with some minor changes.

The smoothing procedure uses Bézier curves to smooth the string's centroid-line. One Bézier curve is used to smooth the centroid-line of two successive beam elements. This entails that if a string consist of n beam elements, $n-1$ Bézier curves are used to smooth the string's centroid-line, and by this, the surface. A typical result of this is shown in Fig. 2.4 for a string of three beams. The smoothing procedure is presented for two adjacent beam elements with indices j and $j+1$. This entails that three nodes are involved. The indices of these nodes are i, $i+1$ and $i+2$.

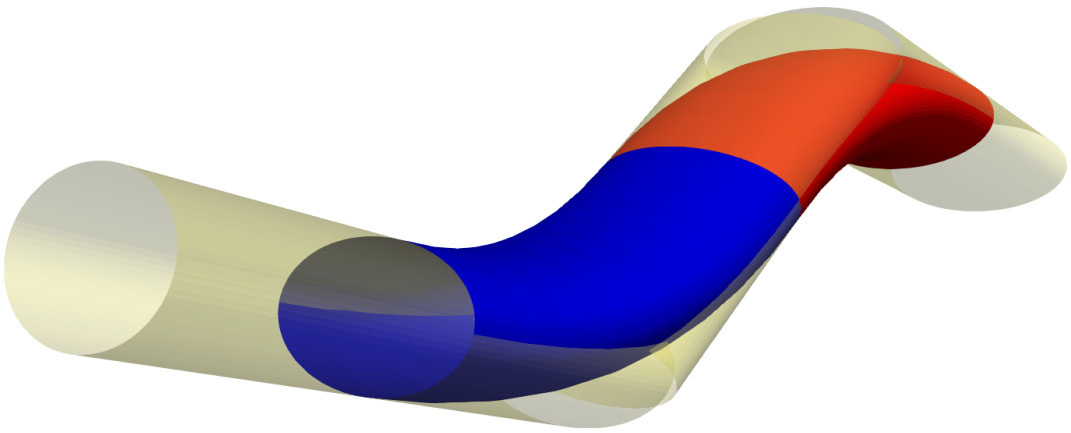

Figure 2.4: The surface of a string of three beam elements and two smoothed surface.

Reference configuration

The smooth centroid-line between two beams in the reference configuration is created using four Bernstein polynomials as follows:

$$\tilde{\mathbf{X}}_c(\eta^1) = \underline{B}(\eta^1) \cdot \underline{\tilde{\mathbf{X}}}_c, \tag{2.35}$$

where $\underline{B}$ denotes the column that includes the four cubical Bernstein polynomials and $\underline{\tilde{\mathbf{X}}}_c$ denotes the column that contains the original location vectors of the four control points (see fig. 2.5):

$$\underline{\tilde{\mathbf{X}}}_c = \left[\tilde{\mathbf{X}}_c^0, \tilde{\mathbf{X}}_c^1, \tilde{\mathbf{X}}_c^2, \tilde{\mathbf{X}}_c^3\right]^T \tag{2.36}$$

with:

$$\tilde{\mathbf{X}}_c^0 = \frac{1}{2}\left(\hat{\mathbf{x}_0}^i + \hat{\mathbf{x}_0}^{i+1}\right) \tag{2.37}$$

$$\tilde{\mathbf{X}}_c^3 = \frac{1}{2}\left(\hat{\mathbf{x}_0}^{i+1} + \hat{\mathbf{x}_0}^{i+2}\right) \tag{2.38}$$

$$\tilde{\mathbf{X}}_c^1 = \tilde{\mathbf{X}}_c^0 + (\hat{\mathbf{x}_0}^{i+2} - \tilde{\mathbf{X}}_c^0)\alpha \tag{2.39}$$

$$\tilde{\mathbf{X}}_c^2 = \tilde{\mathbf{X}}_c^2 + (\tilde{\mathbf{X}}_c^3 - \hat{\mathbf{x}_0}^{i+2})\alpha \tag{2.40}$$

where $\alpha \in [0, 1]$ denotes a parameter to be selected by the user [88] that dictates the location of the second and third control points in Eqs. (2.39) and (2.40). $\eta^1 \in [0, 1]$ parametrises the smoothed centroid-line $\tilde{\mathbf{X}}_c \in \mathbb{R}^3$. $\hat{\mathbf{x}_0}^k$ indicates the location of node k.

The neatest would now be to define the first base vector of the local basis normal to the cross-section in the smoothed reference configuration (i.e. $\tilde{\mathbf{e}}_{01}$) as:

$$\tilde{\mathbf{e}}_{01}(\eta^1) = \frac{\frac{\partial \underline{B}}{\partial \eta^1} \cdot \underline{\tilde{\mathbf{X}}}_c}{\left\| \frac{\partial \underline{B}}{\partial \eta^1} \cdot \underline{\tilde{\mathbf{X}}}_c \right\|}, \tag{2.41}$$

so that cross-sections of the smoothed reference configuration would be orthogonal

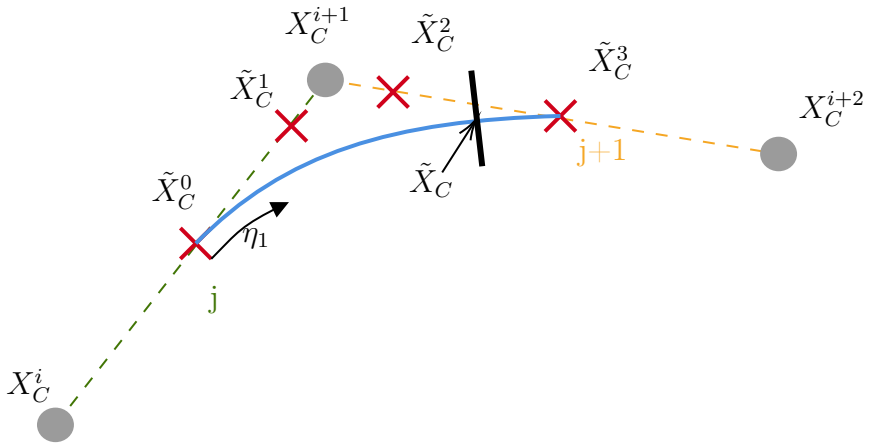

Figure 2.5: Schematic of a smooth centroid-line (plain blue) constructed from the centroid-lines of two beam elements (dashed lines) in the reference configuration. The nodes of the elements are indicated by circle and the control points by crosses. A (fictitious) cross-section attached to $\tilde{\mathbf{X}}_c$ is indicated in black.

to the smoothed centroid-line. This would however also entail that $\tilde{\mathbf{e}}_{02}$ and $\tilde{\mathbf{e}}_{03}$ need to be set by the user, which can be significantly less straightforward for the smooth Bézier curves than setting $\mathbf{e}_{02}$ and $\mathbf{e}_{03}$ for the beam elements. We therefore determine them for the Bézier approximation of the centroid-line as follows:

$$\tilde{\mathbf{e}}_{0i}(\eta^1) = \underline{B}(\eta^1) \cdot \underline{\tilde{\mathbf{e}}}_{0i}, \tag{2.42}$$

where $\underline{\tilde{\mathbf{e}}}_{0i}$, $i \subset \{1, 2, 3\}$ denotes the column that stores $\tilde{\mathbf{e}}_{0i}^k$ at the four control points. For linearly interpolated beam elements $\underline{\tilde{\mathbf{e}}}_{0i}$ contains four times the same base vector for an initially straight strings of beams, and two different base vectors otherwise.

The location vectors of the material points of the string in the smoothed reference configuration are then given by:

$$\tilde{\mathbf{x}_0}(\underline{\eta}) = \tilde{\mathbf{X}}_c(\eta^1) + \tilde{\mathbf{v}_0}(\underline{\eta}), \tag{2.43}$$

where

$$\tilde{\mathbf{v}_0}(\underline{\eta}) = a\cos(\eta^2)\tilde{\mathbf{e}}_{02}(\eta^1) + b\sin(\eta^2)\tilde{\mathbf{e}}_{03}(\eta^1), \tag{2.44}$$

where $\tilde{\mathbf{v}_0}$ denotes a vector connecting $\tilde{\mathbf{X}}_c$ to a point on the perimeter of the (fictitious) cross-section attached to this centroid point (see fig. 2.6), and $\underline{\eta} = \{\eta^1, \eta^2\} \in [0,1] \times [0, 2\pi]$ denotes a column of two local variables parametrising the smooth patch's surface (see Fig. 2.6). a and b denote the dimension of the elliptical cross-section of the underlying series of beams in its principal directions.

Deformed configuration

To determine the smoothed centroid-line in the deformed configuration, we also need the smoothed displacement field of the centroid-line, which is expressed as:

$$\tilde{\mathbf{u}}_c(\eta^1) = \underline{B}(\eta^1) \cdot \underline{\tilde{\mathbf{u}}}_c, \tag{2.45}$$

where $\underline{\tilde{\mathbf{u}}}_c$ denotes the column of displacement vectors at the four control points which are constructed as control points in $\underline{\tilde{\mathbf{X}}}_c$. The smoothed centroid-line in the deformed configuration can then be written as:

$$\tilde{\mathbf{x}}_c(\eta^1) = \tilde{\mathbf{x}_{0c}}(\eta^1) + \tilde{\mathbf{u}}_c(\eta^1) = \underline{B}(\eta^1) \cdot (\underline{\tilde{\mathbf{X}}}_c + \underline{\tilde{\mathbf{u}}}_c). \tag{2.46}$$

To locate all material points in the approximated deformed configuration, instead of just those on the centroid-line, we also need to smooth the rotation vector field, for which we similarly write:

$$\tilde{\boldsymbol{\theta}}_c(\eta^1) = \underline{B}(\eta^1) \cdot \underline{\tilde{\boldsymbol{\theta}}}, \tag{2.47}$$

where $\underline{\tilde{\boldsymbol{\theta}}}$ denotes the column containing rotation vectors at the four control points. Corresponding rotation tensor $\tilde{\boldsymbol{\Lambda}}(\eta^1)$ can then again be determined using Rodrigues' formula (Eq. (2.32)).

The location vectors of the material points of the string in the smoothed deformed configuration can now be written as (see Fig. 2.6):

$$\tilde{\mathbf{x}}(\boldsymbol{\eta}) = \tilde{\mathbf{X}}_c(\eta^1) + \tilde{\mathbf{v}}(\boldsymbol{\eta}), \tag{2.48}$$

where

$$\tilde{\mathbf{v}}(\boldsymbol{\eta}) = \tilde{\boldsymbol{\Lambda}}(\eta^1)\tilde{\mathbf{v}}_0(\underline{\eta}). \tag{2.49}$$

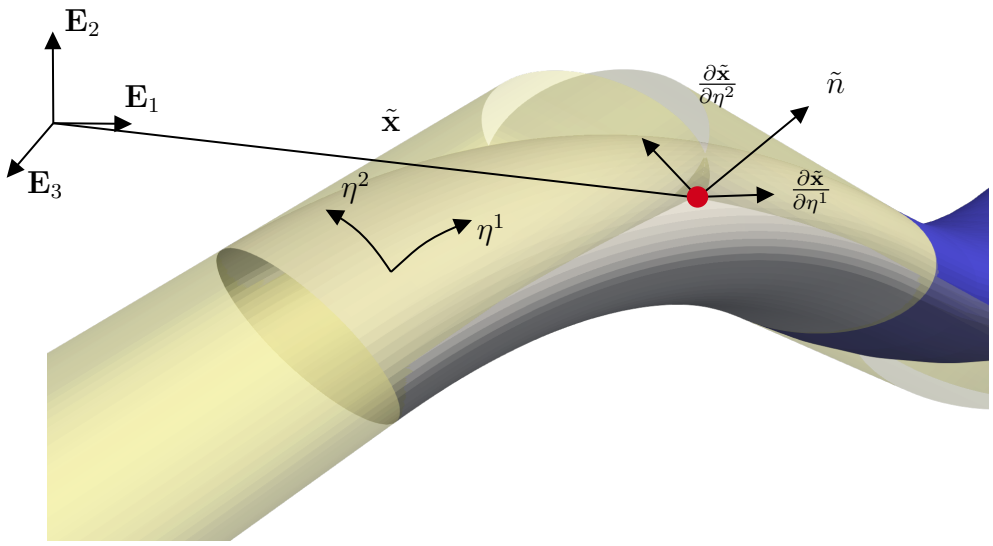

Figure 2.6: A surface point $\tilde{\mathbf{x}}$ and its local surface basis $\{\frac{\partial \tilde{\mathbf{x}}}{\partial \eta^1}, \frac{\partial \tilde{\mathbf{x}}}{\partial \eta^2}, \tilde{\mathbf{n}}\}$. The surface of the two beams from which the smooth surface is constructed are presented in yellow.

Note that vector $\tilde{\mathbf{v}}$ is generally not in the plane normal to $\tilde{\mathbf{X}}_c$, because, as stated above, the (pseudo) cross-sections are in general not normal to the smoothed centroid-line in the reference configuration, but also because of the relative rotation of the (pseudo) cross-section around the (pseudo) centroid point $\tilde{\mathbf{x}}_c$.

To adapt the contact framework to the smoothed geometry introduced above, one needs to replace the local coordinates in $\underline{h}$ by the local coordinates of the smooth surface coordinates $\underline{\eta}$. For an integration point, $\tilde{\mathbf{x}}^{\mathtt{I}}$, on the slave side with local coordinates $\underline{\eta}^1$, the procedure is as follows:

- The projection point of $\tilde{\mathbf{x}}^{\mathtt{I}}$ on the master surface, $\tilde{\mathbf{x}}^{\mathtt{J}}(\bar{\underline{h}}^{\mathtt{J}})$, is found by solving the local problem in Eq. (2.10) adapted to the smoothed surfaces, i.e. the column of local parameters $\bar{\underline{q}}$ to solve for is now $\bar{\underline{q}} = [\bar{\eta}_1^{\mathtt{J}}, \bar{\eta}_2^{\mathtt{J}}, g]$,

- If $\tilde{\mathbf{x}}^{\mathtt{I}}$ is penetrated, the contribution of this integration point to weak form is

computed using Eq. (2.19). The kinematic variables involved are the nodal degrees of freedom used to construct the smooth patches that are stored in columns $\underline{p}^{\mathcal{M}}$ and $\underline{p}^{\mathcal{N}}$. Three beam nodes are necessary to construct each patch so that $\underline{p}^{\mathcal{M}}$ and $\underline{p}^{\mathcal{N}}$ have 18 components each. Consequently, contact residual $\underline{r}_c$ in Eq. (2.25) has a length of 36 and the dimensions of contact tangent matrix $\underline{\underline{K}}_c$ are 36×36.

2.5 Numerical Results

In the current Section, we present initial results that can be achieved with the contact scheme. We first focus on two strings of beam elements that come in contact with each other under different loading conditions. Second, we focus on the twisting of several parallel strings of successive beam elements as a simplified manufacturing process for wire ropes.

Different possibilities exist to place quadrature points. At the beginning of each time step, integration points could be placed in the region where beams' surfaces are close to each other. This would entail several update of the integration points' surface coordinates.

Another option, that is less accurate but computationally less expensive is to compute the coordinates and weights of a grid of integration points on the entire beam surface in the undeformed configuration. This means that the number of quadrature points is constant and that their surface coordinates and weight do not need to be recomputed. This approach that has been adopted in the following numerical examples, in which a grid of quadrature point regularly spaced in the reference domain has been used.

2.5.1 Two orthogonal strings

In the first example, we consider two beams with elliptical cross-sections denoted by A and B (see Fig. 2.7) discretised with strings of successive beam elements. These strings are initially orthogonal in space, and they both have the same geometrical properties (length and dimensions of the cross-sections), mechanical properties and

discretisation (see ahead to the top row of Fig. 2.10). The aim of this numerical example is to show that the presented scheme is able to treat contact problems in which large sliding displacements occur (i.e. slave points in contact can slide from one smooth surface approximation to another without compromising convergence at the global level), whilst the deformation of the contacting surfaces is substantial. The geometrical and material parameters are, together with the numerical parameters of the discretisation and the contact scheme, presented in Tables 2.1 and 2.2. Various Dirichlet boundary conditions (BCs) are applied at the end nodes of string A during the interval of (fictitious) time $t \in [0, 6]$. The kinematic variables of the end nodes of string B are retained. We apply the following Dirichlet BCs to string A (see Fig. 2.8):

- $t = 0$: the strings are slightly detached; $g_N \approx 0$ in the middle of the strings at a single surface point.
- $0 < t \leq 1$: the end nodes are moved by 1.5 10^{-2}m in $\mathbf{E}_2$-direction.
- $1 < t \leq 2$: the end nodes are moved in $[1, 0, 1]$ direction by 1 cm.
- $2 < t \leq 3$: the centroid point in the middle of string A is used as the center of rotation of string A around $\mathbf{E}_2$ with an amplitude of $\frac{\pi}{3}$. This rotation is applied to nodes at the end string A.
- $3 < t \leq 4$: the end nodes undergo the reverse rotation around the same axis of rotation.
- $4 < t \leq 5$: the end nodes undergo the reverse displacement as the one that was performed for $1 < t \leq 2$.
- $5 < t \leq 6$: the end nodes are moved vertically until the two strings completely detach.

The number of quadrature points placed on the surface of each slave patch (at fixed material coordinates) to evaluate Eq. (2.16) is given in Table 2.2. The number of surface points is important because at the beginning of the interval $0 < t \leq 1$ and

at the end of the interval $5 < t \leq 6$, contact is localised and hence, contact is poorly approximated with a coarse grid of surface points.

Table 2.2 also provides the initial penalty stiffness employed. This value should be related to the mechanical parameters of the contacting bodies as well as the geometrical features of the surfaces at the contact area and the penetration [70] (note that a penalty stiffness directly dependent on the kinematic variables would result in more complex expressions for $\underline{r}_c$ and $\underline{\underline{K}}$). Here, the penalty stiffness is adapted if the local penetration measured for one or several of the slave points is larger than a certain user-defined threshold. In the present case, we choose to increase the penalty stiffness by 10% if the penetration is larger than 5% of the smallest cross-sectional radius (see also [21] for another example of regularization of the contact constraint by increasing the penalty stiffness). The update of the penalty stiffness is performed after an increment of the global solver has converged. Directly after the update, the nodal equilibrium is again solved for, since the increase of the penalty stiffness results in a loss of equilibrium. Additional iterations are therefore needed to restore force equilibrium before moving to the next increment. If, after convergence with this new penalty stiffness, the violation of contact constraint g_N is still too large, the process is repeated.

The configurations after each second of the fictitious time are presented in Fig. 2.10. Contact tractions in the contact area are presented in Fig. 2.9 for $t = 1, 2$ and 3 seconds. The evolution of two components of the reaction forces at the end nodes of a string are presented in the top diagrams of Fig. 2.11. The number of active contact points is presented in the same figure. During the 1^{st} second, contact does not change location but increases in magnitude over time. This can be observed by the substantial increase of the number of active slave points during the first half of the 1^{st} second (right diagram in Fig. 2.11). Consequently, the reaction force in $\mathbf{E}_2$-direction (middle diagram in Fig. 2.11) increases qualitatively almost the same as the number of penetrating surface points. During the second half of the first second, the number of penetrating points oscillates. This is due to the adjustment of the penalty stiffness.

During the 2^{nd} second ($1 < t \leq 2$), string A slides with respect to string B. Consequently, the number of penetrating surface points remains similar, which is to

expected. The reaction force in $\mathbf{E}_2$ direction reduces somewhat, whilst the reaction force in $\mathbf{E}_1$ direction slightly increases. Concluding we can state that the contact framework is able to accurately treat large sliding displacements (penetrating slave points can move from one surface approximation to another and new slave points become active, whilst active ones become inactive).

In the 3$^{\text{rd}}$ second ($2 < t \leq 3$), the location of the contact area remains largely at the same location, but the contact area increases due to the prescribed rotation. We nevertheless see a decrease of the number of active slave points, because the employed grid of slave points has a wider spacing in the string's longitudinal direction than in the tangential direction. The change of contact area has substantial influences on the reaction forces. The interesting issue here is that the present loading would have no influence on the reaction forces for a point-wise contact scheme (which would be inaccurate as contact does not occur at a single point but over a finite area).

In the last 3 seconds, the entire loading is reversed and consequently, we see that the reaction-force time diagrams are symmetrical around $t = 3$. Once again, the reason that the number of active slave points is not symmetrical is because the penalty stiffness is increased if necessary, but not reduced if possible. These results are highly satisfactory.

Beam length (cm)	8
Radius 1 of the elliptical cross-section(cm)	0.6
Radius 2 of the elliptical cross-section (cm)	0.2
Young's modulus (GPa)	100
Poisson's ratio	0.3
Beams Finite Elements per beam	60

Table 2.1: Example 2.5.1: General properties of each beam.

Surface points in axial direction	5
Surface points in tangential direction	80
α	$\frac{2}{3}$
Initial ϵ_N (GPa)	10

Table 2.2: Example 2.5.1: Contact parameters.

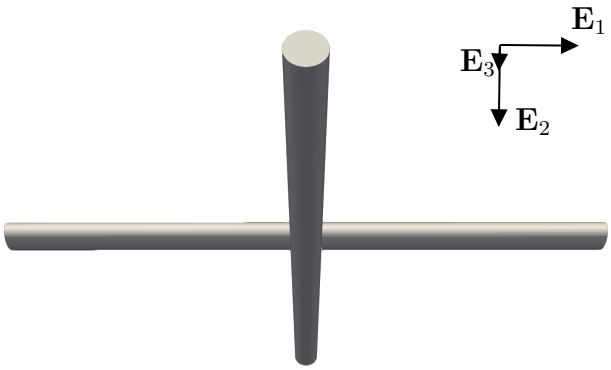

Figure 2.7: Example 2.5.1: Initial configuration.

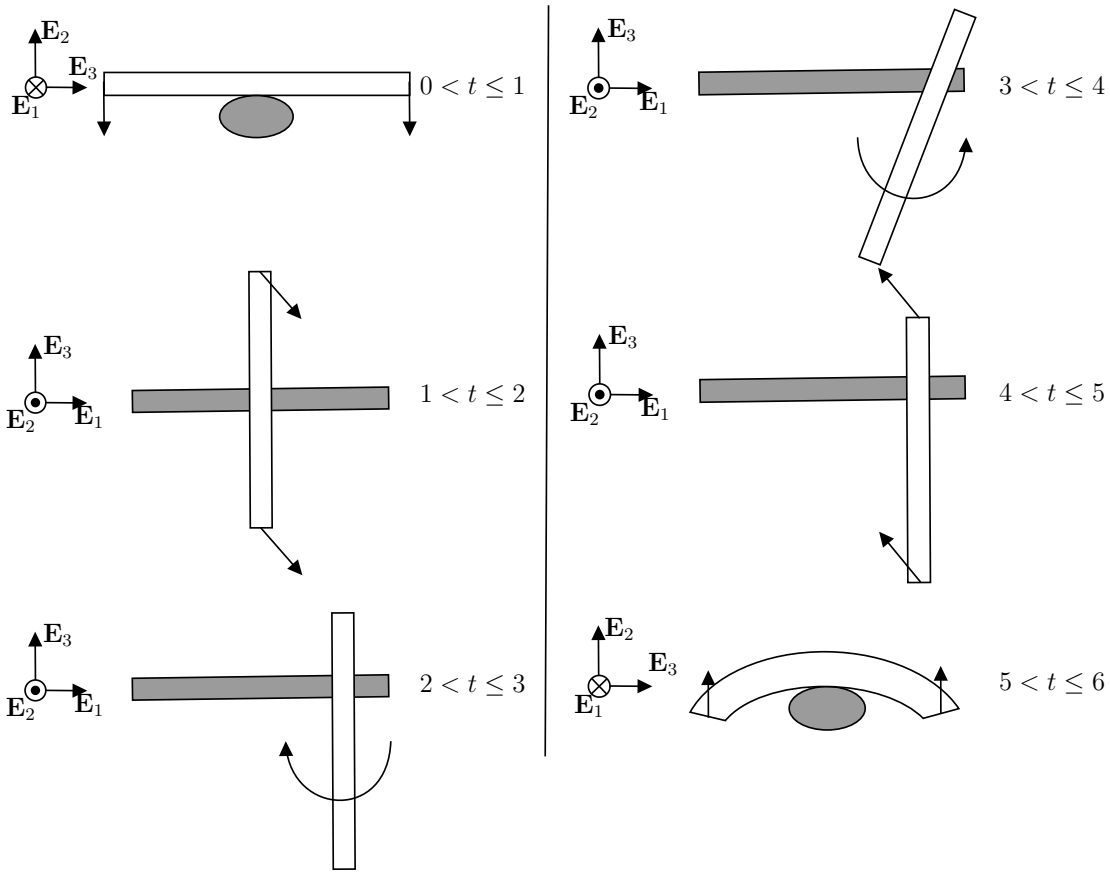

Figure 2.8: Example 2.5.1: Boundary conditions applied during the different phases of the loading. The schematics are not to scale. String A is presented in white and string B in grey.

$t\,(s)$	
1	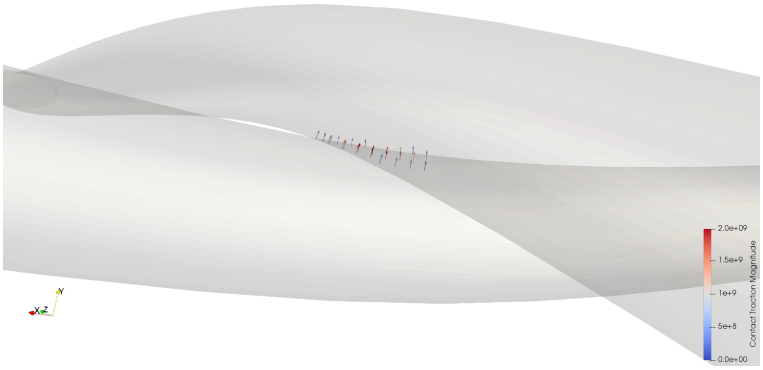
2	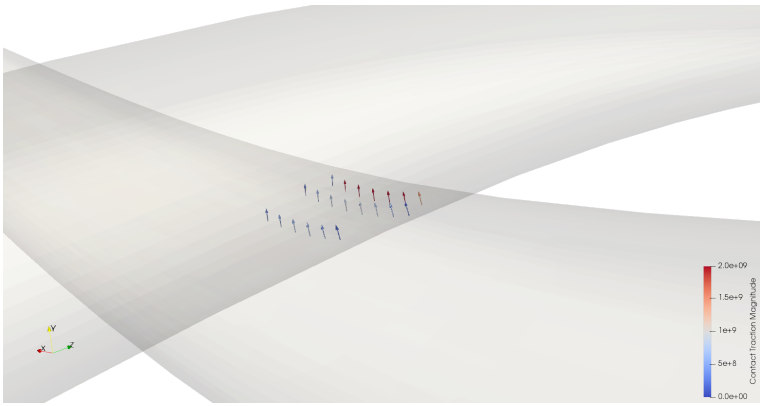
3	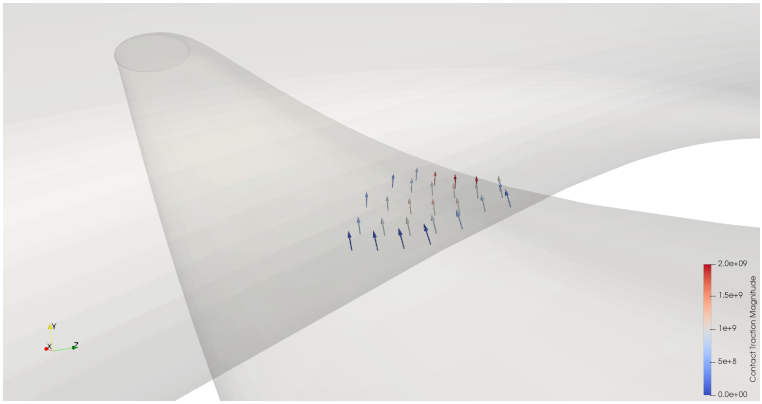

Figure 2.9: Example 2.5.1: Contact traction acting in the normal direction to the slave surface at the quadrature points for different times of the simulation.

$t(s)$	Top view	Side view	Perspective
0	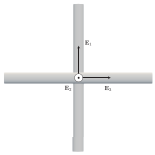	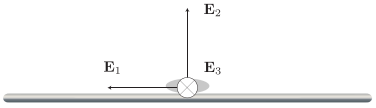	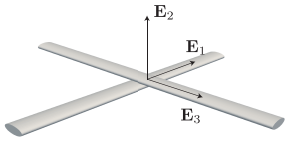
1	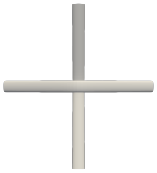		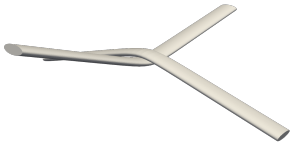
2	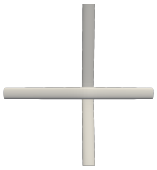		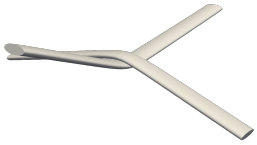
3	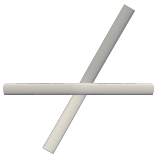		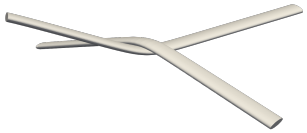
4	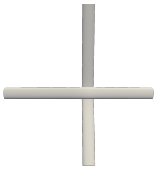		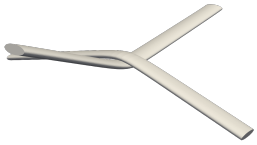
5	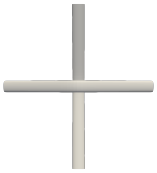		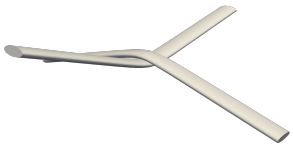

Figure 2.10: Example 2.5.1: Three views of the deformed beams after different pseudo-times (without scaling of the deformations).

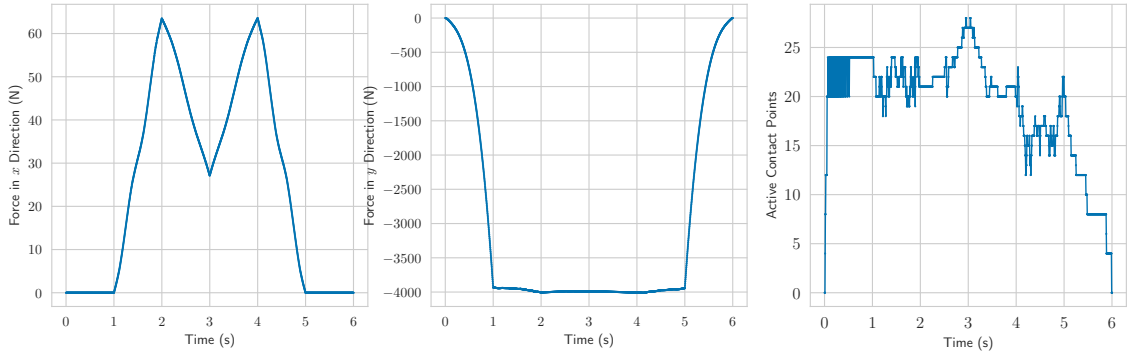

Figure 2.11: Example 2.5.1: Evolution of the reaction force in $\mathbf{E}_2$ direction (left) and in $\mathbf{E}_1$ direction (middle). Evolution of the number of active contact points (right). Note that the order of magnitude of the forces in the left and central diagram is a factor of two different.

2.5.2 Twisting

In the next example, we consider two setups of several parallel beams which are twisted (see Fig. 2.13). For setup A, the central beam has a circular cross-section and the beams around it have an elliptical cross-section. In setup B however, the central beam is elliptical and the peripheral beams have a circular cross-section. For both setups, the central beams have the same cross-sectional area. Similarly, each peripheral beam in setup A has the same cross-sectional area as the peripheral beams in setup B.

The cross-sections at the two ends of the beams are rigidly rotated around the longitudinal beams' direction in the reference configuration with an angle of π. The planes containing these cross-sections are kept at a constant distance during the simulation. This problem is challenging for a contact framework as the contact forces increase substantially, the contact is non-local and contacting surfaces increasingly deform and curve during time.

The employed beam properties are presented in Table 2.3. The initial and final configurations are shown in Fig. 2.13. Fig. 2.14 shows the evolution of the total reaction force in longitudinal direction and the total torque at one of the end cross-sections. The evolution of the number of penetrated contact points is also presented.

The results clearly show that the cross-sectional shape has a major influence on the simulation results.

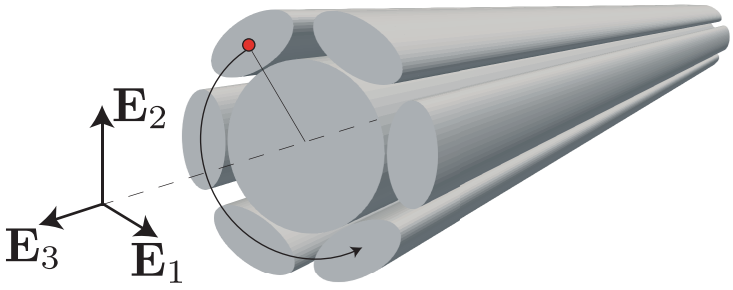

Figure 2.12: Example 2.5.2: Illustration of the Dirichlet boundary condition applied to one end of one discretized beam (red circle). The rotation of Π around the axis of rotation (dashed line) applied incrementally is illustrated with the black arrow.

	Central Beam	Peripheral Beams
Beam length (cm)	15	15
Radius 1 of the elliptical cross-section (cm)	0.5	$\frac{3}{10}$
Radius 2 of the elliptical cross-section (cm)	0.5	$\frac{3}{20}$
Young's modulus (GPa)	100	100
Poisson's ratio	0.3	0.3
Beam finite elements per beam	60	60

(a) Setup A.

	Central Beam	Peripheral Beams
Beam length (cm)	15	15
Radius 1 of the elliptical cross-section (cm)	$\frac{2}{3}$	$\frac{1}{3\sqrt{200}}$
Radius 2 of the elliptical cross-section (cm)	$\frac{3}{8}$	$\frac{1}{3\sqrt{200}}$
Young's modulus (MPa)	1000	1000
Poisson's ratio	0.3	0.3
Beam finite elements per beam	60	60

(b) Setup B.

Surface points in axial direction	4
Surface points in tangential direction	80
α	$\frac{2}{3}$
Initial ϵ_N (MPa)	100

(c) Contact properties of each slave patch.

Table 2.3: Example 2.5.2: Properties of the beams used for the twisting.

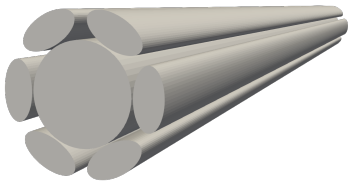

(a) setup A, $t = 0$.

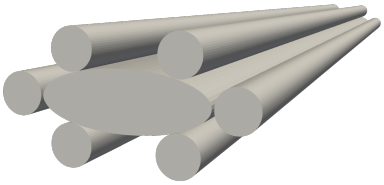

(b) setup B, $t = 0$.

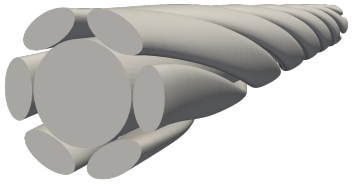

(c) setup A, $t = t_{final}$.

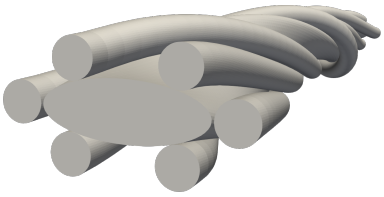

(d) setup B, $t = t_{final}$.

(e) setup A, $t = t_{final}$, side view.

(f) setup B, $t = t_{final}$, side view.

Figure 2.13: Example 2.5.2: Setup A and B in their initial and final configuration.

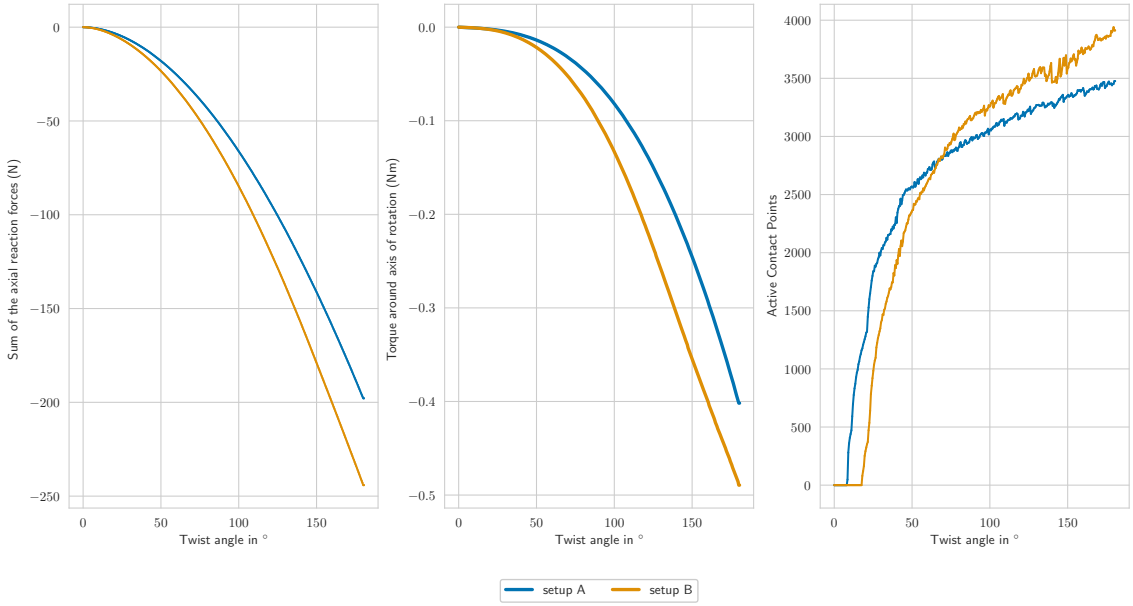

Figure 2.14: Example 2.5.2; Left: Axial reaction forces; Middle: The reaction torque around the axis of rotation; Right: evolution of the number of active contact points.

2.6 Conclusion

Slender structural components are typically represented by beams in mechanical models, in turn discretized with beam finite elements. They are often characterized by circular cross-sections, but elliptical cross-sections are regularly required instead. Contact between shear-deformable beams with elliptical cross-sections cannot only be based on the centroid-lines, as is most often done in contact schemes for beams with circular cross-sections.

The contact framework proposed in this work therefore relies on the beams' surface. It allows to deal with scenarios in which the distance between contacting surfaces has no clear minimum, as is the case for parallel beams, for example. Thus, this contribution is a first attempt to complete the frameworks of [24, 25], which are limited by the assumption of a unique and localised contact location.

Our framework places points on one of the two surfaces candidates for contact

(slave) and then projects them on the other surface (the master). This projection differs from the conventional closest point projection (CPP), because the CPP is not unique and may change drastically for small variations (in case of non-circular cross-sections). Instead, we determine the amount of penetration based on surface points and a point on the centroid-line.

Since the employed geometrically exact beam elements furthermore use a linear interpolation of the kinematic variables, the associated surface of a string may be C^0-continuous in the deformed configuration and even C^{-1}-continuous in the reference and deformed configuration. To overcome this issue, a smoothing procedure of the strings' surfaces is formulated that makes the surfaces C^1-continuous.

The proposed contact approach is computationally more demanding than the approaches of [24, 25] due to the seeding of many points for which penetration is considered. If no unique maximum penetration occurs, as is the case for many practical applications on the other hand, a less efficient approach than [24, 25] appears to be unavoidable. Future work will therefore focus on more efficient generations of surface points and the optimisation of the implementation.

CHAPTER III

Non-localised contact between beams with circular and elliptical cross-sections[1]

3.1 Introduction

Many engineering materials such as paper, fabrics or open-cell high-porosity foams consist of slender fiber-like constituents at the microscopic scale [67, 28]. Various approaches to describe their mechanical behavior explicitly incorporate their discrete micro-structure [5, 55, 82, 46, 33]. In many cases beam models are used to represent single fibers, yarns or struts [44, 4, 6]. It is often crucial to incorporate beam-to-beam contact in order to obtain accurate mechanical predictions. However, due to the specificity of beam kinematics, standard techniques developed to treat contact between 3D solids cannot be directly adopted. Thus special formulations dedicated to beams are developed [62, 89, 95, 37, 51, 50, 59, 22, 21].

Beam-to-beam contact schemes are in general built upon assumptions on the contacting systems, which restrict their use to specific contact scenarios. The formulation of a particular contact scheme is typically determined by three main issues: (i) whether or not contact remains localized (in other words if contact interactions are confined to a small part of the beams' surfaces), (ii) what are the beams' cross-

[1]Reproduced from: M. Magliulo, J. Lengiewicz, A. Zilian, Beex L. A. A., Non-localised contact between beams with circular and elliptical cross-sections, Computational Mechanics, accepted for publication.

sectional shapes and (iii) are the cross-sections rigid or deformable. This contribution is limited to rigid cross-sections.

A point-wise contact force approach is generally used to model localized contact between beams. For beams with circular sections for example, the contact conditions are enforced at the closest pair of centroid points [89, 95, 62]. If the beam's cross-sections are elliptical, the contact force can be applied at the closest pair of surface points where the tangent planes of the contacting surfaces are parallel. This was demonstrated by Gay Neto et al. [24, 25] for the frictionless and frictional case, respectively.

If no unique minimum distance between the beams' surfaces exists (*e.g.* in case of parallel beams or if one beam is wrapped around the other), the aforementioned frameworks are difficult to apply. In such cases, and if both beams in contact have circular sections, Chamekh et al. [11] (for beams undergoing self-contact) and Meier et al. [59] have demonstrated that contact can be modeled as a continuous force acting along one of the beams' centroid-lines. If elliptical sections are employed however, the contact scheme of [59] is not directly applicable as the centroid-lines are not sufficient to locate possible contact interactions. This is because the beams' surface cannot be determined from its centroid-line in this case

An alternative is then to integrate contact forces (contact virtual work) over the surface [54]. In such an approach, fixed material points on one of the beams' surface are projected on the other beam's surface to then determine if they are penetrated. As each projection requires the solution of a (small) non-linear problem, and because many projections are required to accurately approximate the contact area, the associated computational costs are substantial.

In the approach proposed in the current contribution, the contact virtual work is integrated along the centroid-line of one of the beams (slave). The contact kinematics are based on an appropriately defined projection procedure between the contacting surfaces, which assumes that the cross-sections are planar and rigid. In this procedure, for a pair of contacting beams, points are fixed along the centroid-line of one of the body called the slave. For each point, the projection problem solves for the circumferential parameter of the cross-section attached to the fixed slave centroid-point

and both surface parameters of the counter-surface (master).

Two different projection schemes are presented and compared. The first one is based on the minimisation of a constrained scalar function and the second one is posed as a set of equations to solve. The latter approach is expected to be more efficient and stable because surface derivatives of lower degrees are involved, which is appealing when interpolated surfaces have a reduced continuity. As the integration is performed along a curve and not over a surface (as in [54]), the computational costs are substantially reduced. Consequently, larger models can be investigated with similar computational efforts, thereby easing the framework's application to industrially and scientifically relevant problems.

In the present contact framework we adapt and study two approaches to integrate the contact virtual work. As a first choice, we use a conventional single-pass algorithm, a master-slave approach, in which we arbitrarily choose one of the beams' surface (slave beam) to integrate contact virtual work. Consequently, the associated contact framework is biased [73, 74].

To avoid this issue, we adapt the idea presented in [73, 74], the so-called "two-half-pass" approach, which symmetrically treats both contacting surfaces, and which has so far only been considered for conventional finite elements and not for beam-to-beam contact. Consequently, this framework is unbiased. In this approach, similarly to the well known two-pass approach, contact conditions are evaluated twice by changing the roles of the contacting surfaces (the slave body during the first half-pass becomes master during the second half-pass and inversely for the master body). The difference between two-half-pass and two-pass algorithms is that for the two-half-pass, contact tractions are only acting on the slave surface for each half-pass.

This paper is organized as follows. In Section 3.2, the kinematics of the proposed contact framework are presented. This includes a discussion on how to determine whether a section penetrates another beam and if so, how to quantify the amount of penetration. Also, a length-specific contact virtual work is introduced, which is integrated over the slave beam's centroid-line. We specify this for single-pass and two-half-pass algorithms. In Section 3.3, the contact kinematics are adapted to the finite element method after the beams are discretized with BFEs. Implementation

details are included. The numerical examples of Section 3.4 indicate the capabilities and efficiency of the contact framework. Finally in Section 3.5, conclusions are presented and possible extensions are discussed.

3.2 Continuum contact framework

This section explains the proposed framework to treat contact between beams with elliptical and circular rigid sections. Simo-Reissner Geometrically Exact Beam theory [77, 78, 79, 29, 31, 59, 72] is utilized here, but the contact framework can be adapted to other beam formulations with rigid cross-sections. We first explain how surfaces of such beams can be parametrised. Based on these beams' surface parametrizations, we then introduce the contact kinematics for the novel contact scheme in the space-continuous setting. This framework will be adapted to the finite element method in Section 3.3.

3.2.1 Surface description of a geometrically exact beam

In this work, a continuous beam (not a beam finite element) is considered as a (slender) body, of which the cross-sections (i) do not deform, (ii) remain planar, (iii) their center of gravity form its centroid line and (iv) their normal vector can rotate with respect to the tangent of its centroid-line (shear deformable).

We consider beam $\mathcal{B}$ and the parametrization of its surface $\mathbf{x}(\underline{h}) \in \mathbb{R}^3, \underline{h} = [h^1, h^2] \in [0, L] \times [0, 2\pi] \in \mathbb{R}^2$, where h^1 and h^2 are longitudinal and circumferential parameters, respectively. L denotes the length of the centroid-line of $\mathcal{B}$ in the undeformed configuration. The current centroid-line position is obtained by adding displacement $\mathbf{u} \in \mathbb{R}^3$ to the initial centroid-line location, $\mathbf{x}_{0c} \in \mathbb{R}^3$:

$$\mathbf{x}_c = \mathbf{x}_{0c} + \mathbf{u}. \tag{3.1}$$

As cross-sections are rigid and remain planar, $\mathbf{x}(\underline{h})$ can be obtained by adding the location vector of a centroid-point, $\mathbf{x}_c(h^1) \in \mathbb{R}^3$, to a vector, $\mathbf{v}(\underline{h}) \in \mathbb{R}^3$, that lies

in the plane of cross-section $\mathcal{C}$ that is attached to $\mathbf{x}_c$ (see Fig. 3.1):

$$\mathbf{x}(\underline{h}) = \mathbf{x}_c(h^1) + \mathbf{v}(\underline{h}). \tag{3.2}$$

For elliptical sections, $\mathbf{v}$ can be expressed as follows:

$$\mathbf{v}(\underline{h}) = a\,\cos(h^2)\,\mathbf{e}_1(h^1) + b\,\sin(h^2)\,\mathbf{e}_2(h^1), \tag{3.3}$$

where a and b denote the two semi-axes of the elliptical section in the ellipse's principal directions. Note that in case $a = b$, a circular cross-section is recovered.
Triad $\{\mathbf{e}_1, \mathbf{e}_2, \mathbf{e}_3\}$ attached to $\mathcal{C}$ forms an orthonormal basis. This local triad in the undeformed configuration denoted by $\{\mathbf{e}_{01}, \mathbf{e}_{02}, \mathbf{e}_{03}\}$ varies as a function of h^1 if the undeformed centroid-line is not straight. The plane containing $\mathcal{C}$ is spanned by vectors $\{\mathbf{e}_1, \mathbf{e}_2\}$ while $\mathbf{e}_3$ denotes its normal (unit) vector. As shear deformation is possible, $\mathcal{C}$ is not necessarily normal to the beam's centroid line, *i.e.* $\frac{\partial \mathbf{x}_c}{\partial h^1} \times \mathbf{e}_3 \neq \mathbf{0}$.

As no cross-sectional deformation occurs furthermore, vector $\mathbf{e}_i$ can be obtained by a rigid rotation of its associated vector in the undeformed configuration, $\mathbf{e}_{0i}$, according to:

$$\mathbf{e}_i = \mathbf{\Lambda}(h^1)\mathbf{e}_{0i}. \tag{3.4}$$

$\mathbf{\Lambda}(h^1) \in SO(3)$ denotes a rotation tensor, where $SO(3)$ is the group of orthogonal transformations [72].

For further use, we define two vectors tangent to the surface at $\mathbf{x}(\underline{h})$ as $\boldsymbol{\tau}_1 = \frac{\partial \mathbf{x}}{\partial h^1}$ and $\boldsymbol{\tau}_2 = \frac{\partial \mathbf{x}}{\partial h^2}$. In general, $\boldsymbol{\tau}_1$ and $\boldsymbol{\tau}_2$ are not necessarily orthogonal to each other. The unit vector normal to the surface at the same surface point is defined as follows:

$$\mathbf{n}(\underline{h}) = \frac{\boldsymbol{\tau}_1(\underline{h}) \times \boldsymbol{\tau}_2(\underline{h})}{\|\boldsymbol{\tau}_1(\underline{h}) \times \boldsymbol{\tau}_2(\underline{h})\|}. \tag{3.5}$$

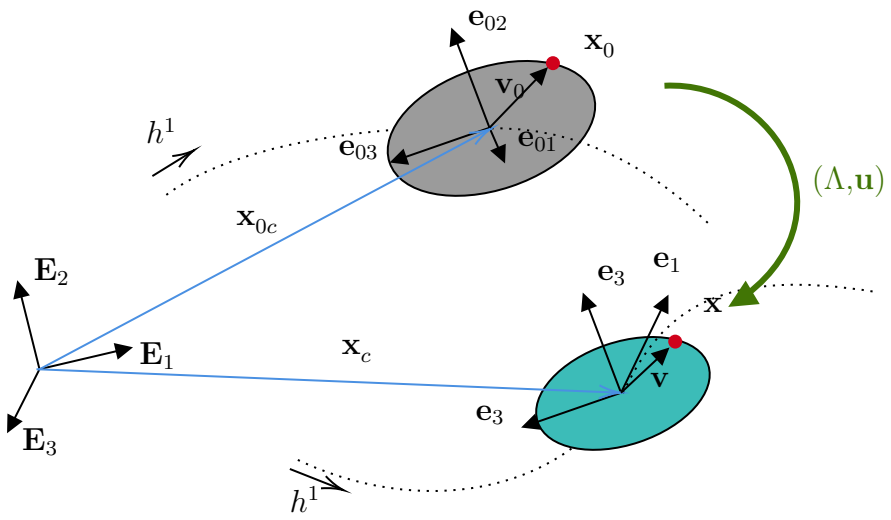

Figure 3.1: An elliptical cross-section in its undeformed (grey) and current configuration (cyan). centroid-lines in both configurations are presented as dashed lines.

3.2.2 The contact scheme

For shear undeformable beams with circular sections, simplified contact kinematics can be found [89, 95, 59]. Simplifications are also possible if only one of the two beams in contact has a circular cross-section [37]. However, if both beams possess non-circular cross-sections and shear deformation is accounted for, a different approach is needed as the surfaces of the beams cannot be deduced from their centroid-line alone.

The contact scheme presented here seeks to treat contact interactions between beams if the signed distance function between the beams' surfaces does not possess a unique minimum (*e.g.* if the beams are parallel to each other or wrapped around each other). This is in contrast to the schemes of [24, 25] in which penetration is prevented by forces between the closest pair of surface points.

3.2.2.1 Projection problem and signed distance function

Let us consider beams $\mathcal{B}^{\mathrm{I}}$ and $\mathcal{B}^{\mathrm{J}}$, and their respective surfaces $\partial\mathcal{B}^{\mathrm{I}}$ and $\partial\mathcal{B}^{\mathrm{J}}$ which may be colliding. In our scheme, for a given cross-section along the centroid-

line of $\mathcal{B}^{\mathrm{I}}$, we determine if it penetrates $\partial\mathcal{B}^{\mathrm{J}}$ and if so, by what amount. $\mathcal{B}^{\mathrm{I}}$ and $\mathcal{B}^{\mathrm{J}}$ thus have a different role and in order to distinguish them, we call $\mathcal{B}^{\mathrm{I}}$ the slave and $\mathcal{B}^{\mathrm{J}}$ the master.

Let's consider cross-section $\mathcal{C}$ and its perimeter $\partial\mathcal{C}$. $\mathcal{C}$ is attached to centroid-point $\mathbf{x}_c^1(h^{\mathcal{C}})$ (see Fig. 3.2). The outward pointing normal (unit vector) at surface point $\mathbf{x}^{\mathrm{I}}(\underline{h}^{\mathrm{I}}) \in \partial\mathcal{C}$ with $\underline{h}^{\mathrm{I}} = \left[h^{\mathcal{C}}, h^{\mathrm{I}2}\right]^T$ is expressed as:

$$\mathbf{n}^{\mathrm{I}}(\underline{h}^{\mathrm{I}}) = \frac{\boldsymbol{\tau}_1^{\mathrm{I}}(\underline{h}^{\mathrm{I}}) \times \boldsymbol{\tau}_2^{\mathrm{I}}(\underline{h}^{\mathrm{I}})}{\left\|\boldsymbol{\tau}_1^{\mathrm{I}}(\underline{h}^{\mathrm{I}}) \times \boldsymbol{\tau}_2^{\mathrm{I}}(\underline{h}^{\mathrm{I}})\right\|}. \tag{3.6}$$

We introduce the following gap vector:

$$\mathbf{g} = \mathbf{x}^{\mathrm{J}} - \mathbf{x}^{\mathrm{I}}, \tag{3.7}$$

pointing from a surface point on $\partial\mathcal{C}$ to a surface point on $\partial\mathcal{B}^{\mathrm{J}}$.

In the following, we present two possibilities to quantify the amount of penetration between $\partial\mathcal{C}$ and $\partial\mathcal{B}^{\mathrm{J}}$. The first approach is based on a constraint minimisation of a scalar function, whereas the second one relies on a set of equations to be solved. Higher order surface derivatives are expected for the first approach which are not necessarily well defined on the surface of a body after discretization with beam finite elements. The first approach also yields complicated expressions that translate into more (and hence less efficient) code.

Approach I: pair of surface points determined from the minimisation of an objective function

One approach to determine if $\partial\mathcal{C}$ penetrates $\partial\mathcal{B}^{\mathrm{J}}$ and if so, by what amount, is to determine the minimum of scalar function $\mathbf{g} \cdot \mathbf{n}^{\mathrm{I}}$. In order to prevent that objective function $\mathbf{g} \cdot \mathbf{n}^{\mathrm{I}}$ has an infinite number minima, we only consider points $\mathbf{x}^{\mathrm{I}} \in \mathcal{C}$ and $\mathbf{x}^{\mathrm{J}} \in \partial\mathcal{B}^{\mathrm{J}}$ that meet constraint c:

$$[\bar{h}^{\mathrm{I}2}, \bar{h}^{\mathrm{J}1}, \bar{h}^{\mathrm{J}2}] = \min_{h^{\mathrm{I}2}, h^{\mathrm{J}1}, h^{\mathrm{J}2}} \quad \mathbf{g} \cdot \mathbf{n}^{\mathrm{I}} \tag{3.8}$$

such that

$$c = \mathbf{g} \cdot \tilde{\mathbf{n}}^{\mathrm{I}} = 0, \tag{3.9}$$

$$\mathbf{x}^{\mathrm{I}}(\bar{\underline{h}}^{\mathrm{I}}) \text{ is in } \mathcal{B}^{\mathrm{J}} \text{ if } \bar{\mathbf{g}} \cdot \bar{\mathbf{n}}^{1} < 0, \tag{3.10}$$

$$\mathbf{x}^{\mathrm{J}}(\bar{\underline{h}}^{\mathrm{J}}) \text{ is in } \mathcal{B}^{\mathrm{I}} \text{ if } \bar{\mathbf{g}} \cdot \bar{\mathbf{n}}^{\mathrm{I}} < 0. \tag{3.11}$$

Here and in the following, a bar over a quantity indicates that it is evaluated at the solution of the local problem (*i.e.*solution of Eq. (3.13) or Eq. (3.21)). Unit vector $\tilde{\mathbf{n}}^{\mathrm{I}}$ in Eq. (3.9) is defined as:

$$\tilde{\mathbf{n}}^{\mathrm{I}}(h^{\mathcal{C}}, h^{\mathrm{I}2}) = \frac{\boldsymbol{\tau}_2^{\mathrm{I}} \times \mathbf{n}^{\mathrm{I}}}{\|\boldsymbol{\tau}_2^{\mathrm{I}} \times \mathbf{n}^{\mathrm{I}}\|} \tag{3.12}$$

and denotes the unit vector normal to the plane spanned by surface vectors $\mathbf{n}^{\mathrm{I}}$ and $\boldsymbol{\tau}_2^{\mathrm{I}}$ (see Fig. 3.2).

At the solution of Eq. (3.8), the gap vector is colinear with $\mathbf{n}^{\mathrm{I}}$ but not with $\mathbf{n}^{\mathrm{J}}$, which differs from conventional master-slave approaches like the node-to-surface algorithm [47]. In this way, the first and second-order derivatives of Eq. (3.8) are shorter. The reason is that $\mathbf{n}^{\mathrm{J}}$ depends on two variables, $h^{\mathrm{J}1}$ and $h^{\mathrm{J}2}$, whereas $\mathbf{n}^{\mathrm{I}}$ only depends on $h^{\mathrm{I}2}$. Note also that if $\mathbf{g}$ is not aligned with $\mathbf{n}^{\mathrm{I}}$ at the solution of Eq. (3.8), the measure of penetration (see Eq. (3.15)) is not measured in the direction of the normal to $\partial\mathcal{B}^{\mathrm{I}}$. This yields non-physical components of the contact traction vector when contact constraints are regularized (see Section 3.2.2.2).

If only the constraint in Eq. (3.9) is present, four solutions are possible. This is graphically illustrated in Fig. 3.3. To prevent this, the last two constraints are added, but they can only be verified once the minimisation problem of Eq. (3.8) is solved.

We solve the minimisation problem using the interior extremum theorem, in which only the first constraint in Eq. (3.9) is incorporated via a Lagrange multiplier:

$$\underline{f}(\bar{\underline{q}}) = \frac{\partial}{\partial \underline{q}} \left(\mathbf{g} \cdot \mathbf{n}^{\mathrm{I}} - \lambda c \right) \Big|_{\underline{q}=\bar{\underline{q}}} = \underline{0}, \tag{3.13}$$

where $\underline{q} = [h^{\mathrm{I}2}, h^{\mathrm{J}1}, h^{\mathrm{J}2}, \lambda]$ denotes the variables that we solve for, which consist of

three surface parameters and Lagrange multiplier $\lambda \in \mathbb{R}$.

To solve Eq. (3.13), we apply Newton's method for which we linearise residual $\underline{f}$ in Eq. (3.13) which requires the following Jacobian:

$$\underline{\underline{H}}(\underline{q}) = \frac{\partial \underline{f}}{\partial \underline{q}}. \tag{3.14}$$

Once the solution of Eq. (3.13) is found, the amount of penetration, which is also called the normal gap or signed distance function, is given by:

$$g_N = (\bar{\mathbf{x}}^{\mathrm{J}} - \bar{\mathbf{x}}^{\mathrm{I}}) \cdot \bar{\mathbf{n}}^{\mathrm{I}} = \bar{\mathbf{g}} \cdot \bar{\mathbf{n}}^{\mathrm{I}}, \tag{3.15}$$

where $\bar{\mathbf{x}}^{\mathrm{I}} = \mathbf{x}^{\mathrm{I}}(h^{\mathcal{C}}, \bar{h}^{\mathrm{I}2})$ and $\bar{\mathbf{x}}^{\mathrm{J}} = \mathbf{x}^{\mathrm{J}}(\bar{h}^{\mathrm{J}1}, \bar{h}^{\mathrm{J}2})$. Eq. (3.15) entails that g_N is only negative in case of penetration, as long as the constraints in Eqs. (3.10) and (3.11) are met.

The problem with Jacobian $\underline{\underline{H}}$ in Eq. (3.14) is the presence of third-order surface derivatives, since $\mathbf{n}^{\mathrm{I}}$ and $\tilde{\mathbf{n}}^{\mathrm{I}}$ are based on first-order surface derivatives. This comes with two disadvantages:

- Third-order surface derivatives are not necessarily smooth across the beams' surface, in particular in the spatially discretized setting (see Section 3.3). This may impair the convergence of the aforementioned Newton's procedure, which for instance yields solutions for which the constraints of (3.10) and (3.11) do not hold (see also Fig. 3.3).

- $\underline{f}$ and $\underline{\underline{H}}$ are inefficient to compute due to their complicated expressions.

Quantifying the amount of penetration in terms of a residual form (i.e. a system of non-linear equations that replaces Eq. (3.13)) in which lower-order surface derivatives are present, may therefore be computationally advantageous.

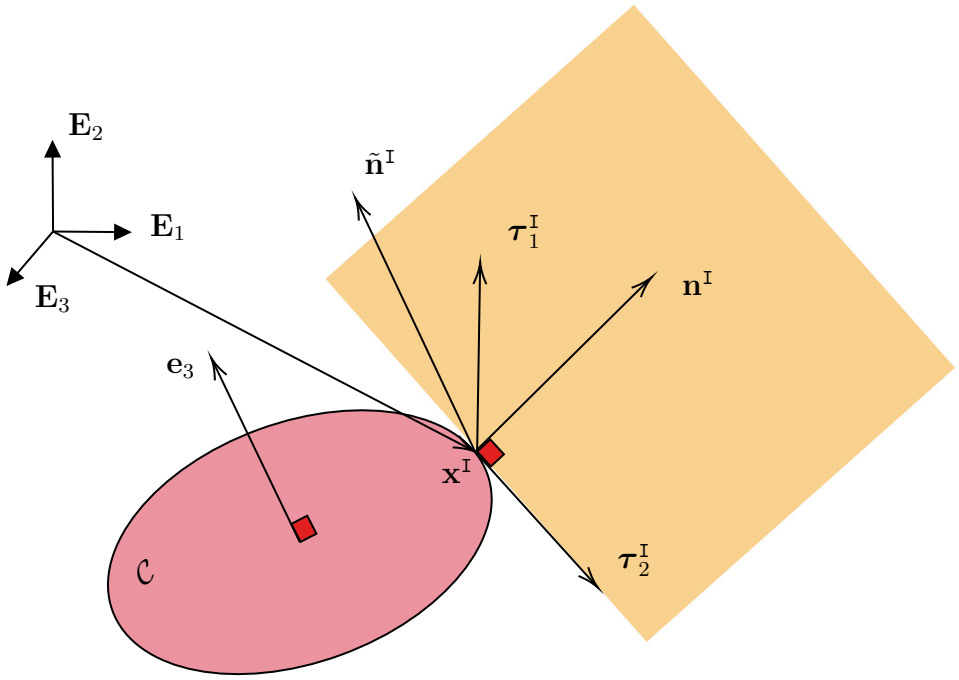

Figure 3.2: Slave section $\mathcal{C}$ (in light red). The plane containing $\mathbf{x}^{\mathrm{I}}$ and spanned by vectors $\boldsymbol{\tau}_2^{\mathrm{I}}(h^{\mathcal{C}})$ and $\mathbf{n}^{\mathrm{I}}(h^{\mathcal{C}})$ is presented in translucent orange. The unit normal vector to this plane is $\tilde{\mathbf{n}}^{\mathrm{I}}$.

Approach II: Pair of surface points determined from a residual form

As an alternative to Eq. (3.13), one can formulate a problem in which no minimization is to be performed explicitly, but where we start from some residual form. The vector equations we solve for are:

$$\mathbf{f}_1(\underline{\bar{q}}) = \bar{\mathbf{x}}^{\mathrm{J}} - \bar{\mathbf{x}}^{\mathrm{I}} - \bar{g}\bar{\mathbf{n}}^{\mathrm{I}} = \mathbf{0}, \tag{3.16}$$

such that:

$$\bar{\mathbf{x}}^{\mathrm{I}}(\underline{\bar{h}}^{\mathrm{I}}) \text{ is in } \mathcal{B}^{\mathrm{J}} \text{ if } \bar{g} < 0, \tag{3.17}$$

$$\bar{\mathbf{x}}^{\mathrm{J}}(\underline{\bar{h}}^{\mathrm{J}}) \text{ is in } \mathcal{B}^{\mathrm{I}} \text{ if } \bar{g} < 0. \tag{3.18}$$

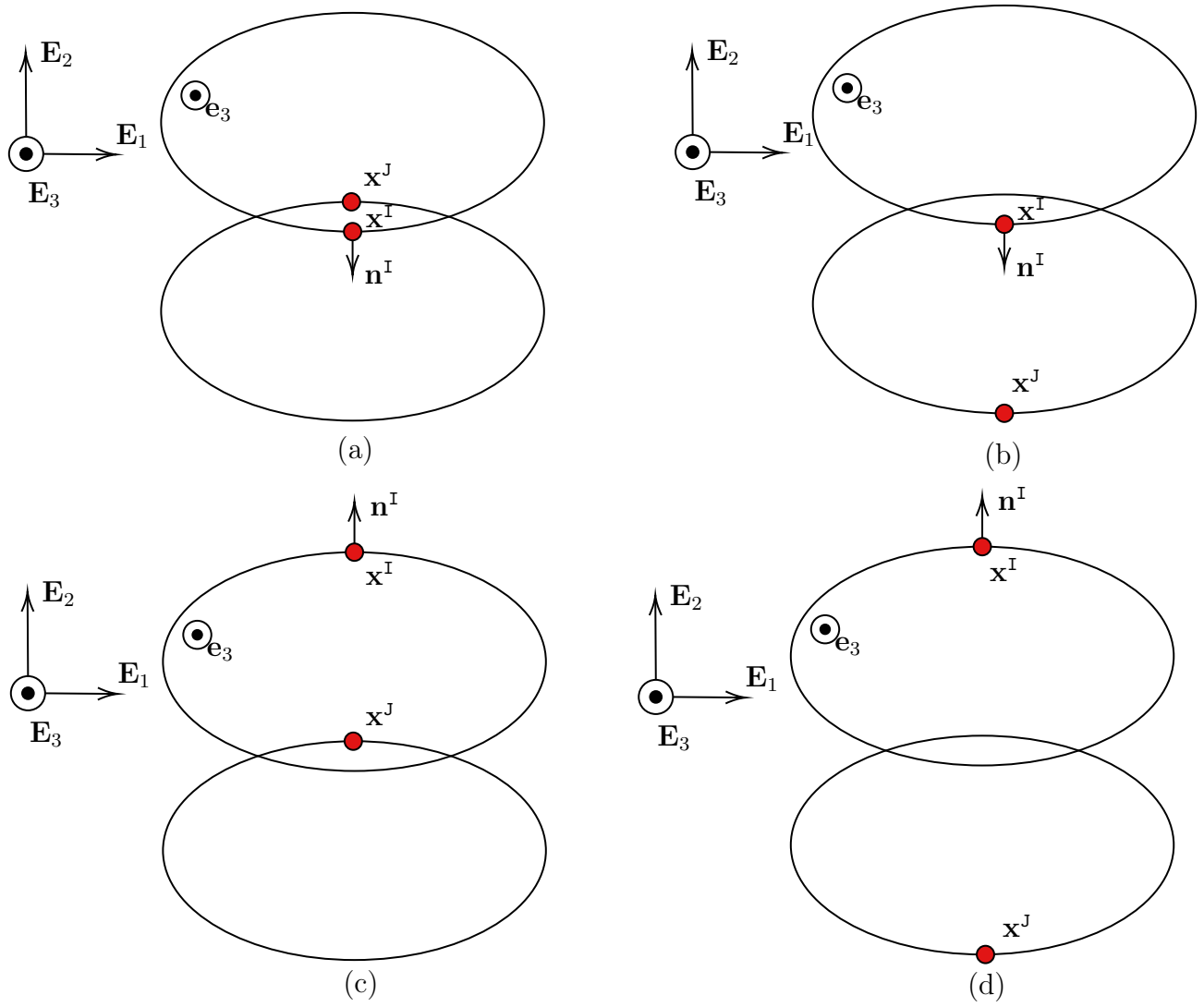

Figure 3.3: Approach I: planar view of the different solutions of the projection problem in Eq. (3.13) in the case of parallel straight beams in contact. (a) Desired solution; (b), (c), (d): Undesired solutions for which the constraints in Eqs. (3.10) and (3.11) do not hold. The undesired solutions can be obtained if a poor first guess is provided to the non-linear solver. This problem comes from the cyclic property of the cylindrical coordinate system of the cross-sections [37].

where $\underline{q} = [h^{\mathrm{I}2}, h^{\mathrm{J}1}, h^{\mathrm{J}2}, g]$. At the solution of the local problem, $\bar{g} = g_N$ where g_N has been defined in Eq. (3.15). The obvious problem with Eq. (3.16) is that four unknowns are present in a system of three non-linear equations. We therefore add one more equation:

$$f_2(\bar{\underline{q}}) = a^1(\mathbf{n}^{\mathrm{I}} + \mathbf{n}^{\mathrm{J}p}) \cdot \boldsymbol{\tau}_2^{\mathrm{J}} = 0, \tag{3.19}$$

with:

$$\mathbf{n}^{\mathrm{J}p} = \frac{\mathbf{n}^{\mathrm{J}} - (\mathbf{n}^{\mathrm{J}} \cdot \tilde{\mathbf{n}}^{\mathrm{I}})\tilde{\mathbf{n}}^{\mathrm{I}}}{\|\mathbf{n}^{\mathrm{J}} - (\mathbf{n}^{\mathrm{J}} \cdot \tilde{\mathbf{n}}^{\mathrm{I}})\tilde{\mathbf{n}}^{\mathrm{I}}\|}. \tag{3.20}$$

Eq. (3.19) is motivated by the fact that at the solution sought, both projected normal vectors $\mathbf{n}^{\mathrm{I}}$ and $\mathbf{n}^{\mathrm{J}p}$ must be orthogonal to the vector tangent to the (master) surface, $\boldsymbol{\tau}_2^{\mathrm{J}}$. Also in Eq. (3.19), a^1 is used to make equations from $\mathbf{f}_1$ and f_2 consistent in terms of units. The new set of equations to solve for thus reads:

$$\underline{f}(\bar{\underline{q}}) = [\mathbf{f}_1, f_2]^T = \underline{0}. \tag{3.21}$$

A pair of surface points that abides Eq. (3.21) is shown in Fig. 3.4.

Eq. (3.21) is nonlinear and is solved using Newton's method for which the following Jacobian is required:

$$\underline{\underline{H}}(\underline{q}) = \frac{\partial \underline{f}}{\partial \underline{q}}. \tag{3.22}$$

The Jacobian however includes only second-order surface derivatives, whereas the Jacobian of Eq. (3.14) includes third-order surface derivatives.

Thanks to the lower order of surface derivatives of Approach II, it is expected that Approach II is more robust than Approach I and that $\underline{f}$ and $\underline{\underline{H}}$ are faster to compute (see Section 3.4.1 for a comparison between the two approaches).

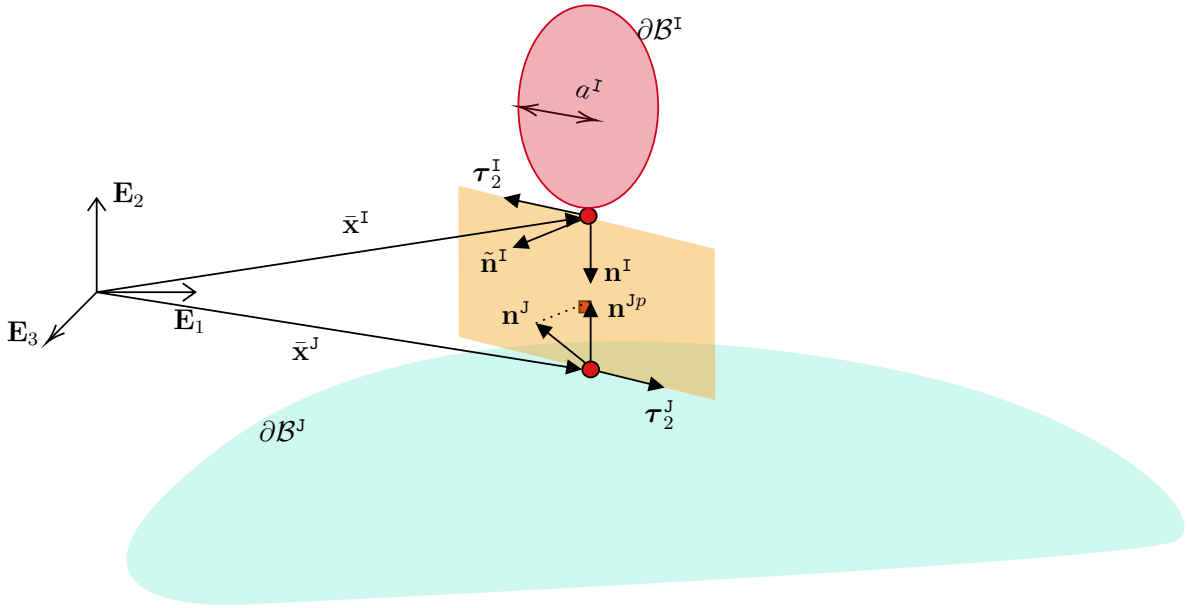

Figure 3.4: Approach II: solution sought of the projection problem in Eq. (3.21) illustrated for one slave section $\mathcal{C}$. The plane of (unit) normal vector $\tilde{\mathbf{n}}^{\mathrm{I}}$ spanned by vectors $\boldsymbol{\tau}_2^{\mathrm{I}}$ and $\mathbf{n}^{\mathrm{I}}$ is again shown in translucent orange. The pair of red surface points corresponding to the solution of Eq. (3.16) lies on this plane. At the solution, vectors $\mathbf{n}^{\mathrm{I}}$ and $\mathbf{n}^{\mathrm{J}p}$ point in opposite directions and are both orthogonal to $\boldsymbol{\tau}_2^{\mathrm{J}}$, thus verifying Eq. (3.19).

3.2.2.2 Frictionless contact conditions and penalty regularization

The unilateral contact conditions are for both approaches given by:

$$g_N \geq 0, \quad T_N \leq 0, \quad g_N T_N = 0, \tag{3.23}$$

where g_N is given by Eq. (3.15) and T_N denotes the magnitude of the nominal traction vector, *i.e.* the traction acting in the current configuration, yet integrated over the contact area in the reference configuration.

If a penalty formulation is used, contact traction T_N, acting at the pair of surface points used to measure penetration, is given by:

$$T_N = -\epsilon_N \langle -g_N \rangle \tag{3.24}$$

where $\epsilon_N > 0$ denotes a user-defined parameter, usually referred to as the penalty stiffness, and $\langle \bullet \rangle$ denote the Macaulay brackets.
Nominal contact traction vector $\mathbf{T}$ acting on the section acts in the normal direction to the slave surface at surface point $\bar{\mathbf{x}}^{\mathrm{I}}$ such that:

$$\mathbf{T} = T_N \bar{\mathbf{n}}^{\mathrm{I}}. \tag{3.25}$$

The corresponding virtual work of the contact force is then given by:

$$d\delta\Pi_c = T_N \delta g_N dL^{\mathcal{B}^{\mathrm{I}}} = -\epsilon_N \langle -g_N \rangle \delta g_N \left\| \frac{\partial \mathbf{x}^{\mathrm{I}}_{0c}}{\partial h^{\mathrm{I}1}} \right\| dh^{\mathrm{I}1}, \tag{3.26}$$

where δg_N denotes the variation of the normal gap g_N with respect to all involved kinematic variables: the displacement vector components and rotations of the two beams in contact gathered in $\underline{p}^{\mathrm{IJ}} = \left[\underline{p}^{\mathrm{I}}, \underline{p}^{\mathrm{J}}\right]^T$. A detailed derivation of δg_N is presented in Appendix III.A. $dL^{\mathcal{B}^{\mathrm{I}}}$ denotes an infinitesimal length of $\mathbf{x}^{\mathrm{I}}_{0c}$ and $dh^{\mathrm{I}1}$ denotes the differential of $h^{\mathrm{I}1}$.

3.2.2.3 Contact virtual work

The virtual work equation for the two-body system $\mathcal{B}^{\mathrm{I}}, \mathcal{B}^{\mathrm{J}}$ including contact interactions reads:

$$\delta\Pi_{\mathcal{B}^{\mathrm{I}}}(\underline{p}^{\mathrm{I}}, \delta\underline{p}^{\mathrm{I}}) + \delta\Pi_{\mathcal{B}^{\mathrm{J}}}(\underline{p}^{\mathrm{J}}, \delta\underline{p}^{\mathrm{J}}) + \delta\Pi_c(\underline{p}^{\mathrm{IJ}}, \delta\underline{p}^{\mathrm{IJ}}) = 0, \tag{3.27}$$

where $\delta\Pi_{\mathcal{B}^i}$ denotes the internal and external virtual work of $\mathcal{B}^i$ (excluding contact interactions). $\underline{p}^{\mathrm{IJ}}$ and $\delta\underline{p}^{\mathrm{IJ}}$ are admissible functions of the trial and test spaces, respectively. $\delta\Pi_c$ denotes the virtual work of the contact forces between $\mathcal{B}^{\mathrm{I}}$ and $\mathcal{B}^{\mathrm{J}}$.

As stated above, cases of interest in this contribution are configurations in which contact interactions arise over a finite length along the beams in contact. T_N, introduced in Eq. (3.24), can be seen as a length-specific contact traction because it only accounts for a single (slave) section. The virtual work of all penetrated sections follows from the integration of the virtual work $d\delta\Pi_c$ along the centroid-line of $\mathcal{B}^{\mathrm{I}}$ as

follows:

$$\delta\Pi_c = \int_{h_L^{1\mathtt{I}}}^{h_U^{1\mathtt{I}}} d\delta\Pi_c, \tag{3.28}$$

where $h_L^{1\mathtt{I}}$ and $h_U^{1\mathtt{I}}$ denote the lower and upper bound of the integral along $h^{\mathtt{J}1}$. Note that only penetrated sections contribute to $\delta\Pi_c$ (see Eq. (3.26)). Now that the contact kinematics and the virtual work of the contact forces are defined for the space continuous problem, they must be spatially discretized.

3.3 Spatial discretization

The spatial discretization method employed in this contribution is the FE Method. Beam $\mathcal{B}$ is now discretized with beam FEs (BFEs). When needed, subscript K denotes the index of a node. A brief explanation of the interpolation of the surface of a BFE is given in the following. This will serve as the basis for the discretized contact formulation.

3.3.1 Interpolation of the surface

For a BFE that is part of the discretization of beam $\mathcal{B}$, the position of a surface point can still be obtained from Eq. (3.2), where the position of the centroid-line in the undeformed configuration is given by:

$$\mathbf{X}_c(h_1) = \sum_{K=1}^{n_X} N_K^X(h_1)\hat{\mathbf{x}}_{0K}. \tag{3.29}$$

$\hat{\mathbf{x}}_{0K}$ denotes the reference location of node K and N_K^X denotes the associated interpolation functions. The centroid-line position in the current configuration is given by:

$$\mathbf{x}_c(h^1) = \mathbf{x}_{0c} + \sum_{K=1}^{n_u} N_K^u(h^1)\hat{\mathbf{u}}_K, \tag{3.30}$$

where $\hat{\mathbf{u}}_K \in \mathbb{R}^3$ denotes the displacement of node K and N_K^u its displacement interpolation function. Rotation vector $\boldsymbol{\theta}$ used to compute $\boldsymbol{\Lambda}$ using Rodrigues' formula

(see [43]) is interpolated as follows:

$$\boldsymbol{\theta}(h^1) = \sum_{K=1}^{n_\theta} N_K^\theta(h^1)\hat{\boldsymbol{\theta}}_K, \tag{3.31}$$

where $\hat{\boldsymbol{\theta}}_K \in \mathbb{R}^3$ denotes the nodal rotation vector of node K and N_K^θ the associated interpolation function.

For each BFE, n_u nodes are used to interpolate displacements, n_X nodes are used to interpolate positions in the undeformed configuration and n_θ nodes are used to interpolate rotations. Depending on the beam formulation employed n_u, n_X and n_θ can differ[2].

Not every type of BFE yields a C^0-continuous surface of the discretized beam [4, 59]. This obviously makes contact difficult to formulate. For instance, two-node Geometrically Exact BFEs [29] are employed in Section 3.4. The surface of beams discretized with such BFEs is only C^0-continuous if the beam is initially straight. This poor continuity of the surface comes with several disadvantages when contact is considered [93]. This is why for each beam, the smoothing technique of [54] is employed which provides a surface close to discretized beam's surface, but C^1-continuous. Such a smoothed surface is constructed as an assembly of consecutive patches that are based on the original discretized geometry. The resulting surface continuity reduces the risk of abrupt changes in the direction of the contact force between subsequent global iterations of the Newton-Raphson scheme. This is however not elaborated here in order to keep the focus on the contact formulation. However, the numerical examples of Section 3.4 only employ smoothed surfaces of the discretized beams.

[2]The interpolation functions are not specified here in order to keep the formulation valid for different beam formulations. Also, the physical meaning of the rotation variables can change depending on the beam theory employed.

3.3.2 Discretized contact weak form and linearization.

Let us now consider two BFEs, $\mathcal{M}$ and $\mathcal{N}$ which are part of the discretizations of $\mathcal{B}^{\mathrm{I}}$ and $\mathcal{B}^{\mathrm{J}}$, respectively. Surfaces of these elements are denoted by $\partial\mathcal{S}^{\mathcal{M}}$ and $\partial\mathcal{S}^{\mathcal{N}}$. We store the nodal variables of both beams in vectors $\underline{p}^{\mathcal{M}} = \left[\hat{\mathbf{u}}_1^{\mathcal{M}}, \ldots, \hat{\mathbf{u}}_{n_u}^{\mathcal{M}}, \hat{\boldsymbol{\theta}}_1^{\mathcal{M}}, \ldots, \hat{\boldsymbol{\theta}}_{n_\theta}^{\mathcal{M}}\right]$ and $\underline{p}^{\mathcal{N}} = \left[\hat{\mathbf{u}}_1^{\mathcal{N}}, \ldots, \hat{\mathbf{u}}_{n_u}^{\mathcal{N}}, \hat{\boldsymbol{\theta}}_1^{\mathcal{N}}, \ldots, \hat{\boldsymbol{\theta}}_{n_\theta}^{\mathcal{N}}\right]$.

The surfaces of both elements are assumed to collide. Consequently, force vector $\underline{r}_c$ and stiffness matrix $\underline{\underline{K}}_c$ associated with this contact must be computed and assembled in the global force residual and global stiffness matrix. Different approaches to compute these entities exist:

1. In a single-pass approach, $\mathcal{M}$ is assumed to be the slave and $\mathcal{N}$ the master. The discretized version of Eq. (3.28) is integrated along $h^{\mathcal{M}1}$. The resulting contact traction vector acting on $\partial\mathcal{S}^{\mathcal{M}}$ is $\mathbf{t} = \mathbf{t}_{\mathcal{M}}$ and acts along the normal to the surface of $\mathcal{M}$, but not necessarily along the normal to the surface of $\mathcal{N}$. On $\partial\mathcal{S}^{\mathcal{N}}$, the traction vector acting at the surface point solution of the projection problem $\mathbf{x}^{\mathcal{N}}(\underline{h}^{\mathcal{N}})$ is $-\mathbf{t}_{\mathcal{M}}$. Traction continuity is preserved locally, but the approach introduces a bias, *i.e.* the choice of which body is the slave and which one is the master influences the results.

2. In a double-pass approach, a single-pass procedure as in 1. is performed twice. First, $\mathcal{M}$ acts as the slave and $\mathcal{N}$ as the master, then their roles are inverted, *i.e.* $\mathcal{N}$ becomes the slave and $\mathcal{M}$ the master. This results in a unbiased approach. Besides doubling the computational costs associated with contact, the problem might also become over-constrained [74].

3. The "two-half-pass" algorithm was first introduced in [73] and [74] for the frictionless and frictional cases, respectively. During the first half-pass where $\mathcal{M}$ is the slave and $\mathcal{N}$ the master, contact traction vector $\mathbf{t} = \mathbf{t}_{\mathcal{M}}$ only acts on $\partial\mathcal{S}^{\mathcal{M}}$ and no traction vector affects $\partial\mathcal{S}^{\mathcal{N}}$. During the second half-pass, $\mathcal{N}$ acts as the slave and $\mathcal{M}$ as the master. The traction vector for the second half-pass is $\mathbf{t}_{\mathcal{N}}$ (and not $-\mathbf{t}_{\mathcal{M}}$) and only acts on $\partial\mathcal{S}^{\mathcal{N}}$. This leads to additional computational effort relative to the single-pass algorithm, but entails an unbiased treatment

of contact. Over-constraining is less likely to occur than with a double-pass scheme, and [73] and [74] have shown an increased robustness for the two-half-pass algorithm relative to the other two options, if applied to standard FE models.

The procedures necessary to obtain the contact residual and contact stiffness for a single-pass (1.) and a two-half-pass (3.) approach are described next. The double-pass algorithm (2.) can be trivially obtained by performing a single-pass procedure for a second time after inverting the roles of the slave and the master. We therefore do not detail it in the following.

We now assume for simplicity that all sections attached to integration points along the centroid-line of $\mathcal{M}$ have their projection according to Eq. (3.13) or Eq. (3.21) on $\partial\mathcal{S}^{\mathcal{N}}$, and not on another element's surface. Similarly, it is assumed that points on the perimeter of sections of $\mathcal{N}$ have their projections on $\partial\mathcal{S}^{\mathcal{M}}$ and not on another element's surface. In practice, different sections of a slave element may have their projections on different master elements. Kinematic variables associated with contact between $\mathcal{M}$ and $\mathcal{N}$ are gathered in vector $\underline{p}^{\mathtt{IJ}} = \left[\underline{p}^{\mathcal{M}}, \underline{p}^{\mathcal{N}}\right]^T$.

3.3.2.1 Single pass algorithm

Eq. (3.28) specialized to the contact between two BFEs can be written as:

$$\delta\Pi_c = -\epsilon_N \int_{-1}^{1} \langle -g_N(\eta)\rangle \, \delta g_N(\eta) \, \|\mathcal{J}(\eta)\| \, d\eta \tag{3.32}$$

$$\approx -\epsilon_N \sum_{k}^{n_{IP}^{\mathcal{M}}} w_k \, \langle -g_N(\eta_k)\rangle \, \delta g_N(\eta_k) \, \|\mathcal{J}(\eta_k)\| \, , \tag{3.33}$$

$$\approx -\epsilon_N \sum_{k}^{n_{IP}^{\mathcal{M}}} w_k \, \langle -g_{Nk}\rangle \, \delta g_{Nk} \, \|\mathcal{J}_k\| \, , \tag{3.34}$$

where $\eta \in [-1, 1]$ denotes the centroid-point coordinate in the parameter space and $\mathcal{J} = \frac{\partial \mathbf{x}_c^{\mathrm{I}}}{\partial \eta}$. Eq. (3.33) is a quadrature where $n_{IP}^{\mathcal{M}}$ integration points are used. The weight and coordinates of the k^{th} integration point is denoted by w_k and η_k,

respectively. The normal gap measured at this integration point is denoted by g_{Nk}, and $\mathcal{J}_k = \mathcal{J}(h^{\mathcal{M}1}(\eta_k))$.

To find contact-residual $\underline{r}_c$, one must recast Eq. (3.33) into:

$$\delta\Pi_c = \delta\underline{p}^{\mathtt{IJ}\,T}\underline{r}_c, \tag{3.35}$$

where $\delta\underline{p}^{\mathtt{IJ}}$ denotes the variation of the nodal kinematic variables. To this end, the variation of normal gap δg_{Nk} related to the k^{th} integration point must be expressed solely in terms of variations of the kinematic variables such that we can write:

$$\delta g_{Nk} = \underline{b}_k^T \delta\underline{p}^{\mathtt{IJ}}. \tag{3.36}$$

$\underline{b}_k$ is obtained from Eq. (3.61) by evaluating all quantities at the surface points obtained from the solution of the local problem at this integration point.

If the formalism introduced in [47, 41] is used, the implicit dependency of g_{Nk} on variables in $\underline{p}^{\mathtt{IJ}}$ can be included via an exception in the automatic differentiation (AD). In this case, $\underline{b}_k$ can be equivalently obtained from:

$$\delta g_{Nk} = \left(\frac{\hat{\partial} g_{Nk}}{\hat{\partial}\underline{p}^{\mathtt{IJ}}}\bigg|_{\frac{\partial \bar{q}_k}{\partial \underline{p}^{\mathtt{IJ}}} = \underline{\underline{A}}_k} \right)^T \delta\underline{p}^{\mathtt{IJ}} = \underline{b}_k^T \delta\underline{p}^{\mathtt{IJ}}, \tag{3.37}$$

where $\underline{\underline{A}}_k$ is obtained from Eq. (3.49) and operator $\frac{\hat{\partial}}{\hat{\partial}\underline{w}}$ denotes differentiation with respect to variables $\underline{w}$ performed by the automatic differentiation algorithm [47, 41].

By summing the contribution of the $n_{IP}^{\mathcal{M}}$ integration points, $\underline{r}_c$ can be rewritten as:

$$\underline{r}_c(\underline{p}^{\mathcal{M}}, \underline{\bar{q}}_1^{\mathcal{M}}, ..., \underline{\bar{q}}_{n_{IP}^{\mathcal{M}}}) \approx -\epsilon_N \sum_k^{n_{IP}^{\mathcal{M}}} w_k \langle -g_{Nk} \rangle \underline{b}_k \left\| \mathcal{J}_k \right\|. \tag{3.38}$$

The associated stiffness matrix can also be obtained using the AD procedure for

which we write:

$$\underline{\underline{K}}_c = -\epsilon_N \sum_k^{n_{IP}^{\mathcal{M}}} \frac{\hat{\partial}}{\hat{\partial}\underline{p}^{\mathtt{IJ}}}(\underline{r}_{ck})\Big|_{\frac{\partial \bar{q}_k}{\partial \underline{p}^{\mathtt{IJ}}}=\underline{\underline{A}}_k} = -\epsilon_N \left(\sum_k^{n_{IP}^{\mathcal{M}}} w_k \frac{\hat{\partial}}{\hat{\partial}\underline{p}^{\mathtt{IJ}}} \left(\langle -g_{Nk} \rangle \, \|\mathcal{J}_k\| \, \underline{b}_k \right) \Big|_{\frac{\partial \bar{q}_k}{\partial \underline{p}^{\mathtt{IJ}}}=\underline{\underline{A}}_k} \right). \tag{3.39}$$

3.3.2.2 Two-half-pass algorithm

In the two-half-pass approach, the contact traction vector is computed independently for element $\mathcal{B}^{\mathcal{M}}$ and $\mathcal{B}^{\mathcal{N}}$. To indicate to which half-pass quantities refer to, superscripts "$\mathcal{M} \to \mathcal{N}$" and "$\mathcal{N} \to \mathcal{M}$" are employed.

For the first half-pass in which $\mathcal{B}^{\mathcal{M}}$ is the slave, we write for the contact residual:

$$\underline{r}_c^{\mathcal{M}\to\mathcal{N}}(\underline{p}^{\mathcal{M}}, \bar{\underline{q}}_1, ..., \bar{\underline{q}}_{n_{IP}^{\mathcal{M}}}) \approx -\epsilon_N \sum_k^{n_{IP}^{\mathcal{M}}} w_k \left\langle -g_{Nk}^{\mathcal{M}\to\mathcal{N}} \right\rangle \underline{b}_k^{\mathcal{M}\to\mathcal{N}} \, \|\mathcal{J}_k\| \, . \tag{3.40}$$

The difference between $\underline{b}_k^{\mathcal{M}\to\mathcal{N}}$ in Eq. (3.40) and $\underline{b}$ in Eq. (3.36) is that only the kinematic variables of $\mathcal{B}^{\mathcal{M}}$ are used to construct $\underline{b}_k^{\mathcal{M}\to\mathcal{N}}$. The reason is that the contact traction is considered to only act on $\partial\mathcal{S}^{\mathcal{M}}$. However, every $g_{Nk}^{\mathcal{M}\to\mathcal{N}}$ (and consequently $\underline{r}_c^{\mathcal{M}\to\mathcal{N}}$) in Eq. (3.40) depends on $\underline{p}^{\mathcal{N}}$ because of the (implicit) dependency of the local problem with respect to $\underline{p}^{\mathcal{N}}$. The linearization of $\underline{r}_c^{\mathcal{M}\to\mathcal{N}}$ then yields the two following sub-matrices:

$$\underline{\underline{K}}_{\mathcal{M}\mathcal{M}} = -\epsilon_N \sum_k^{n_{IP}^{\mathcal{M}}} w_k \frac{\hat{\partial}}{\hat{\partial}\underline{p}^{\mathcal{M}}} \left(\left\langle -g_{Nk}^{\mathcal{M}\to\mathcal{N}} \right\rangle \underline{b}_k^{\mathcal{M}\to\mathcal{N}} \, \|\mathcal{J}_k\| \right) \Big|_{\frac{\partial \bar{q}_k}{\partial \underline{p}^{\mathtt{IJ}}}=\underline{\underline{A}}_k^{\mathcal{M}\to\mathcal{N}}}, \tag{3.41}$$

$$\underline{\underline{K}}_{\mathcal{M}\mathcal{N}} = -\epsilon_N \sum_k^{n_{IP}^{\mathcal{M}}} w_k \frac{\hat{\partial}}{\hat{\partial}\underline{p}^{\mathcal{N}}} \left(\left\langle -g_{Nk}^{\mathcal{M}\to\mathcal{N}} \right\rangle \underline{b}_k^{\mathcal{M}\to\mathcal{N}} \, \|\mathcal{J}_k\| \right) \Big|_{\frac{\partial \bar{q}_k}{\partial \underline{p}^{\mathtt{IJ}}}=\underline{\underline{A}}_k^{\mathcal{M}\to\mathcal{N}}}. \tag{3.42}$$

For the second half-pass, the roles of the two bodies are inverted. This entails that for this half-pass the measure of penetration, $g_{Nk}^{\mathcal{N}\to\mathcal{M}}$, is measured from the perimeter of cross-sections of $\mathcal{N}$ to $\partial\mathcal{S}^{\mathcal{M}}$. The contact residual that corresponds to this half-pass

can be expressed as:

$$\underline{r}_c^{\mathcal{N}\to\mathcal{M}}(\underline{p}^{\mathcal{N}}, \bar{\underline{q}}_1, ..., \bar{\underline{q}}_{n_{IP}^{\mathcal{N}}}) \approx -\epsilon_N \sum_k^{n_{IP}^{\mathcal{N}}} w_k \left\langle -g_{Nk}^{\mathcal{N}\to\mathcal{M}} \right\rangle \underline{b}_k^{\mathcal{N}\to\mathcal{M}} \left\| \mathcal{J}_k \right\|. \tag{3.43}$$

Only the kinematic variables in $\underline{p}^{\mathcal{N}}$ are used to construct $\underline{b}_k^{\mathcal{N}\to\mathcal{M}}$. Thus, $\underline{r}_c^{\mathcal{N}\to\mathcal{M}}$ only affects the entries corresponding to the kinematic variables of $\mathcal{N}$. The linearization of $\underline{r}_c^{\mathcal{N}\to\mathcal{M}}$ yields two new sub-matrices:

$$\underline{\underline{K}}_{\mathcal{N}\mathcal{N}} = -\epsilon_N \sum_k^{n_{IP}^{\mathcal{N}}} w_k \frac{\hat{\partial}}{\hat{\partial}\underline{p}^{\mathcal{N}}} \left(\left\langle -g_{Nk}^{\mathcal{N}\to\mathcal{M}} \right\rangle \underline{b}_k^{\mathcal{N}\to\mathcal{M}} \left\| \mathcal{J}_k \right\| \right) \Big|_{\frac{\partial \bar{\underline{q}}_k}{\partial \underline{p}^{\mathrm{IJ}}} = \underline{\underline{A}}_k^{\mathcal{N}\to\mathcal{M}}}, \tag{3.44}$$

$$\underline{\underline{K}}_{\mathcal{N}\mathcal{M}} = -\epsilon_N \sum_k^{n_{IP}^{\mathcal{N}}} w_k \frac{\hat{\partial}}{\hat{\partial}\underline{p}^{\mathcal{M}}} \left(\left\langle -g_{Nk}^{\mathcal{N}\to\mathcal{M}} \right\rangle \underline{b}_k^{\mathcal{N}\to\mathcal{M}} \left\| \mathcal{J}_k \right\| \right) \Big|_{\frac{\partial \bar{\underline{q}}_k}{\partial \underline{p}^{\mathrm{IJ}}} = \underline{\underline{A}}_k^{\mathcal{N}\to\mathcal{M}}}. \tag{3.45}$$

We can also note that $\underline{\underline{K}}_c^{\text{two-half-pass}}$, defined as:

$$\underline{\underline{K}}_c^{\text{two-half-pass}} = \begin{bmatrix} \underline{\underline{K}}_{\mathcal{M}\mathcal{M}} & \underline{\underline{K}}_{\mathcal{M}\mathcal{N}} \\ \underline{\underline{K}}_{\mathcal{N}\mathcal{M}} & \underline{\underline{K}}_{\mathcal{N}\mathcal{N}} \end{bmatrix} \tag{3.46}$$

is not symmetric, unlike $\underline{\underline{K}}_c$ in Eq. (3.39).

3.4 Numerical examples

In the previous sections, we have introduced a scheme to treat non-localized contact between beams discretized with BFEs, possibly shear-deformable and with circular or elliptical sections. In the current section, we investigate its capabilities based on three numerical examples. First, a semi-circular arch is brought in contact with an initially straight beam. In the second example, aligned beams are twisted. Finally, we consider the bending of a wire rope.

For all examples, the contact force is a linear function of g_N (see Eq. (3.25)). The

penalty stiffness employed is given by:

$$\epsilon_N = \frac{\pi E}{8(1-\nu^2)}, \tag{3.47}$$

where E denotes the Young's modulus of the beams and ν their Poisson's ratio. The penalty stiffness in Eq. (3.47) corresponds to the (length-specific) apparent stiffness relating penetration and contact force for parallel, isotropic, linear elastic cylinders in Hertz's theory (see [70]). Note also that the radius of curvature of contacting surfaces is not present in Eq. (3.47), which is convenient. Note that finite penalty stiffness ϵ_N can be interpreted as the elastic compliance of, the otherwise rigid, cross-sections.

In the three presented numerical examples, only one integration point per slave patch (see [54]) is used to evaluate $\underline{r}_c$ and $\underline{\underline{K}}_c$. The total number of integration points employed is thus low. This reduces the computational cost and also alleviates the risk of over-constraining.

3.4.1 Example 1: contact between a semi-circular arch and a straight beam

In the first example, a semi-circular arch is brought in contact with a straight beam. Young's moduli of the beams are set to 100 GPa and their Poisson's ratios to 0.3. The semi-circular arch has a radius of 0.9 m and the straight beam a length of 2.7 m. Both beams have elliptical sections with principal axis' lengths of 0.1 m and 0.06 m. For both beams, local basis vector $\mathbf{E}_{01}$ points in the $[-1,0,0]_{\mathbf{E}_i}$ direction in the undeformed configuration (see Fig. 3.5).

The nodes at the base of the arch are moved vertically towards the bottom beam with a final vertical displacement of 0.3 m for $0 < t < 1$ in 300 increments, and are then moved horizontally for $1 < t < 2$ with a displacement of 0.1 m in 300 increments. The rotations of these nodes are also blocked. All kinematics variables at the ends of the straight beam are restrained during the entire simulation.

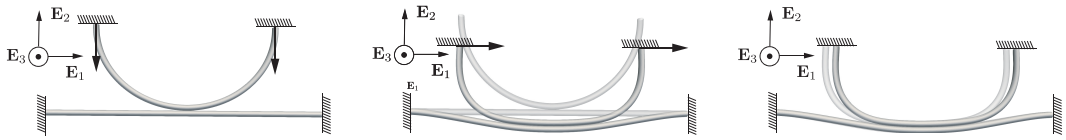

$0 < t < 1$ $1 < t < 2$ $t = 2$

Figure 3.5: Example 3.4.1: Schematic presentation of the structure with BCs and deformed configuration at different times of the loading. The configuration at $t = 0$ and $t = 1$ is presented in translucent in the central and right picture, respectively.

Several numerical aspects are investigated, *i.e.*:

- The number of BFEs: three (uniform) refinements for both beams with a constant ratio of the number of BFEs of both bodies. The mesh of the straight beam is coarser than the one of the arch in order to show a possible influence of the choice of the roles of master and slave. For mesh A, 90 and 60 BFEs are used; have been used for the curved beam and the straight beam, respectively; for mesh B, 120 and 80 BFEs; and for mesh C, 150 and 100 BFEs.
- The integration scheme:
  - Two different settings for the single-pass approach are studied. In the first one, the top arch is used as slave, while the initially straight beam serves as the slave in the second one (denoted as "inverted single-pass" in the following).
  - The two-half-pass scheme is also studied.

Fig. 3.6 reports the sum of the reaction forces at the fixed nodes of the straight beam. The curves of the single-pass schemes match well. This is however not the case for the curves of the two-half-pass schemes, as oscillations are present. For the two-half-pass scheme, furthermore, the sum of the reaction forces at the supports of the two beams does not vanish (see Fig. 3.7), which suggests violation of action-reaction principle at the contact interface. This difference can be explained by the fact that for two colliding patches, a section of the first patch penetrates the other patch during

the first half-pass, whereas this is not necessarily the case for the second half-pass (when the roles of master and slave are inverted). This is illustrated in Fig. 3.9. Thus, this effect violates Newton's third law. In an ideal situation in the continuum formulation in which there is no penetration, the two-half pass does not suffer from this lack of balance of forces. This is because in this case, the tangent planes at the contacting points are parallel. In this case and if no quadrature is employed, when a section is found as penetrated during the first half-pass, a penetration will necessarily be found during the second half-pass.

This phenomenon is exacerbated because the highest contact tractions are located at the ends of the contact zone while in the center of the arch, the contact tractions are considerably smaller.

Similar effects occur for the simple truss structure of Fig. 3.11 for which a node-to-segment contact scheme is employed. Fig. 3.11a presents the single-pass algorithm. Both bodies are deformed due to the effect of the contact applied to the penetrated node and at its projection on the master truss. Fig. 3.11b presents the results of the two-half-pass algorithm. Only the bottom structure is deformed because the contact traction is only applied to the slave body at the penetrated node. As no nodes of the top structure are penetrated, no contact traction is applied to it. Hence, it does not deform. This explains the non-vanishing sum of the reaction forces at the supports for the two-half-pass scheme in Fig. 3.11c. In Appendix III.C, the evolution of the global residual is reported for the finest mesh (mesh C) for the three studied integration schemes.

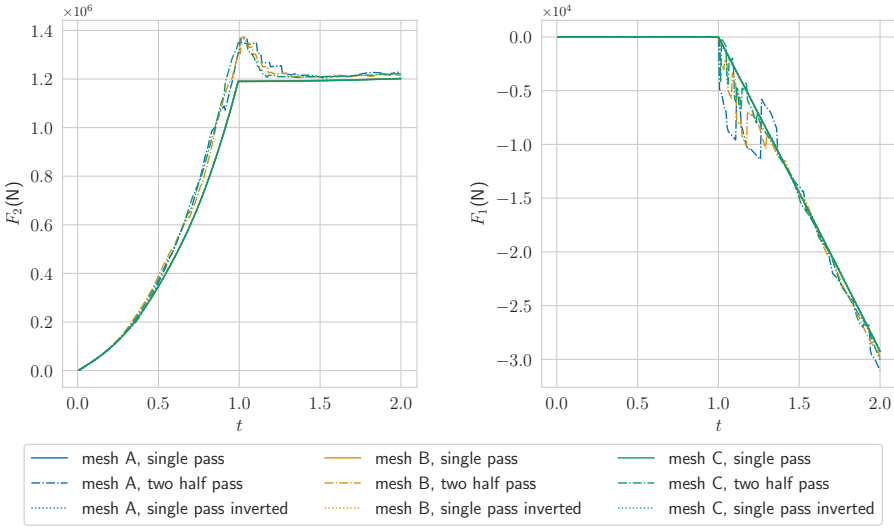

Figure 3.6: Example 3.4.1: Sum of the reaction forces of the fixed nodes of the initially straight beam along the $\mathbf{E}_2$ and $\mathbf{E}_1$ directions.

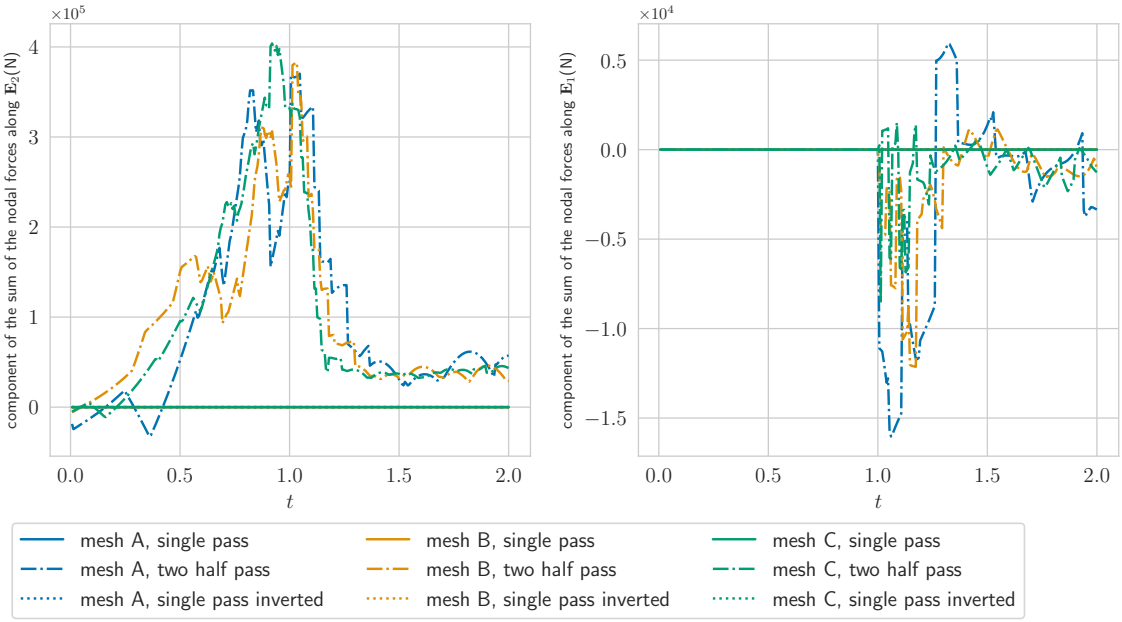

Figure 3.7: Example 3.4.1: Difference between the sum of the reaction forces of the fixed nodes of the straight beam and those of the curved beam.

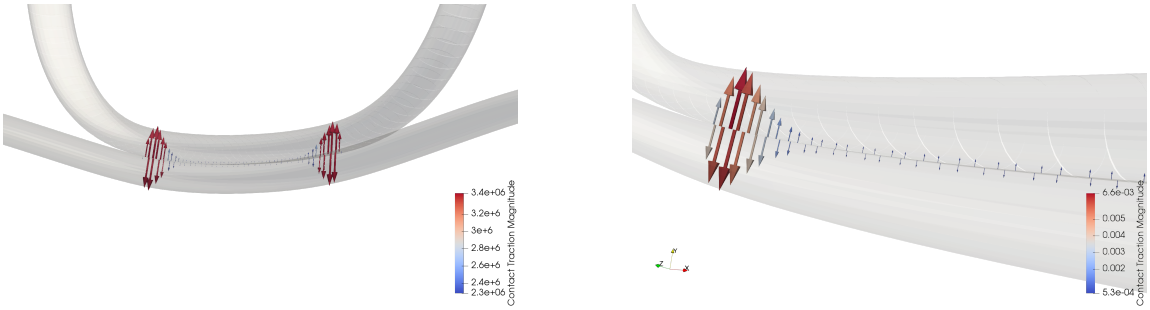

(a) Global view. (b) Zoom.

Figure 3.8: Example 3.4.1: Contact traction at $t = 1$ for the two-half-pass approach. Vectors are located at slave surface points with local coordinates solution of the local problem.

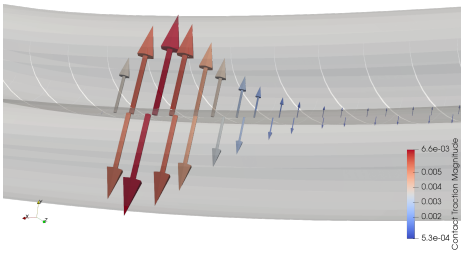

Figure 3.9: Example 3.4.1: Contact tractions applied on the perimeter of sections attached to integration points at $t \approx 1.3$ for the two-half-pass approach for the coarsest mesh (mesh A). On the far left, penetration is only detected for one of the two-half-passes.

Comparison of computational costs for the local problems

In section 3.2.2.1, we have introduced two possible sets of equations to quantify penetration. As discussed, if Eq. (3.13) (Approach I) is employed, higher order derivatives are involved yielding a longer code and potentially a longer execution time than if Eq. (3.21) (Approach II) is used. The lengths of the generated codes to compute $\underline{r}_c$ and $\underline{\underline{K}}_c$ is reported in Table 3.1 for the single-pass approach.

In order to compare execution times, the numerical example in Fig. 3.5 is employed (with mesh A). The loading is applied in 1000 increments such that several

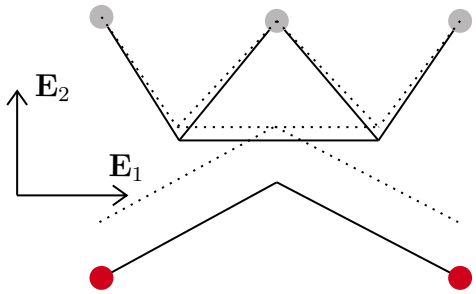

(a) Single-Pass.

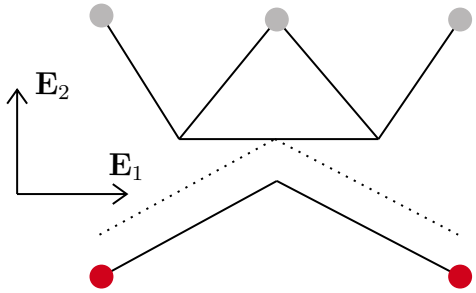

(b) two-half-pass.

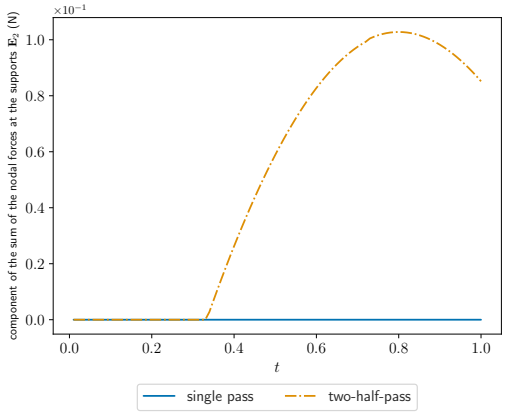

(c) Difference between the sum of the reaction forces acting on the bottom and top structure.

Figure 3.11: Effect of a single and two-half-pass variants of a contact scheme for truss networks with a node-to-segment contact scheme. The boundary conditions applied to the truss networks are such that the nodes in red are shifted upwards, while the grey node are fixed. The undeformed configurations are presented with solid lines while the deformed configurations are presented with dashed lines. For the single-pass scheme, the bottom structure serves as slave. The trusses have a unit Young's modulus and a unit cross-sectional area. (c) shows the vertical component of the sum of the reaction forces for the two contact schemes.

thousands of projection problems and evaluations of $\underline{r}_c$ and $\underline{\underline{K}}$ are performed. For both approaches, the number of penetrated sections and the number of global iterations to converge is similar (see Fig. 3.12). This is also the case for the reaction forces (see Fig. 3.13).

However, the average number of local iterations necessary to converge (such that $\left\|\underline{f}\right\| < 10^{-10}$ with $\underline{f}$ given by Eqs. (3.13) or (3.21)) as well as the average CPU time to determine $\underline{r}_c$ and $\underline{\underline{K}}_c$ are different. The scheme of Eq. (3.21) clearly outperforms the scheme of Eq. (3.13). Note the effect of the simplifications of δg_N (see Appendix III.A).

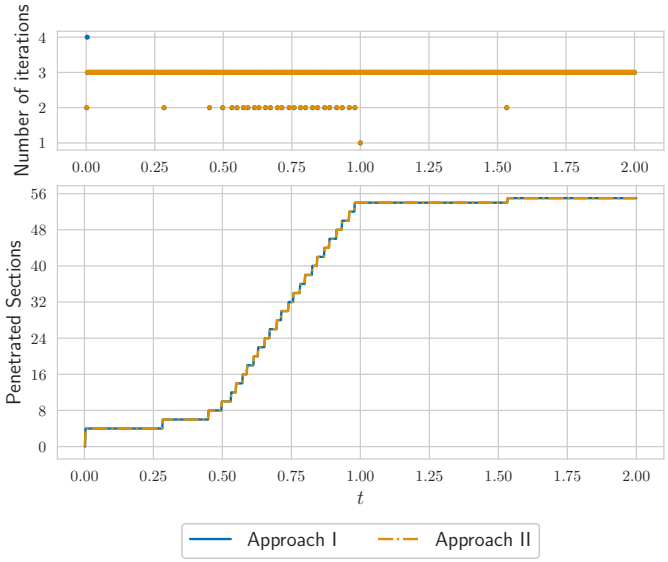

Figure 3.12: Evolution of the number of penetrated sections and number of global iterations necessary to converge for both local schemes. The convergence criterion for the global problem is set as $\left\|\underline{r}_g^{free}\right\| < 10^{-8}$ where $\left\|\underline{r}_g^{free}\right\|$ denotes the components of the global residual force vectors that are not subjected to BCs.

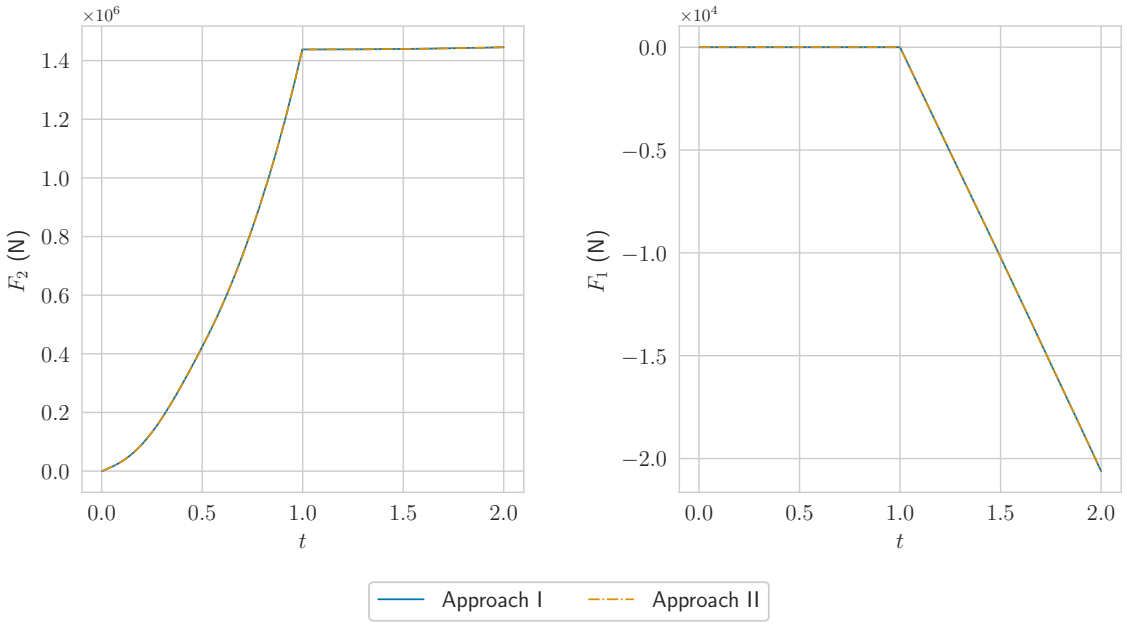

Figure 3.13: Reaction forces for both local schemes introduced.

Equations to solve	Eq. (3.13)		Eq. (3.21)	
δg_N simplified	No	Yes	No	Yes
Length of the C code (kbytes)	330	296	311	272
Average number of iterations to converge (local problem)	2.658		2.307	
Average CPU time (μs)	137	126	118	105

Table 3.1: Performance comparison for the codes generated by *AceGen*. The CPU time includes the solution of the local problem, and the computation of $\underline{r}_c$ and $\underline{\underline{K}}_c$. The convergence criterion for the local problem is set as $\left\|\underline{f}\right\| < 10^{-10}$.

3.4.2 Example 2: twisting of parallel beams

In the second example, we consider three parallel beams (see Figs. 3.14 and 3.15). The orientation of the cross-sections of each beam and their cross-sectional dimensions differ (see Table 3.2 and Fig. 3.14). The end sections on both sides of the three beams are rotated by 180° around the $[0, 0, 1]_{\mathbf{E}_i}$ axis such that the beams wrap

	A	B	C
a (m)	0.01	0.011	1.2
b (m)	0.008	0.006	0.8
$\mathbf{E}_{02}$	$[1, 0, 0]_{\mathbf{E}_i}$	$[0.525, 0.850, 0.]_{\mathbf{E}_i}$	$[-0.448, 0.893, 0.]_{\mathbf{E}_i}$
$\mathbf{E}_{03}$	$[0, -1, 0]_{\mathbf{E}_i}$	$[0.850, -0.525, 0.]_{\mathbf{E}_i}$	$[0.893, 0.448, 0.]_{\mathbf{E}_i}$
L (m)	0.1		
n_{el}	29		
E(Pa)	10^9		
ν	0.3		

Table 3.2: Example 3.4.2: Properties of the three string of BFEs.

around each other. This loading is applied in 540 increments.

The evolution of the number of active (*i.e.* penetrated) slave sections as well as the number of (global) iterations to converge is shown in Fig. 3.16. The amount of penetration, g_N, along the center line of the slave body is shown in Fig. 3.17. g_N is measured twice for each pair of beams in the two-half-pass algorithm. One can observe the good agreement between the penetration measured for the two-half-pass, albeit the single pass performs just as well at roughly half the computational costs.

Finally, the reaction force and torque computed at the end nodes on one side of the beams are reported in Fig. 3.18. One can note the good match between the curves corresponding to the single and two-half-pass algorithms. This is in contrast with Example 3.4.1 and can be explained by the fact that the penetration measured for the two-half-passes is similar for a given pair of patches in contact (see Fig. 3.17). Thus the erroneous effect in results of Example 3.4.1 does not occur in this test case. The deformed structure in the final configuration in Fig. 3.15b is practically the same for the single or two-half-pass algorithms.

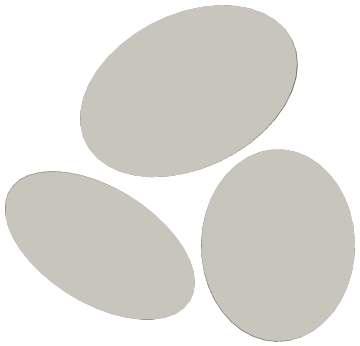

Figure 3.14: Example 2: View in plane $(\mathbf{E}_1, \mathbf{E}_2)$ of the aligned beams in the undeformed configuration. Beam A is at the bottom right, beam B the bottom left, and beam C on top.

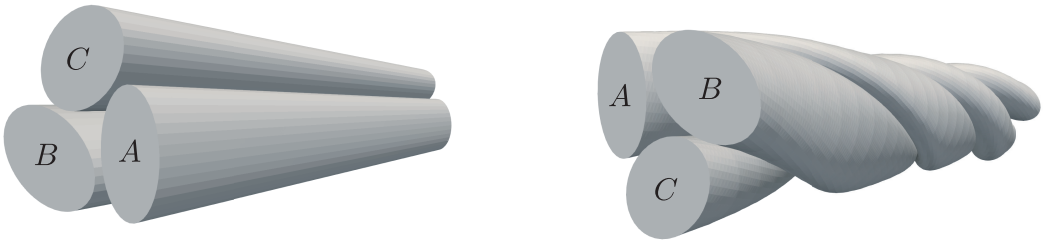

(a) Initial. (b) Final.

Figure 3.15: Example 3.4.2: Initial and final configuration.

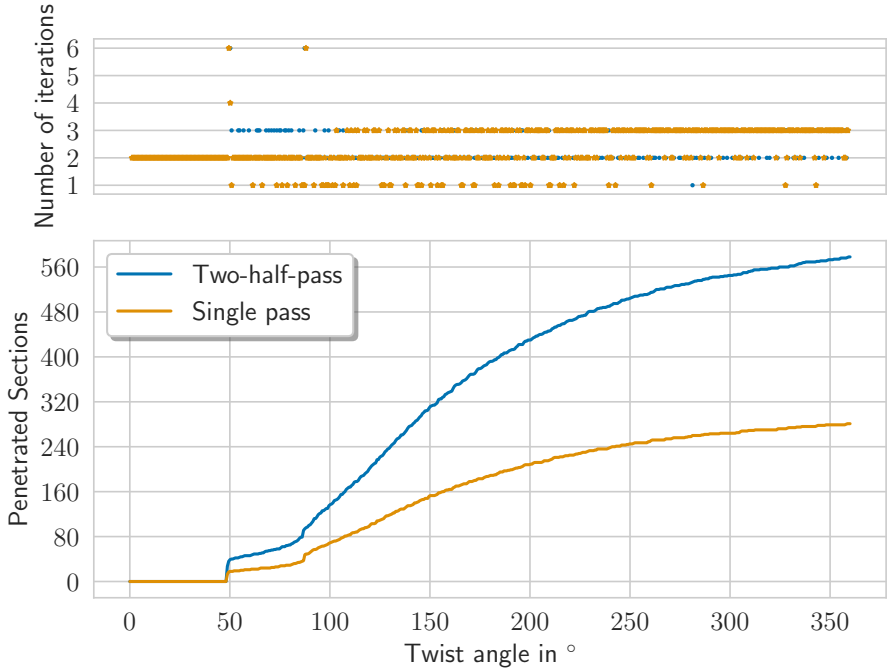

Figure 3.16: Example 3.4.2: evolution of the number of penetrated sections and number of global iterations necessary to converge. For small twist angles, the beams are not in contact due to the small initial separations between them (see Fig. 3.15). The convergence criterion for the global problem is set as $\left\|\underline{r}_g^{free}\right\| < 10^{-8}$.

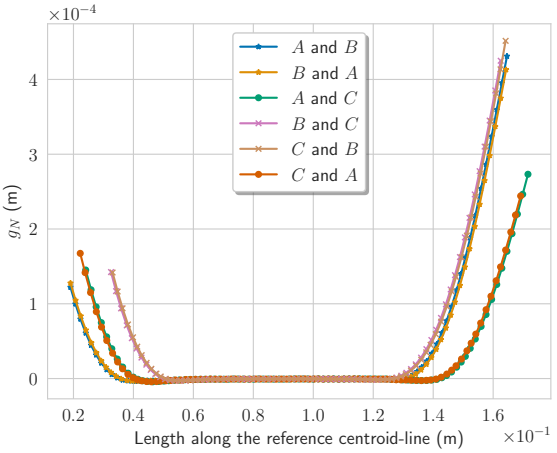

Two-half-pass. Half of the loading.

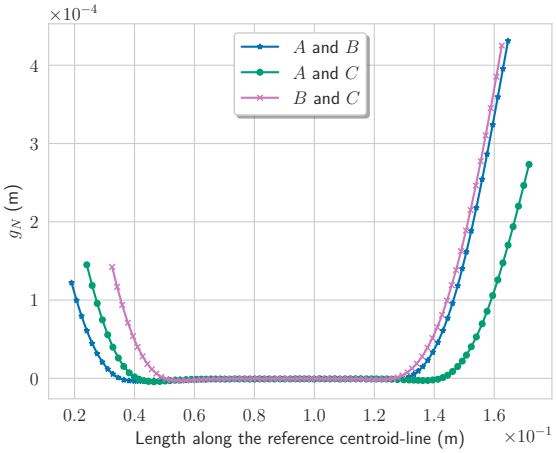

Single-pass. Half of the loading.

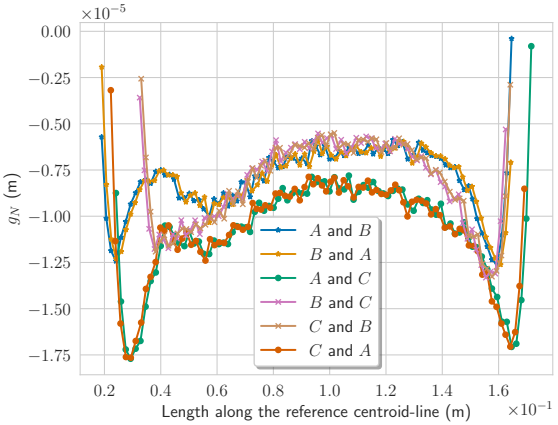

Two-half-pass. End of the loading.

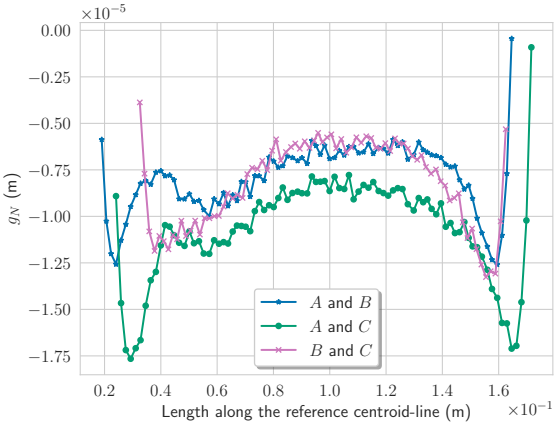

Single-pass. End of the loading.

Figure 3.17: Example 3.4.2: evolution of g_N along the slave centroid-line measured for the different couples of beams in contact for two-half-pass and single-pass approaches, for half of the loading and at the end of the loading.

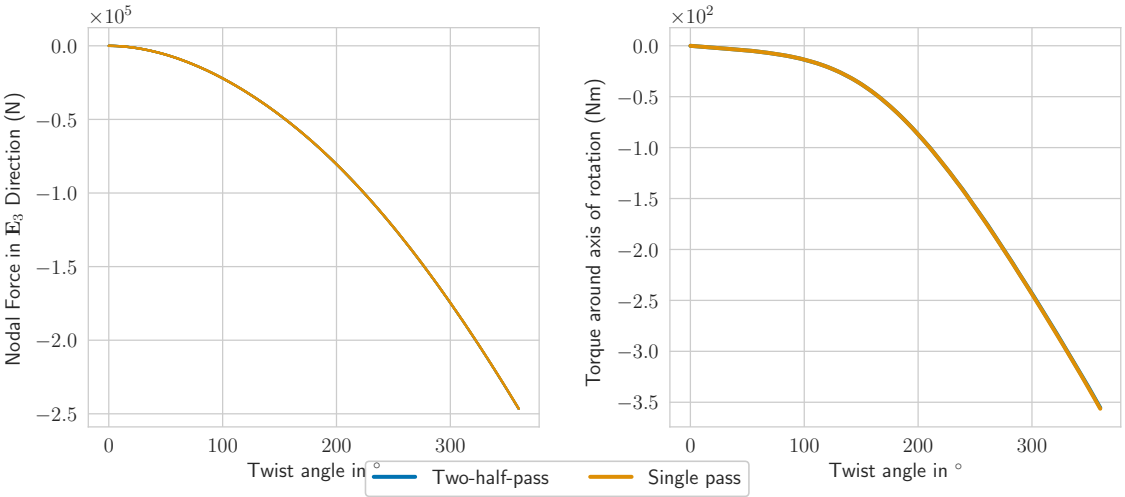

Figure 3.18: Example 3.4.2: reaction force and torque obtained by summing the contributions of nodes of the different beams subject to BCs for a single-pass and two-half-pass algorithms. For this example, no oscillations are present for the two-half-pass.

3.4.3 Example 3: bending of a rope

The last example considers a rope-like structure (see Figs 3.19 and 3.20a). It consists of seven wires (beams) in total; six are wrapped around a central beam that is initially straight. The centroid-lines of the outer beams are parametrised helices [80] in the undeformed configuration. In the undeformed configuration, the beams are slightly detached. The applied BCs are as follows:

1. The sections at the end of the rope undergo a rotation of $\pm\frac{\pi}{4}$ around the $[0,1,0]^T_{\mathbf{E}_i}$ axis. This rotation is applied in 1000 equally spaced increments,
2. the nodes in the center of the rope do not displace but are free to rotate.

All beams are given a Young's modulus of 100 GPa, a Poisson's ratio of 0.3, they are discretized using 89 BFEs and their cross-sections are elliptical with semi-axes of 0.3 m and 0.23 m. The rope has a length of 3 m. A single-pass algorithm is employed. Despite the large number of contact interactions and the substantial deformations, only a few (global) iterations are necessary to converge (see Fig. 3.21). This is thanks to the proper linearization of the contact residual obtained using the Automatic Differentiation technique. Three-dimensional views of the initial and final configurations of the structure are shown in Fig. 3.20. The reaction torque and forces are reported in Fig. 3.22.

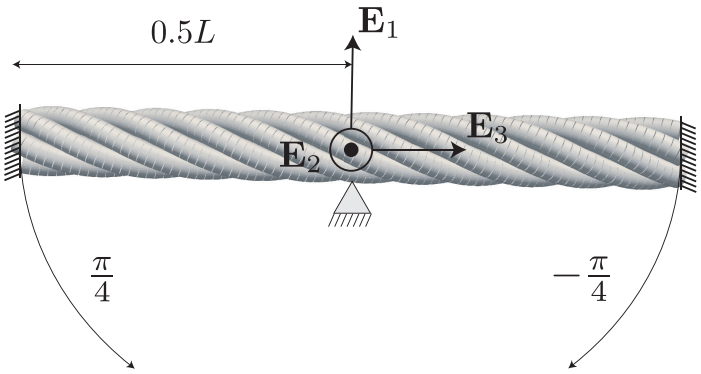

Figure 3.19: Example 3.4.3: Setup. Sections at both ends of the rope are rotated around the $\mathbf{E}_2$ axis. The displacements of the nodes in the center of the rope are restrained but not their rotations.

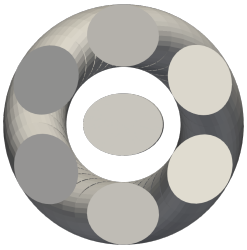

(a) Initial configuration, sectional view.

(b) Initial configuration.

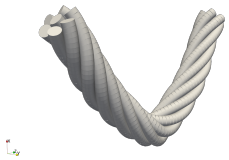

(c) Final configuration.

Figure 3.20: Example 3.4.3: Reference and final configurations of the structure. The discontinuous surface of the strings of BFEs, that is improper for contact treatment, is shown. On the right, one can observe the effect of the rotations applied to the sections at the ends of the rope.

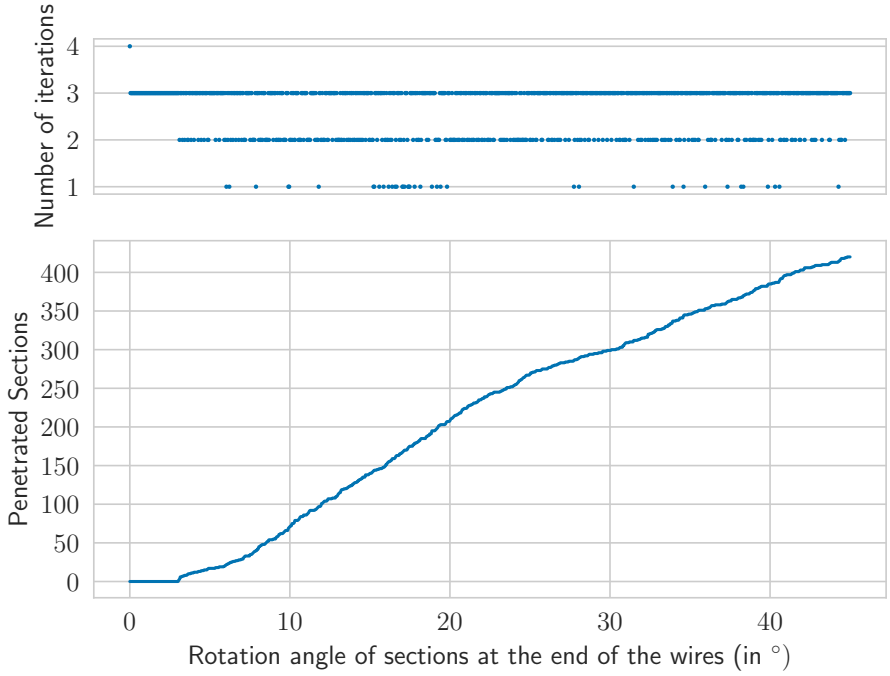

Figure 3.21: Example 3.4.3: Evolution of the number of penetrated sections and number of global iterations necessary to converge. The convergence criterion for the global problem is set as $\left\|\underline{r}_g^{free}\right\| < 10^{-8}$.

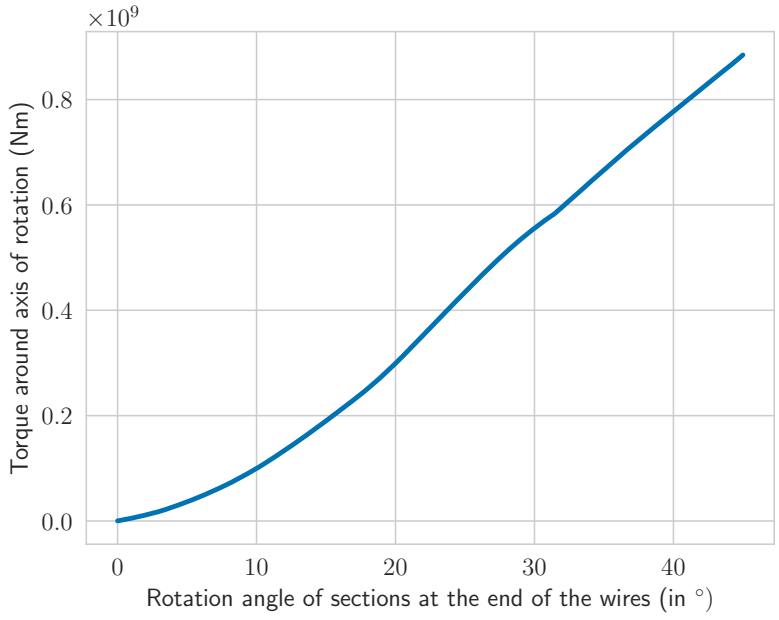

(a) Reaction torque.

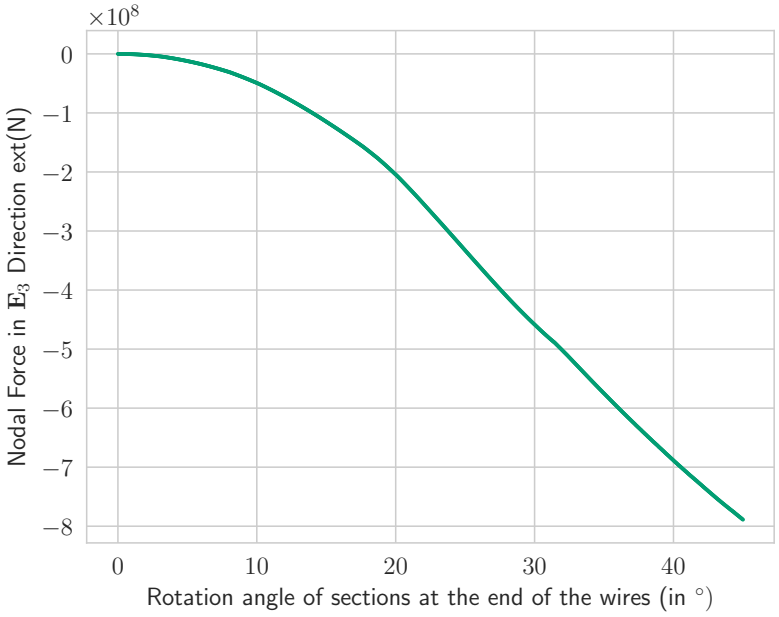

(b) Reaction force.

Figure 3.22: Example 3.4.3: Reaction torque and force at one end of the rope.

3.5 Conclusion

In this contribution, we have introduced an efficient methodology to treat non-localized contact between shear deformable beams with circular and elliptical sections. It treats contact between parallel or almost-parallel beams for which contact interactions cannot be applied at a single pair of surface points. As the presented framework only quantifies penetration once per slave cross-section, it is considerably more efficient than our previous scheme [54] in which the slave surface needs to be seeded with points.

To numerically approximate the contact area, pairs of surface points are determined along the axial direction of the beams in contact. To this end, several cross-sections are considered along one of the contacting beams. For each section, a measure of penetration is computed. The surface of the beams is explicitly used to formulate the contact kinematics. This makes the framework not only applicable to (shear-deformable and shear-undeformable) beams with circular cross sections, but also to beams with elliptical cross-sections. The proposed framework may therefore be considered as an attempt to generalize the "line-to-line" contact scheme of Meier et al. [59] that also treats non-localized contact, but is limited to shear-rigid (Kirchhoff) beams with circular sections.

We have also introduced two approaches to quantify the normal gap. In the first approach it is computed using the minimisation of an objective function. In the second approach it is obtained by solving a set of equations. The first approach requires third order surface derivatives and a lengthier code and is consequently 10-20% slower than the second approach.

The introduced contact framework is a master-slave approach. To overcome the bias introduced in the treatment of contact, we have investigated the "two-half-pass" algorithm and compared it to the classical "single-pass approach". We have observed that the measure of penetration for the two-half-passes can be significantly different, which yields oscillations of the reaction forces. The sum of the reaction forces do not vanish anymore in these cases.

The introduced scheme is well suited to detect non-localised contact (for beams

whose centroid-line is parallel or almost parallel), but it is not appropriate to detect localised contact. A scheme that combines our approach for non-localized contact and the scheme of Gay Neto et al. [24, 25] for localized contact may thus be able to treat more general scenarios. The formulation of such a combined scheme in a variationally consistent manner, as the ABC formulation of Meier et al. [62] for beams with circular cross-sections, is however out of the scope of this work and remains for future work.

Appendix

III.A Variations

In the following, variations of different quantities are derived. These are needed to obtain contact residual $\underline{r}_c$ and its linearisation yielding contact stiffness matrix $\underline{\underline{K}}_c$. All quantities used in this section are computed at the solution of the projection problem.

III.A.1 Variations of the local parameters

Variations of local parameters $\delta\bar{\underline{q}}$ with respect to variations of the kinematic variables in $\delta\underline{p}^{\mathrm{IJ}}$ will be needed in the following. To determine $\delta\bar{\underline{q}}$, we start from the stationarity of the local residual (from Eq. (3.13) or Eq. (3.21)) with respect to $\underline{p}^{\mathrm{IJ}}$ as follows:

$$\frac{d\underline{f}}{d\underline{p}^{\mathrm{IJ}}} = \left(\frac{\partial \underline{f}}{\partial \underline{p}^{\mathrm{IJ}}}\right)\delta\underline{p}^{\mathrm{IJ}} + \left(\frac{\partial \underline{f}}{\partial \underline{q}}\Big|_{\underline{q}=\bar{\underline{q}}}\right)\delta\bar{\underline{q}} = \underline{0}. \tag{3.48}$$

After rearrangement, we obtain:

$$\delta\bar{\underline{q}} = -\left(\underline{\underline{H}}^{-1}\frac{\partial \underline{f}}{\partial \underline{p}^{\mathrm{IJ}}}\right)\delta\underline{p}^{\mathrm{IJ}} = \underline{\underline{A}}\delta\underline{p}^{\mathrm{IJ}}. \tag{3.49}$$

III.A.2 Variation of the length-specific contact potential

If a penalty approach is employed, the virtual work of the contact force is given by Eq. (3.24). Whether approach I or II is employed, the variation of the measure of

penetration, δg_N, is needed. At the solution of the local problem, we have $g_N = \bar{\mathbf{g}} \cdot \bar{\mathbf{n}}^{\mathrm{I}}$, such that we can write:

$$\delta g_N = \delta \bar{\mathbf{g}} \cdot \bar{\mathbf{n}}^{\mathrm{I}} + \bar{\mathbf{g}} \cdot \delta \bar{\mathbf{n}}^{\mathrm{I}}. \tag{3.50}$$

The variations $\delta \bar{\mathbf{g}}$ and $\delta \bar{\mathbf{n}}^{\mathrm{I}}$ are detailed next.

III.A.2.1 $\delta \bar{\mathbf{g}}$ and $\delta \bar{\mathbf{n}}^{\mathrm{I}}$

Vector $\bar{\mathbf{g}}$ depends on the kinematics variables of both beams in contact, but also on $\underline{q}$, which in turn depends again on the kinematic variables of both beams. Its variation can be written as:

$$\delta \bar{\mathbf{g}} = \frac{\partial \bar{\mathbf{g}}}{\partial \underline{p}^{\mathrm{IJ}}} \delta \underline{p}^{\mathrm{IJ}} + \frac{\partial \bar{\mathbf{g}}}{\partial \underline{q}} \delta \underline{q} = \left(\frac{\partial \bar{\mathbf{g}}}{\partial \underline{p}^{\mathrm{IJ}}} + \frac{\partial \bar{\mathbf{g}}}{\partial \underline{q}} \underline{\underline{A}} \right) \delta \underline{p}^{\mathrm{IJ}} = \frac{\hat{\partial} \bar{\mathbf{g}}}{\hat{\partial} \underline{p}^{\mathrm{IJ}}} \Big|_{\frac{\partial \underline{q}}{\partial \underline{p}^{\mathrm{IJ}}} = \underline{\underline{A}}}. \tag{3.51}$$

In a similar fashion, $\delta \bar{\mathbf{n}}^{\mathrm{I}}$ reads:

$$\delta \bar{\mathbf{n}}^{\mathrm{I}} = \left(\frac{\partial \bar{\mathbf{n}}^{\mathrm{I}}}{\partial \underline{p}^{\mathrm{IJ}}} \right) \delta \underline{p}^{\mathrm{IJ}} + \left(\frac{\partial \bar{\mathbf{n}}^{\mathrm{I}}}{\partial \underline{q}} \right) \delta \underline{q} = \left(\frac{\partial \bar{\mathbf{n}}^{\mathrm{I}}}{\partial \underline{p}^{\mathrm{IJ}}} + \frac{\partial \bar{\mathbf{n}}^{\mathrm{I}}}{\partial \underline{q}} \underline{\underline{A}} \right) \delta \underline{p}^{\mathrm{IJ}} = \frac{\hat{\partial} \bar{\mathbf{n}}^{\mathrm{I}}}{\hat{\partial} \underline{p}^{\mathrm{IJ}}} \Big|_{\frac{\partial \underline{q}}{\partial \underline{p}^{\mathrm{IJ}}} = \underline{\underline{A}}}. \tag{3.52}$$

III.A.2.2 δg_N

Whether Eq. (3.13) or Eq. (3.21) is employed, at the solution of the local problem, the gap vector is in the direction of the normal to the slave surface such that $\bar{\mathbf{g}} = g_N \bar{\mathbf{n}}^{\mathrm{I}}$. Inserting this in the first term of Eq. (3.50) yields:

$$\bar{\mathbf{g}} \cdot \delta \bar{\mathbf{n}}^{\mathrm{I}} = g_N \bar{\mathbf{n}}^{\mathrm{I}} \cdot \delta \bar{\mathbf{n}}^{\mathrm{I}} = 0, \tag{3.53}$$

because $\delta \bar{\mathbf{n}}^{\mathrm{I}} \cdot \bar{\mathbf{n}}^{\mathrm{I}} = 0$ (as $\bar{\mathbf{n}}^{\mathrm{I}} \cdot \bar{\mathbf{n}}^{\mathrm{I}} = 1$, $\delta(\bar{\mathbf{n}}^{\mathrm{I}} \cdot \bar{\mathbf{n}}^{\mathrm{I}}) = 2\delta \bar{\mathbf{n}}^{\mathrm{I}} \cdot \bar{\mathbf{n}}^{\mathrm{I}} = 0$). δg_N then simplifies to:

$$\delta g_N = \delta \bar{\mathbf{g}} \cdot \bar{\mathbf{n}}^{\mathrm{I}}. \tag{3.54}$$

Using Eqs. (3.51) and (3.54),we can now write:

$$\delta\bar{\mathbf{g}}\cdot\bar{\mathbf{n}}^{\mathrm{I}}=\delta\underline{p}^{\mathrm{IJ}}\cdot\frac{\partial\bar{\mathbf{g}}}{\partial\underline{p}^{\mathrm{IJ}}}\cdot\bar{\mathbf{n}}^{\mathrm{I}}+\delta\underline{p}^{\mathrm{IJ}}\cdot\underline{\underline{A}}^{T}\frac{\partial\bar{\mathbf{g}}}{\partial\underline{q}}\cdot\bar{\mathbf{n}}^{\mathrm{I}},\tag{3.55}$$

with:

$$\frac{\partial\bar{\mathbf{g}}}{\partial\underline{q}}=[-\boldsymbol{\tau}_2^{\mathrm{I}},\boldsymbol{\tau}_1^{\mathrm{J}},\boldsymbol{\tau}_2^{\mathrm{J}},\mathbf{0}]^{T},\tag{3.56}$$

where $\boldsymbol{\tau}_j^i$ denotes the j^{th} tangent vector to the surface of $\mathcal{B}^i$. We can Eq. (3.55) furthermore expand as follows:

$$\frac{\partial\bar{\mathbf{g}}}{\partial\underline{q}}\cdot\bar{\mathbf{n}}^{\mathrm{I}}=[-\boldsymbol{\tau}_2^{\mathrm{I}},\boldsymbol{\tau}_1^{\mathrm{J}},\boldsymbol{\tau}_2^{\mathrm{J}},\mathbf{0}]\cdot\bar{\mathbf{n}}^{\mathrm{I}}=[\mathbf{0},\boldsymbol{\tau}_1^{\mathrm{J}}\cdot\bar{\mathbf{n}}^{\mathrm{I}},\boldsymbol{\tau}_2^{\mathrm{J}}\cdot\bar{\mathbf{n}}^{\mathrm{I}},\mathbf{0}]^{T}=\frac{\partial\bar{\mathbf{x}}^{\mathrm{J}}}{\partial\underline{q}}\cdot\bar{\mathbf{n}}^{\mathrm{I}},\tag{3.57}$$

which shows that at the solution of the local problem, $\frac{\partial\bar{\mathbf{x}}^{\mathrm{I}}}{\partial\underline{q}}\cdot\bar{\mathbf{n}}^{\mathrm{I}}=\underline{0}$. In other words, term $\delta\bar{\mathbf{x}}^{\mathrm{I}}\cdot\bar{\mathbf{n}}^{\mathrm{I}}$, appearing in $\delta g_N=\delta\bar{\mathbf{g}}\cdot\bar{\mathbf{n}}^{\mathrm{I}}=\delta\bar{\mathbf{x}}^{\mathrm{J}}\cdot\bar{\mathbf{n}}^{\mathrm{I}}-\delta\bar{\mathbf{x}}^{\mathrm{I}}\cdot\bar{\mathbf{n}}^{\mathrm{I}}$ in Eq. (3.54), is independent of the local parameters in $\underline{q}$. Thus, Eq. (3.54) can be further simplified as follows:

$$\begin{aligned}
\delta g_N &= \delta\bar{\mathbf{g}}\cdot\bar{\mathbf{n}}^{\mathrm{I}} && (3.58)\\
&= \delta\bar{\mathbf{x}}^{\mathrm{J}}\cdot\bar{\mathbf{n}}^{\mathrm{I}}-\delta\bar{\mathbf{x}}^{\mathrm{I}}\cdot\bar{\mathbf{n}}^{\mathrm{I}} && (3.59)\\
&= \left(\frac{\hat{\partial}\bar{\mathbf{x}}^{\mathrm{J}}}{\hat{\partial}\underline{p}^{\mathrm{IJ}}}\Big|_{\frac{\partial\underline{q}}{\partial\underline{p}^{\mathrm{IJ}}}=\underline{\underline{A}}}-\frac{\hat{\partial}\bar{\mathbf{x}}^{\mathrm{I}}}{\hat{\partial}\underline{p}^{\mathrm{IJ}}}\Big|_{\frac{\partial\underline{q}}{\partial\underline{p}^{\mathrm{IJ}}}=\underline{\underline{0}}}\right)\cdot\bar{\mathbf{n}}^{\mathrm{I}} && (3.60)\\
&= \delta\underline{p}^{\mathrm{IJ}}\cdot\underline{b}. && (3.61)
\end{aligned}$$

III.B Newton-Raphson scheme for projection problem

As mentioned in Section 3.2, a projection problem must be solved for each section to determine if it penetrates the master surface or not. The equations to solve are Eqs. (3.13) or (3.21), and they must be solved iteratively. A Newton-Raphson scheme is usually employed to this end, which we detail here. In the following, a left superscript indicates the iteration of the (local) nonlinear problem to be solved.

The Newton-Raphson scheme relies on the linearization of the local residual in $\underline{f}$. At (local) iteration j, this linearization reads:

$$^{(j)}\underline{f} +^{(j)} \underline{\underline{H}}\, ^{(j)}\triangle\underline{\bar{q}} = \mathbf{0}, \tag{3.62}$$

with:

$$^{(j)}\underline{f} \leftarrow \frac{\partial(^{(j)}\mathrm{f})}{\partial(^{(j)}\underline{q})}, \tag{3.63}$$

if Eq. (3.13) is used, or:

$$^{(j)}\underline{f} \leftarrow \left[^{(j)}\mathbf{f}_1, ^{(j)}f_2\right], \tag{3.64}$$

if Eq. (3.21) is employed. The Jacobian is also needed:

$$^{(j)}\underline{\underline{H}} \leftarrow \frac{\partial(^{(j)}\underline{f})}{\partial(^{(j)}\underline{q})}. \tag{3.65}$$

$^{(j)}\triangle\underline{\bar{q}}$ is the correction to the estimate solution. It is used to compute the new estimate as follows:

$$^{(j+1)}\underline{q} \leftarrow ^{(j)}\underline{q} + ^{(j)}\triangle\underline{\bar{q}}. \tag{3.66}$$

This updating procedure is repeated until convergence is achieved. The pseudo-algorithm is given in Algorithm 1.

III.C Convergence table for mesh C, Example 1

From a theoretical point of view, because of the consistent linearization of the contact virtual work performed with Automatic Differentiation, we expect a quadratic convergence rate for $\underline{r}_g$. The following show such an evolution for the three integration strategies tested in the first numerical example (see Sec. 3.4.1) with the finest mesh (mesh C).

Algorithm 1 Pseudo-algorithm to iteratively solve the projection problem (Eq. (3.13) or Eq. (3.21))

$\varepsilon \leftarrow 10^{-10}$
$j \leftarrow 0$
${}^{(j)}\underline{q} \leftarrow$ first guess
$res \leftarrow \varepsilon + 1$
while $res > \varepsilon$ **do**
  compute ${}^{(j)}\underline{f}$
  compute ${}^{(j)}\underline{\underline{H}}$
  ${}^{(j)}\triangle\underline{\bar{q}} \leftarrow \left(-{}^{(j)}\underline{\underline{H}}\right)^{-1} {}^{(j)}\underline{f}$
  ${}^{(j+1)}\underline{q} \leftarrow {}^{(j)}\underline{q} + {}^{(j)}\triangle\underline{\bar{q}}$
  $res \leftarrow \left\| {}^{(j)}\underline{f} \right\|$
  $j \leftarrow j + 1$
end while

increment number	iteration number	$\left\|\underline{r}_g^{free}\right\|$
150	1	5.926580071707624950e-04
	2	2.481540346553358163e-07
	3	6.736398127960610256e-13
300	1	7.863796093621699956e-03
	2	1.453563530307313077e-06
	3	5.764187410345059703e-11

Table III.C.1: Example 1: convergence table for mesh C, simple pass.

increment number	iteration number	$\left\|\underline{r}_g^{free}\right\|$
150	1	7.854604647348625499e-03
	2	4.606085537361694276e-06
	3	5.913512181466532264e-10
300	1	7.854604647348625499e-03
	2	4.606085537361694276e-06
	3	5.913512181466532264e-10

Table III.C.2: Example 1: convergence table for mesh C, simple pass with roles of slave and master inverted.

increment number	iteration number	$\|\underline{r}_g^{free}\|$
150	1	3.019595298099190736e-02
	2	4.598944684147788462e-05
	3	3.071265914180119654e-09
300	1	8.046983975060467004e-03
	2	7.931955555476486125e-05
	3	1.964167114903565962e-09

Table III.C.3: Example 1: convergence table for mesh C, two half-pass.

CHAPTER IV

Beam-inside-beam contact: Mechanical simulations of slender medical instruments inside the human body[1]

4.1 Introduction

Mechanical simulations of surgical interventions can be used to train surgeons, reveal patient-specific complications that may occur during surgery and plan interventions patient-specifically. In the future, mechanical simulations of surgical interventions may even be used to optimize medical instruments for each patient (*e.g.* shape and stiffness) and be exploited to autonomously perform interventions.

Numerous frameworks to numerically simulate surgical interventions can be found in the literature. For instance, one set of frameworks simulates cutting through soft tissues in real-time [13, 64, 90, 15, 14] to provide haptic feedback to the trainee performing the "intervention". Another set of approaches aims to simulate the insertion of needles [17, 2, 12, 19, 76]. These frameworks may also be used to provide haptic feedback and/or to help to accurately steer the needle to the target of interest during surgery.

[1]Reproduced from: M. Magliulo, J. Lengiewicz, A. Zilian, Beex L. A. A., Beam-inside-beam contact: Mechanical simulations of slender medical instruments inside the human body, Computer Methods and Programs in Biomedicine. Submitted for publication.

However, the framework presented in this contribution focuses on mechanical simulations that involve the insertion (or removal) of a slender medical instrument inside a tubular structure such as an artery, the cochlea or another slender instrument such as a catheter. In other words, our simulations do not involve the damaging of tissues due to cutting or needle insertion. The aim of this contribution is not to target one type of intervention in particular, but to present the first mechanically consistent formulation that can handle contact between one slender deformable body inside another slender deformable body, if both bodies are represented by beams.

Thus, the proposed framework is similar to the frameworks presented in [1, 49, 18, 27, 83] in which the insertion of guide-wires and catheters in arteries and the insertion of slender implants in the human cochlea are simulated. The difference between the proposed framework and the frameworks of [1, 49, 18, 27, 83] is that our framework represents both the slender medical instrument and the tubular structure as beams, whereas the frameworks of [1, 49, 18, 27, 83] only represent the slender medical instrument with beams whilst conventional 3D finite elements are used to represent the tubular structure.

A wide variety of schemes to handle contact between beams can be distinguished in the literature. All existing "beam-to-beam" contact frameworks are formulated to repel penetrating beams. Several of these beam-to-beam contact frameworks are only applicable if the beams' cross-sections are circular, shear deformations are ignored and the contact area remains small, since unilateral contact conditions are enforced at the closest pair of centroid points [89, 95, 62]. Thus, if two beams collide, a contact force is applied at the closest pair of centroid points to repel the two beams. If the beams' cross-sections are elliptical, the consideration of the centroid-lines alone is insufficient to determine the contact locations. Instead, contact forces must be applied at the closest pair of surface points where the tangent planes of the contacting surfaces are parallel. This was demonstrated by Gay Neto et al. [24, 25] for frictionless and frictional cases, respectively.

Furthermore, in case of non-localized contact (e.g. for parallel beams in contact), the assumption of point-wise contact does not hold. Meier et al. [59] have therefore proposed a contact framework to handle non-localized beam-to-beam contact, but

the cross-sectional shape is restricted to (rigidly) circular and shear deformation is not accounted for. These restrictions enable quantifying the penetration solely using the centroid-lines of the beams, which yields rapid simulations.

Magliulo et al. [53, 54] presented other master-slave frameworks for beam-to-beam contact applicable to both shear-deformable and shear-undeformable beams, with both circular as well as elliptical cross-sections. Both schemes consider the beam's surfaces explicitly, which has resulted in wider applicability than the scheme of Meier et al. [59], albeit at the expense of the simulation speed. A two-half pass algorithm was furthermore formulated in [54] to remove the bias of master-slave approaches for beam-to-beam contact, but with limited benefits for the results.

The beam conglomerates of interest to this contribution differ from the aforementioned works [53, 54], since the focus is on "beam-inside-beam" contact instead of "beam-to-beam" contact. In other words, the beams must remain embedded for the beam conglomerates of interest in our contribution, whereas existing beam-to-beam contact frameworks repel penetrating beams. The measure of penetration in our beam-inside-beam framework, on the other hand, shows similarities with the measure of penetration for the "beam-to-beam" contact framework of [53]. Penetration is measured between sections distributed along the inner beam and the interior surface of the outer beam. In case of contact, unilateral constraints are regularized with the penalty method, which brings compliance to the otherwise rigid cross-sections.

The outline of the remainder of this contribution is as follows. In Section 4.2, the contact framework is presented in the space-continuous setting along with the associated contact virtual work. Also in this section, spatial discretization applied to the finite element method is discussed. Contact kinematics and the contact virtual work are subsequently discretized. Implementation details are also included. The numerical examples of Section 4.3 indicate the promising capabilities of the contact framework. Section 4.4 discusses possible extensions and concludes this contribution.

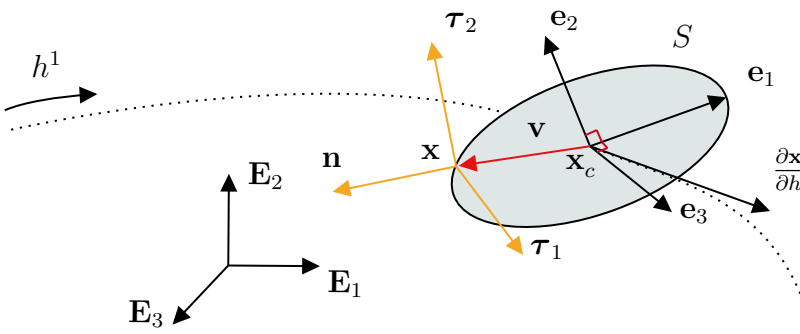

Figure 4.1: Beam kinematics for current configuration. The beam's centroid-line is presented with a dashed line. Local basis vector $\mathbf{e}_3$ is not aligned with the vector tangent to the centroid-line $\frac{\partial \mathbf{x}_c}{\partial h^1}$ due to shear deformation. A typical vector $\mathbf{v}$ lying on $\mathcal{C}$ (grey ellipse) is presented with a red arrow.

4.2 Methods

4.2.1 Space-continuous contact formulation

The contact kinematics employed in this contribution are presented in this section [24, 25, 53, 54]. First, the beam's surface parametrization is explained. Then, the procedure to quantify penetration is detailed. The formulation of the contact virtual work is presented for a penalty approach.

4.2.1.1 Parametrization of the surface

The geometrically exact beam (GEB) Simo-Reissner theory [16, 79, 72, 78, 61, 29, 30] is used in this contribution. This entails that the beams are shear-deformable and that rigid cross-sections are considered, which cannot warp.

The surface of beam $\mathcal{B}$ is parameterized with two convective parameters $\underline{h} = [h^1, h^2]^T$. $h^1 \in [0, L]$, denotes the arc-length parameter of the beam's centroid line $\mathbf{x}_{0c} : (0, L) \to \mathbb{R}^3$ while $h^2 \in [0, 2\pi]$ is a circumferential parameter of the perimeter of cross-section $\mathcal{C}$ attached to $\mathbf{x}_{0c}(h^1)$ (see [24] and Fig. 4.1). L denotes the initial length of the beam. The location of a surface point in the undeformed configuration

in the global coordinate system, $\mathbf{x}_0$, can be obtained from:

$$\mathbf{x}_0(\underline{h}) = \mathbf{x}_{0c}(h^1) + \mathbf{v}_0(\underline{h}), \tag{4.1}$$

where $\mathbf{v}_0$ denotes a vector contained in $\mathcal{C}$. Here, we assume that $\mathbf{v}_0$ always connects $\mathbf{x}_{0c}$ to a surface point. In case $\mathcal{C}$ is elliptical, $\mathbf{v}_0$ can be expressed as:

$$\mathbf{v}_0(\underline{h}) = a\cos(h^2)\mathbf{e}_{01}(h^1) + b\sin(h^2)\mathbf{e}_{02}(h^1), \tag{4.2}$$

where a and b denote the dimensions of the elliptical cross-sections in its principal directions. $\mathbf{e}_{01}$ and $\mathbf{e}_{02}$ are orthonormal basis vectors of the plane containing $\mathcal{C}$. $\mathbf{e}_{03}$ denotes the normal vector to $\mathcal{C}$. The triad $\{\mathbf{e}_{01}, \mathbf{e}_{02}, \mathbf{e}_{03}\}$ forms an orthonormal basis.

Due to the hypothesis of rigid sections, the location of the same material point in the deformed configuration can similarly be obtained from:

$$\mathbf{x}(\underline{h}) = \varphi(\mathbf{x}_0(\underline{h})) = \mathbf{x}_c(h^1) + \mathbf{v}(\underline{h}), \tag{4.3}$$

where:

$$\mathbf{x}_c = \mathbf{x}_{0c} + \mathbf{u}, \tag{4.4}$$

denotes the location of the centroid point in the deformed configuration. $\mathbf{u} : (0, L) \to \mathbb{R}^3$ denotes the centroid-line's displacement. φ denotes the deformation mapping relating the current location of a point to its location in the undeformed configuration such that $\mathbf{x}(\underline{h}) = \varphi(\mathbf{X}(\underline{h}))$. $\mathbf{v}$ is obtained from:

$$\mathbf{v}(\underline{h}) = \mathbf{\Lambda}(h^1) \cdot \mathbf{v}_0(\underline{h}) = a\cos(h^2)\mathbf{e}_1 + b\sin(h^2)\mathbf{e}_2, \tag{4.5}$$

where $\mathbf{\Lambda} : (0, L) \to SO(3)$, with $SO(3)$ the rotation group, is a rotation tensor that rotates $\mathbf{e}_{0i}$ to $\mathbf{e}_i$ for $i \in \{1, 2, 3\}$. Because shear deformation can be present, $\mathbf{e}_3$ is not necessarily aligned with the tangent to the centroid-line (see Fig. 4.1). In such cases, *i.e.*:

$$\mathbf{e}_3 \times \frac{\partial \mathbf{x}_c}{\partial h^1} \neq \mathbf{0}, \tag{4.6}$$

where $\times$ denotes the cross product.

For further use, we define two (covariant) tangent vectors to the surface of $\mathcal{B}$ at $\mathbf{x}(\underline{h})$, denoted by $\boldsymbol{\tau}_1 = \frac{\partial \mathbf{x}}{\partial h^1}$ and $\boldsymbol{\tau}_2 = \frac{\partial \mathbf{x}}{\partial h^2}$ (see Fig. 4.1). In general, $\boldsymbol{\tau}_1$ and $\boldsymbol{\tau}_2$ are not orthogonal to each other.

4.2.1.2 Contact Kinematics

We focus here on a system consisting of two bodies: $\mathcal{B}^{\mathrm{I}}$ denotes the thin inner beam and $\mathcal{B}^{\mathrm{J}}$ denotes the hollow outer beam. We assume here that both $\mathcal{B}^{\mathrm{I}}$ and $\mathcal{B}^{\mathrm{J}}$ are modeled as a GEB with plain and hollow cross-sections, respectively. We denote by $\partial\mathcal{B}^{\mathrm{J}}$ the *interior* surface of $\mathcal{B}^{\mathrm{J}}$.

To quantify the penetration of $\mathcal{B}^{\mathrm{I}}$ with $\partial\mathcal{B}^{\mathrm{J}}$, and to quantify the contact area over which this penetration occurs, we:

1. Seed sections along the centroid-line of $\mathcal{B}^{\mathrm{I}}$ (see Fig. 4.3),

2. For each seeded section, we solve a projection (local) problem to determine if it penetrates $\partial\mathcal{B}^{\mathrm{J}}$ and if so, by how much. This projection problem yields two surface points: one on the perimeter of the seeded section and one on $\partial\mathcal{B}^{\mathrm{J}}$. These points are used to establish a measure of penetration, which in turn determines the amplitude of the contact forces (if penetration is present).

As $\mathcal{B}^{\mathrm{I}}$ and $\mathcal{B}^{\mathrm{J}}$ have a different role, the proposed framework is a master-slave approach. We call $\mathcal{B}^{\mathrm{I}}$ the slave and $\mathcal{B}^{\mathrm{J}}$ the master [86]. Next, we discuss how to compute if a given section of $\mathcal{B}^{\mathrm{I}}$, denoted by $\mathcal{C}$ with perimeter $\partial\mathcal{C}$, penetrates $\partial\mathcal{B}^{\mathrm{J}}$ and if so, how the amount of penetration is computed.

It must be noted that the proposed contact algorithm can only be used if one contact area occurs for each cross-sections (left in Fig. 4.2). The contact framework can thus not handle scenarios as presented on the right in Fig. 4.2. If the cross-sections of $\mathcal{B}^{\mathrm{I}}$ is perfectly aligned with the cross-sections of $\mathcal{B}^{\mathrm{J}}$, only one contact area occurs if:

$$\frac{(a_{inner})^2}{b_{inner}} < \frac{(b_{outer})^2}{a_{outer}} \qquad a_{inner} \geq b_{inner} \qquad a_{outer} \geq b_{outer}, \tag{4.7}$$

where subscript *inner* refers to the inner beam and subscript *outer* refers to the inner cross-sections of the outer beam.

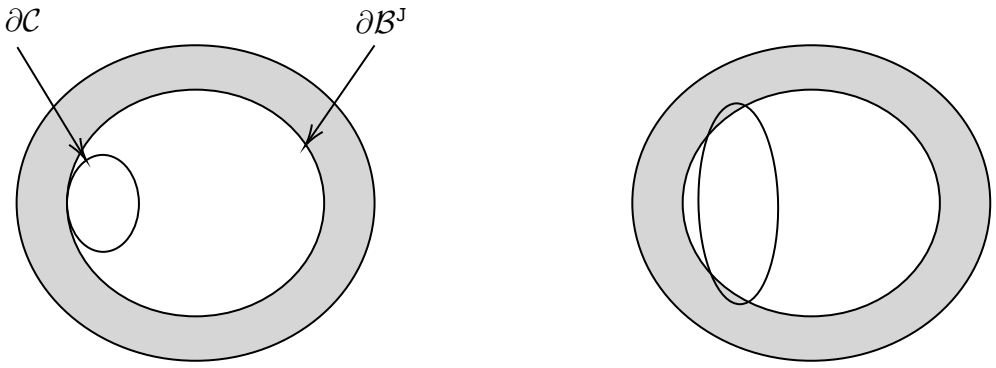

Figure 4.2: Problem of multiple contact areas: (a) single contact area and (b) two contact areas.

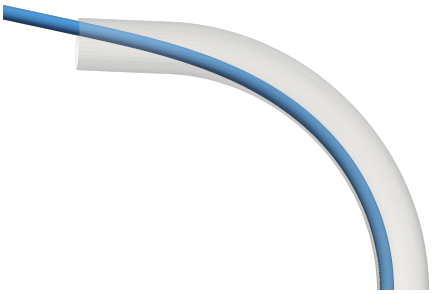

(a) Example of beam-inside-beam contact. The surface of the outer beam is shown in translucent and the one of the inner beam in cyan.

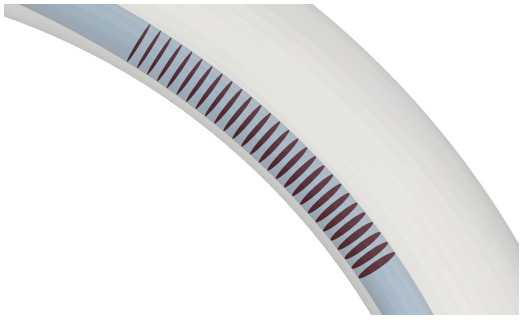

(b) Zoom around the region of contact. The penetrated sections are indicated in red.

Figure 4.3: (a) Two beams in contact. (b) Sections for which penetration has been detected

We now introduce $\mathbf{n}^{\mathrm{I}}$, an outward pointing unit vector normal to $\partial\mathcal{B}^{\mathrm{I}}$. It is defined as follows:

$$\mathbf{n}^{\mathrm{I}}\left(\underline{h}^{\mathrm{I}}\right) = \frac{\boldsymbol{\tau}_1^{\mathrm{I}}(\underline{h}^{\mathrm{I}}) \times \boldsymbol{\tau}_2^{\mathrm{I}}(\underline{h}^{\mathrm{I}})}{\left\|\boldsymbol{\tau}_1^{\mathrm{I}}(\underline{h}^{\mathrm{I}}) \times \boldsymbol{\tau}_2^{\mathrm{I}}(\underline{h}^{\mathrm{I}})\right\|}. \tag{4.8}$$

$\mathbf{n}^{\mathrm{J}}$ on the other hand is the *inward* pointing unit vector normal to $\partial\mathcal{B}^{\mathrm{J}}$. It is defined as follows:

$$\mathbf{n}^{\mathrm{J}}\left(\underline{h}^{\mathrm{J}}\right) = \frac{\boldsymbol{\tau}_1^{\mathrm{J}}(\underline{h}^{\mathrm{J}}) \times \boldsymbol{\tau}_2^{\mathrm{J}}(\underline{h}^{\mathrm{J}})}{\left\|\boldsymbol{\tau}_1^{\mathrm{J}}(\underline{h}^{\mathrm{J}}) \times \boldsymbol{\tau}_2^{\mathrm{J}}(\underline{h}^{\mathrm{J}})\right\|}. \tag{4.9}$$

Local problem and measure of penetration between $\partial\mathcal{C}$ and $\partial\mathcal{B}^{\mathrm{J}}$

We will now investigate if $\mathcal{C}$, the cross-section uniquely defined by convective coordinate $h^{\mathcal{C}}$, penetrates $\partial\mathcal{B}^{\mathrm{J}}$ and if so, by how much. The so-called gap vector $\mathbf{g}$ connects a point on the perimeter of $\mathcal{C}$, $\mathbf{x}^{\mathrm{I}} \in \partial\mathcal{C}$, to a surface point on $\partial\mathcal{B}^{\mathrm{J}}$, $\mathbf{x}^{\mathrm{J}}$:

$$\mathbf{g}(h^{\mathcal{C}}, h^{\mathrm{I2}}, h^{\mathrm{J1}}, h^{\mathrm{J2}}) = \mathbf{x}^{\mathrm{J}}(h^{\mathrm{J1}}, h^{\mathrm{J2}}) - \mathbf{x}^{\mathrm{I}}(h^{\mathcal{C}}, h^{\mathrm{I2}}). \tag{4.10}$$

A local (or projection) problem must now be solved, which yields points $\bar{\mathbf{x}}^{\mathrm{I}}$ and $\bar{\mathbf{x}}^{\mathrm{J}}$, such that an appropriate measure of penetration is established. Four convective coordinates are involved in the local problem: $h^{\mathcal{C}}$, which is fixed, as well as h^{I2}, h^{J1} and h^{J2} that are to be determined.

A possibility to determine the unknown convective coordinates would be to solve an optimization problem by minimizing an objective function. Another possibility [62, 24, 25, 26, 40, 37] is to solve for a set of equations that does not stem from an objective function, generally unilateral or bilateral orthogonality conditions. Previously, we have shown that the latter makes resolution of the local problem 20-30% faster to solve for beam-to-beam contact [53]. We therefore consider a similar approach for the beam-inside-beam contact of this contribution. Three of the equations we solve for are expressed as:

$$\mathbf{f}_1(\underline{\bar{q}}) = \bar{\mathbf{x}}^{\mathrm{J}} - \bar{\mathbf{x}}^{\mathrm{I}} - \bar{g}\bar{\mathbf{n}}^{\mathrm{I}} = \mathbf{0}, \tag{4.11}$$

where:

$$\underline{q} = \left[h^{\mathrm{I2}}, h^{\mathrm{I1}}, h^{\mathrm{J2}}, g\right]^T, \tag{4.12}$$

denotes the array of unknowns. Here and in the following, an overhead bar over a quantity indicates that it is evaluated at the solution of the projection problem. Thus, $\underline{\bar{q}}$ denotes the array solution of Eq. (4.11). The independent variable $\bar{g}$ quantifies

penetration measured in the normal direction, usually denoted as g_N and defined as:

$$g_N = \bar{g} = (\bar{\mathbf{x}}^{\mathrm{J}} - \bar{\mathbf{x}}^{\mathrm{I}}) \cdot \bar{\mathbf{n}}^{\mathrm{I}}. \tag{4.13}$$

As four variables are present for only three equations, the system of Eq. (4.11) is under-determined An additional equation is required. To this end, we introduce plane $\mathcal{P}$ spanned by $\mathbf{n}^{\mathrm{I}}$ and $\boldsymbol{\tau}_2^{\mathrm{I}}$ with the following normal vector:

$$\tilde{\mathbf{n}}^{\mathrm{I}} = \boldsymbol{\tau}_2^{\mathrm{I}} \times \mathbf{n}^{\mathrm{I}}. \tag{4.14}$$

Also, we define $\mathbf{n}^{\mathrm{J}p}$ as the normalized projection of $\mathbf{n}^{\mathrm{J}}$ on $\mathcal{P}$:

$$\mathbf{n}^{\mathrm{J}p} = \frac{\mathbf{n}^{\mathrm{J}} - (\mathbf{n}^{\mathrm{J}} \cdot \tilde{\mathbf{n}}^{\mathrm{I}})\tilde{\mathbf{n}}^{\mathrm{I}}}{\|\mathbf{n}^{\mathrm{J}} - (\mathbf{n}^{\mathrm{J}} \cdot \tilde{\mathbf{n}}^{\mathrm{I}})\tilde{\mathbf{n}}^{\mathrm{I}}\|}. \tag{4.15}$$

At the solution of the local problem, we want $\mathbf{n}^{\mathrm{I}}$ and $\mathbf{n}^{\mathrm{J}p}$ to be orthogonal to $\boldsymbol{\tau}_2^{\mathrm{J}}$ (see Fig. 4.4). This is true if the following equation holds:

$$f_2(\underline{\bar{q}}) = a^{\mathcal{C}}(\bar{\mathbf{n}}^{\mathrm{I}} + \bar{\mathbf{n}}^{\mathrm{J}p}) \cdot \bar{\boldsymbol{\tau}}_2^{\mathrm{J}} = 0, \tag{4.16}$$

where $a^{\mathcal{C}}$ denotes the dimension of $\mathcal{C}$ along its largest semi-axis which is used to scale $\mathbf{f}_1$ such that $\mathbf{f}_1$ and f_2 have the same units. The set of equations to solve for is now abbreviated as follows:

$$\underline{f}(\underline{\bar{q}}) = \left[\mathbf{f}_1(\underline{\bar{q}}), f_2(\underline{\bar{q}})\right]^T = \underline{0}. \tag{4.17}$$

The set of equations to solve for in Eq. (4.17) is nonlinear. To solve it, we apply Newton's method for which we linearise residual $\underline{f}$ which requires the following Jacobian:

$$\underline{\underline{H}}(\underline{q}) \;=\; \frac{\partial \underline{f}}{\partial \underline{q}} = \begin{bmatrix} \frac{\partial \mathbf{f}_1}{\partial \underline{q}} \\ \left(\frac{\partial f_2}{\partial \underline{q}}\right)^T \end{bmatrix}. \tag{4.18}$$

To compute the components of $\underline{\underline{H}}$, we need to introduce the following quantities:

1. Contravariant components $M^{\mathcal{K}ij}$ of $\boldsymbol{M}^{\mathcal{K}}$, the metric tensor of the surface of body $\mathcal{K}$, read:

$$\begin{bmatrix} M^{\mathcal{K}11} & M^{\mathcal{K}12} \\ M^{\mathcal{K}21} & M^{\mathcal{K}22} \end{bmatrix} = \begin{bmatrix} M^{\mathcal{K}}_{11} & M^{\mathcal{K}}_{12} \\ M^{\mathcal{K}}_{21} & M^{\mathcal{K}}_{22} \end{bmatrix}^{-1} = \begin{bmatrix} \boldsymbol{\tau}^{\mathcal{K}}_1 \cdot \boldsymbol{\tau}^{\mathcal{K}}_1 & \boldsymbol{\tau}^{\mathcal{K}}_1 \cdot \boldsymbol{\tau}^{\mathcal{K}}_2 \\ \boldsymbol{\tau}^{\mathcal{K}}_2 \cdot \boldsymbol{\tau}^{\mathcal{K}}_1 & \boldsymbol{\tau}^{\mathcal{K}}_2 \cdot \boldsymbol{\tau}^{\mathcal{K}}_2 \end{bmatrix}^{-1}. \tag{4.19}$$

2. The second order surface derivatives:

$$\boldsymbol{\tau}^{\mathcal{K}}_{ij} = \frac{\partial \boldsymbol{\tau}^{\mathcal{K}}_i}{\partial h^{\mathcal{K}}_j}. \tag{4.20}$$

3. The covariant components of curvature tensor $\boldsymbol{C}^{\mathcal{K}}$:

$$C^{\mathcal{K}}_{ij} = \boldsymbol{\tau}^{\mathcal{K}}_{ij} \cdot \mathbf{n}^{\mathcal{K}} \tag{4.21}$$

4. Weingarten's formula:

$$\frac{\partial \mathbf{n}^{\mathcal{K}}}{\partial h_j} = -M^{\mathcal{K}jk} C^{\mathcal{K}}_{ki} \boldsymbol{\tau}^{\mathcal{K}}_j. \tag{4.22}$$

Making use of Eq. (4.22), the partial derivatives of $\mathbf{f}_1$ with respect to $\underline{q}$ in Eq. (4.18) yield:

$$\frac{\partial \mathbf{f}_1}{\partial \underline{q}} = \left[\frac{\partial \mathbf{f}_1}{\partial h^{\mathtt{I}2}}, \frac{\partial \mathbf{f}_1}{\partial h^{\mathtt{J}1}}, \frac{\partial \mathbf{f}_1}{\partial h^{\mathtt{J}2}}, \frac{\partial \mathbf{f}_1}{\partial g} \right] = \left[-\boldsymbol{\tau}^{\mathtt{I}}_2 + g\left(M^{\mathtt{I}jk} C^{\mathtt{I}}_{k2} \boldsymbol{\tau}^{\mathtt{I}}_j\right), \boldsymbol{\tau}^{\mathtt{J}}_1, \boldsymbol{\tau}^{\mathtt{J}}_2, -\mathbf{n}^{\mathtt{I}} \right]. \tag{4.23}$$

The differentiation of f_2 with respect to $\underline{q}$ gives:

$$\frac{\partial f_2}{\partial \underline{q}} = \left[\tfrac{\partial f_2}{\partial h^{\mathtt{I}2}}, \tfrac{\partial f_2}{\partial h^{\mathtt{J}1}}, \tfrac{\partial f_2}{\partial h^{\mathtt{J}2}}, \tfrac{\partial f_2}{\partial g} \right]^T. \tag{4.24}$$

Corresponding expressions are more complicated, in particular because $\mathbf{n}^{\mathtt{J}p}$ depends on $h^{\mathtt{I}2}, h^{\mathtt{J}1}$ and $h^{\mathtt{J}2}$.

We now rewrite $\mathbf{n}^{\mathtt{J}p}$ as:

$$\mathbf{n}^{\mathtt{J}p} = \frac{\mathbf{N}^{\mathbf{n}^{\mathtt{J}p}}}{l^{\mathbf{n}^{\mathtt{J}p}}}, \tag{4.25}$$

where:

$$\mathbf{N}^{\mathbf{n}^{\mathtt{J}p}} = \mathbf{n}^{\mathtt{J}} \cdot (\boldsymbol{I} - \tilde{\mathbf{n}}^{\mathtt{I}} \otimes \tilde{\mathbf{n}}^{\mathtt{I}}) = \mathbf{n}^{\mathtt{J}} \cdot \boldsymbol{D}, \tag{4.26}$$

and:

$$l^{\mathbf{n}^{\mathtt{J}p}} = \left\| \mathbf{N}^{\mathbf{n}^{\mathtt{J}\mathbf{p}}} \right\|. \tag{4.27}$$

The partial derivative of $\mathbf{n}^{\mathtt{J}p}$ with respect to the k^{th}-surface parameter of body $\mathtt{1}$ reads:

$$\frac{\partial \mathbf{n}^{\mathtt{J}p}}{\partial h^{\mathtt{1}k}} = \frac{1}{l^{\mathbf{n}^{\mathtt{J}p}}} \left(\mathbf{I} - \mathbf{n}^{\mathtt{J}\mathbf{p}} \otimes \mathbf{n}^{\mathtt{J}\mathbf{p}} \right) \cdot \frac{\partial \mathbf{N}^{\mathbf{n}^{\mathtt{J}\mathbf{p}}}}{\partial h^{\mathtt{1}k}} = \boldsymbol{E} \cdot \frac{\partial \mathbf{N}^{\mathbf{n}^{\mathtt{J}\mathbf{p}}}}{\partial h^{\mathtt{1}k}}, \tag{4.28}$$

where:

$$\begin{aligned}
\frac{\partial \mathbf{N}^{\mathbf{n}^{\mathtt{J}\mathbf{p}}}}{\partial h^{\mathtt{1}k}} &= \frac{\partial \mathbf{n}^{\mathtt{J}}}{\partial h^{\mathtt{1}k}} \cdot \boldsymbol{D} - \mathbf{n}^{\mathtt{J}} \cdot \frac{\partial \boldsymbol{D}}{\partial h^{\mathtt{1}k}} \\
&= \frac{\partial \mathbf{n}^{\mathtt{J}}}{\partial h^{\mathtt{1}k}} \cdot \boldsymbol{D} - \mathbf{n}^{\mathtt{J}} \cdot \left(\frac{\partial \tilde{\mathbf{n}}^{\mathtt{I}}}{\partial h^{\mathtt{1}k}} \otimes \tilde{\mathbf{n}}^{\mathtt{I}} + \tilde{\mathbf{n}}^{\mathtt{I}} \otimes \frac{\partial \tilde{\mathbf{n}}^{\mathtt{I}}}{\partial h^{\mathtt{1}k}} \right) \qquad (4.29) \\
&= \delta^{l\mathtt{J}} \left(-M^{\mathtt{J}lm} C_{mk} \boldsymbol{\tau}_{\mathcal{K}} \right) \cdot \boldsymbol{D} - \mathbf{n}^{\mathtt{J}} \cdot \left(\frac{\partial \tilde{\mathbf{n}}^{\mathtt{I}}}{\partial h^{\mathtt{1}k}} \otimes \tilde{\mathbf{n}}^{\mathtt{I}} + \tilde{\mathbf{n}}^{\mathtt{I}} \otimes \frac{\partial \tilde{\mathbf{n}}^{\mathtt{I}}}{\partial h^{\mathtt{1}k}} \right), \qquad (4.30)
\end{aligned}$$

where δ denotes the Kronecker symbol (not to be confused with the variation symbol). The term $\frac{\partial \tilde{\mathbf{n}}^{\mathtt{I}}}{\partial h^{\mathtt{1}k}}$, where:

$$\tilde{\mathbf{n}}^{\mathtt{I}} = \frac{\mathbf{N}^{\tilde{\mathbf{n}}^{\mathtt{J}}}}{l^{\mathbf{N}^{\tilde{\mathbf{n}}^{\mathtt{J}}}}}, \tag{4.31}$$

with:

$$\mathbf{N}^{\tilde{\mathbf{n}}^{\mathtt{J}}} = \boldsymbol{\tau}_2^{\mathtt{I}} \times \mathbf{n}^{\mathtt{I}}, \tag{4.32}$$

and:

$$l^{\mathbf{N}^{\tilde{\mathbf{n}}^{\mathtt{J}}}} = \left\| \boldsymbol{\tau}_2^{\mathtt{I}} \times \mathbf{n}^{\mathtt{I}} \right\|, \tag{4.33}$$

reads:

$$\frac{\partial \tilde{\mathbf{n}}^{\mathtt{I}}}{\partial h^{\mathtt{1}k}} = \frac{1}{l^{\mathbf{N}^{\tilde{\mathbf{n}}^{\mathtt{J}}}}} \left(\mathbf{I} - \tilde{\mathbf{n}}^{\mathtt{I}} \otimes \tilde{\mathbf{n}}^{\mathtt{I}} \right) \cdot \frac{\partial \mathbf{N}^{\tilde{\mathbf{n}}^{\mathtt{J}}}}{\partial h^{\mathtt{1}k}} = \boldsymbol{F} \cdot \frac{\partial \mathbf{N}^{\tilde{\mathbf{n}}^{\mathtt{J}}}}{\partial h^{\mathtt{1}k}}. \tag{4.34}$$

We can write:

$$\frac{\partial \mathbf{N}^{\tilde{\mathbf{n}}^{\mathtt{J}}}}{\partial h^{\mathtt{1}k}} = \delta^{\mathtt{1}\mathtt{I}} \left(\boldsymbol{\tau}_{2k}^{\mathtt{I}} \times \mathbf{n}^{\mathtt{I}} + \boldsymbol{\tau}_2^{\mathtt{I}} \times \left(-M^{\mathtt{I}ij} C_{jk}^{\mathtt{I}} \boldsymbol{\tau}_i^{\mathtt{I}} \right) \right) = \mathbf{c}, \tag{4.35}$$

such that:

$$\frac{\partial \tilde{\mathbf{n}}^{\mathtt{I}}}{\partial h^{\mathtt{l}k}} = \boldsymbol{F} \cdot \mathbf{c}. \tag{4.36}$$

Finally, this yields:

$$\begin{aligned}\frac{\partial \mathbf{n}^{\mathtt{J}p}}{\partial h^{\mathtt{l}k}} =& \frac{1}{l^{\mathbf{n}^{\mathtt{J}p}}} \left(\mathbf{I} - \mathbf{n}^{\mathtt{J}\mathtt{P}} \otimes \mathbf{n}^{\mathtt{J}\mathtt{P}}\right) \cdot \frac{\partial \mathbf{N}^{\mathbf{n}^{\mathtt{J}\mathtt{P}}}}{\partial h^{\mathtt{I}2}} \\ =& \boldsymbol{E} \cdot \left(\delta^{l\mathtt{J}} \left(-M^{\mathtt{J}lm} C_{mk} \boldsymbol{\tau}_{\mathcal{K}}\right) \cdot \boldsymbol{D} - \mathbf{n}^{\mathtt{J}} \cdot \left((\boldsymbol{F} \cdot \mathbf{c}) \otimes \tilde{\mathbf{n}}^{\mathtt{I}} + \tilde{\mathbf{n}}^{\mathtt{I}} \otimes (\boldsymbol{F} \cdot \mathbf{c})\right)\right) \\ =& \mathbf{d}^{\mathtt{l}k}. \end{aligned} \tag{4.37}$$

Using Eq. (4.37), compact expressions for the components of $\frac{\partial f_2}{\partial \underline{q}}$ in Eq. (4.24) can be obtained:

$$\begin{aligned}\frac{\partial f_2}{\partial h^{\mathtt{I}2}} &= a^{\mathcal{C}} \left(\frac{\partial \mathbf{n}^{\mathtt{I}}}{\partial h^{\mathtt{I}2}} + \frac{\partial \mathbf{n}^{\mathtt{J}p}}{\partial h^{\mathtt{I}2}}\right) \cdot \boldsymbol{\tau}_2^{\mathtt{J}} \\ &= a^{\mathcal{C}} \left(-M^{\mathtt{I}jk} C_{k2}^{\mathtt{I}} \boldsymbol{\tau}_j^{\mathtt{I}} + \mathbf{d}^{\mathtt{I}2}\right) \cdot \boldsymbol{\tau}_2^{\mathtt{J}}, \end{aligned} \tag{4.38}$$

$$\begin{aligned}\frac{\partial f_2}{\partial h^{\mathtt{J}1}} =& a^{\mathcal{C}} \left(\frac{\partial \mathbf{n}^{\mathtt{J}p}}{\partial h^{\mathtt{J}1}} \cdot \boldsymbol{\tau}_2^{\mathtt{J}} + \mathbf{n}^{\mathtt{J}p} \cdot \frac{\partial \boldsymbol{\tau}_2^{\mathtt{J}}}{\partial h^{\mathtt{J}1}}\right) \\ =& a^{\mathcal{C}} \left(\mathbf{d}^{\mathtt{J}1} \cdot \boldsymbol{\tau}_2^{\mathtt{J}} + \mathbf{n}^{\mathtt{J}p} \cdot \boldsymbol{\tau}_{21}^{\mathtt{J}}\right), \end{aligned} \tag{4.39}$$

$$\begin{aligned}\frac{\partial f_2}{\partial h^{\mathtt{J}2}} &= a^{\mathcal{C}} \left(\frac{\partial \mathbf{n}^{\mathtt{J}p}}{\partial h^{\mathtt{J}2}} \cdot \boldsymbol{\tau}_2^{\mathtt{J}} + \mathbf{n}^{\mathtt{J}p} \cdot \frac{\partial \boldsymbol{\tau}_2^{\mathtt{J}}}{\partial h^{\mathtt{I}2}}\right) \\ &= a^{\mathcal{C}} \left(\mathbf{d}^{\mathtt{J}2} \cdot \boldsymbol{\tau}_2^{\mathtt{J}} + \mathbf{n}^{\mathtt{J}p} \cdot \boldsymbol{\tau}_{22}^{\mathtt{J}}\right). \end{aligned} \tag{4.40}$$

Combining Eqs. (4.23), (4.38), (4.39), (4.40), $\underline{\underline{H}}$ reads:

$$\underline{\underline{H}} = \begin{bmatrix} \boldsymbol{\tau}_2^{\mathtt{I}} + g\left(M^{\mathtt{I}jk} C_{k2}^{\mathtt{I}} \boldsymbol{\tau}_j^{\mathtt{I}}\right) & \boldsymbol{\tau}_1^{\mathtt{J}} & \boldsymbol{\tau}_2^{\mathtt{J}} & -\mathbf{n}^{\mathtt{I}} \\ a^{\mathcal{C}} \left(-M^{\mathtt{I}jk} C_{k2}^{\mathtt{I}} \boldsymbol{\tau}_j^{\mathtt{I}} + \mathbf{d}^{\mathtt{I}2}\right) \cdot \boldsymbol{\tau}_2^{\mathtt{J}} & a^{\mathcal{C}} \left(\mathbf{d}^{\mathtt{J}1} \cdot \boldsymbol{\tau}_2^{\mathtt{J}} + \mathbf{n}^{\mathtt{J}p} \cdot \boldsymbol{\tau}_{21}^{\mathtt{J}}\right) & a^{\mathcal{C}} \left(\mathbf{d}^{\mathtt{J}2} \cdot \boldsymbol{\tau}_2^{\mathtt{J}} + \mathbf{n}^{\mathtt{J}p} \cdot \boldsymbol{\tau}_{22}^{\mathtt{J}}\right) & 0 \end{bmatrix}. \tag{4.41}$$

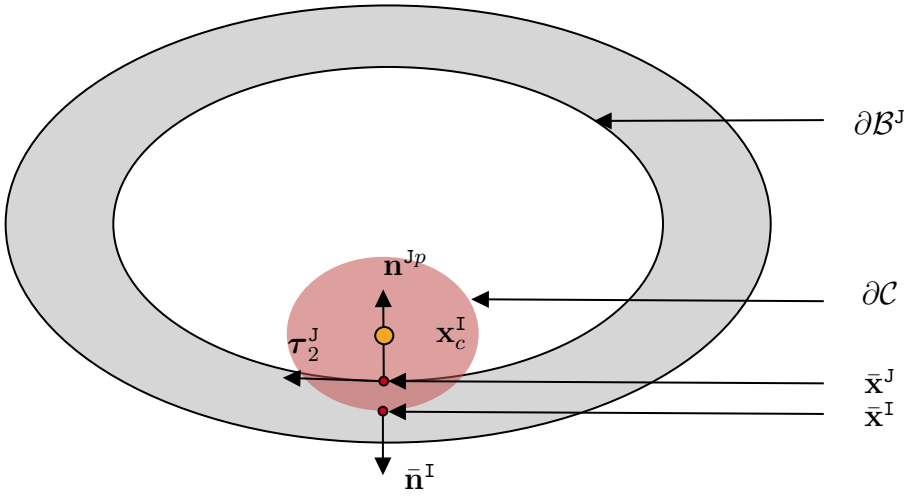

(a)

Figure 4.4: Perpendicular view to the plane $\mathcal{P}$ of $\partial\mathcal{C}$. Surface points $\bar{\mathbf{x}}^{\mathrm{I}}$ and $\bar{\mathbf{x}}^{\mathrm{J}}$, obtained after solving Eq. (4.17), are presented as red dots. Vectors $\bar{\mathbf{n}}^{\mathrm{I}}$ and $\bar{\mathbf{n}}^{\mathrm{J}p}$ are both orthogonal to $\bar{\boldsymbol{\tau}}_2^{\mathrm{J}}$.

First-guess procedure

As stated above, Eq. (4.17) is solved iteratively. An initial guess of the local parameters $\underline{q}$ must be provided to the solver employed to solve it. We employ a simple two-step procedure to establish an appropriate first guess:

1. We (approximately) find the centroid point of the master body that is the closest to the centroid point of the slave cross-section, $\mathbf{x}_c^{\mathrm{I}}(h^{\mathcal{C}})$. A simple way of achieving this is by sampling cross-section points along the master beam's centroid-line and pick the closest centroid-point from $\mathbf{x}_c^{\mathrm{I}}(h^{\mathcal{C}})$. The associated convective parameter of the closest sampled centroid point is denoted by $h^{\mathrm{J}1,fg}$.

2. To determine the initial values of circumferential parameters $h^{\mathrm{I}2,fg}$ and $h^{\mathrm{J}2,fg}$, we locate a pair of perimeter points on the cross-sections attached to $\mathbf{x}_c^{\mathrm{I}}(h^{\mathcal{C}})$ and $\mathbf{x}_c^{\mathrm{J}}(h^{\mathrm{J}1,fg})$. This procedure is depicted in Fig. 4.5. We start by sampling four points on the perimeter of both cross-sections. The pair of closest points is then chosen. Next, for each cross-section, we seed a point on the middle of each

sub-curve attached to the point previously selected ((c) in Fig. 4.5). Again, the closest pair of points is selected. This procedure is repeated several times. In our simulations, it was repeated until the relative change of the distance between the pair of closest points falls below 10%.

Note that in practice, the approach to establish the initial guess is only performed for a given slave cross-section if it is not active but close to the master surface. If a slave cross-section is active (meaning that it already penetrated the master surface in a previous contact detection), the solution of the local problem of the previous contact detection ($\bar{q}$) are used as the first guess.

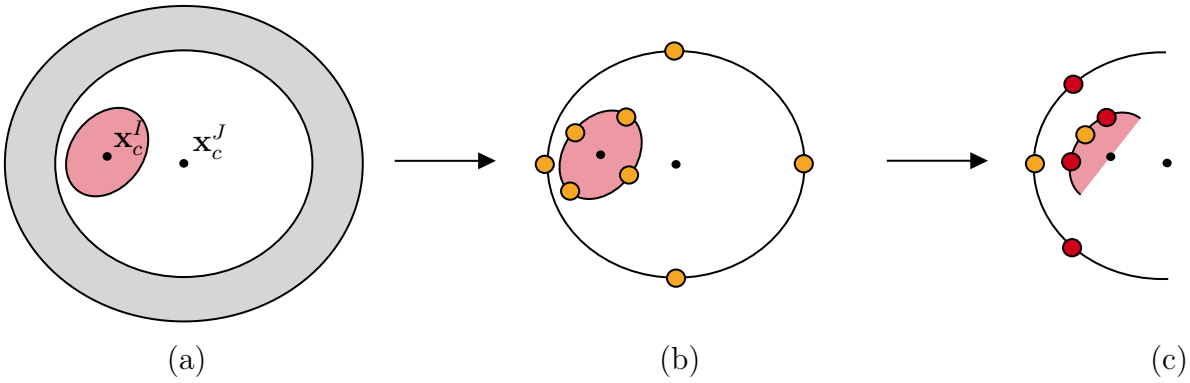

Figure 4.5: Illustration of the procedure to determine a good initial guess for the local problem. (a) Determination of centroid point $\mathbf{x}_c^{\mathrm{J}}(h^{\mathrm{J1},fg})$ that must be as close as possible to $\mathbf{x}_c^{\mathrm{I}}(h^{\mathcal{C}})$; (b) Determination of the closest pair of points amongst sampled points on $\partial\mathcal{C}$ and the perimeters of the cross-section attached to $\mathbf{x}_c^{\mathrm{J}}(h^{\mathrm{J1},fg})$; (c) Determination of the closest pair of points amongst the closest pair of points from (b) (in orange) and points in the middle of the curve connected to theses points (in red).

4.2.1.3 Contact constraints and virtual work equation including contact

The impenetrability of $\partial\mathcal{C}$ and $\partial\mathcal{B}^{\mathrm{J}}$ is enforced via unilateral contact conditions:

$$g_N \geq 0 \qquad T_N < 0 \qquad g_N T_N = 0, \tag{4.42}$$

where T_N denotes the nominal contact traction, meaning that it refers to the reference surface area.

In case of contact, a contact virtual work, $\delta\Pi_c$, is added to the virtual work equation for the two-body system and the space of admissible variations $\mathscr{V}$ is modified [86]. In the quasi-static setting, the virtual work reads:

$$\delta\Pi(\underline{p}^{\mathtt{IJ}}, \delta\underline{p}^{\mathtt{IJ}}) = \delta\Pi_{\mathcal{B}^{\mathtt{I}}}(\underline{p}^{\mathtt{I}}, \delta\underline{p}^{\mathtt{I}}) + \delta\Pi_{\mathcal{B}^{\mathtt{J}}}(\underline{p}^{\mathtt{J}}, \delta\underline{p}^{\mathtt{J}}) + \delta\Pi_c(\underline{p}^{\mathtt{IJ}}, \delta\underline{p}^{\mathtt{IJ}}) = 0, \ \forall \delta\underline{p}^{\mathtt{IJ}} \in \mathscr{V}, \quad (4.43)$$

where $\delta\Pi_{\mathcal{B}^i}$ denotes the internal and external virtual work of beam $\mathcal{B}^i$ (excluding contact interactions). Kinematic variables associated with $\mathcal{B}^i$ are denoted by $\underline{p}^i = \left[\mathbf{u}^i, \boldsymbol{\theta}^i\right]^T : (0, L) \to \mathbb{R}^3 \times \mathbb{R}^3$ and the associated test functions by $\delta\underline{p}^i$. $\mathbf{u}^i$ denotes the displacement field of the $\mathcal{B}^i$'s centroid-line and $\boldsymbol{\theta}^i$ its field of rotation vectors parametrizing SO(3) [29]. $\underline{p}^i$ is only admissible if $\underline{p}^i(\mathbf{X}^{\mathcal{B}^i}) = \underline{p}^i_D(\mathbf{X}^{\mathcal{B}^i}), \ \forall \mathbf{X}^{\mathcal{B}^i} \in \partial\mathcal{B}^i_D$. $\partial\mathcal{B}^i_D$ denotes the part of the boundary of $\partial\mathcal{B}^i$ where Dirichlet boundary conditions are imposed [86].

$\underline{p}^{\mathtt{IJ}} = \left[\underline{p}^{\mathtt{I}}, \underline{p}^{\mathtt{J}}\right]^T$ gathers the kinematic variables of both beams. Similarly, test functions are gathered in $\delta\underline{p}^{\mathtt{IJ}} = \left[\delta\underline{p}^{\mathtt{I}}, \delta\underline{p}^{\mathtt{J}}\right]^T$.

In Eq. (4.43), the virtual work due to contact, $\delta\Pi_c$, accounts for all the sections penetrated. The infinitesimal virtual work produced at a single section, denoted by $d\delta\Pi_c$, can be written as [53]:

$$d\delta\Pi_c = T_N \delta g_N \left\| \frac{\partial \mathbf{x}^{\mathtt{I}}_{0c}}{\partial h^{\mathtt{I1}}} \right\| dh^{\mathtt{I1}}, \quad (4.44)$$

where δg_N denotes the variation of g_N that depends on all kinematic variables in $\underline{p}^{\mathtt{IJ}}$, and $dh^{\mathtt{I1}}$ denotes the differential of the slave's centroid line parameter associated to $\mathcal{C}$. $dh^{\mathtt{I1}}$ is related to the differential length of the undeformed centroid-line according to:

$$dL^{\mathcal{B}^{\mathtt{I}}} = \left\| \frac{\partial \mathbf{x}^{\mathtt{I}}_{0c}}{\partial h^{\mathtt{I1}}} \right\| dh^{\mathtt{I1}}, \quad (4.45)$$

Next, we discuss how to calculate T_N for the penalty approach used in this contribution and also how to compute δg_N. The nominal traction vector has been preferred

over the current traction vector as the former must be integrated in the length of the slave beam in the reference configuration, while the latter has to be integrated over the current configuration. As the reference configuration does not depend on $\underline{p}^{\mathtt{IJ}}$, the linearization of $\delta\Pi$ yields shorter expressions than if the current traction vector was employed [47].

Penalty method

If a penalty formulation is used, contact traction T_N, acting at the pair of surface points $\bar{\mathbf{x}}^{\mathtt{J}}$ and $\bar{\mathbf{x}}^{\mathtt{I}}$, is given by:

$$T_N = -\epsilon_N \langle -g_N \rangle \,, \tag{4.46}$$

where $\epsilon_N > 0$ denotes the penalty stiffness and $\langle \bullet \rangle$ denote the Macaulay brackets, representing the positive part of its operand [45]. The fact that ϵ_N must be selected can be seen as a weakness of the penalty method. Indeed, other constraint enforcement methods like the Lagrange multipliers method do not need such user-defined parameters. On the other hand, in the context of contact frameworks for beams that are characterized by rigid cross sections, the penalty parameter can be interpreted as some compliance of the beams in the transversal directions [53, 62]. Inserting Eq. (4.46) into Eq. (4.44), the virtual work of the contact force reads:

$$d\delta\Pi_c = -\epsilon_N \langle -g_N \rangle \, \delta g_N \left\| \frac{\partial \mathbf{x}^{\mathtt{I}}_{0c}}{\partial h^{\mathtt{I1}}} \right\| dh^{\mathtt{I1}}. \tag{4.47}$$

The virtual work of all penetrated sections follows from the integration of the infinitesimal virtual work of a single penetrated section, $d\delta\Pi_c$, along the centroid-line of $\mathcal{B}^{\mathtt{I}}$ as follows:

$$\delta\Pi_c = \int_{h_L^{\mathtt{1I}}}^{h_U^{\mathtt{1I}}} d\delta\Pi_c, \tag{4.48}$$

where $h_L^{\mathtt{1I}}$ and $h_U^{\mathtt{1I}}$ are the lower and upper bounds of the integral, respectively.

Variation of the normal gap, δg_N

$g_N = \bar{\mathbf{g}} \cdot \bar{\mathbf{n}}^{\mathtt{I}}$, measured for a fixed $h^{\mathtt{I}1}$, depends on $\underline{p}^{\mathtt{IJ}}$ but also on the local variables in $\underline{q}$, which in turn implicitly depend on $\underline{p}^{\mathtt{IJ}}$. Eventually, δg_N must be solely expressed in terms of the variations of the primary variables, here $\delta \underline{p}^{\mathtt{IJ}}$. The variational operator applied to g_N gives:

$$\delta g_N = \delta \bar{\mathbf{g}} \cdot \bar{\mathbf{n}}^{\mathtt{I}} + \bar{\mathbf{g}} \cdot \delta \bar{\mathbf{n}}^{\mathtt{I}}. \tag{4.49}$$

Also, we have:

$$\bar{\mathbf{g}} \cdot \delta \bar{\mathbf{n}}^{\mathtt{I}} = g_N \bar{\mathbf{n}}^{\mathtt{I}} \cdot \delta \bar{\mathbf{n}}^{\mathtt{I}} = 0, \tag{4.50}$$

as $\delta \bar{\mathbf{n}}^{\mathtt{I}} \cdot \bar{\mathbf{n}}^{\mathtt{I}} = 0$. Noting that $\bar{\mathbf{g}}$ depends on $\underline{p}^{\mathtt{IJ}}$ and $\bar{\underline{q}}(\underline{p}^{\mathtt{IJ}})$, we get:

$$\delta \bar{\mathbf{g}} = \left(\frac{\partial \mathbf{g}}{\partial \underline{p}^{\mathtt{IJ}}} \Big|_{\underline{q}=\bar{\underline{q}}} \right)^T \delta \underline{p}^{\mathtt{IJ}} + \left(\frac{\partial \mathbf{g}}{\partial \underline{q}} \Big|_{\underline{q}=\bar{\underline{q}}} \right)^T \delta \underline{q} \tag{4.51}$$

$$= \left(\frac{\partial \mathbf{g}}{\partial \underline{p}^{\mathtt{IJ}}} \Big|_{\underline{q}=\bar{\underline{q}}} \right)^T \delta \underline{p}^{\mathtt{IJ}} + \left(\frac{\partial \mathbf{g}}{\partial \underline{q}} \Big|_{\underline{q}=\bar{\underline{q}}} \right)^T \left(\frac{d \underline{q}}{d \underline{p}^{\mathtt{IJ}}} \Big|_{\underline{q}=\bar{\underline{q}}} \right) \delta \underline{p}^{\mathtt{IJ}}. \tag{4.52}$$

The relationships between $\underline{q}$ and $\underline{p}^{\mathtt{IJ}}$ can be found on the basis of the stationarity of $\underline{f}(\underline{p}^{\mathtt{IJ}}, \bar{\underline{q}}(\underline{p}^{\mathtt{IJ}}))$ with respect to $\underline{p}^{\mathtt{IJ}}$:

$$\frac{d \underline{f}}{d \underline{p}^{\mathtt{IJ}}} = \left(\frac{\partial \underline{f}}{\partial \underline{p}^{\mathtt{IJ}}} \Big|_{\underline{q}=\bar{\underline{q}}} \right) \delta \underline{p}^{\mathtt{IJ}} + \Big(\underbrace{\frac{\partial \underline{f}}{\partial \underline{q}}}_{\underline{\underline{H}}} \Big|_{\underline{q}=\bar{\underline{q}}} \Big) \delta \bar{\underline{q}} = \underline{0}, \tag{4.53}$$

which leads after some rearrangement to:

$$\delta \bar{\underline{q}} = - \left(\underline{\underline{H}}^{-1} \Big|_{\underline{q}=\bar{\underline{q}}} \frac{\partial \underline{f}}{\partial \underline{p}^{\mathtt{IJ}}} \Big|_{\underline{q}=\bar{\underline{q}}} \right) \delta \underline{p}^{\mathtt{IJ}}. \tag{4.54}$$

For further use, we define $\underline{\underline{A}}$ as follows:

$$\underline{\underline{A}} = - \underline{\underline{H}}^{-1} \Big|_{\underline{q}=\bar{\underline{q}}} \frac{\partial \underline{f}}{\partial \underline{p}^{\mathtt{IJ}}} \Big|_{\underline{q}=\bar{\underline{q}}}. \tag{4.55}$$

such that:

$$\delta\underline{\bar{q}} = \underline{\underline{A}}\delta\underline{p}^{\mathtt{IJ}}. \tag{4.56}$$

Inserting this in Eq. (4.52) yields:

$$\delta\bar{\mathbf{g}} = \left(\left(\frac{\partial \mathbf{g}}{\partial \underline{p}^{\mathtt{IJ}}}\Big|_{\underline{q}=\bar{\underline{q}}} \right)^T + \left(\frac{\partial \mathbf{g}}{\partial \underline{q}}\Big|_{\underline{q}=\bar{\underline{q}}} \right)^T \underline{\underline{A}} \right) \delta\underline{p}^{\mathtt{IJ}}. \tag{4.57}$$

Inserting this into Eq. (4.49) yields:

$$\begin{aligned} \delta g_N = \delta\bar{\mathbf{g}} \cdot \bar{\mathbf{n}}^{\mathtt{I}} &= \left(\frac{\partial \bar{\mathbf{g}}}{\partial \underline{p}^{\mathtt{IJ}}} \right)^T \delta\underline{p}^{\mathtt{IJ}} \cdot \bar{\mathbf{n}}^{\mathtt{I}} + \left(\frac{\partial \bar{\mathbf{g}}}{\partial \underline{q}} \right)^T \underline{\underline{A}}\delta\underline{p}^{\mathtt{IJ}} \cdot \bar{\mathbf{n}}^{\mathtt{I}} && (4.58) \\ &= (\delta\underline{p}^{\mathtt{IJ}})^T \left(\frac{\partial \bar{\mathbf{g}}}{\partial \underline{p}^{\mathtt{IJ}}} \cdot \bar{\mathbf{n}}^{\mathtt{I}} + \underline{\underline{A}}^T \frac{\partial \bar{\mathbf{g}}}{\partial \underline{q}} \cdot \bar{\mathbf{n}}^{\mathtt{I}} \right) && (4.59) \\ &= (\delta\underline{p}^{\mathtt{IJ}})^T \underline{z}. && (4.60) \end{aligned}$$

Note for further use that $\frac{\partial \bar{\mathbf{g}}}{\partial \underline{p}^{\mathtt{IJ}}} \bar{\mathbf{n}}^{\mathtt{I}}$ reads:

$$\begin{aligned} \frac{\partial \mathbf{g}}{\partial \underline{p}^{\mathtt{IJ}}}\Big|_{\underline{q}=\bar{\underline{q}}} \cdot \bar{\mathbf{n}}^{\mathtt{I}} &= \frac{\partial \bar{\mathbf{x}}^{\mathtt{J}}{}^T}{\partial \underline{q}} \cdot \bar{\mathbf{n}}^{\mathtt{I}} - \frac{\partial \bar{\mathbf{x}}^{\mathtt{I}}{}^T}{\partial \underline{q}} \cdot \bar{\mathbf{n}}^{\mathtt{I}} && (4.61) \\ &= \begin{bmatrix} 0 \\ \boldsymbol{\tau}_1^{\mathtt{J}} \cdot \bar{\mathbf{n}}^{\mathtt{I}} \\ \boldsymbol{\tau}_2^{\mathtt{J}} \cdot \bar{\mathbf{n}}^{\mathtt{I}} \end{bmatrix} - \begin{bmatrix} \boldsymbol{\tau}_1^{\mathtt{I}} \cdot \bar{\mathbf{n}}^{\mathtt{I}} \\ 0 \\ 0 \end{bmatrix} && (4.62) \\ &= \begin{bmatrix} 0 \\ \boldsymbol{\tau}_1^{\mathtt{J}} \cdot \bar{\mathbf{n}}^{\mathtt{I}} \\ \boldsymbol{\tau}_2^{\mathtt{J}} \cdot \bar{\mathbf{n}}^{\mathtt{I}} \end{bmatrix} - \begin{bmatrix} 0 \\ 0 \\ 0 \end{bmatrix}, && (4.63) \end{aligned}$$

where is it obvious from Eq. (4.63) that $\frac{\partial \bar{\mathbf{x}}^{\mathtt{I}}{}^T}{\partial \underline{q}} \cdot \bar{\mathbf{n}}^{\mathtt{I}}$ is independent of $\underline{q}$.

All in all, we can write:

$$\delta\Pi_c = \int_{h_L^{\mathtt{II}}}^{h_U^{\mathtt{II}}} -\epsilon_N \langle -g_N \rangle \underline{z}^T \delta\underline{p}^{\mathtt{IJ}} \left\| \frac{\partial \mathbf{x}_{0c}^{\mathtt{I}}}{\partial h^{\mathtt{I1}}} \right\| dh^{\mathtt{I1}}. \tag{4.64}$$

4.2.2 Spatial discretization

4.2.2.1 Interpolation of the beams' surface

The Finite Element Method (FEM) is the discretisation method used in this work. Each beam is now discretized with a set of beam finite elements (BFEs) [78, 79, 29]. The rotation vectors are the primary rotational kinematic variables [29] that are interpolated. For a BFE $\mathcal{E}$, we denote by $\mathbf{X}_c^h(h^1) : \left(0, L^{\mathcal{E}}\right) \to \mathbb{R}^3$ the interpolated position of its centroid-line, where $L^{\mathcal{E}}$ denotes the length of the centroid-line in the undeformed configuration. $\mathbf{u}_c^h(h_1) : \left(0, L^{\mathcal{E}}\right) \to \mathbb{R}^3$ and $\boldsymbol{\theta}^h(h^1) : \left(0, L^{\mathcal{E}}\right) \to \mathbb{R}^3$ denote the interpolated displacement field of the centroid-line and the interpolated field of rotation vectors, respectively. Rodrigues' formula is used to obtain rotation tensor $\boldsymbol{\Lambda}$ from the interpolated rotation vector[2], denoted $\boldsymbol{\theta}^h$. The displacement of node K is denoted by $\hat{\mathbf{u}}_K^{\mathcal{E}}$ and its rotation vector by $\hat{\boldsymbol{\theta}}_K^{\mathcal{E}}$. The kinematic variables of element $\mathcal{E}$ are gathered in:

$$\underline{p}^{\mathcal{E}} = \left[\hat{\mathbf{u}}_1^{\mathcal{E}}, \ldots, \hat{\mathbf{u}}_{n_u}^{\mathcal{E}}, \hat{\boldsymbol{\theta}}_1^{\mathcal{E}}, \ldots, \hat{\boldsymbol{\theta}}_{n_\theta}^{\mathcal{E}}\right]^T, \tag{4.65}$$

where n_u and n_θ denote the number of nodes used to interpolate the displacement and the rotation vector, respectively. Since the nodal variables of all BFEs of $\mathcal{B}^{\mathrm{I}}$ and $\mathcal{B}^{\mathrm{J}}$ are denoted by $\underline{\hat{p}}$, the associated variations are denoted by $\delta\underline{\hat{p}}$.

4.2.2.2 Contact residual and stiffness

The discretized form of the virtual work in Eq. (4.43) leads to a set of nonlinear equations. Newton's method is generally used to iteratively determine the solution $\underline{\hat{p}}^{sol}$ of the virtual work statement. This requires the linearization of Eq. (4.43) around an estimate of $\underline{\hat{p}}^{sol}$, $\underline{\hat{p}}$, which yields:

$$\delta\Pi(\underline{\hat{p}} + \triangle\underline{\hat{p}}, \delta\underline{\hat{p}}) \simeq \delta\Pi(\underline{\hat{p}}, \delta\underline{\hat{p}}) + \underline{\underline{\triangle\delta\Pi}}(\underline{\hat{p}}, \delta\underline{\hat{p}})\triangle\underline{\hat{p}} = \delta\underline{\hat{p}}^T(\underline{r}_g + \underline{\underline{K}}_g\triangle\underline{\hat{p}}) \simeq 0, \tag{4.66}$$

where $\underline{r}_g$ and $\underline{\underline{K}}_g$ denote the global residual force and the global stiffness matrix, respectively. $\triangle\underline{\hat{p}}$ denotes an increment of the nodal variables. The global forces

[2]It is well known that the corresponding finite element formulation does not share the strain-invariance property of the underlying geometrically exact theory [31].

read:

$$\underline{r}_g(\underline{\hat{p}}) = \underline{f}_{int}(\underline{\hat{p}}) + \underline{r}_c(\underline{\hat{p}}) - \underline{f}_{ext}(\underline{\hat{p}}), \tag{4.67}$$

where $\underline{f}_{int}$ denotes the internal force vector stemming from the contribution of all BFEs, and $\underline{f}_{ext}$ the external force vector. $\underline{r}_c$ contains all the contact contributions from all contact elements, where a contact element refers to a seeded section attached at an integration point (see below) along $\mathcal{B}^{\mathtt{I}}$ and its projection on discretized surface $\partial\mathcal{B}^{\mathtt{J}}$.

Assuming here that $\underline{f}_{ext}$ does not depend on $\underline{p}^{\mathtt{IJ}}$, the global stiffness obtained after the linearization of $\underline{r}_g$, can be decomposed as follows:

$$\underline{\underline{K}}_g = \underline{\underline{K}}_{int} + \underline{\underline{K}}_c, \tag{4.68}$$

where $\underline{\underline{K}}_{int}$ denotes the stiffness matrix of the BFEs, and $\underline{\underline{K}}_c$ denotes the stiffness matrix of all contact elements.

The contact virtual work is the sum of all contact contributions:

$$\delta\Pi_c(\underline{\hat{p}}, \delta\underline{\hat{p}}) = \sum_{e \in \mathtt{S}} \delta\Pi_{c,e}(\underline{\hat{p}}_e, \delta\underline{\hat{p}}_e), \tag{4.69}$$

where $\mathtt{S}$ denotes the set of active contact elements (*i.e.* those for which $g_N < 0$), and $\delta\Pi_{c,e}$ denotes the contact virtual work associated with contact element e. If no smoothing procedure of the surface is required [47], each contact elements involves two BFEs, one which is part of the discretization $\mathcal{B}^{\mathtt{I}}$, and the other which is part of the discretization of $\mathcal{B}^{\mathtt{J}}$. However, if a smoothing of the beam's surface is performed, each contact element directly depends on several BFEs of $\mathcal{B}^{\mathtt{I}}$ and of $\mathcal{B}^{\mathtt{J}}$. The set of elements of $\mathcal{B}^{\mathtt{I}}$ and $\mathcal{B}^{\mathtt{J}}$ used to construct contact element e are denoted by $\mathcal{M}$ and $\mathcal{N}$, respectively. The involved nodal variables are gathered in array $\underline{\hat{p}}_e = \left[\underline{\hat{p}}^{\mathcal{M}}, \underline{\hat{p}}^{\mathcal{N}}\right]^T$. Similarly, the involved nodal variations are denoted by $\delta\underline{\hat{p}}_e$.

The linearization of $\delta\Pi_c$ reads:

$$\begin{aligned}\delta\Pi_c(\hat{\underline{p}} + \triangle\hat{\underline{p}}, \delta\hat{\underline{p}}) &= \sum_{e\in\mathbb{S}} \delta\Pi_{c,e}(\hat{\underline{p}}_e + \triangle\hat{\underline{p}}_e, \delta\hat{\underline{p}}_e) \\ &\approx \sum_{e\in\mathbb{S}} \delta\Pi_c(\hat{\underline{p}}_e, \delta\hat{\underline{p}}_e) + \underline{\underline{\triangle\delta\Pi_c}}(\hat{\underline{p}}_e, \delta\hat{\underline{p}}_e)\triangle\hat{\underline{p}}_e \qquad (4.70) \\ &\approx \sum_{e\in\mathbb{S}} \delta\hat{\underline{p}}_e^T(\underline{r}_{ce} + \underline{\underline{K}}_{ce}\triangle\hat{\underline{p}}_e). \qquad (4.71)\end{aligned}$$

Next, we discuss how to construct element contributions $\underline{r}_{ce}$ and $\underline{\underline{K}}_{ce}$ to the global residual (force) vector and the global stiffness matrix, respectively.

Force vector and stiffness of contact element e

We numerically integrate Eq. (39) with a quadrature (Gauss or Lobato-type). To this end, we place $n_{IP}^{\mathcal{M}}$ integration points of a single subdomain along the centroid-line of $\mathcal{M}$ [37, 62]. This yields:

$$\begin{aligned}\delta\Pi_c &= -\epsilon_N \int_{-1}^{1} \langle -g_N(\eta)\rangle\, \delta g_N(\eta)\, \|\mathcal{J}(\eta)\|\, d\eta \qquad (4.72) \\ &\approx -\epsilon_N \sum_{k}^{n_{IP}^{\mathcal{M}}} w_k\, \langle -g_N(\eta_k)\rangle\, \delta g_N(\eta_k)\, \|\mathcal{J}(\eta_k)\|\,, \qquad (4.73) \\ &\approx \sum_{k}^{n_{IP}^{\mathcal{M}}} w_k\, \langle -g_{Nk}\rangle\, \delta g_{Nk}\, \|\mathcal{J}_k\|\,, \qquad (4.74)\end{aligned}$$

where $\eta \in [-1, 1]$ denotes the centroid point coordinate in the parameter space and $\mathcal{J} = \frac{\partial \mathbf{x}_{0c}^{\mathrm{I}}}{\partial \eta}$. The weight and coordinates of the k^{th} integration point are denoted by w_k and η_k, respectively. Given the section along $\mathcal{M}$ attached to $\mathbf{x}_c(\eta)$ for which we solve the local problem of Eq. (4.17), two surface points, $\bar{\mathbf{x}}^{\mathcal{M}}$ and $\bar{\mathbf{x}}^{\mathcal{N}}$, are computed. In Eq. (4.73), $\underline{r}_{cek}$ is expressed as:

$$\underline{r}_{cek} = -\epsilon_N\, \langle -g_N\rangle\, \frac{dg_N}{d\hat{\underline{p}}_e}. \qquad (4.75)$$

If the Automatic Differentiation (AD) formalism is employed [41, 43], the dependency of the local variables with respect to $\underline{\hat{p}}_e$ as well as relations of Eq. (4.63) can be directly incorporated as follows:

$$\begin{aligned} \delta g_N &= \delta\bar{\mathbf{g}} \cdot \bar{\mathbf{n}}^{\mathtt{I}} && (4.76)\\ &= \delta\bar{\mathbf{x}}^{\mathtt{J}} \cdot \bar{\mathbf{n}}^{\mathtt{I}} - \delta\bar{\mathbf{x}}^{\mathtt{I}} \cdot \bar{\mathbf{n}}^{\mathtt{I}} && (4.77)\\ &= \left(\frac{\hat{\partial}\mathbf{x}^{\mathtt{J}}}{\hat{\partial}\underline{\hat{p}}_e}\Big|_{\frac{\partial \underline{q}}{\partial \underline{\hat{p}}_e}=\underline{\underline{A}}} - \frac{\hat{\partial}\mathbf{x}^{\mathtt{I}}}{\hat{\partial}\underline{\hat{p}}_e}\Big|_{\frac{\partial \underline{q}}{\partial \underline{\hat{p}}_e}=\underline{0}} \right) \cdot \bar{\mathbf{n}}^{\mathtt{I}}, && (4.78) \end{aligned}$$

where operator $\frac{\hat{\partial}\square}{\hat{\partial}\underline{w}}$ denotes the Automatic Differentiation (AD) of function $\square$ with respect to the variables in $\underline{w}$ ([47, 41]) and the mechanism of AD exceptions is used to overwrite some partial derivatives.

$\underline{\underline{K}}_{cek}$, stemming for the contribution of the k^{th} integration point placed along $h_1^{\mathcal{M}}$, can be obtained using AD as follows:

$$\underline{\underline{K}}_{cek} = \frac{\hat{\partial}\underline{r}_{cek}}{\hat{\partial}\underline{\hat{p}}_e}\Big|_{\frac{\partial \underline{\bar{q}}}{\partial \underline{\hat{p}}_e}=\underline{\underline{A}}}. \tag{4.79}$$

$\underline{r}_c$ and $\underline{\underline{K}}_c$, which contain the contributions of all contact elements in set $\mathtt{S}$, are obtained from:

$$\underline{r}_c = \mathop{\mathsf{A}}_{e\in\mathtt{S}} \sum_{k}^{n_{IP}^{\mathcal{M}}} w_k \underline{r}_{cek} = \mathop{\mathsf{A}}_{e\in\mathtt{S}} \underline{r}_{ce}, \tag{4.80}$$

$$\underline{\underline{K}}_c = \mathop{\mathsf{A}}_{e\in\mathtt{S}} \sum_{k}^{n_{IP}^{\mathcal{M}}} w_k \underline{\underline{K}}_{cek} = \mathop{\mathsf{A}}_{e\in\mathtt{S}} \underline{\underline{K}}_{ce}. \tag{4.81}$$

where A denotes the finite-element assembly operator. Note that the exception in differentiation in Eq. (4.81) allows to properly linearise $\underline{r}_{cek}$ such that the exception $\frac{\partial \underline{q}}{\partial \underline{\hat{p}}_e} = \underline{0}$ in Eq. (4.78) is replaced by $\frac{\partial \underline{q}}{\partial \underline{\hat{p}}_e} = \underline{\underline{A}}$ during linearization.

4.3 Results

In this section, the beam-inside-beam contact scheme is applied to two numerical examples. First, a thin beam is pulled out from another beam in which it is initially inserted. Second, a thin beam is inserted in a curved beam. For these two examples, a single integration point is used to evaluate $\underline{r}_{ce}$ and $\underline{\underline{K}}_{ce}$ in Eqs. (4.80) and (4.81), respectively.

In both examples, large relative displacements of the contacting surfaces take place. This implies that for a contact element, if projection point $\bar{\mathbf{x}}^{\mathrm{J}}$ lies on the surface of BFE $\mathcal{M}$, this projection might go off the bound of the surface $\partial\mathcal{M}$. If this happens, projection point $\bar{\mathbf{x}}^{\mathrm{J}}$ should lie on an adjacent element's surface, namely the surface of element $\mathcal{B}^{\mathcal{M}+1}$ or $\mathcal{B}^{\mathcal{M}-1}$. However, as two-node geometrically exact beam elements are employed, gaps and overlaps of the different BFE's surfaces are present if the beam is not initially straight. For this reason, it might be difficult or impossible to define the new location of $\bar{\mathbf{x}}^{\mathrm{J}}$.

To palliate this problem, a dedicated surface smoothing technique was introduced in [54]. The resulting auxiliary surface has C^1-continuity which is convenient for contact treatment. This procedure is used in the following examples.

Due to the discretization of the contact kinematics, a sudden loss of contact near the inlet and outlet of the outer beam may result in loss of convergence. The methodology presented in Appendix IV.A is therefore adopted in the following examples to avoid this complications.

4.3.1 Example 1: Pull out

In the first example, two elastic beams with the same initial centroid-line form a part of a helix (Fig. 4.6a). They have the same centroid-line as a parameterized helix. The outer beam is hollow with an elliptical cross-section defined by $a = 22.3$ mm and $b = 17.8$ mm. Its wall thickness is 0.2 mm. Its Young's modulus is $E = 0.15$ MPa [36] and 75 BFEs are employed to discretize it. The thin beam has an elliptical section with semi-axes $a = 3.9$ mm and $b = 3$ mm. It is stiffer than the hollow beam as its Young's modulus is $E = 1.5$ MPa. Its Poisson's ratio is $\nu = 0.3$ and it is

discretized with 100 BFEs. A penalty stiffness of 1 N/m is used. The displacements and rotations of both end nodes of the outer beam are restrained. One end of the thin beam is pulled away from the outer beam by 1200 mm in 300 equally spaced increments.

Contact interactions substantially deform the thin beam, (Fig. 4.6b). As the (prescribed) end node of the thin beam continues to move away from the outer beam, sliding of the contacting surfaces occurs until the final configuration is reached (Fig 4.6c). As the prescribed beam deforms and moves along the outer beam, the number of penetrated sections changes (Fig. 4.7). The components of the reaction force and torque at the prescribed end of the thin beam are reported in Fig. 4.8a and Fig. 4.8b, respectively.

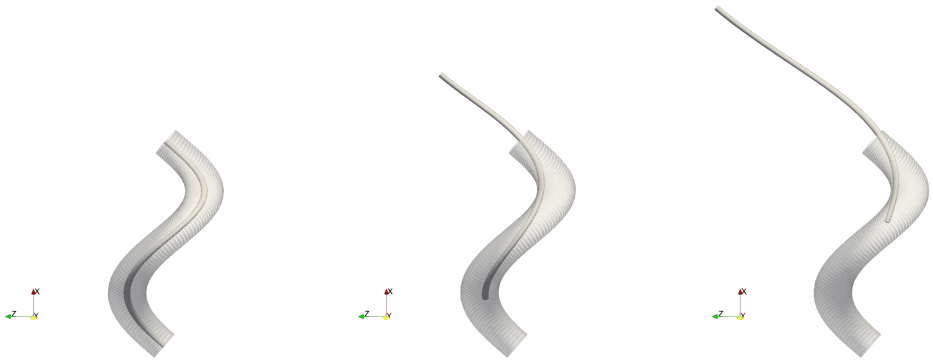

(a) (b) (c)

Figure 4.6: Example 1: (a) Initial configuration; (b) configuration halfway through the loading, and (c) final configuration.

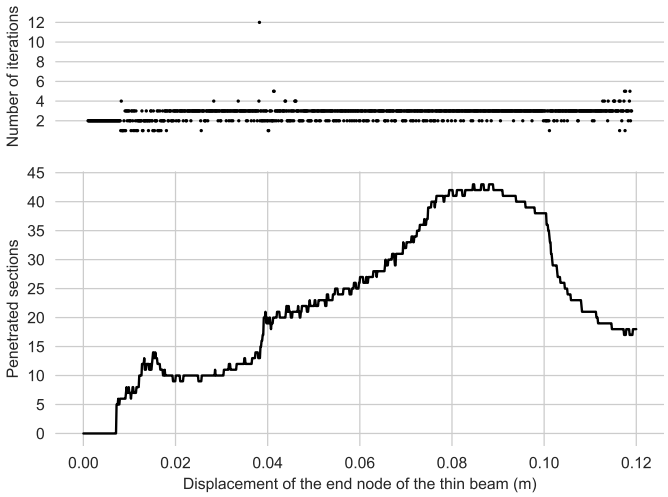

Figure 4.7: Example 1: top: number of global iterations to reach the convergence criteria $\left\| \underline{f}_{int} + \underline{r}_c - \underline{f}_{ext} \right\| < 10^{-8}$; bottom: number of penetrated sections as a function of the displacement of the end node of the thin beam. The peak in the number of iterations corresponds to the sliding of a cross-section of the slave beam in contact out of the hollow beam. The peak in the number of iterations corresponds to the sliding of a cross-section of the slave beam in contact out of the hollow beam.

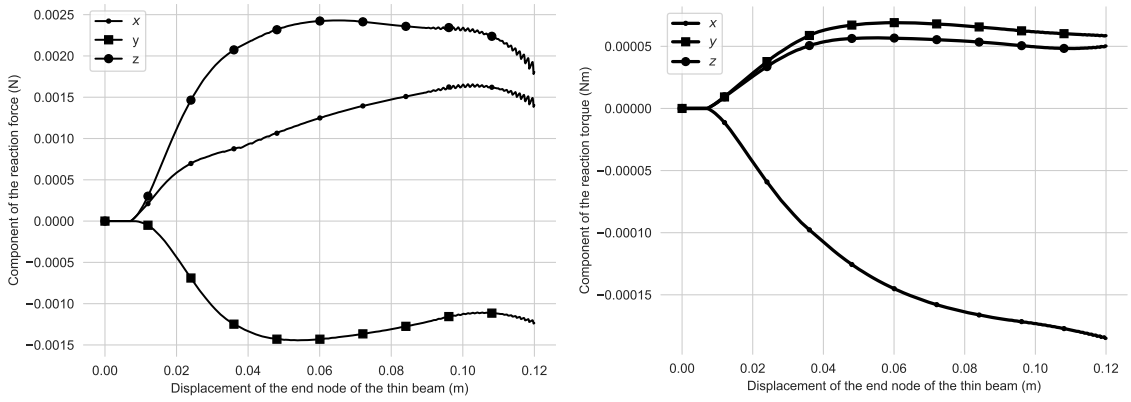

(a) (b)

Figure 4.8: Example 1: (a) components of the reaction force and (b) reaction torque at the prescribed end of the thin beam.

4.3.2 Example 2: Insertion

The second example involves an initially straight thin beam that is pushed in a hollow, largely circular beam (see Fig. 4.9). Initially, only a small part of the thin beam is inserted in the hollow one. The kinematic variables of the outer beam's end node near the thin beam are restrained. The z-displacement of the inner beam's end node furthest away from the outer beam is prescribed to reach 270 mm in 300 increments, whilst the other kinematic variables at this end node are restrained.

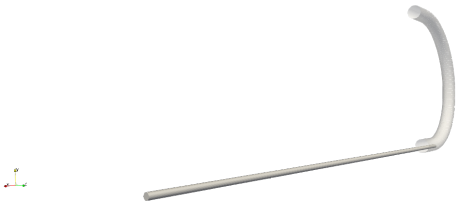

Figure 4.9: Example 2: Initial configuration.

This inner beam has a length of 54 cm, and a Young's modulus of 1.5 MPa. The cross sectional shapes are given by $a = 5.4\,\text{mm}$ and $b = 4.3\,\text{mm}$. The outer hollow beam is more compliant with $E = 0.15$ MPa. Its wall thickness is 1 mm and its cross-sectional semi-axes are $a = 20\,\text{mm}$ and $b = 16\,\text{mm}$. 100 and 180 BFEs are employed to discretize the inner and outer beam, respectively. The Poisson's ratio of both beams is 0.33.

Both structures deform due to contact, see Fig. 4.10. Fig. 4.11 shows that numerous sections of the inner beam penetrate the wall of the outer beam, which indicates that the contact is non-localized. This confirms that in the present case, as well as for the first example, contact cannot be described by a single force acting at the closest pair of surface points. Master-master contact frameworks [26, 25, 24, 89, 95] where bi-orthogonality equations must be solved to determine the contact location are difficult to apply in these situations. The reason is that they rely on the determination of a minimum of a distance function that is almost constant if surfaces are close to each other on a finite region. The top diagram of Fig. 4.11, furthermore, shows that only a few iterations are required to reach convergence. This was the same as for

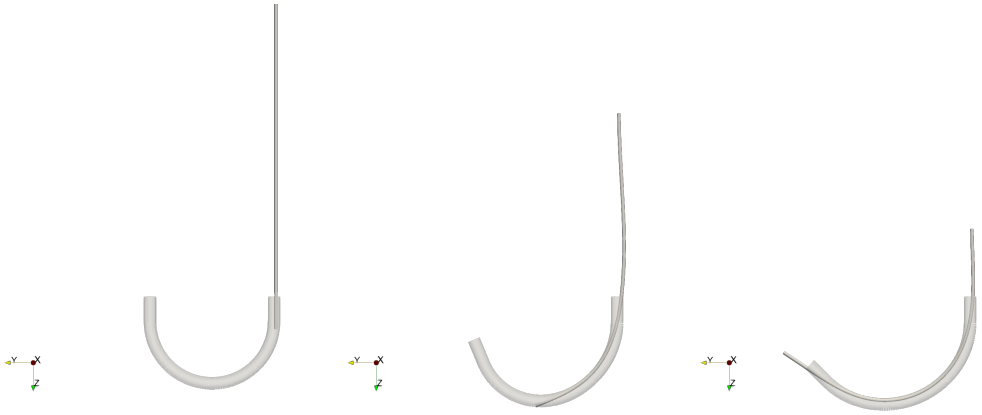

(a) (b) (c)

Figure 4.10: Example 2: (a) Initial configuration; (b) configuration halfway through the loading, and (c) final configuration.

the first example, as revealed in the top diagram of Fig. 4.7. The force-displacement and torque-displacement diagrams of Fig. 4.12 clearly show that different regimes are present, where each regime is governed by a different number of contact areas.

In the current example, the Young's modulus of the inner beam is ten times larger than that of the outer beam. To demonstrate that the framework is also robust for an entirely different ratio of Young's moduli, the example is repeated with exactly the same geometrical, material and numerical parameters, except for the Young's modulus of the inner beam. Instead of 1.5 MPa, we set the modulus to 150 MPa such that it is thousand times larger than that of the outer beam.

The figures for this additional test case are reported in Appendix IV.B. They show that, although the predicted deformations as well as the force- and torque-curves are completely different (cf. Figs. 4.10, 4.11 and 4.12), the maximum number of iterations is again not more than two.

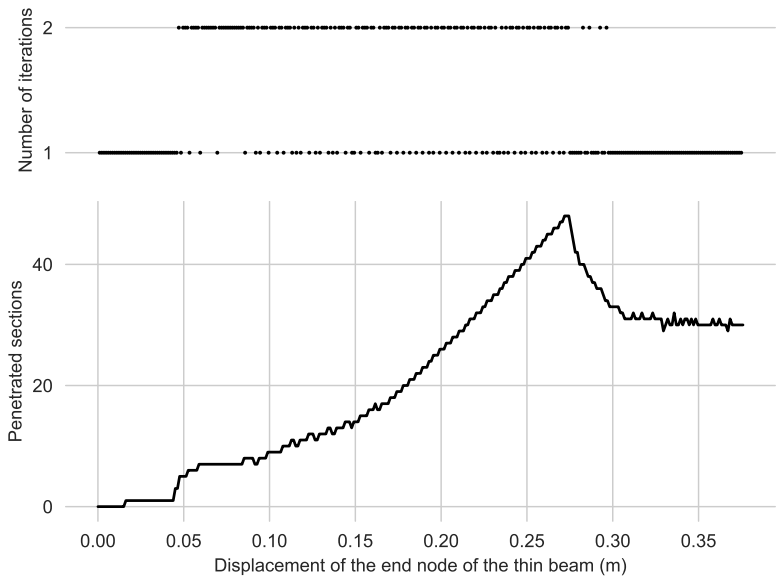

Figure 4.11: Example 2: Top: number of global iterations to reach convergence criteria: $\left\| \underline{f}_{int} + \underline{r}_c - \underline{f}_{ext} \right\| < 10^{-8}$; Bottom: evolution of the number of contact interactions between sections of the thin beam and the surface of the outer beam.

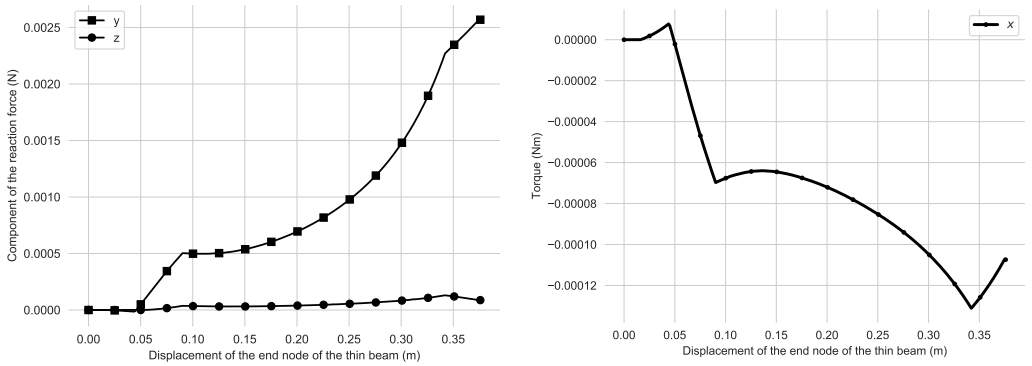

(a) (b)

Figure 4.12: Example 2: components of the reaction force (a) and torque (b) at the prescribed end of the thin beam.

Mesh convergence study

The second example is repeated with different meshes in order to show that the

results converge to the same solution. For the different meshes, the displacement field of the inner beam is compared to a reference solution, which is obtained with 180 elements for the inner beam. Figs. 4.13a and 4.13b show that the displacement fields converge to the reference displacement fields.

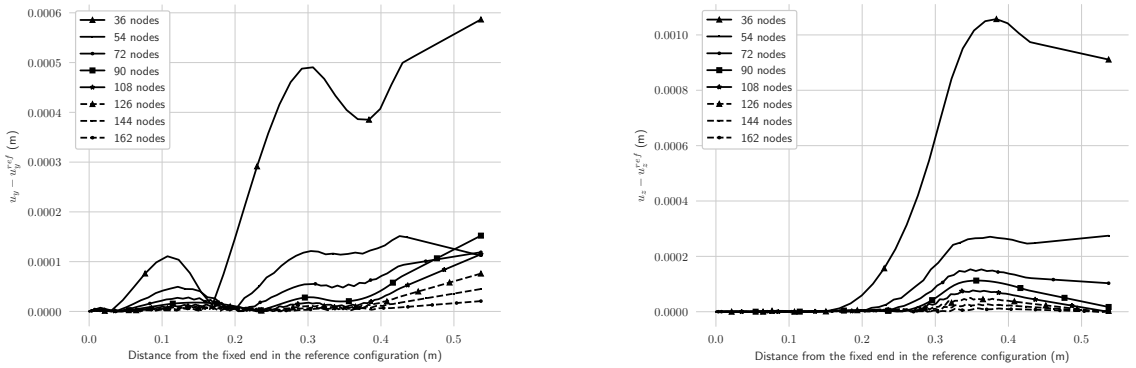

(a) (b)

Figure 4.13: Effect of the mesh refinement on the final displacement of the nodes of the thin beam. The displacements in the final configuration are compared to the ones with the finest mesh (180 nodes) (a) Difference of the $Y-$displacements ; (b) Difference of the $Z-$displacements.

4.4 Discussion

The beam-inside-beam contact framework presented in this contribution is the first approach to ensure that an inner beam remains embedded inside an outer, hollow beam because all existing contact frameworks for beams aim to achieve the opposite: they repel beams from each other.

The advantage of using beams over conventional 3D finite elements is the potential to achieve faster simulations (although our particular implementation can surely not compete with frameworks such as SOFA [23]). The disadvantage of using beams over conventional finite elements is a reduction of the simulation accuracy. Hence, the framework proposed in this contribution may be perceived to be beneficial if simulation speed is preferred over simulation accuracy. On the other hand,

our framework can handle slender medical instruments with both circular and elliptical cross-sections, whereas the frameworks of [1, 49, 18, 27, 83] have only been demonstrated to handle circular ones. The reason that beams, formulated to rapidly simulate the mechanical behavior of slender bodies, are faster for mechanical simulations involving contact is twofold. First, beams come with fewer degrees of freedom (i.e. kinematic variables) than if the tubes' surfaces are represented by conventional finite elements, because in most beam theories the beams' cross-sections are rigid (*i.e.* the cross-sections cannot deform). Hence, the entire beam's geometry can be constructed from its centroid line description and the cross-sections' orientation. This drastically reduces the number of degrees of freedom necessary to discretise a slender body. Second, and seemingly even more important is the fact that the penetration can be quantified for an entire (rigid) cross-section at once, which drastically reduces the number of local problems that need to be solved.

One possible extension of the beam-inside-beam contact framework is the incorporation of fluid flows inside the hollow beam to represent blood flow. Frictional sliding between the inner and outer beam also seems like a necessary extension for the future. Surrounding tissues were furthermore neglected in the presented simulations, which did not focus on a particular type of intervention in order to highlight the generality of the framework.

The accuracy of the framework is not as high as that of the frameworks presented in [18, 49, 83, 35]. However, simulation speed and simulation accuracy are two competing interests and if speed is preferred over accuracy, our new framework is a promising alternative to existing frameworks.

Appendix

IV.A Treatment of contact at the ends of the outer beam.

In the numerical examples of Section 4.3, the section at the tip of the inner beam slides along the wall of the outer beam until it exits the outer beam (first two images in Fig. IV.A.1). The occurrence of this is monitored, because when it occurs, the contact constraint between the section attached to the last integration point of the inner beam and the outer beam must be deactivated and the increment repeated. Then, no contact interactions to embed the inner beam inside the outer beam may be left. If this is the case, a sudden release of the inner beam may occur which makes the simulation diverge (bottom left in Fig. IV.A.1).

To avoid this, an additional constraint is added to the outlet of the hollow beam. It enforces the section at the edge of the outer beam to be in contact with the surface of the inner beam (bottom right in Fig. IV.A.1). The local problem to that must be solved to quantify penetration is again given by Eq. (4.17), except that this time $\mathcal{B}^{\mathrm{I}}$ denotes the outer beam and $\mathcal{B}^{\mathrm{J}}$ the inner one. The method of Lagrange multipliers is used to enforce this constraint. The reason is that if the penalty method is employed and the section at the end of the outer beam is detached from the surface of the inner beam, even with the constraint just added, no penetration is detected and the sudden release of the inner tube would not be avoided.

Ideally, a contact at the closest pair of surface points [24, 25] should be applied at the tip of the inner beam in Fig. IV.A.1. In this case, the treatment discussed in this session would not be required. However, this necessitates a framework able to automatically decide which type of contact element to use, as in the ABC formulation

of Meier et al. [56]. The development of such a framework for shear-deformable beams with elliptical cross-sections remains for future work.

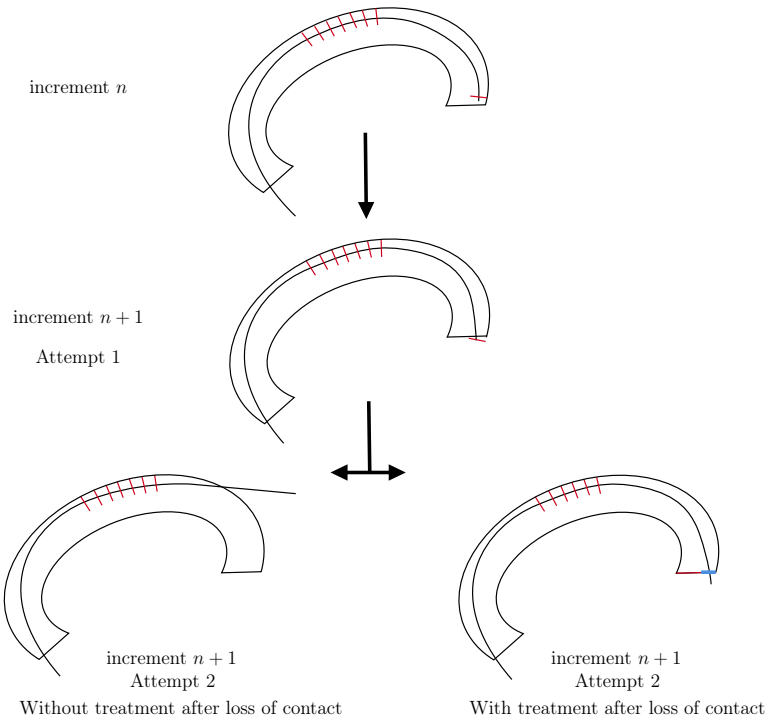

Figure IV.A.1: Sliding of the inner beam outside the limits of the outer beam. Penetrated sections are shown in red. At increment n, the last section placed along the inner beam is still inside the cavity. At increment $n+1$, it has slid outside the cavity. Bottom left: If no treatment is applied, the contact point at the tip of the inner beam is deactivated and it results in a sudden loss of contact; bottom right: the additional constraint is enforced between the section at the end of the outer beam (in red) and the surface of the inner beam.

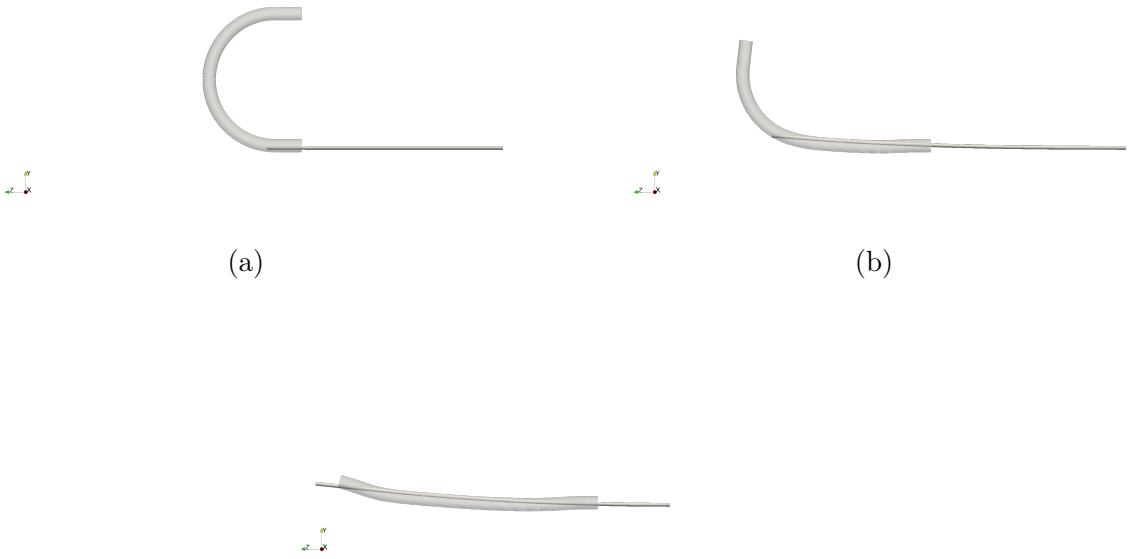

(a) (b)

(c)

Figure IV.B.1: Example 2 with a stiffer inner beam: (a) Initial configuration; (b) configuration halfway through the loading, and (c) final configuration.

IV.B Figures for Example 2 with $E = 150$ MPa for the inner beam.

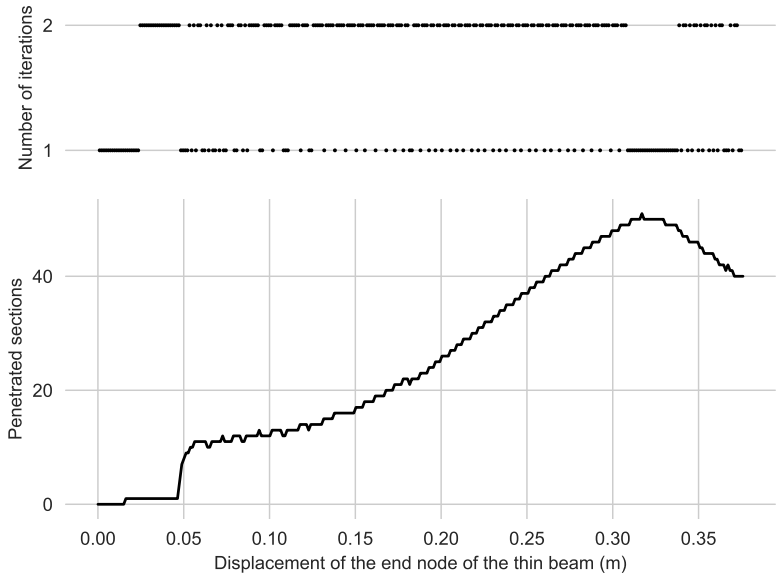

Figure IV.B.2: Example 2 with a stiffer inner beam: Top: number of global iterations to reach convergence criteria: $\left\| \underline{f}_{int} + \underline{r}_c - \underline{f}_{ext} \right\| < 10^{-8}$; Bottom: evolution of the number of contact interactions between sections of the thin beam and the surface of the outer beam.

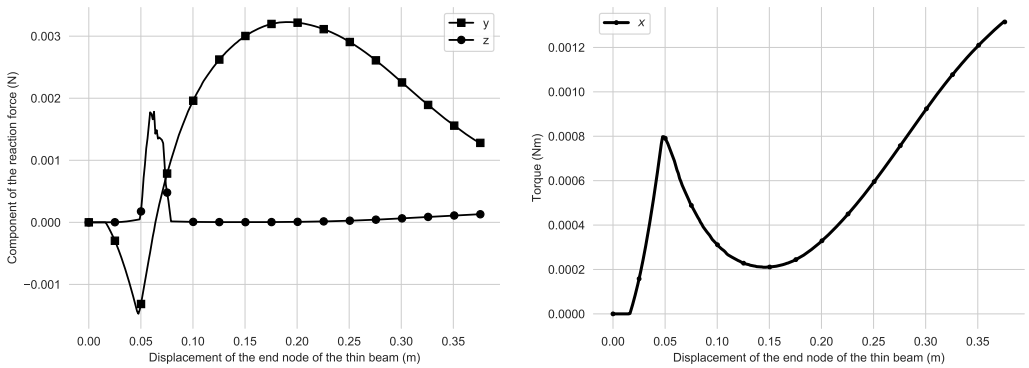

(a) (b)

Figure IV.B.3: Example 2 with a stiffer inner beam: components of the reaction force (a) and torque (b) at the prescribed end of the thin beam.

CHAPTER V

Frictional interactions for non-localised beam-to-beam and beam-inside-beam contact

5.1 Introduction

Beams are widely used to describe the mechanical behaviour of slender structures [77, 78, 29, 57, 58, 56, 61]. The contact description between the beams (with or without friction [25, 38]) is often an essential part of these mechanical models.

Large-deformation frameworks to treat contact between beams with rigid cross-sections can be classified in different ways. Most of the schemes are formulated for shear-undeformable beams [62, 89, 95, 50], whereas others can also treat shear-deformable beams [53]. Most schemes can only be used for beams with circular cross-sections [62, 89, 95], whereas a few can also be used for beams with elliptical cross-sections [50, 24, 25, 53, 54, 52]. Most schemes can only be used for small contact areas [24, 25] (assuming point-wise contact interactions), whereas others are able to treat finite contact areas [62, 38, 53, 54, 52]. Of all the frameworks able to treat frictional contact between beams, only a few are capable to not only account for frictional sliding in the beams' axial directions, but also in the circumferential directions [25, 39].

Finally, all frameworks are beam-to-beam contact schemes, *i.e.* they repel beams if they touch each other. Only recently, we have proposed a beam-inside-beam contact approach that enforce one beam to remain *inside* another beam [52]. Its goal

is the exact opposite of beam-to-beam contact schemes: to keep beams embedded inside each other.

To date, no frictional beam-to-beam contact scheme exists for the general case of shear-deformable beams, with both circular and elliptical cross-sections, that experience finite contact areas (non-localized contacts). A frictional beam-inside-beam contact scheme is also missing.

The aim of this contribution is to fill this gap by extending our previously developed contact frameworks [54, 52] towards frictional interactions. Because the frameworks use the true beam surfaces to quantify penetration - instead of surfaces implicitly deduced from the beams' centroid lines - frictional sliding is not only quantified in beams' axial direction, but also in the circumferential direction. To this end, the local problem to quantify penetration (or exclusion) does not only involve the unknown surface parameters of the master beam. It also involves one unknown surface parameter of the slave beam. This (circumferential) surface parameter describes the location of the (slave) contact point around the cross-section's perimeter for which penetration is quantified.

Although the aims of the beam-to-beam and beam-inside-beam contact frameworks are the exact opposite, their methodology is similar. Both schemes follow a master-slave approach, and select cross-sections along one of the two beams in contact (the slave). For each selected cross-section, the penetration between two beams is quantified (although arguably for the beam-inside-beam scheme it may be a called a measure of exclusion, instead of a measure of penetration). This measure is then used to establish a contact virtual work in order to repel beams from each other (for the beam-to-beam scheme) or to keep them embedded (for the beam-inside-beam scheme). The similarities between the beam-to-beam and the beam-inside-beam schemes also manifest when quantifying the amount of frictional sliding.

The structure of the paper is the following. The penalty formulation for large deformation frictional contact in the continuum setting is provided in Section 5.2. Section 5.3 details the spatial discretisation of the finite element framework and provides implementation details. Section 5.4 presents a set of multi-body numerical examples for beam-to-beam contact and beam-inside-beam contact and compares

the results of the frictional frameworks with those of the frictionless frameworks. Conclusions are provided in Section 5.5.

5.2 Space-continuous formulation

5.2.1 Parametrization of the beams' surface

We consider beams consisting of rigid cross-sections which are attached to the beam's centroid lines at the cross-sectional centers of gravity. The beams of interest can deform in two ways. First, their centroid lines can elongate, bend and revolve. Second, due to shear deformation, the normal vector to the cross-section's plane is not necessarily aligned with the tangent to the centroid line, see Fig. 5.1.

In the following, we consider beam $\mathcal{B}$ and its surface denoted by $\partial\mathcal{B}$. We also consider a two-parameter vector function, $\mathbf{x} = \mathbf{x}(\underline{h})$, that maps any surface point on $\partial\mathcal{B}$, with surface coordinates $\underline{h} = [h^1, h^2]^T$, to its location in the global coordinate system. $h^1 \in [0, L]$ denotes the arc-length parameter of the beam's undeformed centroid line $\mathbf{x}_{0c} : (0, L) \to \mathbb{R}^3$ and L denotes the length of the undeformed centroid line. $h^2 \in [0, 2\pi]$ denotes a circumferential parameter of the perimeter of the cross-section attached to $\mathbf{x}_{0c}(h^1)$ (see [24, 25, 53, 54, 52]).

The location of a surface point in the undeformed configuration can be obtained from:

$$\mathbf{x}_0 = \mathbf{x}_{0c}(h^1) + \mathbf{v}_0(\underline{h}), \tag{5.1}$$

where $\mathbf{v}_0$ denotes a vector in the plane of the cross-section attached to $\mathbf{x}_{0c}(h^1)$.

In the deformed configuration, the centroid line deforms according to:

$$\mathbf{x}_c = \mathbf{x}_{0c}(h^1) + \mathbf{u}(h^1), \tag{5.2}$$

where $\mathbf{u} : (0, L) \to \mathbb{R}^3$ denotes the centroid-line's displacement. The location of any surface point in the deformed configuration with surface coordinates $\underline{h}$ is given by:

$$\mathbf{x} = \varphi(\mathbf{x}_0) = \mathbf{x}_c(h^1) + \mathbf{v}(\underline{h}), \tag{5.3}$$

where φ denotes the deformation mapping relating the location of a surface point in the deformed configuration to its location in its undeformed configuration. As the beams' cross-sections are assumed to be rigid, there exists a rotation tensor $\mathbf{\Lambda}(\boldsymbol{\theta}, h^1) \in SO(3)$, where $SO(3)$ is the rotation group, such that:

$$\mathbf{v} = \mathbf{\Lambda}(\boldsymbol{\theta}, h^1) \cdot \mathbf{v}_0(\underline{h}), \tag{5.4}$$

where $\boldsymbol{\theta}$ denotes the field of variables used to parametrize $SO(3)$, *e.g.* quaternions [77, 78] or the smallest rotation with respect to a reference triad [57] or rotation vectors [29] as used in this work.

For further use, we define the local basis vectors at surface point $\mathbf{x}$. For $\beta \in \{1, 2\}$, the covariant tangent surface vectors are given by:

$$\boldsymbol{\tau}_\beta = \frac{\partial \mathbf{x}}{\partial h^\beta}. \tag{5.5}$$

Assuming proper orientation of $\boldsymbol{\tau}_1$ and $\boldsymbol{\tau}_2$, the outward-pointing normal unit vector to the surface is computed from:

$$\mathbf{n}\left(\underline{h}\right) = \xi \frac{\boldsymbol{\tau}_1 \times \boldsymbol{\tau}_2}{\|\boldsymbol{\tau}_1 \times \boldsymbol{\tau}_2\|}, \tag{5.6}$$

where $\xi = -1$ for the inner surface of the master body for the beam-inside-beam contact scheme (such that $\mathbf{n}$ points towards the center of the hollow beam), and 1 otherwise. Note that local basis $\{\boldsymbol{\tau}_1, \boldsymbol{\tau}_2, \mathbf{n}\}$ is not necessarily orthonormal in the deformed configuration, meaning that in general $\boldsymbol{\tau}_1 \cdot \boldsymbol{\tau}_2 \neq 0$ and $\|\boldsymbol{\tau}_\beta\| \neq 1$.

Remark: If a Geometrically Exact Beam formulation is used, $\mathbf{\Lambda}$ in Eq. (5.4) is an element of the solution. Different FE formulations exist to suitably treat the parametrization of $\mathbf{\Lambda}$ (see [60, 72]), but are not discussed here in order to not distract from the contact formulation. In our approach, we use the vector-like parametrization of three-dimensional finite rotations provided in [29].

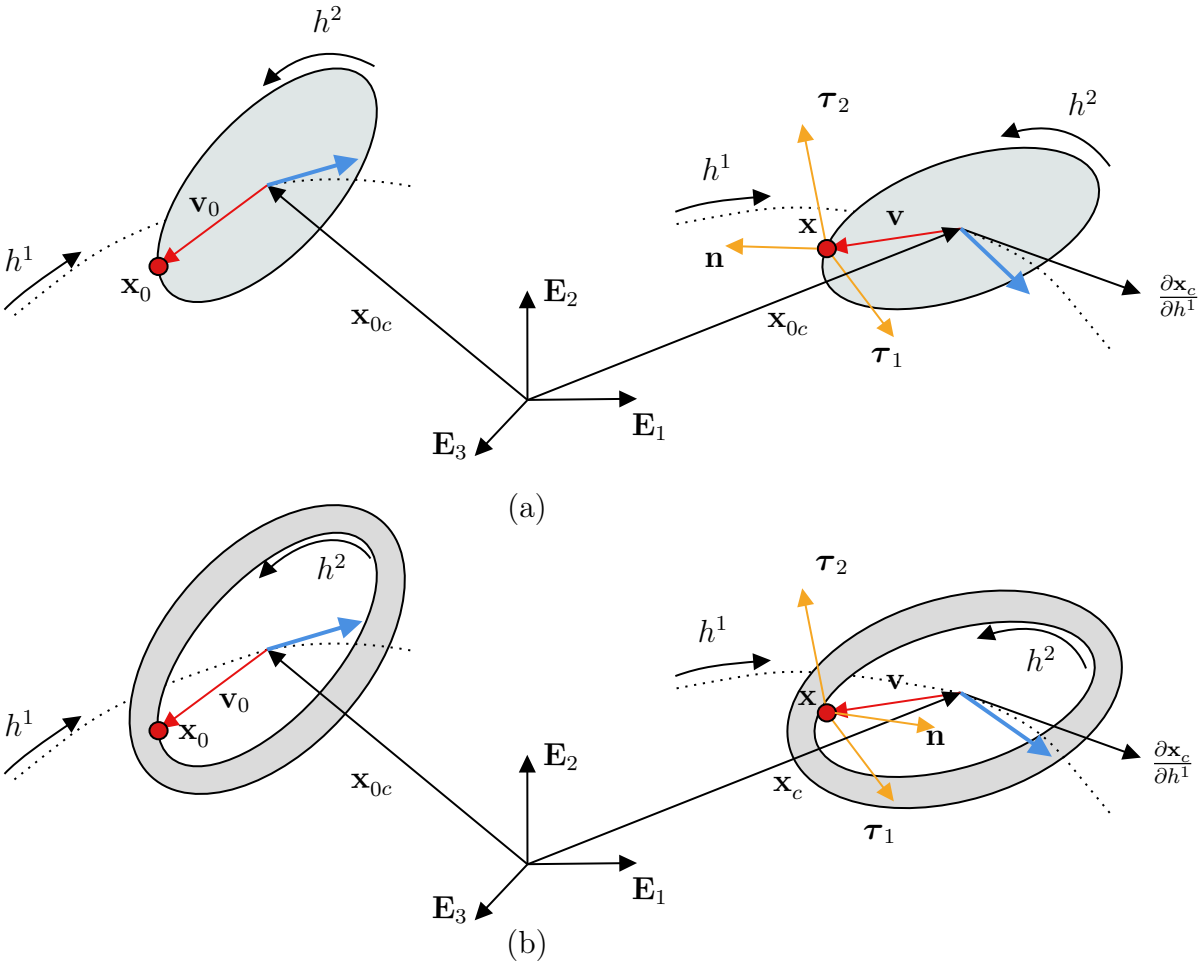

Figure 5.1: A typical cross-section (in grey) in the undeformed (left) and deformed (right) configurations for (a) a plain cross-section, (b) a hollow cross-section. The centroid-line is presented with a dotted line in both configurations. A surface point is represented with a red dot. Surface basis vectors are presented with orange arrows. The normal vector to the cross-sections' plane is presented with a blue arrow.

5.2.2 Contact kinematics

In the present contribution, we focus on non-localized contact between beams, meaning that the contact area is finite. This stands in contrast to localized contact, which occurs on a narrow area of the surface. In general, localized contact is modeled with a point-wise contact interaction, see [24, 25, 89, 95], which is not suitable for non-localized contact cases.

Although the present framework is applicable for multi-beam systems, for the sake of clarity we only discuss systems of two beams, denoted by $\mathcal{B}^{\mathrm{I}}$ and $\mathcal{B}^{\mathrm{J}}$. To repel these two beams in case of penetration (in the beam-to-beam scheme) or to keep them embedded (in the beam-inside-beam scheme), we integrate the contact virtual work along the centroid line of $\mathcal{B}^{\mathrm{I}}$. $\mathcal{B}^{\mathrm{I}}$ is therefore called the slave and $\mathcal{B}^{\mathrm{J}}$ the master [86].

5.2.2.1 Local problem and normal gap

In the following, we focus on a cross-section of $\mathcal{B}^{\mathrm{I}}$ denoted by $\mathcal{C}$, that is attached to centroid point $\mathbf{x}_c^{\mathrm{I}}(h^{\mathcal{C}})$, where $h^{\mathcal{C}}$ denotes the (fixed) arc-length parameter locating $\mathcal{C}$ along the centroid line. The perimeter of $\mathcal{C}$ is denoted $\partial\mathcal{C}$. We first quantify penetration of $\partial\mathcal{C}$ into $\partial\mathcal{B}^{\mathrm{J}}$, where $\partial\mathcal{B}^{\mathrm{J}}$ denotes the surface of $\mathcal{B}^{\mathrm{J}}$. For that purpose, we determine two surface points, one on $\partial\mathcal{C}$ and one on $\partial\mathcal{B}^{\mathrm{J}}$. These points are denoted by $\bar{\mathbf{x}}^{\mathrm{I}} = \mathbf{x}^{\mathrm{I}}(\bar{\underline{h}}^{\mathrm{I}})$ and $\bar{\mathbf{x}}^{\mathrm{J}} = \mathbf{x}^{\mathrm{J}}(\bar{\underline{h}}^{\mathrm{J}})$, respectively, and will be used to quantify penetration and relative sliding of contacting surfaces. $\mathbf{x}^{\mathrm{I}}$ and $\mathbf{x}^{\mathrm{I}}$ map surface parameters to the location of the corresponding surface point in the global coordinate system.

To determine the surface coordinates of these two points, denoted by $\bar{\underline{h}}^{\mathrm{I}}$ and $\bar{\underline{h}}^{\mathrm{J}}$, we solve a set of equations. This is usually referred to as the *local problem* or the *projection problem* [86]. The local problem presented here involves three surface parameters: the circumferential parameter of $\mathcal{C}$, $h^{\mathrm{I}2}$, and the two surface parameters of $\partial\mathcal{B}^{\mathrm{J}}$, $h^{\mathrm{J}1}$ and $h^{\mathrm{J}2}$. $h^{\mathrm{I}1}$ does not need to be determined as $\mathcal{C}$ is fixed at $\mathbf{x}_c^{\mathrm{I}}(h^{\mathrm{I}1} = h^{\mathcal{C}})$. Three of the equations we solve for are expressed as:

$$\mathbf{f}_1(\bar{\underline{q}}) = \bar{\mathbf{x}}^{\mathrm{J}} - \bar{\mathbf{x}}^{\mathrm{I}} - g\bar{\mathbf{n}}^{\mathrm{I}} = \mathbf{0}, \tag{5.7}$$

where:

$$\underline{q} = \left[h^{\mathrm{I2}}, h^{\mathrm{J1}}, h^{\mathrm{J2}}, g\right]^T, \tag{5.8}$$

denotes the array of unknowns. $\underline{\bar{q}}$ denotes the array solution of Eq. (5.7). In the following, a bar over a quantity indicates that this quantity is evaluated at the solution of the local problem.

Variable g denotes an unknown scalar, for which we can write at the solution of Eq. (5.7):

$$g_N = \bar{g} = (\bar{\mathbf{x}}^{\mathrm{J}} - \bar{\mathbf{x}}^{\mathrm{I}}) \cdot \bar{\mathbf{n}}^{\mathrm{I}} = \bar{\mathbf{g}} \cdot \bar{\mathbf{n}}^{\mathrm{I}}, \tag{5.9}$$

where $\bar{\mathbf{g}}$ denotes the so-called "gap vector". Hence, $\bar{g} = g_N$ denotes the amount of penetration.

As the system of equations of Eq. (5.7) is under-determined, an additional equation is needed. Here, we impose that at the solution of the local problem, $\mathbf{n}^{\mathrm{I}}$ and $\mathbf{n}^{\mathrm{J}p}$ must be orthogonal to $\boldsymbol{\tau}_2^{\mathrm{J}}$ (see Fig. 5.2). $\mathbf{n}^{\mathrm{J}p}$ denotes the (normalized) projection of $\mathbf{n}^{\mathrm{J}}$ on the plane spanned by vectors $\boldsymbol{\tau}_2^{\mathrm{I}}$ and $\mathbf{n}^{\mathrm{I}}$. This plane has the following normal unit vector:

$$\tilde{\mathbf{n}}^{\mathrm{I}} = \frac{\boldsymbol{\tau}_2^{\mathrm{I}} \times \mathbf{n}^{\mathrm{I}}}{\|\boldsymbol{\tau}_2^{\mathrm{I}} \times \mathbf{n}^{\mathrm{I}}\|}. \tag{5.10}$$

$\mathbf{n}^{\mathrm{J}p}$ is then obtained from:

$$\mathbf{n}^{\mathrm{J}p} = \frac{\mathbf{n}^{\mathrm{J}} - (\mathbf{n}^{\mathrm{J}} \cdot \tilde{\mathbf{n}}^{\mathrm{I}})\tilde{\mathbf{n}}^{\mathrm{I}}}{\|\mathbf{n}^{\mathrm{J}} - (\mathbf{n}^{\mathrm{J}} \cdot \tilde{\mathbf{n}}^{\mathrm{I}})\tilde{\mathbf{n}}^{\mathrm{I}}\|}. \tag{5.11}$$

The additional equation to be added to the system reads:

$$f_2(\underline{\bar{q}}) = \kappa(\mathbf{n}^{\mathrm{I}} \cdot \boldsymbol{\tau}_2^{\mathrm{J}} + \mathbf{n}^{\mathrm{J}p} \cdot \boldsymbol{\tau}_2^{\mathrm{J}}) = 0, \tag{5.12}$$

where κ has the dimension of length and is used to ensure that components of $\mathbf{f}_1$ and f_2 have the same units (if $\mathcal{C}$ is elliptical, we can for example set $\kappa = a^{\mathcal{C}}$ where $a^{\mathcal{C}}$ denotes the dimension of $\mathcal{C}$ along its largest semi-axis). The final set of equations of

the local problem is abbreviated as follows:

$$\underline{f}(\underline{\bar{q}}) = \left[\mathbf{f}_1(\underline{\bar{q}}), f_2(\underline{\bar{q}})\right]^T = \underline{0}. \tag{5.13}$$

Eq. (5.13) is nonlinear and can be solved using Newton's method for which the following Jacobian is required:

$$\underline{\underline{H}}(\underline{q}) = \frac{\partial \underline{f}}{\partial \underline{q}}. \tag{5.14}$$

5.2.2.2 Sliding increment

The true novelty of this contribution lies in the treatment of frictional contact interactions. We introduce the formulation directly in the time-discretized setting *i.e.* we assume that the simulation time is divided in numerous time increments. From here onward, subscript n refers to the previous time increment. If no subscript is present, the quantity refers to the current time increment.

The particularity of the contact kinematics employed in this contribution prevents the use of conventional frictional frameworks, as for instance developed for the Node-to-surface (NTS) approach [47, 45]. In the NTS approach, it is sufficient to measure the relative sliding of the slave node (that has fixed surface coordinates) over the master surface. In the present contribution however, also the circumferential coordinate of the slave contact point ($\bar{h}^{\mathrm{I2}}$) generally varies between two time increments.

In more detail, as h^{I2} is not fixed, $\bar{\mathbf{x}}^{\mathrm{I}}$ can be located at a different surface point on $\partial\mathcal{C}$ in the previous and current configuration. Thus, both slidings of $\bar{\mathbf{x}}^{\mathrm{I}}$ and $\bar{\mathbf{x}}^{\mathrm{J}}$ must be incorporated. The change in the location of $\bar{\mathbf{x}}^{\mathrm{I}}$ between two increments can be approximated as (see Fig. 5.3):

$$\Delta\bar{\mathbf{x}}^{\mathrm{I}} = \mathbf{x}_n^{\mathrm{I}}(\underline{\bar{h}}^{\mathrm{I}}) - \mathbf{x}_n^{\mathrm{I}}(\underline{\bar{h}}_n^{\mathrm{I}}), \tag{5.15}$$

where:

- $\mathbf{x}_n^{\mathrm{I}}$ maps any surface coordinates to the location of the associated surface point

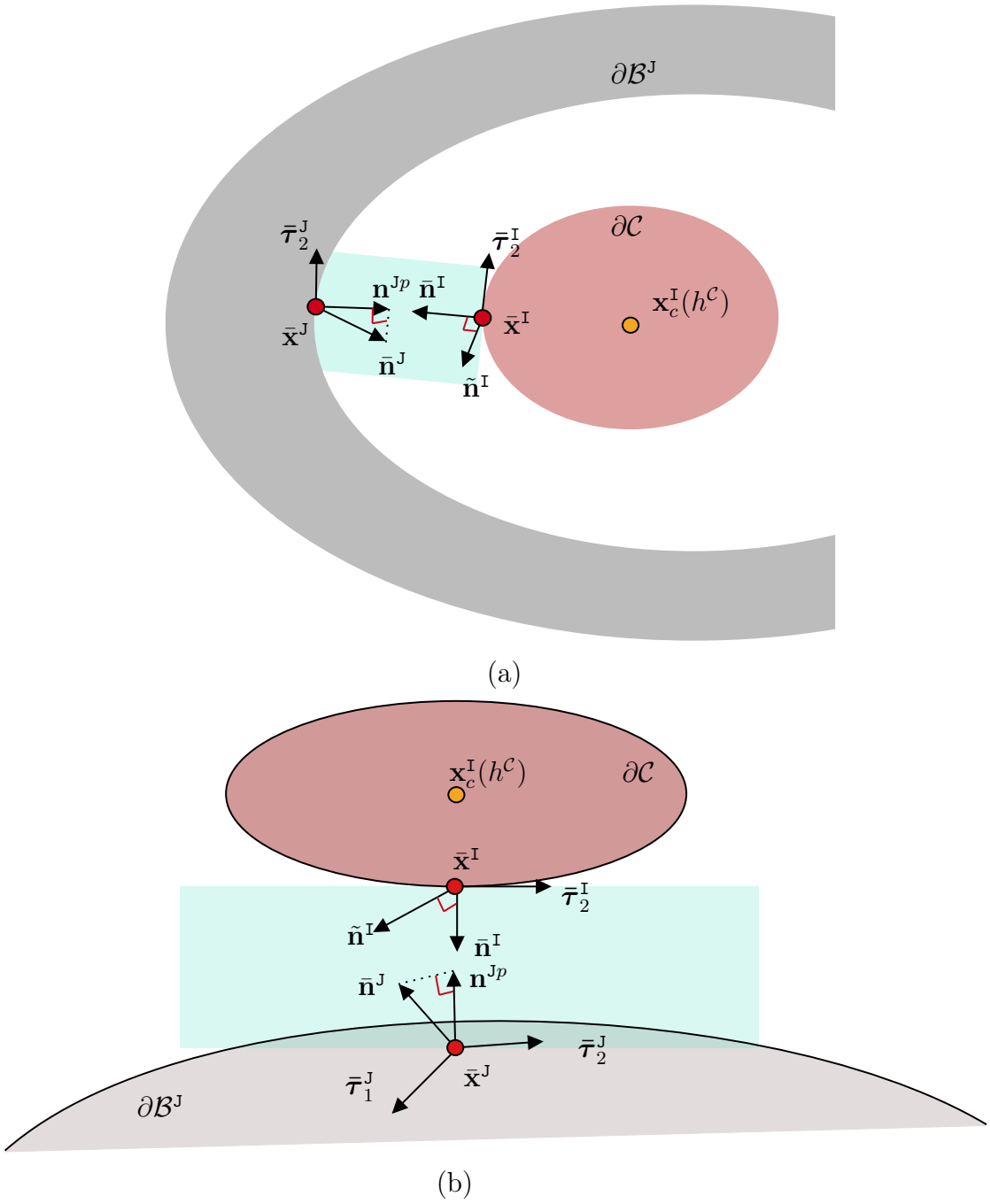

Figure 5.2: Solution of the local problem for (a) beam-inside-beam contact; (b) beam-to-beam contact. The slave cross-section attached to $\mathbf{x}_c^{\mathrm{I}}(h^{\mathcal{C}})$ is shown in red. The master surface is shown in grey.

in the *previous* configuration in the global coordinate system,

- $\bar{\underline{h}}_n^{\mathtt{I}}$ denotes surface coordinates (part of the solution $\bar{\underline{q}}_n$ of the local problem) of the previously converged simulation increment.

Similarly, we introduce $\Delta\bar{\mathbf{x}}^{\mathtt{J}}$ as:

$$\Delta\bar{\mathbf{x}}^{\mathtt{J}} = \mathbf{x}_n^{\mathtt{J}}(\bar{\underline{h}}^{\mathtt{J}}) - \mathbf{x}_n^{\mathtt{J}}(\bar{\underline{h}}_n^{\mathtt{J}}). \tag{5.16}$$

The fact that the position of the contact points are mapped to the previous configuration ensures that the sliding distance is not affected by rigid body motions. Note that $\mathbf{x}_n^{\mathtt{I}}(\bar{\underline{h}}_n^{\mathtt{I}})$ and $\mathbf{x}_n^{\mathtt{J}}(\bar{\underline{h}}_n^{\mathtt{J}})$ are history variables stored at the end of each simulation increment, while $\mathbf{x}_n^{\mathtt{I}}(\bar{\underline{h}}^{\mathtt{I}})$ and $\mathbf{x}_n^{\mathtt{J}}(\bar{\underline{h}}^{\mathtt{J}})$ are to be computed for every new configuration. Further on, in the spatially-discretized setting, the proposed measure is able to handle cases where $\mathbf{x}_n^{\mathtt{J}}(\bar{\underline{h}}^{\mathtt{J}})$ and $\mathbf{x}_n^{\mathtt{J}}(\bar{\underline{h}}_n^{\mathtt{J}})$ are located on different finite elements.

We express $\Delta\mathbf{g}_T$, the increment of tangential sliding between two increments, as the following frame-indifferent measure (see also Fig. 5.3):

$$\Delta\mathbf{g}_T = \Delta g_T^{\alpha}\boldsymbol{\tau}_{\alpha}^{\mathtt{I}}(\bar{\underline{h}}^{\mathtt{I}}), \tag{5.17}$$

where the summation on repeated indices holds. Components Δg_T^{α} are approximated by the following projection:

$$\Delta g_T^{\alpha} = (\Delta\bar{\mathbf{x}}^{\mathtt{I}} - \Delta\bar{\mathbf{x}}^{\mathtt{J}}) \cdot \boldsymbol{\tau}_n^{\mathtt{I}\alpha}(\bar{\underline{h}}_n^{\mathtt{I}}), \tag{5.18}$$

where $\boldsymbol{\tau}_n^{\mathtt{I}\alpha}$ denotes the contravariant basis vector in the configuration from the previous time increment:

$$\boldsymbol{\tau}_n^{\mathtt{I}\alpha} = M_n^{\mathtt{I}\alpha\beta}\boldsymbol{\tau}_{n\beta}^{\mathtt{I}}. \tag{5.19}$$

$M_n^{\mathtt{I}\alpha\beta}$ are contravariant components of the metric tensor of the surface of $\mathcal{B}^{\mathtt{I}}$ in the previous configuration, $\partial\mathcal{B}_n^{\mathtt{I}}$:

$$\begin{bmatrix} M_n^{\mathtt{I}11} & M_n^{\mathtt{I}12} \\ M_n^{\mathtt{I}21} & M_n^{\mathtt{I}22} \end{bmatrix} = \begin{bmatrix} M_{n11}^{\mathtt{I}} & M_{n12}^{\mathtt{I}} \\ M_{n21}^{\mathtt{I}} & M_{n22}^{\mathtt{I}} \end{bmatrix}^{-1}, \tag{5.20}$$

where covariant components of the metric tensor of $\partial\mathcal{B}_n^{\mathtt{I}}$ are given by:

$$M_{n\alpha\beta}^{\mathtt{I}} = \boldsymbol{\tau}_{n\alpha}^{\mathtt{I}} \cdot \boldsymbol{\tau}_{n\beta}^{\mathtt{I}}, \tag{5.21}$$

and in Eq. (5.21), $\boldsymbol{\tau}_{n\beta}^{\mathtt{I}}$ denotes a covariant surface tangent vector in the previous configuration at surface coordinates $\underline{h}_n^{\mathtt{I}}$ defined as:

$$\boldsymbol{\tau}_{n\beta}(\underline{h}_n^{\mathtt{I}}) = \frac{\partial \mathbf{x}_n^{\mathtt{I}}(\underline{h}_n^{\mathtt{I}})}{\partial h_n^{\mathtt{I}\beta}}. \tag{5.22}$$

The measure of relative sliding proposed in Eq. (5.17) is validated in a series of numerical examples presented in the Appendix.

Remark: In Eq. (5.18), we use tangent surface vectors at $\mathbf{x}_n^{\mathtt{I}}(\bar{\underline{h}}_n^{\mathtt{I}})$ to project vector $\Delta\bar{\mathbf{x}}^{\mathtt{I}} - \Delta\bar{\mathbf{x}}^{\mathtt{J}}$. Another possibility would have been to use vectors of the tangent plane at $\mathbf{x}_n^{\mathtt{I}}(\bar{\underline{h}}^{\mathtt{I}})$. However, the tangent surface vector at $\mathbf{x}_n^{\mathtt{I}}(\bar{\underline{h}}^{\mathtt{I}})$ are deformation-dependent via the coupling between $\bar{\underline{q}}$ and $\underline{p}^{\mathtt{IJ}}$, see Section 5.2.3.4. Thus, the first solution is adopted in this work.

Remark: If one assumes exact normal contact in the previous time increment such that:

$$\mathbf{x}_n^{\mathtt{I}}(\bar{\underline{h}}_n^{\mathtt{I}}) = \mathbf{x}_n^{\mathtt{J}}(\bar{\underline{h}}_n^{\mathtt{J}}), \tag{5.23}$$

then the right-hand-side of Eq. (5.18) reduces to:

$$\Delta g_T^{\alpha} = \left(\mathbf{x}_n^{\mathtt{J}}(\bar{\underline{h}}^{\mathtt{J}}) - \mathbf{x}_n^{\mathtt{I}}(\bar{\underline{h}}^{\mathtt{I}})\right) \cdot \boldsymbol{\tau}_n^{\mathtt{I}\alpha}(\bar{\underline{h}}_n^{\mathtt{I}}). \tag{5.24}$$

In this case, no internal variables would need to be stored from the previous increment, while $\mathbf{x}_n^{\mathtt{I}}(\bar{\underline{h}}_n^{\mathtt{I}})$ and $\mathbf{x}_n^{\mathtt{J}}(\bar{\underline{h}}_n^{\mathtt{J}})$ are needed in Eq. (5.18). In the present contribution, however, we use Eq. (5.18) because the penalty method is used (see below). Thus, condition (5.23) is not exactly fulfilled.

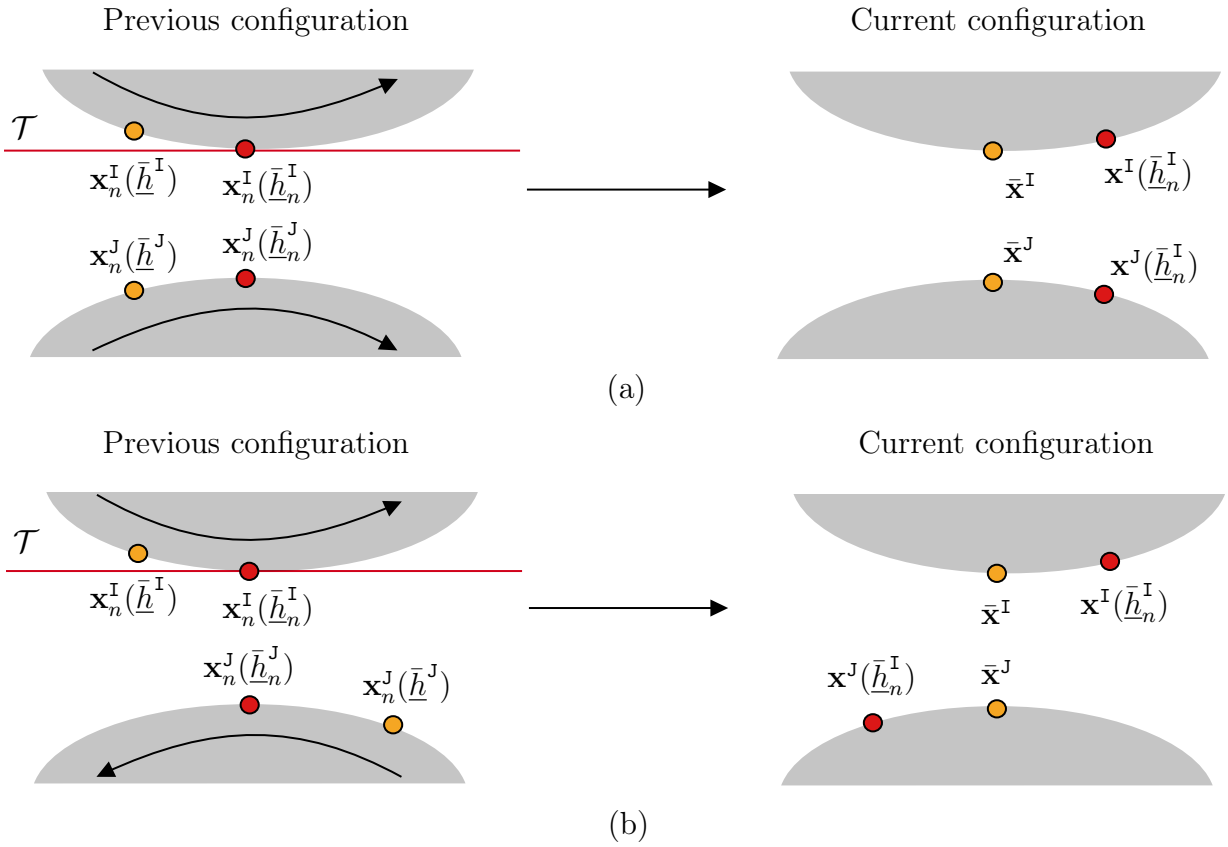

Figure 5.3: Cross-sectional view of the previous (left) and current (right) configuration of (a) two cross-sections perfectly rolling at two successive time increments; (b) Two cross-sections rotating in opposite direction causing relative displacement of contact points. The plane $\mathcal{T}$ shown as a red line is spanned by vectors $\boldsymbol{\tau}_n^{\mathtt{I}1}(\underline{\bar{h}}^{\mathtt{I}})$ and $\boldsymbol{\tau}_n^{\mathtt{I}2}(\underline{\bar{h}}^{\mathtt{I}})$ used in the projection of Eq. (5.18). Contact points in the current configuration are shown as red dots and contact points in the previous configuration as orange dots.

5.2.3 Contact constraints, their regularization and contact virtual work.

5.2.3.1 Normal contact

For a given cross-section $\mathcal{C}$, the impenetrability of $\partial\mathcal{C}$ and $\partial\mathcal{B}^{\mathrm{J}}$ is enforced via unilateral contact conditions:

$$g_N \geq 0 \qquad T_N < 0 \qquad g_N T_N = 0. \tag{5.25}$$

where:

$$T_N = \mathbf{T} \cdot \bar{\mathbf{n}}^{\mathrm{I}}, \tag{5.26}$$

where $\mathbf{T}$ denotes the nominal traction vector *i.e.* the traction acting in the current configuration, yet integrated over the contact area in the reference configuration.

Penalty regularization of the constraint The penalty method is employed to enforce the constraints of Eq. (5.25). Typical for the method is that after enforcing the constraint, some residual penetration remains. This can be interpreted as some compliance of the otherwise rigid cross-sections (see [54, 52]). Contact traction T_N, acting between surface points $\bar{\mathbf{x}}^{\mathrm{J}}$ and $\bar{\mathbf{x}}^{\mathrm{I}}$, is given by:

$$T_N = -\epsilon_N \langle -g_N \rangle \,, \tag{5.27}$$

where $\epsilon_N > 0$ denotes the penalty stiffness and $\langle\rangle$ denote the Macaulay brackets.

Coulomb's friction law The Coulomb friction law [40, 45, 86] is used in this work to describe the magnitude of the tangential forces. For two bodies in contact, the corresponding constraints are specified by the limit friction condition, the slip rule and the complementarity condition, respectively [47]:

$$\Phi(\mathbf{T}_T) = \|\mathbf{T}_T\| + \mu T_N \leq 0, \quad \|\Delta\mathbf{g}_T\|\,\mathbf{T}_T = \Delta\mathbf{g}_T\,\|\mathbf{T}_T\|\,, \quad \Phi\,\|\Delta\mathbf{g}_T\| = 0, \tag{5.28}$$

where $\mathbf{T}_T$ denotes the nominal frictional contact traction vector, μ the static friction coefficient, and Φ the yield function. Simply stated, Eq. (5.28) implies that if $\|\mathbf{T}_T\| <$

$-\mu T_N$, surfaces do not slide with respect to each other. If they slide, the tangential traction, $\|\mathbf{T}_T\|$, is equal to $-\mu T_N$.

5.2.3.2 Penalty regularization of Coulomb friction

The penalty regularization is applied to regularize tangential contact constraints. In practice, it means that we allow for a small elastic relative displacement of the surfaces. The tangential gap vector reads:

$$\mathbf{g}_T = \mathbf{g}_{Tel\,n\,updated} + \Delta\mathbf{g}_T, \tag{5.29}$$

where $\mathbf{g}_{Tel\,n\,updated}$ denotes the previous elastic tangent gap transferred to the current configuration (see Equations (5.30) to (5.36)). The tangential gap vector can also be split as follows:

$$\mathbf{g}_T = \mathbf{g}_{Tel} + \Delta\mathbf{g}_{Tsl}, \tag{5.30}$$

where $\mathbf{g}_{Tel}$ denotes the elastic part of $\mathbf{g}_T$ and $\Delta\mathbf{g}_{Tsl}$ the increment in irreversible tangential sliding. Both quantities can be obtained from a return-mapping procedure, see Eq. (5.41) and thereof.

Transfer of $\mathbf{g}_{Tel\,n}$ and update of the tangential gap The (stored) elastic gap of the previous configuration, $\mathbf{g}_{Tel\,n}$ must be transferred to the current configuration to properly treat rigid body motions [47]. In the current configuration, the contravariant components of the (projected) elastic tangential gap of the previous increment read:

$$g^{\beta}_{Tel\,n\,proj} = \mathbf{g}_{Tel\,n} \cdot \boldsymbol{\tau}^{\mathtt{I}\beta}_{n}. \tag{5.31}$$

These components are associated to covariant basis vectors (see Eq. (5.5)) in the current configuration such that:

$$\mathbf{g}_{Tel\,n\,proj} = g^{\beta}_{Tel\,n\,proj}\boldsymbol{\tau}^{\mathtt{I}}_{\beta}. \tag{5.32}$$

To preserve the elastic gap's norm, the following scaling of the components is performed:

$$g^{\beta}_{Tel\,n\,updated} = \zeta g^{\beta}_{Tel\,n\,proj}, \tag{5.33}$$

with:

$$\zeta = \begin{cases} \frac{\|\mathbf{g}_{Tel\,n}\|}{\|\mathbf{g}_{Tel\,n\,proj}\|} & \text{if } \|\mathbf{g}_{Tel\,n\,proj}\| > 10^{-8} \\ 1 & \text{otherwise} \end{cases}. \tag{5.34}$$

Contravariant components of $\mathbf{g}_T$ are computed according to:

$$g^{\beta}_{T} = g^{\beta}_{Tel\,n\,updated} + \Delta g^{\beta}_{T}, \tag{5.35}$$

such that:

$$\mathbf{g}_T = g^{\alpha}_{T}\boldsymbol{\tau}^{\mathtt{I}}_{\alpha} = g_{T\alpha}\boldsymbol{\tau}^{\mathtt{I}\alpha}. \tag{5.36}$$

Once $\mathbf{g}_T$ is computed, a return mapping procedure is employed to compute the split into $\mathbf{g}_{Tel}$ and $\Delta\mathbf{g}_{Tsl}$, see Eq. (5.30).

Return mapping procedure First, the trial state is computed, assuming $\mathbf{g}_T$ is entirely elastic:

$$\mathbf{T}_{T\,tr} = \epsilon_T \mathbf{g}_T, \tag{5.37}$$

where ϵ_T denotes the (user-defined) tangential penalty stiffness. Inserting $\mathbf{T}_{T\,tr}$ into Φ in Eq. (5.28).1 gives:

$$\Phi(\mathbf{T}_{T\,tr}) = \|\mathbf{T}_{T\,tr}\| + \mu T_N. \tag{5.38}$$

Depending on the sign of $\Phi(\mathbf{T}_{T\,tr})$, frictional sliding occurs or not, which is referred to the sliding and sticking case, respectively. The two cases are treated as shown below.

Sticking: $\Phi(\mathbf{T}_{T\,tr}) \leq 0$ In this case, $\|\mathbf{T}_{T\,tr}\|$ does not exceed the threshold value $-\mu T_N$ in Eq. (5.28). The trial state fulfills the Coulomb friction conditions Eq. (5.28) and:

$$\mathbf{T}_T = \mathbf{T}_{T\,tr}. \tag{5.39}$$

We can note here that the constraint in Eq. (5.28).3 is not respected in general as the penalty regularization allows small elastic sliding displacements, but is respected for $\Delta\mathbf{g}_{Tsl}$ as $\Phi\left\|\Delta\mathbf{g}_{Tsl}\right\| = 0$. The higher ϵ_T, the lower the magnitude of $\mathbf{g}_{Tel}$ for a given T_N. However, large values of ϵ_T increase the condition number of the global stiffness matrix [91].

Sliding: $\Phi(\mathbf{T}_{T\,tr}) > 0$ In this case $\|\mathbf{T}_{T\,tr}\|$ exceeds μT_N and Eq. (5.28).1 is violated. The trial frictional traction is corrected to take the limit frictional traction given by the Coulomb's law:

$$\mathbf{T}_T = -\mu T_N \frac{\mathbf{T}_{T\,tr}}{\|\mathbf{T}_{T\,tr}\|}. \tag{5.40}$$

In both cases ($\Phi(\mathbf{T}_{T\,tr}) \leq 0$ and $\Phi(\mathbf{T}_{T\,tr}) > 0$), the elastic tangential vector $\mathbf{g}_{Tel}$ is given by:

$$\mathbf{g}_{Tel} = \frac{1}{\epsilon_T}\ \|\mathbf{T}_T\|\ \frac{\mathbf{g}_T}{\|\mathbf{g}_T\|}, \tag{5.41}$$

where the tangential traction, $\mathbf{T}_T$, is defined by Eq. (5.39) or Eq. (5.40) for the sticking and sliding case, respectively. Note that frictional sliding increment, $\Delta\mathbf{g}_{Tsl}$, can be explicitly retrieved from Eq. (5.30).

5.2.3.3 Contact virtual work

In case of contact, a contact virtual work, $\delta\Pi_c$, is added to the virtual work equation of the system and the space of admissible variations $\mathscr{V}$ is modified [86]. In the quasi-static settings as considered in this contribution, the virtual work including contact reads:

$$\delta\Pi(\underline{p}^{\mathrm{IJ}}, \delta\underline{p}^{\mathrm{IJ}}) = \delta\Pi_{\mathcal{B}^{\mathrm{I}}}(\underline{p}^{\mathrm{I}}, \delta\underline{p}^{\mathrm{I}}) + \delta\Pi_{\mathcal{B}^{\mathrm{J}}}(\underline{p}^{\mathrm{J}}, \delta\underline{p}^{\mathrm{J}}) + \delta\Pi_c(\underline{p}^{\mathrm{IJ}}, \delta\underline{p}^{\mathrm{IJ}}) = 0,\ \forall\delta\underline{p}^{\mathrm{IJ}} \in \mathscr{V}, \tag{5.42}$$

where $\delta\Pi_{\mathcal{B}^i}$ denotes the internal and external virtual work of beam $\mathcal{B}^i$ (excluding contact interactions). Kinematic variables associated with $\mathcal{B}^i$ are stored in $\underline{p}^i$ and the associated test functions in $\delta\underline{p}^i$. $\underline{p}^i$ gathers the field of displacement of the centroid line, $\mathbf{u}^{\mathcal{B}^i}$, as well as the field of variables used to parametrize SO^3, $\boldsymbol{\theta}^{\mathcal{B}^i}$. $\underline{p}^i$ is only admissible if $\underline{p}^i(\mathbf{X}^{\mathcal{B}^i}) = \underline{p}^i_D(\mathbf{X}^{\mathcal{B}^i}),\ \forall\,\mathbf{X}^{\mathcal{B}^i} \in \partial\mathcal{B}^i_D$, where $\partial\mathcal{B}^i_D$ denotes the part of

$\partial\mathcal{B}_D^i$ where Dirichlet boundary conditions are imposed [86]. $\underline{p}^{\mathtt{IJ}} = \left[\underline{p}^{\mathtt{I}}, \underline{p}^{\mathtt{J}}\right]^T$ gathers the kinematic variables of both beams. Similarly, test functions are gathered in $\delta\underline{p}^{\mathtt{IJ}} = \left[\delta\underline{p}^{\mathtt{I}}, \delta\underline{p}^{\mathtt{J}}\right]^T$.

Following [45], by using the action-reaction principle, the contact virtual work, $\delta\Pi_c$, can be suitably expressed with respect to the slave part only. The infinitesimal virtual work produced by $dL^{\mathcal{B}^{\mathtt{I}}}$, an infinitesimal part of $\mathcal{B}^{\mathtt{I}}$'s centroid line, denoted by $d\delta\Pi_c$, can be written as in [53]:

$$d\delta\Pi_c = \left(\left(T_N \mathbf{n}^{\mathtt{I}} + \mathbf{T}_T\right) \cdot \frac{\partial \bar{\mathbf{g}}}{\partial \underline{p}^{\mathtt{IJ}}}\bigg|_{\frac{\partial \bar{q}}{\partial \underline{p}^{\mathtt{IJ}}}=0} \right) dL^{\mathcal{B}^{\mathtt{I}}}, \tag{5.43}$$

where:

$$\frac{\partial \bar{\mathbf{g}}}{\partial \underline{p}^{\mathtt{IJ}}}\bigg|_{\frac{\partial \bar{q}}{\partial \underline{p}^{\mathtt{IJ}}}=0} = \left(\frac{\partial \bar{\mathbf{x}}^{\mathtt{J}}}{\partial \underline{p}^{\mathtt{IJ}}} - \frac{\partial \bar{\mathbf{x}}^{\mathtt{I}}}{\partial \underline{p}^{\mathtt{IJ}}} \right) \bigg|_{\frac{\partial \bar{q}}{\partial \underline{p}^{\mathtt{IJ}}}=0} \cdot \delta\underline{p}^{\mathtt{IJ}}. \tag{5.44}$$

$dL^{\mathcal{B}^{\mathtt{I}}}$ is related to the differential of $h^{\mathtt{I1}}$, $dh^{\mathtt{I1}}$, by:

$$dL^{\mathcal{B}^{\mathtt{I}}} = \left\| \frac{\partial \mathbf{x}_{0c}^{\mathtt{I}}}{\partial h^{\mathtt{I1}}} \right\| dh^{\mathtt{I1}}. \tag{5.45}$$

Integration over all penetrated slave sections gives:

$$\begin{aligned} \delta\Pi_c &= \int_{h_L^{\mathtt{1I}}}^{h_U^{\mathtt{1I}}} \left(\left(T_N \mathbf{n}^{\mathtt{I}} + \mathbf{T}_T\right) \cdot \frac{\partial \bar{\mathbf{g}}}{\partial \underline{p}^{\mathtt{IJ}}}\bigg|_{\frac{\partial \bar{q}}{\partial \underline{p}^{\mathtt{IJ}}}=0} \right) dL^{\mathcal{B}^{\mathtt{I}}} \\ &= \underbrace{\int_{h_L^{\mathtt{1I}}}^{h_U^{\mathtt{1I}}} \left(\left(T_N \mathbf{n}^{\mathtt{I}}\right) \cdot \frac{\partial \bar{\mathbf{g}}}{\partial \underline{p}^{\mathtt{IJ}}}\bigg|_{\frac{\partial \bar{q}}{\partial \underline{p}^{\mathtt{IJ}}}=0} \right) dL^{\mathcal{B}^{\mathtt{I}}}}_{\delta\Pi_{c,N}} + \underbrace{\int_{h_L^{\mathtt{1I}}}^{h_U^{\mathtt{1I}}} \left(\left(\mathbf{T}_T\right) \cdot \frac{\partial \bar{\mathbf{g}}}{\partial \underline{p}^{\mathtt{IJ}}}\bigg|_{\frac{\partial \bar{q}}{\partial \underline{p}^{\mathtt{IJ}}}=0} \right) dL^{\mathcal{B}^{\mathtt{I}}}}_{\delta\Pi_{c,T}}. \end{aligned} \tag{5.46}$$

$h_L^{\mathtt{1I}}$ and $h_U^{\mathtt{1I}}$ denote the lower and upper bounds of the integral, respectively, corresponding to the first and last penetrated slave sections if we assume a unique contact area.

5.2.3.4 Variation of the local parameters, $\delta \underline{q}$

For the purpose of linearization procedure introduced below, variations of local parameters $\delta \underline{q}$ with respect to variations of the kinematic variables $\delta \underline{p}^{\mathrm{IJ}}$ are needed. Again, the corresponding equations were previously provided in [54, 52], but are repeated here to make the contribution self-contained. To express $\delta \bar{\underline{q}}$, in terms of $\delta \underline{p}^{\mathrm{IJ}}$, we start from the stationarity of local residual $\underline{f}$ in (5.13) with respect to $\underline{p}^{\mathrm{IJ}}$ as follows:

$$\frac{d\underline{f}}{d\underline{p}^{\mathrm{IJ}}} = \left(\frac{\partial \underline{f}}{\partial \underline{p}^{\mathrm{IJ}}} \right) \delta \underline{p}^{\mathrm{IJ}} + \left(\frac{\partial \underline{f}}{\partial \underline{q}} \Big|_{\underline{q}=\bar{\underline{q}}} \right) \delta \bar{\underline{q}} = \underline{0}, \tag{5.47}$$

where we recognize the Jacobian of the local problem, $\underline{\underline{H}}$, defined in Eq. (5.14). After rearrangement, we obtain:

$$\delta \bar{\underline{q}} = [\delta \bar{h}^{\mathrm{I2}}, \delta \bar{h}^{\mathrm{J1}}, \delta \bar{h}^{\mathrm{J2}}, \delta g_N]^T = \underline{\underline{A}} \delta \underline{p}^{\mathrm{IJ}}, \tag{5.48}$$

where:

$$\underline{\underline{A}} = - \left(\underline{\underline{H}} \Big|_{\underline{q}=\bar{\underline{q}}} \right)^{-1} \frac{\partial \underline{f}}{\partial \underline{p}^{\mathrm{IJ}}} \Big|_{\underline{q}=\bar{\underline{q}}} \tag{5.49}$$

5.3 Spatial discretization, discretization and linearization

5.3.1 Interpolation of the beams' surfaces

Beams $\mathcal{B}^{\mathrm{I}}$ and $\mathcal{B}^{\mathrm{J}}$ are now discretized with a series of consecutive beam finite elements (BFEs). The nodal variables of all BFEs are gathered in array $\hat{\underline{p}}$, and the associated variations in array $\delta \hat{\underline{p}}$. The finite dimensional trial and test functions, $\underline{p}^h$ and $\delta \underline{p}^h$, obtained by combining $\hat{\underline{p}}$ and $\delta \hat{\underline{p}}$ to properly chosen interpolation functions, replace their infinite dimensional counterparts $\underline{p}^{\mathrm{IJ}}$ and $\delta \underline{p}^{\mathrm{IJ}}$, respectively.

A variety of beam finite elements exists [56]. They usually differ by whether or not shear deformations can occur, by the type of rotational variables used, the interpolation schemes employed for the different types of variables and the treatment of locking. In order to remain as general as possible, we do not restrict ourselves to one specific type of beam finite element in this section. We assume that the discretized

surface is sufficiently smooth. In the numerical examples in Section 5.4, however, we have used two-nodes beam elements with rotation vectors as rotational variables. The associated discretized surface is discontinuous with gaps and overlappings at the nodes. To overcome this problem, we work with an alternative surface which possesses the desired continuity, which was previously introduced in [53]. Thus, each contact element constructed for every integration point involves two beam finite-elements on the slave side and two on the master side. The contact element's nodal variables are denoted as $\underline{\hat{p}}_e$ (see below).

In the following, we detail the procedure to obtain the contact contributions to the global force vector and the global stiffness matrix, denoted by $\underline{r}_g$ and $\underline{\underline{K}}_g$, respectively.

5.3.2 Contact residual and stiffness

The discretized form of the virtual work in Eq. (5.42) leads to a set of nonlinear equations. Newton's method is generally used to iteratively determine global solution $\underline{\hat{p}}^{sol}$ of the virtual work statement. This requires the linearization of Eq. (5.42) around an estimate of $\underline{\hat{p}}^{sol}$, denoted $\underline{\hat{p}}$, which yields:

$$\delta\Pi(\underline{\hat{p}} + \triangle\underline{\hat{p}}, \delta\underline{\hat{p}}) \simeq \delta\Pi(\underline{\hat{p}}, \delta\underline{\hat{p}}) + \underline{\underline{\triangle\delta\Pi}}(\underline{\hat{p}}, \delta\underline{\hat{p}})\triangle\underline{\hat{p}} = \delta\underline{\hat{p}}^T(\underline{r}_g + \underline{\underline{K}}_g\triangle\underline{\hat{p}}) \simeq 0, \quad (5.50)$$

where $\triangle\underline{\hat{p}}$ denotes an increment of the nodal variables. The global residual force column, $\underline{r}_g$, reads:

$$\underline{r}_g(\underline{\hat{p}}) = \underline{f}_{int}(\underline{\hat{p}}) + \underline{r}_c(\underline{\hat{p}}) - \underline{f}_{ext}(\underline{\hat{p}}), \quad (5.51)$$

where $\underline{f}_{int}$ denotes the internal force column stemming from the contributions of all BFEs, and $\underline{f}_{ext}$ the external force column. $\underline{r}_c$ contains all the (assembled) contact contributions from all contact elements, where a contact element refers here to all cross-sections attached to an integration point (see below) along $\mathcal{B}^{\mathrm{I}}$'s centroid line and their projection on discretized surface $\partial\mathcal{B}^{\mathrm{J}}$.

Since $\underline{f}_{ext}$ generally does not depend on $\underline{\hat{p}}$, the global stiffness obtained after the

linearization of $\underline{r}_g$, can be decomposed as follows:

$$\underline{\underline{K}}_g = \underline{\underline{K}}_{int} + \underline{\underline{K}}_c, \tag{5.52}$$

where $\underline{\underline{K}}_{int}$ denotes the stiffness matrix associated with the BFEs, and $\underline{\underline{K}}_c$ denotes the stiffness matrix associated with all contact elements.

The contact virtual work consists of the contributions of all contact elements:

$$\delta\Pi_c(\underline{\hat{p}}, \delta\underline{\hat{p}}) = \sum_{e \in \mathtt{S}} \delta\Pi_{c,e}(\underline{\hat{p}}_e, \delta\underline{\hat{p}}_e), \tag{5.53}$$

where $\mathtt{S}$ denotes the set of active contact elements (*i.e.* those for which $g_N < 0$), and $\delta\Pi_{c,e}$ denotes the contact virtual work associated with contact element e. $\underline{\hat{p}}_e$ denotes the column of nodal variables involved in this contact element.

If no smoothing procedure of the surface is required, each contact element involves two BFEs: the first one is part of the discretization of $\mathcal{B}^{\mathtt{I}}$, and the second one is part of the discretization of $\mathcal{B}^{\mathtt{J}}$. As mentioned above however, if a smoothing of the beam's surface is necessary to improve its surface continuity, each contact element depends on several BFEs of $\mathcal{B}^{\mathtt{I}}$ and of $\mathcal{B}^{\mathtt{J}}$ [47, 53, 54, 52]. The elements of $\mathcal{B}^{\mathtt{I}}$ and $\mathcal{B}^{\mathtt{J}}$ required to construct contact element e are denoted by $\mathcal{M}$ and $\mathcal{N}$, respectively. The associated nodal variables are denoted by $\underline{\hat{p}}^{\mathcal{M}}$ and $\underline{\hat{p}}^{\mathcal{N}}$ such that $\underline{\hat{p}}_e = \left[\underline{\hat{p}}^{\mathcal{M}}, \underline{\hat{p}}^{\mathcal{N}}\right]^T$. Associated nodal variations are denoted by $\delta\underline{\hat{p}}_e$.

The linearization of $\delta\Pi_c$ then reads:

$$\begin{aligned}
\delta\Pi_c(\underline{\hat{p}} + \triangle\underline{\hat{p}}, \delta\underline{\hat{p}}) &= \sum_{e \in \mathtt{S}} \delta\Pi_{c,e}(\underline{\hat{p}}_e + \triangle\underline{\hat{p}}_e, \delta\underline{\hat{p}}_e) && (5.54)\\
&\approx \sum_{e \in \mathtt{S}} \delta\Pi_c(\underline{\hat{p}}_e, \delta\underline{\hat{p}}_e) + \underline{\underline{\triangle\delta\Pi_c}}(\underline{\hat{p}}_e, \delta\underline{\hat{p}}_e)\triangle\underline{\hat{p}}_e && (5.55)\\
&\approx \sum_{e \in \mathtt{S}} \delta\underline{\hat{p}}_e^T(\underline{r}_{ce} + \underline{\underline{K}}_{ce}\triangle\underline{\hat{p}}_e). && (5.56)
\end{aligned}$$

Next, we discuss how to construct the contributions of a single contact element to the total force column and stiffness matrix. The force column and stiffness matrix

associated with element e are denoted by $\underline{r}_{ce}$ and $\underline{\underline{K}}_{ce}$. We distinguish the contributions stemming from normal and tangential contact. Hence, $\underline{r}_{ce}$ is decomposed as:

$$\underline{r}_{ce} = \underline{r}_{cNe} + \underline{r}_{cTe}, \tag{5.57}$$

where $\underline{r}_{cNe}$ and $\underline{r}_{cTe}$ denote the normal and tangential contact element contact contribution. Similarly, the contact element stiffness is decomposed as follows:

$$\underline{\underline{K}}_{ce} = \underline{\underline{K}}_{cNe} + \underline{\underline{K}}_{cTe} \tag{5.58}$$

5.3.2.1 Force vector and stiffness of a single contact element

To numerically integrate $\delta\Pi_{c,N}$ in Eq. (5.46), $n_{IP}^{\mathcal{M}}$ integration points (to which a cross-section is attached where penetration is to be quantified) are placed along $\mathcal{M}$'s centroid-line. Whether we integrate along the centroid line of a beam element or an artificial smoothed centroid line constructed from several BFEs, the variable over which we integrate is denoted by η (and hence, a mapping is constructed between h_1^M and η if necessary). The contact virtual work of the normal contact interactions reads:

$$\begin{aligned}
\delta\Pi_{cN} &= -\epsilon_N \int_{-1}^{1} \langle -g_N(\eta)\rangle \left(\delta\bar{\mathbf{g}}(\eta)\cdot\bar{\mathbf{n}}^{\mathtt{I}}(\eta)\right) \|\mathcal{J}(\eta)\|\, d\eta \\
&\approx -\epsilon_N \sum_{k}^{n_{IP}^{\mathcal{M}}} w_k \langle -g_N(\eta_k)\rangle \left(\delta\bar{\mathbf{g}}(\eta_{\mathbf{k}})\cdot\bar{\mathbf{n}}^{\mathtt{I}}(\eta_k)\right) \|\mathcal{J}(\eta_k)\| \\
&\approx \sum_{k}^{n_{IP}^{\mathcal{M}}} \left(w_k \underline{r}_{cNek}\right)^T \delta\underline{\hat{p}}_e.
\end{aligned} \tag{5.59}$$

Jacobian $\mathcal{J} = \frac{\partial h_1^{\mathcal{M}}}{\partial \eta}$ maps differential length $dh_1^{\mathcal{M}}$ to differential increment $d\eta$. The weight of the k^{th} integration point is denoted by w_k and its coordinate in the parameter space is denoted by η_k.

For a given cross-section of $\mathcal{M}$ attached to $\mathbf{x}_c(\eta_k)$, $\underline{r}_{cek}$ in Eq. (5.59) is expressed

as:

$$\underline{r}_{cNek} = -\epsilon_N \left\langle -g_N(\eta_k) \right\rangle \bar{\mathbf{n}}^{\mathtt{I}}(\eta_k) \frac{\hat{\partial}\bar{\mathbf{g}}(\eta_k)}{\hat{\partial}\underline{\hat{p}}_e}\Big|_{\frac{\partial \bar{q}}{\partial \underline{\hat{p}}_e}=\underline{\underline{0}}} \|\mathcal{J}(\eta_k)\|\,, \tag{5.60}$$

where $\frac{\hat{\partial}}{\hat{\partial}\underline{p}}$ denotes the total derivative with respect to variables $\underline{p}$ performed by the Automatic Differentiation (AD) algorithm [47, 41]. Here, the exception in automatic differentiation indicates that the variation of the gap vector, $\mathbf{g}(\eta_k)$, is not influenced by the local variables as discussed in our previous work [53]. $\underline{\underline{K}}_{cNek}$, stemming from the contribution of the k^{th} integration point, can be obtained using AD. It allows to include the implicit dependency of local variables $\bar{q}$ on global variables $\underline{p}^{\mathtt{IJ}}$ (see Eq. (5.48)):

$$\underline{\underline{K}}_{cNek} = \frac{\hat{\partial}\underline{r}_{cNek}}{\hat{\partial}\underline{\hat{p}}_e}\Big|_{\frac{\partial \bar{q}}{\partial \underline{\hat{p}}_e}=\underline{\underline{A}}}. \tag{5.61}$$

Similarly to Eq. (5.59), the numerical integration of the frictional term $\delta\Pi_{cT}$ in Eq. (5.46) governing friction reads:

$$\begin{aligned}
\delta\Pi_{cT} &= \int_{-1}^{1} \mathbf{T}_{\mathbf{T}}(\eta) \cdot \frac{\hat{\partial}\bar{\mathbf{g}}(\eta_k)}{\hat{\partial}\underline{\hat{p}}_e}\Big|_{\frac{\partial \bar{q}}{\partial \underline{\hat{p}}_e}=\underline{\underline{0}}} \|\mathcal{J}(\eta)\|\, d\eta \\
&\approx \sum_{k}^{n_{IP}^{\mathcal{M}}} w_k \mathbf{T}_T(\eta_k) \cdot \frac{\hat{\partial}\bar{\mathbf{g}}(\eta_k)}{\hat{\partial}\underline{\hat{p}}_e}\Big|_{\frac{\partial \bar{q}}{\partial \underline{\hat{p}}_e}=\underline{\underline{0}}} \|\mathcal{J}(\eta_k)\| \\
&\approx \sum_{k}^{n_{IP}^{\mathcal{M}}} \left(w_k \underline{r}_{cTek}\right)^T \delta\underline{\hat{p}}_e,
\end{aligned} \tag{5.62}$$

where:

$$\underline{r}_{cTek} = \|\mathcal{J}(\eta_k)\|\, \mathbf{T}_T(\eta_k) \cdot \frac{\hat{\partial}\bar{\mathbf{g}}(\eta_k)}{\hat{\partial}\underline{\hat{p}}_e}\Big|_{\frac{\partial \bar{q}}{\partial \underline{\hat{p}}_e}=\underline{\underline{0}}}. \tag{5.63}$$

The corresponding contribution to the tangent stiffness can once again be obtained with AD:

$$\underline{\underline{K}}_{cTek} = \frac{\hat{\partial}\underline{r}_{cTek}}{\hat{\partial}\underline{\hat{p}}_e}\Big|_{\frac{\partial \bar{q}}{\partial \underline{\hat{p}}_e}=\underline{\underline{A}}}. \tag{5.64}$$

5.3.2.2 Contribution of all contact elements

$\underline{r}_c$ and $\underline{\underline{K}}_c$, which contain the contributions of all contact elements in set $\mathtt{S}$, are assembled as follows:

$$\underline{r}_c = \mathop{\mathsf{A}}_{e\in\mathtt{S}} \sum_{k}^{n_{IP}^{\mathcal{M}}} w_k(\underline{r}_{cNek} + \underline{r}_{cTek}) = \mathop{\mathsf{A}}_{e\in\mathtt{S}} \underline{r}_{ce}, \tag{5.65}$$

$$\underline{\underline{K}}_c = \mathop{\mathsf{A}}_{e\in\mathtt{S}} \sum_{k}^{n_{IP}^{\mathcal{M}}} w_k(\underline{\underline{K}}_{cTek} + \underline{\underline{K}}_{cNek}) = \mathop{\mathsf{A}}_{e\in\mathtt{S}} \underline{\underline{K}}_{ce}. \tag{5.66}$$

where A denotes the finite-element assembly operator.

5.4 Numerical examples

In this Section, the proposed frictional framework is applied to three beam-to-beam examples and one beam-inside-beam example. So far, we have presented our contact framework without specifically referring to a certain type of beam finite-elements. In all presented simulations however, Simo-Reissner geometrically exact beam elements are used. The associated BFEs have a linearly interpolated centroid line [77, 78, 29]. This entails that the surface of a series of consecutive BFEs is C^0-continuous only if the undeformed configuration is straight. If the string of BFEs is not straight in the reference configuration, the surface associated with such strings of BFEs is not C^0-continuous and hence, contact constraints are hard (if not impossible) to apply.

An approximated but C^1-continuous surface description was proposed in [54] to alleviate this issue, see also Fig. 5.4. This surface is used in all the numerical examples below and is only used for the contact treatment; it has no influence on the employed beam theory, nor on the BFEs.

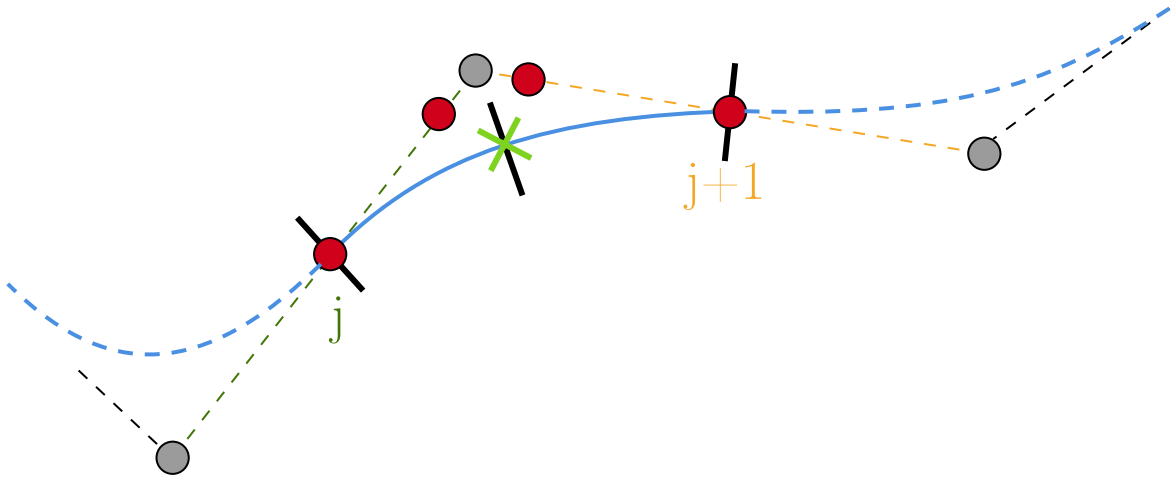

Figure 5.4: Two connected beams j and $j+1$ whose centroid lines is shown with a green and orange dashed line, respectively. Their nodes are shown with grey circles. The smoothed centroid line constructed for these two beams is shown with a plain blue curve. The associated control points are shown with red circles. As an example, the quadrature points of the three-point Gauss-Lobatto rule are indicated by black lines and the single quadrature point of the one-point Gauss-Legendre rule is indicated by a green cross.

5.4.1 Beam-to-beam contact: a 1+6 strand in tension

Strands are assemblies of wires used in tire reinforcement or as components of wire ropes. In this example, we focus on a 1+6 (a central wire surrounded by six helical wires) strand subjected to tension. The geometry of the strand is reported in Table 5.1. A gap of 0.05 mm is inserted between the central wire and its six surrounding wires in order to prevent numerical issues at the strand's ends. The Young modulus is set to $E = 188$ GPa and its Poisson ratio to 0.3.

Central wire diameter	3.94 mm
Helical wire diameter	3.73 mm
Pitch length	115 mm

Table 5.1: Geometrical parameter for the $1 + 6$ strand (a straight wire surrounded by 6 helical wires). [32]

Only one pitch of the strand is modeled. 20 BFEs are used to discretize each wire. One strand's end is clamped while the nodes at the other end are moved in the $z-$direction by a final displacement $\mathbf{u}_{end}$ such that the strand's axial engineering strain reaches $\epsilon_{strand} = 0.015$, see Fig. 5.5. Only one Gauss integration point is used per smoothed patch for the integration of the contact virtual work.

The initial penalty stiffness is estimated using the Hertz theory for parallel cylinders [70], resulting in $\epsilon_N = \frac{\pi E^2}{8(1-\nu)^2} = 82 \times 10^9$ N/m. As the tensile force gradually increases with the loading, the contact forces between the wires increase. Thus, the residual penetration due to the use of the penalty method increases. As soon as the penetration measured at an integration point according to Eq. (5.9) falls below -5% of the smaller slave beam cross-section dimension at the end of a time step, the penalty stiffness of all quadrature points of the slave BFE/smoothed curve is increased by 10% and the corresponding time step is repeated.

The tangential penalty stiffness is set to $\epsilon_T = 8.2 \times 10^9$ N/m and allows for reasonably small elastic relative displacements of the contacting surfaces without causing convergence issues. The friction coefficient is set to $\mu = 0.115$.

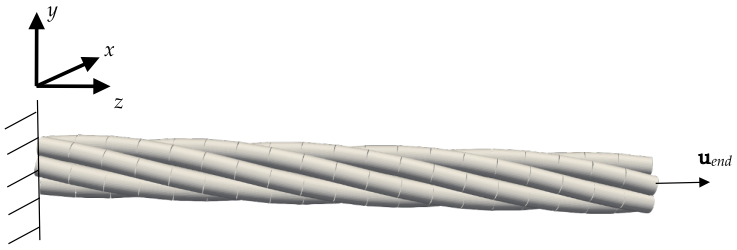

Figure 5.5: Beam-to-beam contact 5.4.1: 1+6 strand subjected to an axial displacement $\mathbf{u}_{end}$ at one of this end while the other end is clamped.

The loading is applied in 150 equally spaced time steps. Reaction forces in the axial direction are shown in Fig. 5.6. It can be observed that for small strains, the response predicted by our model has the same slope as the one predicted by Costello's theory. Fig. 5.6 also shows the reaction force predicted for two equivalent strand models in commercial FE software Abaqus©. One uses C3D8R elements (hexahedra with reduced integration and hourglass control) and the other B31 elements (linearly interpolated beam elements). Both simulations give a similar response and capture the first experimental points well. As the material behavior is elastic, the reduction of the reaction force's slope due to the wires' plastification is not captured.

Fig. 5.7 shows the evolution of the number of active contact points. Initially, the wires are not in contact due to the (small) initial gap between the core wire and the helical ones. Then, as the strand elongates, wires come in contact in the center of the strand. The contact propagates towards the strand's ends. Despite a relatively large number of contact interactions, only a few global Newton-Raphson iterations are necessary to converge, see Fig. 5.7.

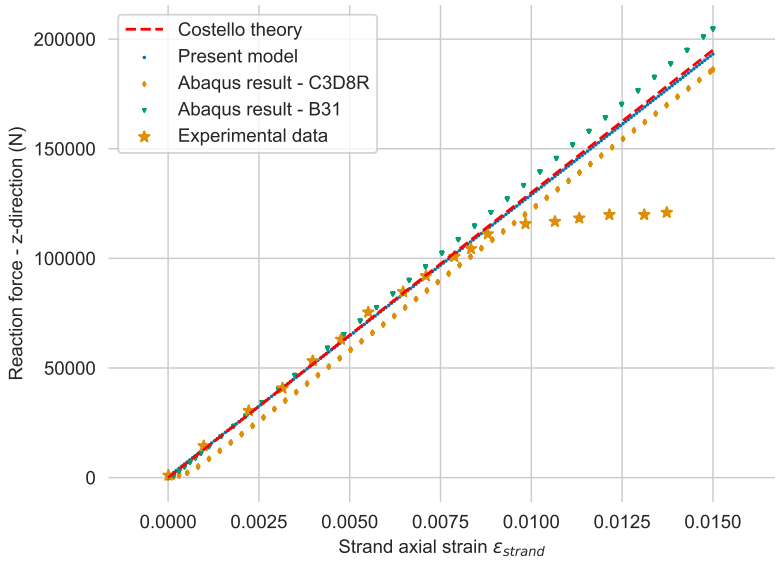

Figure 5.6: Beam-to-beam contact 5.4.1: component of the reaction forces in the $z-$direction.

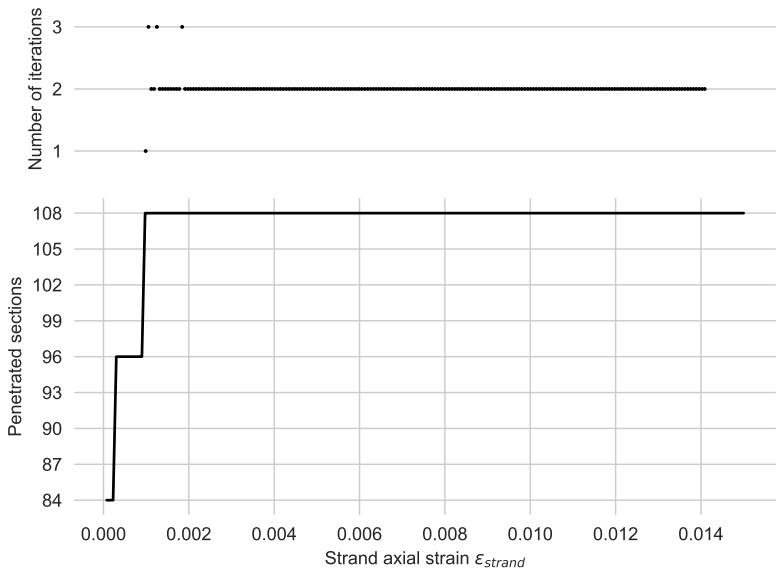

Figure 5.7: Beam-to-beam contact, example 5.4.1: top: number of global iterations to reach convergence criterion $\left\| \underline{f}_{int} + \underline{r}_c - \underline{f}_{ext} \right\| < 10^{-8}$; bottom: number of penetrated sections.

5.4.1.1 The choice of the quadrature rule and penalty stiffness

The influence of the choice of the quadrature rule and the penalty parameter is studied. The goal is to investigate if contact locking appears when more quadrature points are used and/or for high values of the penalty stiffness. The numerical example of Figure 5.5 is repeated with:

- Different number of quadrature points, nQP, going from 1 to 4 with the Gauss-Legendre quadrature rule, and from 2 to 4 with the Gauss-Lobatto quadrature rule, see [75],
- different values of ϵ_N with $\epsilon_N = k\frac{\pi E^2}{8(1-\nu)^2}$ [70] with $k \in \{0.5, 1, 2, 10\}$. The tangential penalty stiffness is always set to$\epsilon_T = \frac{\epsilon_N}{10}$.

To study the influence of the quadrature rule on contact traction T_N, the contact traction of the different contact elements between the central wire and a chosen peripheral wires have been reported for:

- $k = 1$ but a varying number of Gauss-Legendre quadrature points, see Fig. 5.8,
- 1 and 2 Gauss-Legendre quadrature points but $k \in \{0.5, 1, 2, 10\}$, see Fig. 5.9,
- $k = 1$ but a varying number of Gauss-Lobatto quadrature points, see Fig. 5.10,
- 3 Gauss-Lobatto quadrature points but $k \in \{0.5, 1, 2\}$, see Fig. 5.11.

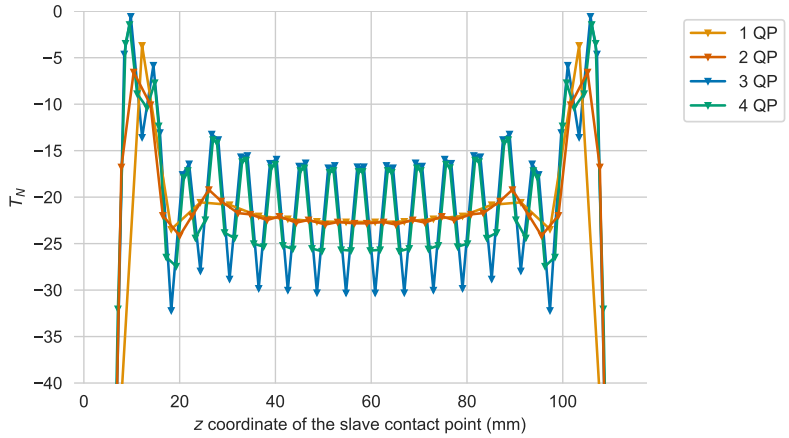

Figure 5.8: Beam-to-beam contact, example 5.4.1: influence of the number of quadrature points on contact traction T_N for a Gauss-Legendre quadrature with $k = 1$.

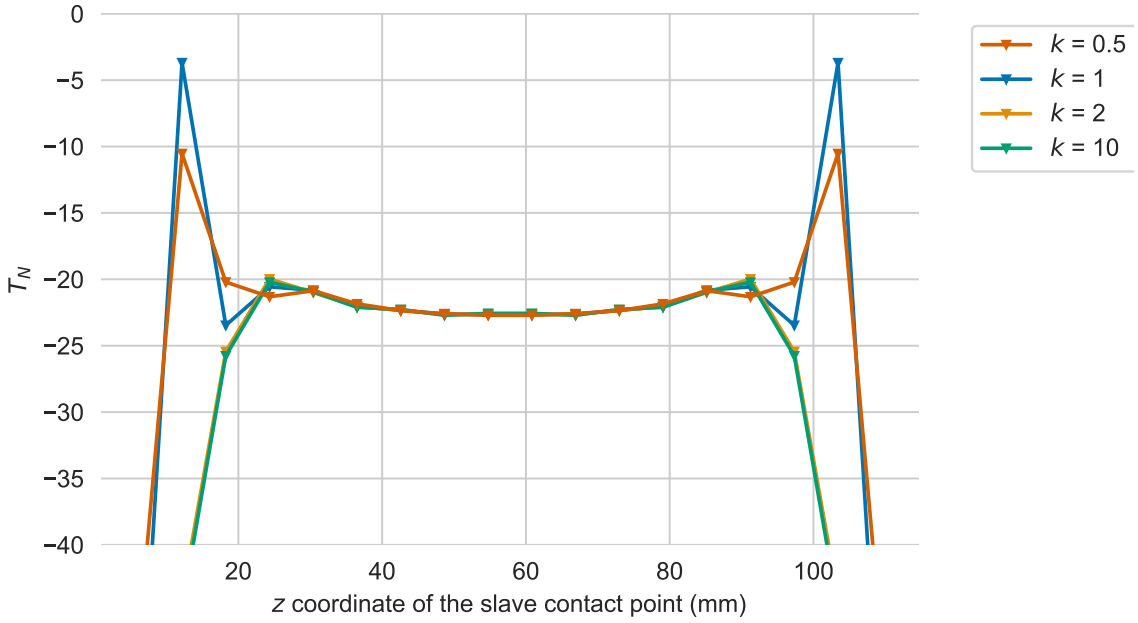

(a) $nQP = 1$

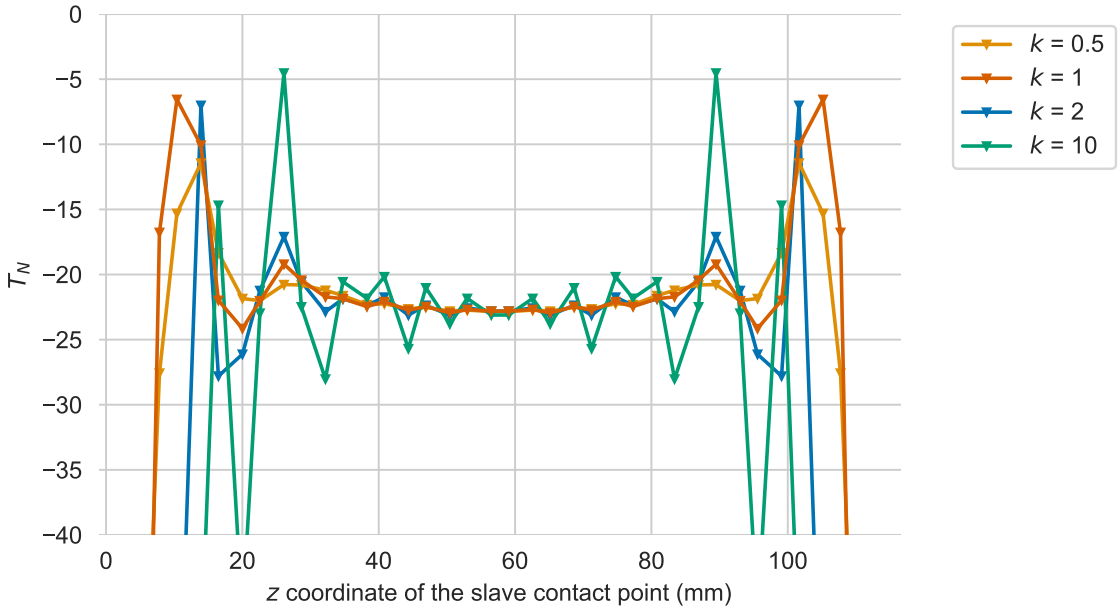

(b) $nQP = 2$

Figure 5.9: Beam-to-beam contact, example 5.4.1: influence of k on contact traction T_N for a Gauss-Legendre quadrature with (a) $nQP = 1$, and (b) $nQP = 2$.

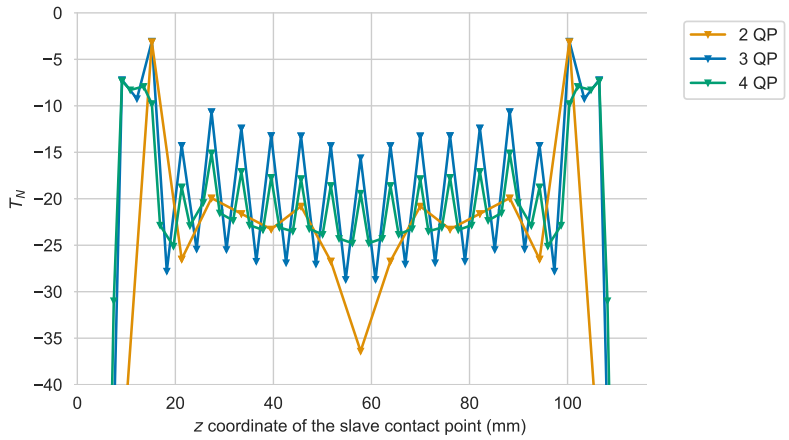

Figure 5.10: Beam-to-beam contact, example 5.4.1: influence of the number of quadrature points on contact traction T_N for a Gauss-Lobatto quadrature with $k = 1$.

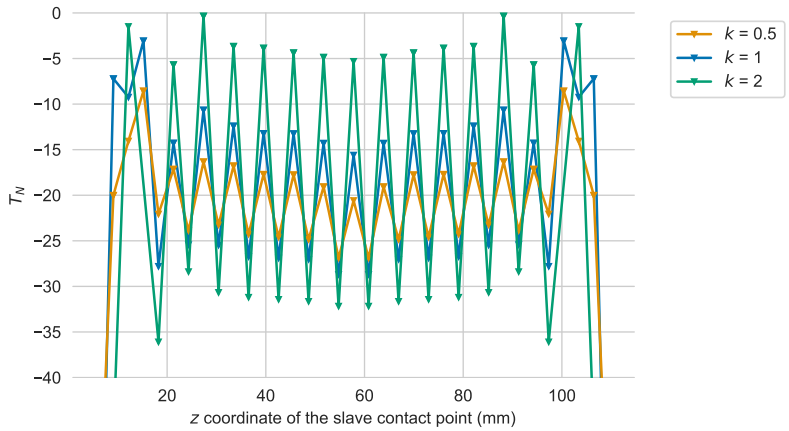

Figure 5.11: Beam-to-beam contact, example 5.4.1: influence of k on contact traction T_N for a Gauss-Lobatto quadrature with $nQP = 3$.

Fig. 5.8 shows that when the number of Gauss-Legendre quadrature points nQP is more than two, T_N oscillates along the contact line. Fig. 5.9(a) shows that for a 1-point Gauss-Legendre quadrature rule, T_N does not oscillate, even for $k = 10$. Fig. 5.9(b) shows that for a 2-point Gauss-Legendre quadrature rule, T_N does not oscillate for $k \leq 1$, but higher values of k (and thus ϵ_N) induce oscillations. For a

Gauss-Lobatto integration rule, Fig. 5.10 shows that even with a number of quadrature points as low as 2, oscillations of T_N are present.

Fig. 5.11 shows that increasing k increases the amplitude of these oscillations. None of the simulations using $k = 10$ converges with a Gauss-Lobatto quadrature. For all converging simulations, the evolution of the reaction force and the reaction torque is very similar for all the quadrature rules tested here and is not shown. As T_N does not oscillate for a 1-point Gauss-Legendre quadrature rule, even with a high penalty stiffness, this quadrature rule is used in all remaining numerical examples in this paper.

5.4.2 Beam-to-beam contact: twisting

20 beams of length $L = 70 \times 10^{-3}$ m are aligned in the z direction, see Fig. 5.12. Each beam is clamped at one end, while the cross-sections at the other end are rotated around the z axis with an angle of 180° in 720 increments. 40 BFEs are used to discretize each beam. The nodes at the rotated ends are free to move in the z direction while the other degrees of freedom are prescribed. The beams' Young's modulus is 100 GPa and their Poisson's ratio is 0.33. To show the influence of friction, the simulation is performed with three different friction coefficients μ: 0, 0.25 and 1. The initial penalty stiffness is again estimated using Hertz contact theory for two parallel cylinders, resulting in $\epsilon_N = \frac{\pi E^2}{8(1-\nu)^2} \approx 4.3 \times 10^{10}$ N/m [70]. The tangential penalty stiffness is set to $\epsilon_T = \epsilon_N/10 = 4.3 \times 10^9$ N/m.

As the rotation increases, beams wrap around each other, which causes the contact area and the number of penetrated sections to increase (bottom diagram in Fig. 5.13). The deformed configuration is similar for all simulations and is shown on the right in Fig. 5.12. Despite the substantial number of penetrated sections, the number of global iterations required to converge according to $\left\| \underline{f}_{int} + \underline{r}_c - \underline{f}_{ext} \right\| < 10^{-8}$, remains low (top diagram on Fig. 5.13). This is thanks to the proper linearization of $\underline{r}_c$, see Eqs. (5.61) and (5.64), with the Automatic Differentiation tool.

Fig. 5.14 reports the evolution of the reaction forces and the total torques around z axis at the support. The influence of friction is relatively small for this example,

although friction does have a substantial influence on the reaction force in the axial direction of the beams (top-right diagram in Fig. 5.14).

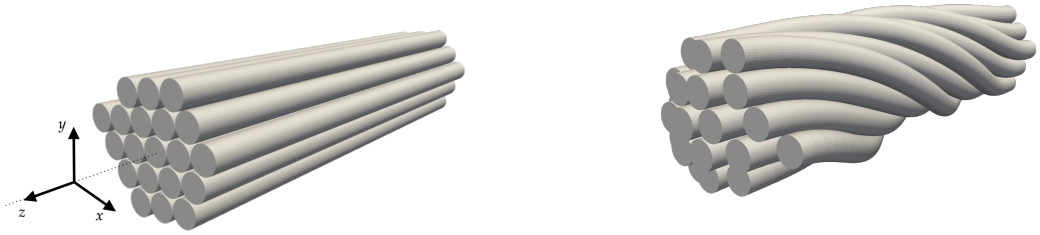

(a) (b)

Figure 5.12: Beam-to-beam contact, Example 5.4.2: (a) Initial configuration; (b) final configuration for $\mu = 0.25$.

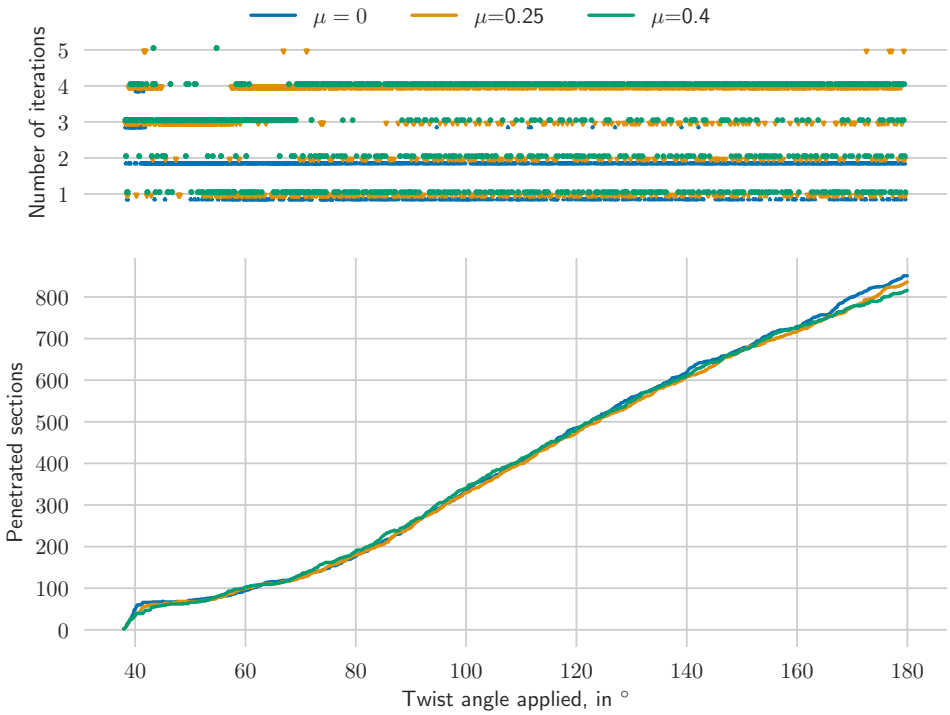

Figure 5.13: Beam-to-beam contact, example 5.4.2: top: number of global iterations to reach convergence criterion $\left\| \underline{f}_{int} + \underline{r}_c - \underline{f}_{ext} \right\| < 10^{-8}$; bottom: number of penetrated sections.

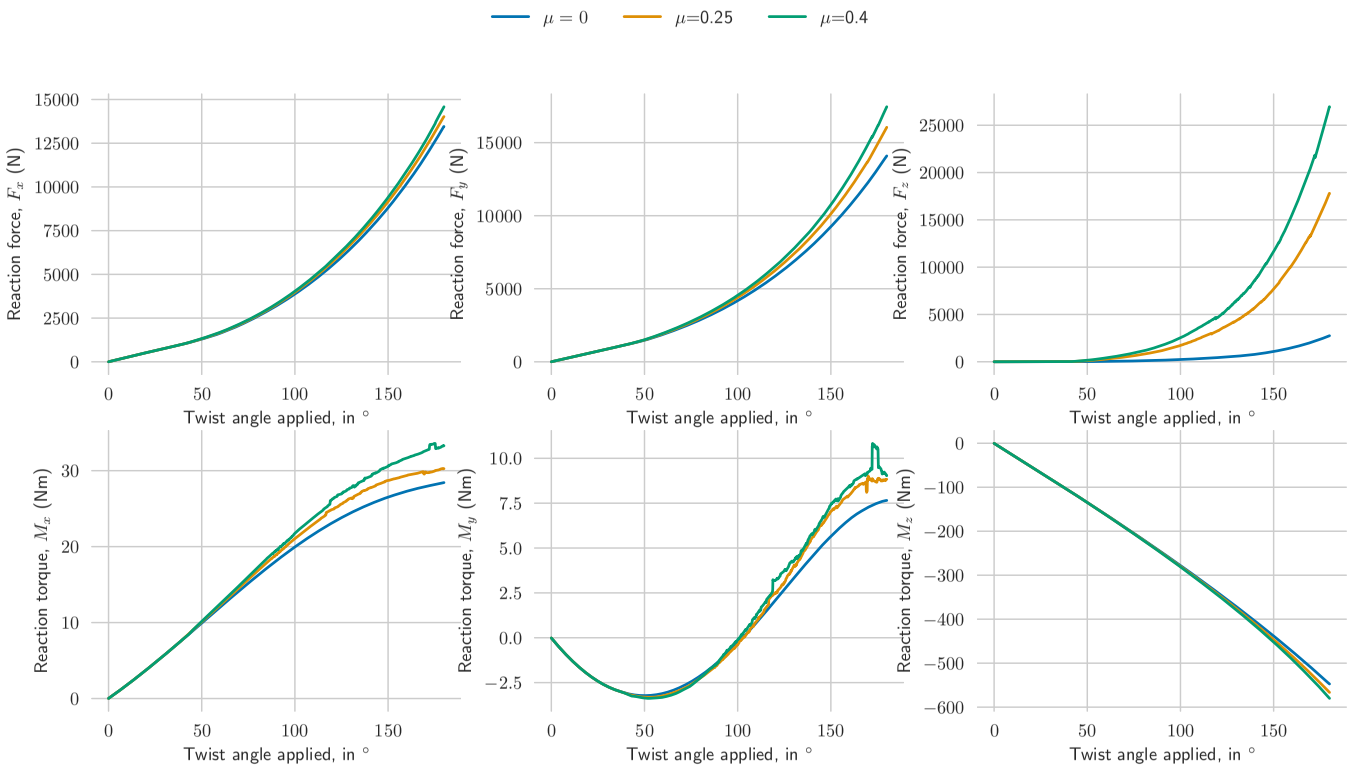

Figure 5.14: Beam-to-beam contact, example 5.4.2: Reaction forces and reaction torque.

5.4.3 Beam-to-beam contact: twisting and pulling of a fiber

In this example, four beams of length $L = 120 \times 10^{-3}$m are aligned along the z direction (Fig. 5.15). The beams' cross-sections are circular with a radius of 3.6×10^{-3}m. During the first part of the simulation, the displacements and rotations of all beam nodes at one end are fully restrained. The sections at the other end are rotated around the z axis with an angle of 180°. This loading is applied in 1800 increments. Each beam is discretized with 40 BFEs. The nodes at the rotated end of the beams are only free to move along z while the other kinematic variables are prescribed. During the second part of the loading, one of the beam is extracted from the deformed structure by pulling it (at the end node) in the z direction.

The initial penalty stiffness is once again estimated using Hertz theory for the case of perfectly parallel cylinders in contact, resulting in $\epsilon_N = 4.4 \times 10^{10}$ N/m. The tangential penalty stiffness is set to $\epsilon_T = \epsilon_N/10 = 4.4 \times 10^9$ N/m. A one-point Gauss-Legendre quadrature rule is used to integrate the contact virtual work.

The simulation is performed without friction and with a friction coefficient of 0.25. It is also performed for circular (with a radius of 3.6×10^{-3}m) and elliptical cross-sections (with the same cross-sectional area as the circular cross sections, with $a = 2.16 \times 10^{-3}$m).

The undeformed configuration as well as the deformed configuration at the end of the two part of the simulation is shown in Fig. 5.15 for circular and elliptical cross-sections. The number of global iterations required to attain the desired accuracy, $\left\| \underline{f}_{int} + \underline{r}_c - \underline{f}_{ext} \right\| < 10^{-8}$ is shown in Fig. 5.16. Fig. 5.17 shows the reaction force, revealing that both friction as well as cross-sectional shape have a substantial influence. The force-displacement curves of the cases with friction are less smooth than their frictionless counterparts. This is because of the change in the sticking/slipping status of contact points.

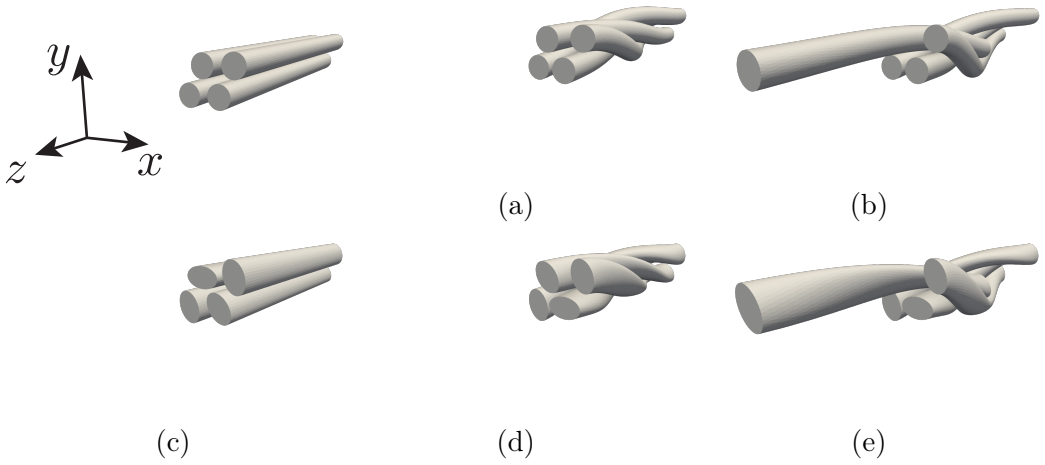

Figure 5.15: Beam-to-beam contact, example 5.4.3: Initial configuration (left column); configuration halfway through the loading (central column), and final configuration (right column) for circular cross-sections (a, b and c) and elliptical cross-sections (d, e and f).

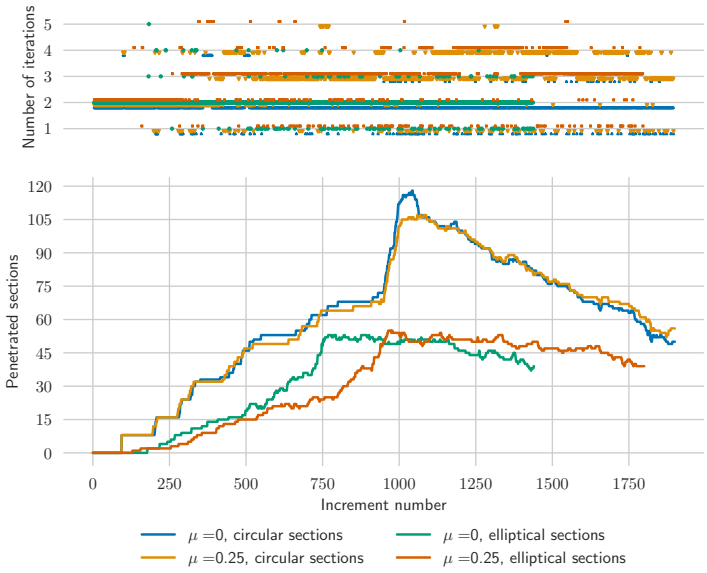

Figure 5.16: Beam-to-beam contact, example 5.4.3: top: number of global iterations to reach the convergence criterion $\left\| \underline{f}_{int} + \underline{r}_c - \underline{f}_{ext} \right\| < 10^{-8}$; bottom: number of penetrated sections.

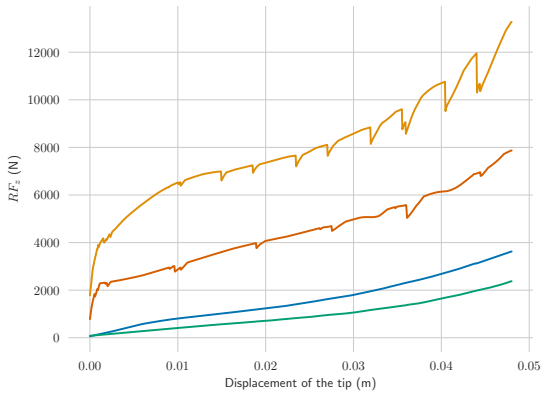

Figure 5.17: Beam-to-beam contact, example 5.4.3: Reaction force at the end nodes of the pulled beam during the second part of the simulation.

5.4.4 Beam-inside-beam contact: insertion

This example involves an initially straight thin beam that is pushed in a hollow beam (see Fig. 5.18a). Both beams have elliptical cross-sections. Initially, only a small part of the inner beam is present in the hollow one. The curved part of the hollow beam's centroid-line is a half-circle of radius 150×10^{-3}m. The kinematic variables of the outer beam's end node near the thin beam's insertion location are restrained. Its wall thickness is 10^{-3}m and the lengths of its cross-sectional semi-axes are $a = 20 \times 10^{-3}$m and $b = 16 \times 10^{-3}$m.

The inner beam has a length of 54×10^{-2}m, and a Young's modulus of 100 GPa. The cross-sectional shape is given by $a = 5.4 \times 10^{-3}$m and $b = 4.3 \times 10^{-3}$m. The outer hollow beam is more compliant with $E = 10$ GPa. The z-displacement of the inner beam's end node furthest away from the outer beam is prescribed to reach 54×10^{-2}m in 300 increments, whilst the other kinematic variables at this end node are restrained. The thin beam is discretized with 20 BFEs and the hollow beam with 45 BFEs. A one-point Gauss-Legendre quadrature rule is used to integrate the

contact virtual work.

Once again the simulation is performed with different static friction coefficients: 0, 0.5, and 1. Both beams have a Poisson's ratio of 0.33. The initial penalty stiffness is set to $\epsilon_N = 1 \times 10^3$ N/m which is several order of magnitude less than for the examples in Sections 5.4.2 and 5.4.3. A higher penalty stiffness causes convergence issues with oscillations of the contact status, meaning that some contact elements penetrate the thick beam wall and then detach ($g_N > 0$) from one iteration to the next. The tangential penalty stiffness is set to $\epsilon_T = 1 \times 10^2$ N/m and allows acceptably small elastic tangential gaps, while allowing the (global) Newton-Raphson scheme to converge.

Both structures deform due to contact, see Fig. 5.18. Fig. 5.19 shows that numerous sections of the inner beam penetrate the wall of the outer beam, which indicates that the contact is non-localized. Only a few iterations are necessary to reach convergence for the "beam-inside-beam" framework as Fig. 5.19 shows. Fig. 5.20 shows the component of the reaction force in the z direction. The presence of friction clearly has a substantial influence on the force-displacement response, indicating that friction not only influences the results of beam-to-beam contact schemes, but also those of beam-inside-beam contact schemes.

The contact of the tip of the inner beam plays a crucial role during the entire simulation. It is enforced with a contact at the closest pair of surface points between the surface of the last section of the inner beam and the inner surface of the tube. A similar contact element was used in [25]. This contact interaction needs a specific treatment in order to avoid a complete loss of contact between the tip and the inner surface when the tip slides out. More details can be found in [52].

(a) (b) (c)

Figure 5.18: Beam-inside-beam contact, example 5.4.4: (a) Initial configuration; (b) configuration halfway through the loading, and (c) final configuration.

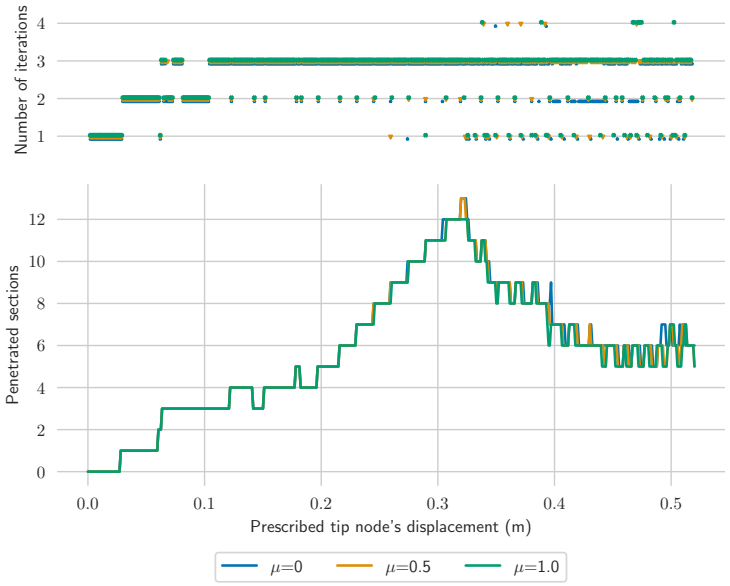

Figure 5.19: Beam-inside-beam contact, example 5.4.4: top: number of global iterations to reach convergence criterion: $\left\| \underline{f}_{int} + \underline{r}_c - \underline{f}_{ext} \right\| < 10^{-8}$; Bottom: evolution of the number penetrated cross-sections.

5.5 Conclusion

This contribution presents the extension of beam-to-beam and beam-inside-beam contact frameworks towards friction. It is applicable to to shear-deformable and shear-undeformable beams with circular and elliptical cross sections. The framework is not only able to account for frictional sliding in the beams' axial direction, but also in the circumferential direction. It is suitable for non-localized contact interactions, occurring for instance when beams are parallel to each other or wrapped around

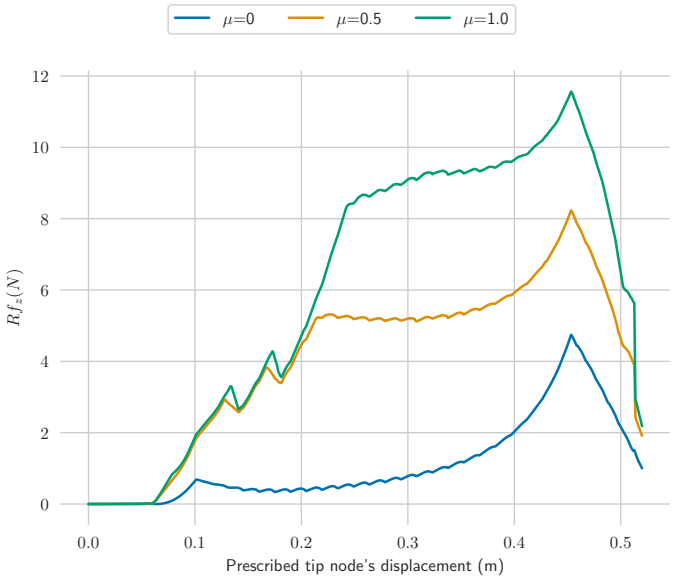

Figure 5.20: Beam-inside-beam contact, example 5.4.4: Reaction force at the inner beam's prescribed node in the beam's axial direction.

each other. The contact kinematics are formulated in terms of surface parameters of the master and slave beams. Thus, the introduced framework can be exploited for a variety of beam finite element formulations, provided that their cross-sections are rigid and their discretized surface is C^1-continuous.

An important specificity of the introduced framework is that both slave and master contact points change their location at the beams' surfaces during the relative tangential motion of beams. This is unlike common node-to-segment approaches, in which the location of the slave contact points are fixed. We propose a measure of relative tangential displacement that is frame indifferent and does not involve higher-order dependencies on global kinematic variables. Thanks to that, the measure is suitable for finite-deformation and finite-sliding problems, and also leads to computationally efficient linearization.

The presented formulation is shown to efficiently regularize contact constraints in a series of numerical examples for beam-to-beam and beam-inside-beam contact interactions, with and without friction for beams with circular and elliptical cross-sections. Even if numerous contact interactions are present and the beams' deformations, rotations and curvatures are substantial, only a few global iterations are

necessary to converge. This is thanks to the consistent linearizations achieved using Automatic Differentiation, which automatically incorporates the dependencies between global and local variables.

While the present formulation is suitable for non-localized beam-to-beam contact, it is not truly adapted to enforce localized contact. In such cases, frameworks as presented by Gay Neto et al. [24, 25], which enforce contact at a single pair of points, seem more accurate. A scheme that automatically decides to use between a point-wise contact scheme and the presented scheme remains for future work. Although [62] provides a geometrically-based choice of the contact formulation which depends on the spatial arrangement of the two beams' centroid-lines, it cannot be used here because it is limited to beams with circular cross-sections. Another geometrical criterion would be necessary to decide which formulation to employ for beams with elliptical cross-sections (point-wise surface-to-surface contact [24, 25, 26] or surface-to-surface non-localized contact).

Appendix

Eq. (5.18) approximates the increment in the tangential gap between two time-steps. Five test cases in which the displacements and rotations of two beams in contact are completely prescribed are performed to reveal how the error of the tangential gap decreases with the number of increments. In every test, both beams have circular cross-sections with a radius $r = 1$ m. The beams are initially in contact such that $g_N \approx 0$. The examples are presented in Fig. V..21. The error of the total relative sliding of the surfaces are reported in Fig. V..22. For every example, a tangential penalty parameter $\epsilon_T = 10^5$ has been used.

Test $0, 1$ and 2 correspond to perfect rolling scenarios. We thus expect the measure of relative displacement to decrease as the number of increments, n_{inc}, increases. On the contrary, some relative sliding of the surface is expected in tests 3 and 4.

Below, each test is briefly described along with the measure of error employed. $\mathbf{g}_{Tel,final}$ denotes the elastic gap measured at the end of the simulation.

- Test 0: the slave beam is rotated around the master beam with an angle $\beta = \pi$. The slave is rotated around its centroid-axis with an angle $\alpha = 2\beta$. The master beam does not move.

- Test 1: it is identical to Test 0 except that the roles of slave and master are inverted.

- Test 2: both beams are rotated around their centroid lines by angle of $\frac{\pi}{2}$ in opposite direction.

- Test 3: both beams are rotated around their centroid lines by angle of $\alpha = \frac{\pi}{2}$ in the same direction. We thus expect a total relative sliding of $2r\alpha$.

- Test 4: the slave beam is rotated around the master beam with an angle of $\alpha = 2\pi$ and longitudinally displaced with $v_{disp} = 0.1$ m. Therefore, the master contact point follows an hellicoidal trajectory. As the slave beam is rotated with an angle of α around its centroid line, the surface parameters of the slave contact point, $\underline{\bar{h}}^{\mathtt{I}}$, do not change. Hence, the slave contact point does not contribute to the total sliding of contacting surfaces.

For each test, the measure of error on $(\sum^{n_{inc}} \|\Delta \mathbf{g}^i_{Tsl}\|)$ at the end of the fictitious loading is plotted in Fig. V..22. The measure of error employed is:

- For tests 0, 1 and 2: error $= (\sum_{i=1}^{n_{inc}} \|\Delta \mathbf{g}^i_{Tsl}\|) + \|\mathbf{g}_{Tel,final}\|$
- For test 3: error $= 2r\alpha - (\sum_{i=1}^{n_{inc}} \|\Delta \mathbf{g}^i_{Tsl}\|) + \|\mathbf{g}_{Tel,final}\|$,
- For test 4: error $= \left(\alpha\sqrt{r^2 + \left(\frac{v_{disp}}{\alpha}\right)^2} - \sum_{i=1}^{n_{inc}} \|\Delta \mathbf{g}^i_{Tsl}\|\right) + \|\mathbf{g}_{Tel,final}\|$

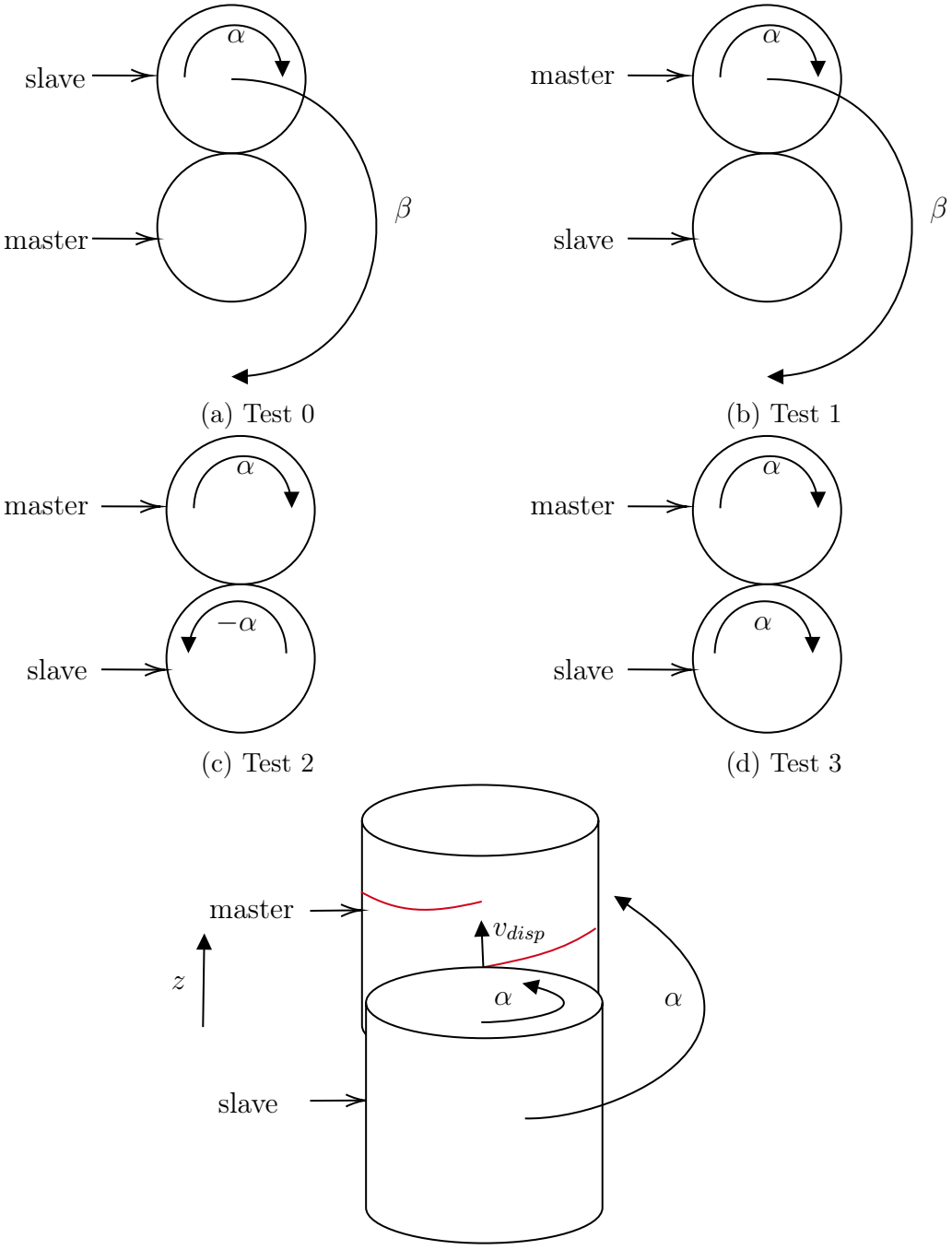

(a) Test 0

(b) Test 1

(c) Test 2

(d) Test 3

(e) Test 4

Figure V..21: Schematics of the different tests performed.

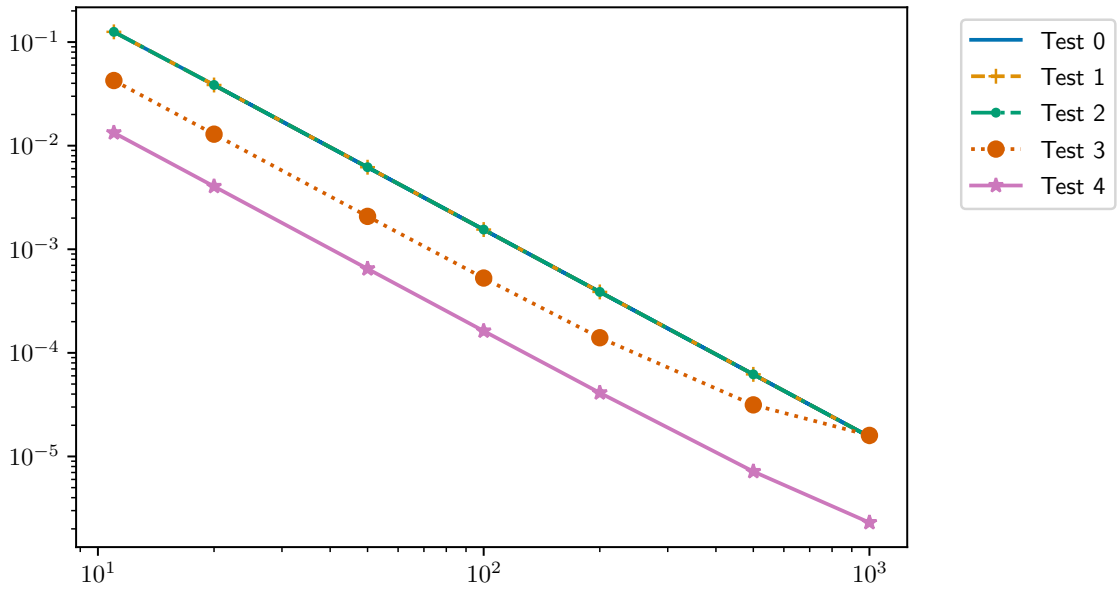

Figure V..22: Error on the total tangential gap measured at the end of the fictitious loading.

Conclusion

This thesis presents three unique frameworks to treat mechanical contact between beams. All frameworks are dedicated to cases with finite contact areas, instead of local (point-wise) contact. The approaches are applicable to both shear-deformable and shear-undeformable beams, with both circular as well as elliptical rigid cross sections. For two of the three presented frameworks an extension is furthermore presented that accounts for friction. This extension is also unique, as it not only describes frictional sliding in the beams' axial directions, but also in their circumferential directions.

The first contribution of this thesis is the formulation of a smooth surface approximation, which guarantees that a consecutive series of beams possesses a C^1-continuous surface to which contact can be applied. Chapter II reports this surface approximation, but it is used throughout the entire thesis.

Chapter II introduces a first framework in which a grid of surface (integration) points is distributed on the slave beam's surface. For each point, a measure of penetration is established, and a contact force is applied if this point penetrates another beam. This technique allows treating non-localized contact; for instance in case of parallel/almost parallel beams and when a beam is bent over another beam. The local problem to determine the amount of penetration is similar to that of Node-to-surface approaches [47] since the slave point is fixed and the only question is to find its projection on the master surface. The penalty approach is employed to regularize unilateral contact constraints. In order for each point to represent the surface area that surrounds it, a deformation-dependent weight is associated to it.

As the numerical examples rely on the smoothed surface introduced in Section

2.4.2, partial derivatives of contact variables with respect to nodal variables are intricate and error-prone. Automatic differentiation (AD) [41, 42, 43] has been used to obtain contact residuals and stiffnesses. The framework has been shown to work in the range of large displacements and curvatures of the contacting surfaces as well as for large relative displacements of the surfaces. The drawback of this framework is that for the contact area to be captured accurately, a fine grid of surface points must be used around the contact area, which cannot be easily determined *a priori*. A fine grid is then used on an extensive part of the slave beam's surface. This makes the simulations relatively slow.

The framework in Chapter III has been designed with the primary goal of reducing the number of local problems to solve of Chapter II. This approach differs from the one introduced in Chapter II as no (integration) points need to be distributed on the (slave) surface, but only along the (slave) centroid line. In other words, the amount of penetration is not measured from a slave surface point to the master beam's surface, but between the perimeter of a slave cross-section and the master beam's surface.

Although the number of local problems is indeed significantly smaller and hence, the computational time is greatly reduced, the local problem to solve is slightly more complex than the one of Chapter II. It involves four unknowns (one surface parameter of the slave surface, two surface parameter of master surface and the normal gap) while the one in Chapter II only involves two unknowns (i.e. the surface parameters of the master surface).

Since the framework is a master-slave framework (similar to the one of Chapter II), the choice of the master and the slave surfaces influences the results. To remove this "bias", the framework was reformulated with the double half-pass method [73, 74], although the asymmetry in the measure of penetration between the two half-passes leads to a violation of the action-reaction principle. The results reported in Chapter III have indicated that the double half-pass method has no advantage for contact between beams and in some cases even negatively influences the results.

Furthermore, the efficiency of generated code with AD for different local problems is assessed. It is apparent that the local problem based on a residual form (in other words a set of equations) leads to more efficient code than the local problem based on

an objective function to minimize. All in all, the computational cost associated with the regularization of contact constraint is greatly reduced compared to the framework of Chapter II.

A similar strategy to enforce non-local contact between beams both shear-deformable and shear-undeformable beams with both circular and elliptical rigid cross-sections is also employed in Chapter IV. However, whereas all previous contact frameworks for beams (as those of Chapter II and III) intend to repel penetrating beams from each other, the framework of Chapter IV achieves the exact opposite; it ensures that two beams remain embedded inside each other. Although the technical enhancements of the 'beam-inside-beam' contact framework of Chapter IV are somewhat limited compared to the 'beam-to-beam' contact framework of Chapter III - the measure of penetration is changed to a 'measure of exclusion' and the inlet and outlet of the outer beam has required a special treatment, the beam-inside-beam contact framework greatly widens the applicability of contact frameworks for beams. The new framework can for instance be used to simulate medical interventions in which a slender medical instrument is inserted in a tubular structures of the human body. The speed of the beam-inside-beam contact framework is furthermore high thanks to the fact that penetration is measured at once for entire cross sections (similar as in Chapter III).

The frameworks introduced in Chapters II, III and IV focus on the regularization of unilateral contact constraints, considering only the normal part of the contact traction and omitting frictional efforts. In Chapter V, the frameworks of Chapters III and IV are enhanced to incorporate frictional effects. Difficulties arise from the fact that the material locations of the contact point are not constant on the slave surface, neither on the master surface. Relative frictional sliding is furthermore captured in both the beams' axial directions as well as in their circumferential directions.

Future work

One possible extension of the work presented in this thesis regards the integration of the virtual work due to contact over the slave's centroid line (Chapters III, IV and

V). This integration is performed without the consideration of weak discontinuities of the integrand. This occurs when the projections of a slave patch are not on a single master patch. As reported by Meier et al. [62] and Konyukhov et al. [37], integration over sub-segments is more accurate. This implies deformation-dependent integral bounds.

In engineering applications, contact may be localized in certain regions (and hence, it can be treated with a point-wise contact force), whereas in other regions contact occurs at finite areas. Contact may also start locally and gradually becomes non-localised, or vice versa. Consequently, it is not always possible to determine in advance which type of contact element to employ. In the so-called "All-beam-angle contact" (ABC) formulation, Meier et al. [62] proposed an algorithm to automatically determine which type of contact to use for contact enforcement between shear-undeformable beams with circular sections at any time during a simulation. The choice of the type of contact is based on the angle between the tangent vector to the centroid line of the contacting beams. Establishing the geometrical criterion according to the contacting surfaces' properties [40] to decide which formulation to use to treat contact between shear-deformable beams remains for future work.

Also, by changing the parametrization of the master surface, contact frameworks presented in Chapters III, IV and V) could be modified to model "beam-to-shell" contact.

Finally, this thesis has only elaborated on the "narrow-phase"; the computation of the penetration between a pair of beam elements/patches. Before the narrow-phase is employed however, a 'broad-phase' generally to determines which pairs of beam elements/patches are possibly in contact. The quality of the broad-phase is crucial to reach high simulation speeds. In this thesis, the broad-phase embeds each patch in one or two bounding boxes [63]. The bounding boxes fit the patch geometries well compared to axis-aligned-bounding boxes or bounding spheres, but an efficient detection of their intersections is an important bottleneck of the simulations. Hence, the speed of future simulations can be substantially improved by developing enhanced detection algorithms.

Bibliography

[1] Alderliesten, T., Konings, M.K., and Niessen, W.J. Simulation of minimally invasive vascular interventions for training purposes. *Computer Aided Surgery*, 9(1-2):3–15 (2004). doi:10.3109/10929080400006408.

[2] Alterovitz, R., Goldberg, K., and Okamura, A. Planning for steerable bevel-tip needle insertion through 2D soft tissue with obstacles. In *Proceedings - IEEE International Conference on Robotics and Automation*, volume 2005, pages 1640–1645 (2005). ISBN 078038914X. doi:10.1109/ROBOT.2005.1570348.

[3] Ashby, M.F. The properties of foams and lattices. *Philosophical Transactions of the Royal Society A: Mathematical, Physical and Engineering Sciences*, 364(1838):15–30 (2006). doi:10.1098/rsta.2005.1678.

[4] Beex, L.A.A., Kerfriden, P., Rabczuk, T., and Bordas, S.P.A. Quasicontinuum-based multiscale approaches for plate-like beam lattices experiencing in-plane and out-of-plane deformation. *Computer Methods in Applied Mechanics and Engineering*, 279(February):348–378 (2014). doi:10.1016/j.cma.2014.06.018.

[5] Beex, L.A.A. and Peerlings, R.H.J. On the influence of delamination on laminated paperboard creasing and folding. *Philosophical Transactions of the Royal Society A: Mathematical, Physical and Engineering Sciences*, 370(1965):1912–1924 (2012). doi:10.1098/rsta.2011.0408.

[6] Beex, L.A.A., Peerlings, R.H.J., van Os, K., and Geers, M.G.D. The mechanical reliability of an electronic textile investigated using the virtual-power-based quasicontinuum method. *Mechanics of Materials*, 80(Part A):52–66 (2015). doi:10.1016/j.mechmat.2014.08.001.

[7] Beex, L.A.A., Rokos, O., Zeman, J., and Bordas, S.P.A. Higher-order quasicontinuum methods for elastic and dissipative lattice models: uniaxial defor-

mation and pure bending. *GAMM-Mitteilungen*, 38(2):344–368 (2015). doi: 10.1002/gamm.201510018.

[8] Ben Boubaker, B., Haussy, B., and Ganghoffer, J. Discrete models of woven structures. Macroscopic approach. *Composites Part B: Engineering*, 38(4):498–505 (2007). doi:10.1016/j.compositesb.2006.01.007.

[9] Boisse, P., Gasser, A., and Hivet, G. Analyses of fabric tensile behaviour: determination of the biaxial tension-strain surfaces and their use in forming simulations. *Composites Part A: Applied Science and Manufacturing*, 32(10):1395–1414 (2001). doi:10.1016/S1359-835X(01)00039-2.

[10] Cao, X. and Wu, W. The establishment of a mechanics model of multi-strand wire rope subjected to bending load with finite element simulation and experimental verification. *International Journal of Mechanical Sciences*, 142-143(March):289–303 (2018). doi:10.1016/j.ijmecsci.2018.04.051.

[11] Chamekh, M., Mani-Aouadi, S., and Moakher, M. Stability of elastic rods with self-contact. *Computer Methods in Applied Mechanics and Engineering*, 279:227–246 (2014). doi:10.1016/j.cma.2014.06.027.

[12] Coles, T.R., John, N.W., Gould, D., and Caldwell, D.G. Integrating haptics with augmented reality in a femoral palpation and needle insertion training simulation. *IEEE Transactions on Haptics*, 4(3):199–209 (2011). doi:10.1109/TOH.2011.32.

[13] Cotin, S., Delingette, H., and Ayache, N. Real-time elastic deformations of soft tissues for surgery simulation. *IEEE Transactions on Visualization and Computer Graphics*, 5(1):62–73 (1999). doi:10.1109/2945.764872.

[14] Courtecuisse, H., Allard, J., Kerfriden, P., Bordas, S.P., Cotin, S., and Duriez, C. Real-time simulation of contact and cutting of heterogeneous soft-tissues. *Medical Image Analysis*, 18(2):394–410 (2014). doi:10.1016/j.media.2013.11.001.

[15] Courtecuisse, H., Jung, H., Allard, J., Duriez, C., Lee, D.Y., and Cotin, S. GPU-based real-time soft tissue deformation with cutting and haptic feedback. *Progress in Biophysics and Molecular Biology*, 103(2-3):159–168 (2010). doi: 10.1016/j.pbiomolbio.2010.09.016.

[16] Crisfield, M.A. and Jelenić, G. Objectivity of strain measures in the geometrically exact three-dimensional beam theory and its finite-element implementation. *Proceedings of the Royal Society of London. Series A: Mathematical, Physical and Engineering Sciences*, 455(1983):1125–1147 (1999). doi: 10.1098/rspa.1999.0352.

[17] DiMaio, S.P. and Salcudean, S.E. Needle Insertion Modeling and Simulation. *IEEE Transactions on Robotics and Automation*, 19(5):864–875 (2003). doi: 10.1109/TRA.2003.817044.

[18] Duriez, C., Cotin, S., Lenoir, J., and Neumann, P. New approaches to catheter navigation for interventional radiology simulation. *Computer Aided Surgery*, 11(6):300–308 (2006). doi:10.3109/10929080601090623.

[19] Duriez, C., Guébert, C., Marchal, M., Cotin, S., and Grisoni, L. Interactive simulation of flexible needle insertions based on constraint models. In *Lecture Notes in Computer Science (including subseries Lecture Notes in Artificial Intelligence and Lecture Notes in Bioinformatics)*, volume 5762 LNCS, pages 291–299 (2009). ISBN 3642042708. doi:10.1007/978-3-642-04271-3_36.

[20] Durville, D. A finite element approach of the behaviour of woven materials at microscopic scale. *Lecture Notes in Applied and Computational Mechanics*, 46 LNACM:39–46 (2009). doi:10.1007/978-3-642-00911-2.

[21] Durville, D. Contact Modelling in Entangled Fibrous Materials. In *Trends in Computational Contact Mechanics*, pages 1–22. Springer, Berlin, Heidelberg (2011). doi:10.1007/978-3-642-22167-5_1.

[22] Durville, D. Contact-friction modeling within elastic beam assemblies: An application to knot tightening. *Computational Mechanics*, 49(6):687–707 (2012). doi:10.1007/s00466-012-0683-0.

[23] Faure, F., Duriez, C., Delingette, H., Allard, J., Gilles, B., Marchesseau, S., Talbot, H., Courtecuisse, H., Bousquet, G., Peterlik, I., and Cotin, S. SOFA: A Multi-Model Framework for Interactive Physical Simulation. pages 283–321 (2012). doi:10.1007/8415_2012_125.

[24] Gay Neto, A., Pimenta, P.M., and Wriggers, P. A master-surface to master-surface formulation for beam to beam contact. Part I: frictionless interaction. *Computer Methods in Applied Mechanics and Engineering*, 303:400–429 (2016). doi:10.1016/j.cma.2016.02.005.

[25] Gay Neto, A., Pimenta, P.M., and Wriggers, P. A master-surface to master-surface formulation for beam to beam contact. Part II: Frictional interaction. *Computer Methods in Applied Mechanics and Engineering*, 319:146–174 (2017). doi:10.1016/j.cma.2017.01.038.

[26] Gay Neto, A. and Wriggers, P. Computing pointwise contact between bodies: a class of formulations based on master–master approach. *Computational Mechanics*, (0123456789) (2019). doi:10.1007/s00466-019-01680-9.

[27] Goury, O., Nguyen, Y., Torres, R., Dequidt, J., and Duriez, C. Numerical Simulation of Cochlear-Implant Surgery: Towards Patient-Specific Planning. In *Lecture Notes in Computer Science (including subseries Lecture Notes in Artificial Intelligence and Lecture Notes in Bioinformatics)*, volume 9900 LNCS, pages 500–507. Springer Verlag (2016). ISBN 9783319467191. doi:10.1007/978-3-319-46720-7_58.

[28] Horrocks, A.R. and Anand, S.C. *Handbook of technical textiles. Volume 1, Technical textile processes*. Woodhead Publishing (2015). ISBN 9781782424819.

[29] Ibrahimbegović, A., Frey, F., and Kožar, I. Computational aspects of vector-like parametrization of three-dimensional finite rotations. *International Journal for Numerical Methods in Engineering*, 38(21):3653–3673 (1995). doi:10.1002/nme.1620382107.

[30] Irschik, H. and Gerstmayr, J. A continuum-mechanics interpretation of Reissner's non-linear shear-deformable beam theory. *Mathematical and Computer Modelling of Dynamical Systems*, 17(1):19–29 (2011). doi:10.1080/13873954.2010.537512.

[31] Jelenić, G. and Crisfield, M. Geometrically exact 3D beam theory: implementation of a strain-invariant finite element for statics and dynamics. *Computer Methods in Applied Mechanics and Engineering*, 171(1-2):141–171 (1999). doi:10.1016/S0045-7825(98)00249-7.

[32] Jiang, W.G. and Henshall, J.L. The development and applications of the helically symmetric boundary conditions in finite element analysis. *Communications in Numerical Methods in Engineering*, 15(6):435–443 (1999). doi:10.1002/(SICI)1099-0887(199906/07)15:6<435::AID-CNM257>3.3.CO;2-N.

[33] Jung, A., Beex, L.A.A., Diebels, S., and Bordas, S.P.A. Open-cell aluminium foams with graded coatings as passively controllable energy absorbers. *Materials & Design*, 87:36–41 (2015). doi:10.1016/j.matdes.2015.07.165.

[34] Jung, A., Lach, E., and Diebels, S. New hybrid foam materials for impact protection. *International Journal of Impact Engineering*, 64:30–38 (2014). doi: 10.1016/j.ijimpeng.2013.09.002.

[35] Kazmitcheff, G. *Modélisation dynamique de l'oreille moyenne et des interactions outils organes pour la conception d'un simulateur appliqué à la chirurgie otologique*. Ph.D. thesis (2014).

[36] Khamdaeng, T., Luo, J., Vappou, J., Terdtoon, P., and Konofagou, E.E. Arterial stiffness identification of the human carotid artery using the stress-strain relationship in vivo. *Ultrasonics*, 52(3):402–411 (2012). doi:10.1016/j.ultras.2011.09.006.

[37] Konyukhov, A., Mrenes, O., and Schweizerhof, K. Consistent development of a beam-to-beam contact algorithm via the curve-to-solid beam contact: Analysis for the nonfrictional case. *International Journal for Numerical Methods in Engineering*, 113(7):1108–1144 (2018). doi:10.1002/nme.5701.

[38] Konyukhov, A., Mrenes, O., and Schweizerhof, K. Consistent development of a beam-to-beam contact algorithm via the curve-to-solid beam contact: Analysis for the nonfrictional case. *International Journal for Numerical Methods in Engineering*, 113(7):1108–1144 (2018). doi:10.1002/nme.5701.

[39] Konyukhov, A. and Schweizerhof, K. Geometrically exact covariant approach for contact between curves. *Computer Methods in Applied Mechanics and Engineering*, 199(37-40):2510–2531 (2010). doi:10.1016/j.cma.2010.04.012.

[40] Konyukhov, A. and Schweizerhof, K. *Computational Contact Mechanics*, volume 67 of *Lecture Notes in Applied and Computational Mechanics*. Springer Berlin Heidelberg, Berlin, Heidelberg (2013). ISBN 978-3-642-31530-5. doi: 10.1007/978-3-642-31531-2.

[41] Korelc, J. Multi-language and multi-environment generation of nonlinear finite element codes. *Engineering with Computers*, 18(4):312–327 (2002). doi:10.1007/s003660200028.

[42] Korelc, J. Automation of primal and sensitivity analysis of transient coupled problems. *Computational Mechanics*, 44(5):631–649 (2009). doi:10.1007/s00466-009-0395-2.

[43] Korelc, J. and Wriggers, P. *Automation of Finite Element Methods*. Springer International Publishing, Cham (2016). ISBN 978-3-319-39003-1. doi:10.1007/978-3-319-39005-5.

[44] Kulachenko, A. and Uesaka, T. Direct simulations of fiber network deformation and failure. *Mechanics of Materials*, 51:1–14 (2012). doi:10.1016/j.mechmat.2012.03.010.

[45] Laursen, T.A. and Simo, J.C. A continuum-based finite element formulation for the implicit solution of multibody, large deformation-frictional contact problems. *International Journal for Numerical Methods in Engineering*, 36(20):3451–3485 (1993). doi:10.1002/nme.1620362005.

[46] Lee, K.Y., Aitomäki, Y., Berglund, L.A., Oksman, K., and Bismarck, A. On the use of nanocellulose as reinforcement in polymer matrix composites. *Composites Science and Technology*, 105:15–27 (2014). doi:10.1016/J.COMPSCITECH.2014.08.032.

[47] Lengiewicz, J., Korelc, J., and Stupkiewicz, S. Automation of finite element formulations for large deformation contact problems. *International Journal for Numerical Methods in Engineering*, 85(10) (2011). doi:10.1002/nme.3009.

[48] Lengiewicz, J. and Stupkiewicz, S. Efficient model of evolution of wear in quasi-steady-state sliding contacts. *Wear*, 303(1-2):611–621 (2013). doi:10.1016/j.wear.2013.03.051.

[49] Lenoir, J., Cotin, S., Duriez, C., and Neumann, P. Interactive physically-based simulation of catheter and guidewire. *Computers and Graphics (Pergamon)*, 30(3):416–422 (2006). doi:10.1016/j.cag.2006.02.013.

[50] Litewka, P. *Finite Element Analysis of Beam-to-Beam Contact*, volume 53 of *Lecture Notes in Applied and Computational Mechanics*. Springer Berlin Heidelberg, Berlin, Heidelberg (2010). ISBN 978-3-642-12939-1. doi:10.1007/978-3-642-12940-7.

[51] Litewka, P. Enhanced multiple-point beam-to-beam frictionless contact finite element. *Computational Mechanics*, 52(6):1365–1380 (2013). doi:10.1007/s00466-013-0881-4.

[52] Magliulo, M., Lengiewicz, J., Zilian, A., and Beex, L. Non-localised contact between beams with circular and elliptical cross-sections. *Computational Mechanics*, 65(5) (2020). doi:10.1007/s00466-020-01817-1.

[53] Magliulo, M., Lengiewicz, J., Zilian, A., and Beex, L.A.A. Non-localised contact between beams with circular and elliptical cross-sections. *Computational Mechanics* (2020).

[54] Magliulo, M., Zilian, A., and Beex, L.A.A. Contact between shear-deformable beams with elliptical cross sections. *Acta Mechanica* (2019). doi:10.1007/s00707-019-02520-w.

[55] Mäkelä, P. and Östlund, S. Orthotropic elastic-plastic material model for paper materials. *International Journal of Solids and Structures*, 40(21):5599–5620 (2003). doi:10.1016/S0020-7683(03)00318-4.

[56] Meier, C., Grill, M.J., Wall, W.A., and Popp, A. Geometrically exact beam elements and smooth contact schemes for the modeling of fiber-based materials and structures. *arXiv preprint arXiv:1611.06436*, (November) (2016). doi:10.1016/j.ijsolstr.2017.07.020.

[57] Meier, C., Popp, A., and Wall, W.A. An objective 3D large deformation finite element formulation for geometrically exact curved Kirchhoff rods. *Computer Methods in Applied Mechanics and Engineering*, 278:445–478 (2014). doi:10.1016/j.cma.2014.05.017.

[58] Meier, C., Popp, A., and Wall, W.A. A locking-free finite element formulation and reduced models for geometrically exact Kirchhoff rods. *Computer Methods in Applied Mechanics and Engineering*, 290:314–341 (2015). doi:10.1016/j.cma.2015.02.029.

[59] Meier, C., Popp, A., and Wall, W.A. A finite element approach for the line-to-line contact interaction of thin beams with arbitrary orientation. *Computer Methods in Applied Mechanics and Engineering*, 308:377–413 (2016). doi:10.1016/j.cma.2016.05.012.

[60] Meier, C., Popp, A., and Wall, W.A. Geometrically Exact Finite Element Formulations for Slender Beams: Kirchhoff-Love Theory Versus Simo-Reissner Theory. *Archives of Computational Methods in Engineering*, 26(1):163–243 (2019). doi:10.1007/s11831-017-9232-5.

[61] Meier, C., Popp, A., and Wall, W.A. Geometrically Exact Finite Element Formulations for Slender Beams: Kirchhoff–Love Theory Versus Simo–Reissner Theory. *Archives of Computational Methods in Engineering*, 26(1):163–243 (2019). doi:10.1007/s11831-017-9232-5.

[62] Meier, C., Wall, W.A., and Popp, A. A unified approach for beam-to-beam contact. *Computer Methods in Applied Mechanics and Engineering*, 315(August):972–1010 (2017). doi:10.1016/j.cma.2016.11.028.

[63] Meier, C., Wall, W.A., and Popp, A. ScienceDirect A unified approach for beam-to-beam contact. *Comput. Methods Appl. Mech. Engrg.*, 315(August):972–1010 (2017). doi:10.1016/j.cma.2016.11.028.

[64] Mendoza, C. and Laugier, C. Simulating soft tissue cutting using finite element models. In *Proceedings - IEEE International Conference on Robotics and Automation*, volume 1, pages 1109–1114. Institute of Electrical and Electronics Engineers Inc. (2003). doi:10.1109/robot.2003.1241741.

[65] Miao, Y., Zhou, E., Wang, Y., and Cheeseman, B.A. Mechanics of textile composites: Micro-geometry. *Composites Science and Technology*, 68(7-8):1671–1678 (2008). doi:10.1016/j.compscitech.2008.02.018.

[66] Mozafary, V., Payvandy, P., and Rezaeian, M. A novel approach for simulation of curling behavior of knitted fabric based on mass spring model. *The Journal of The Textile Institute*, 109(12):1620–1641 (2018). doi:10.1080/00405000.2018.1453635.

[67] Niskanen, K. *Mechanics of paper products*. Walter de Gruyter (2012). ISBN 9783110254617.

[68] Onck, P.R., Van Merkerk, R., De Hosson, J.T.M., and Schmidt, I. Fracture of metal foams: In-situ testing and numerical modeling. In *Advanced Engineering Materials*, volume 6, pages 429–431. John Wiley & Sons, Ltd (2004). doi:10.1002/adem.200405156.

[69] Peng, X.Q. and Cao, J. A continuum mechanics-based non-orthogonal constitutive model for woven composite fabrics. *Composites Part A: Applied Science and Manufacturing*, 36(6):859–874 (2005). doi:10.1016/j.compositesa.2004.08.008.

[70] Popov, V.L. *Contact Mechanics and Friction*, volume 52. Springer Berlin Heidelberg, Berlin, Heidelberg (2010). ISBN 978-3-642-10802-0. doi:10.1007/978-3-642-10803-7.

[71] Reissner, E. On one-dimensional finite-strain beam theory: The plane problem. *Zeitschrift für angewandte Mathematik und Physik ZAMP*, 23(5):795–804 (1972). doi:10.1007/BF01602645.

[72] Romero, I. The interpolation of rotations and its application to finite element models of geometrically exact rods. *Computational Mechanics*, 34(2):121–133 (2004). doi:10.1007/s00466-004-0559-z.

[73] Sauer, R.A. and De Lorenzis, L. A computational contact formulation based on surface potentials. *Computer Methods in Applied Mechanics and Engineering*, 253:369–395 (2013). doi:10.1016/j.cma.2012.09.002.

[74] Sauer, R.A. and DeLorenzis, L. An unbiased computational contact formulation for 3D friction. *International Journal for Numerical Methods in Engineering*, 101(4):251–280 (2015). doi:10.1002/nme.4794.

[75] Schellekens, J.C.J. and De Borst, R. On the numerical integration of interface elements. *International Journal for Numerical Methods in Engineering*, 36(1):43–66 (1993). doi:10.1002/nme.1620360104.

[76] Secoli, R. and Baena, F.R.Y. Adaptive path-following control for bio-inspired steerable needles. In *Proceedings of the IEEE RAS and EMBS International Conference on Biomedical Robotics and Biomechatronics*, volume 2016-July, pages 87–93. IEEE Computer Society (2016). ISBN 9781509032877. doi: 10.1109/BIOROB.2016.7523603.

[77] Simo, J. A finite strain beam formulation. The three-dimensional dynamic problem. Part I. *Computer Methods in Applied Mechanics and Engineering*, 49(1):55–70 (1985). doi:10.1016/0045-7825(85)90050-7.

[78] Simo, J. and Vu-Quoc, L. A three-dimensional finite-strain rod model. part II: Computational aspects. *Computer Methods in Applied Mechanics and Engineering*, 58(1):79–116 (1986). doi:10.1016/0045-7825(86)90079-4.

[79] Simo, J. and Vu-Quoc, L. A Geometrically-exact rod model incorporating shear and torsion-warping deformation. *International Journal of Solids and Structures*, 27(3):371–393 (1991). doi:10.1016/0020-7683(91)90089-X.

[80] Stanova, E., Fedorko, G., Fabian, M., and Kmet, S. Computer modelling of wire strands and ropes Part I: Theory and computer implementation. *Advances in Engineering Software*, 42(6):305–315 (2011). doi:10.1016/j.advengsoft.2011.02.008.

[81] Sun, Y., Burgueño, R., Wang, W., and Lee, I. Modeling and simulation of the quasi-static compressive behavior of Al/Cu hybrid open-cell foams. *International Journal of Solids and Structures*, 54:135–146 (2015). doi:10.1016/j.ijsolstr.2014.10.030.

[82] Thakkar, B.K., Gooren, L.G.J., Peerlings, R.H.J., and Geers, M.G.D. Experimental and numerical investigation of creasing in corrugated paperboard. *Philosophical Magazine*, 88(28-29):3299–3310 (2008). doi:10.1080/14786430802342576.

[83] Trivisonne, R., Cotin, S., Kerrien, E., Trivisonne, R., Cotin, S., and Kerrien, E. Constrained Stochastic State Estimation for 3D Shape Reconstruction of Catheters and Guidewires in Fluoroscopic Images (2019).

[84] Vu, T., Durville, D., and Davies, P. Finite element simulation of the mechanical behavior of synthetic braided ropes and validation on a tensile test. *International Journal of Solids and Structures*, 58:106–116 (2015). doi:10.1016/j.ijsolstr.2014.12.022.

[85] Wriggers, P. *Computational Contact Mechanics*. Springer Berlin Heidelberg, Berlin, Heidelberg (2006). ISBN 978-3-540-32608-3. doi:10.1007/978-3-540-32609-0.

[86] Wriggers, P. *Computational Contact Mechanics*. Springer Berlin Heidelberg, Berlin, Heidelberg (2006). ISBN 978-3-540-32608-3. doi:10.1007/978-3-540-32609-0.

[87] Wriggers, P. *Nonlinear finite element methods* (2008). ISBN 9783540710004. doi:10.1007/978-3-540-71001-1.

[88] Wriggers, P., Krstulovic-Opara, L., and Korelc, J. Smooth C1-interpolations for two-dimensional frictional contact problems. *International Journal for Numerical Methods in Engineering*, 51(12):1469–1495 (2001). doi:10.1002/nme.227.

[89] Wriggers, P. and Zavarise, G. On Contact Between Three-Dimensional Beams Undergoing Large Deflections. *Communications in Numerical Methods in Engineering*, 13(6):429–438 (1997). doi:10.1002/(SICI)1099-0887(199706)13:6<429::AID-CNM70>3.0.CO;2-X.

[90] Wu, W. and Heng, P.A. An improved scheme of an interactive finite element model for 3D soft-tissue cutting and deformation. *The Visual Computer*, 21(8-10):707–716 (2005). doi:10.1007/s00371-005-0310-6.

[91] Yastrebov, V.A. and Breitkopf, P. *Numerical Methods in Contact Mechanics*. John Wiley & Sons, Inc., Hoboken, NJ USA (2013). ISBN 9781118647974. doi:10.1002/9781118647974.

[92] Zavarise, G. and De Lorenzis, L. The node-to-segment algorithm for 2D frictionless contact: Classical formulation and special cases. *Computer Methods in Applied Mechanics and Engineering*, 198(41-44):3428–3451 (2009). doi:10.1016/j.cma.2009.06.022.

[93] Zavarise, G. and De Lorenzis, L. The node-to-segment algorithm for 2D frictionless contact: Classical formulation and special cases. *Computer Methods in Applied Mechanics and Engineering*, 198(41-44):3428–3451 (2009). doi:10.1016/j.cma.2009.06.022.

[94] Zavarise, G. and Wriggers, P. A segment-to-segment contact strategy. *Mathematical and Computer Modelling*, 28(4-8):497–515 (1998). doi:10.1016/S0895-7177(98)00138-1.

[95] Zavarise, G. and Wriggers, P. Contact with friction between beams in 3-D space. *International Journal for Numerical Methods in Engineering*, 49(8):977–1006 (2000). doi:10.1002/1097-0207(20001120)49:8<977::AID-NME986>3.0.CO;2-C.

[96] Zienkiewicz, O., Taylor, R., and Zhu, J. *Finite Element Method - Its Basis and Fundamentals (6th Edition)*. Elsevier, London, 6 edition (2005). ISBN 978-0-7506-6431-8.